University College Dublin

Hardware and Embedded Firmware Development of a Gamma-Ray Burst Detector for a 2U CubeSat

Joseph Mangan
Student No. : 12339896

The thesis is submitted to University College Dublin in fulfilment of the requirements for the degree of Doctor of Philosophy

UCD School of Physics

Head of School:	Prof. E. Sokell
PhD Supervisor:	Prof. S. McBreen

Internal Examiner:	Prof. L. Hanlon
External Examiner:	Dr. R. Woolf
Examination Chair:	Prof. P. Dunne

November 2022

Contents

Abstract

Gamma-ray bursts (GRBs) are among the most extreme energetic events in the universe and represent the death knell of massive stars and compact objects. In one scenario, a massive and ancient star has burnt through its fuel reserve resulting in a core collapse event, a supernova. In the other, massive compact binary objects, like black hole - black hole (BH-BH), neutron star - black hole (NS-BH) and NS-NS pairs coalesce through merger events caused by the radiation of gravitational energy. In both cases a GRB may be observed. If the object is orientated just right, a beamed emission directed towards Earth may be detectable as a sudden, intense but brief flash of gamma-ray photons with a later afterglow emission observable in longer wavelengths for days to weeks after the initial event.

The advent of gravitational wave astronomy as a multi-messenger for high-energy astrophysical phenomena, along side recent advancements towards the miniaturisation of detector technology, have made it possible for CubeSat missions to perform cost-effective and fruitful science. Furthermore, widely accessible commercial-off-the-shelf hardware allows small non-agency institutions and universities to build robust missions with custom payloads for technology demonstrations and to contribute to the aims of the scientific community alongside traditional flagship missions.

The Gamma-Ray Module (GMOD) is a CubeSat compatible, scintillation based gamma-ray detecting instrument, with dimensions $<$1U (less than $10\,\mathrm{cm}\times10\,\mathrm{cm}\times10\,\mathrm{cm}$). GMOD has been developed primarily for the detection of GRBs and other high-energy electromagnetic phenomena from Earth orbit. This thesis will introduce GMOD through its origin, development and testing, its mission objectives and future outlook, all with respect to the astrophysical context of current high-energy astronomy and instrumentation.

During its mission, GMOD will experience the mechanical stresses induced during its launch, deployment and the sustained thermal and radiation effects of the harsh space environment. Furthermore, the instrument firmware will be expected to perform over long durations, often operating continuously for weeks on end. The instrument must be capable of performing effectively and to operate continually without disruption to the handling of science data. To achieve this, several tests have been conducted including a high altitude balloon flight, SiPM irradiation testing, subsystem thermal vacuum and vibration testing and a full benchmarking of the firmware performance and response to simulated GRB events.

The GMOD hardware has been fully tested in accordance with European Space Agency standards and the firmware has been rigorously assessed, while the methodology has been subject to peer-review. GMOD has been accepted for flight and will be flown in 2023 onboard EIRSAT-1, Ireland's first satellite, with an expected detection yield of $\sim$11–14 GRB triggers at 10σ significance. Once in operation, GMOD will contribute to the high-energy astronomy community and will be a demonstrator for future GRB detecting instruments.

Statement of Original Authorship

I hereby certify that the submitted work is my own work, was completed while registered as a candidate for the degree of Doctor of Philosophy, and I have not obtained a degree elsewhere on the basis of the research presented in this submitted work.

Joseph Mangan
(UCD)

Acknowledgements

I would like to begin by sincerely thanking Prof. Sheila McBreen for her guidance and support over the course of this PhD. The opportunity to undertake this work was an invaluable experience and I am forever grateful to have been given the chance to learn from her and to have been part of the EIRSAT-1 and GMOD project teams. I must mention particular appreciation for the thorough feedback which she provided, her advice which I frequently sought, along with my deep gratitude for our lengthy discussions which have made the work presented here and its foundation all the more robust. I couldn't have asked for a better supervisor.

In their capacity as my viva examination panel, I would like to thank Prof. Padraig Dunne, Prof. Lorraine Hanlon and Dr. Richard Woolf for taking the time to be part of the examination process, for their examination of this work, their efforts and for making this defence a thoroughly enjoyable and insightful experience for me.

I would like to express my gratitude and appreciation to the students and academics of the EIRSAT-1 team, members of the Fermi GBM Burst Advocacy team and in particular, the GMOD team who I have enjoyed working with over the last four years, have learned so much from and have become very fond of.

A special mention of gratitude is extended to Mike Hibbett, Dr. Brian Shortt and the academic and Physics Office staff of UCD, with particular thanks to Prof. Emma Sokell, Prof. Martin Grunewald, Prof. Lorraine Hanlon, Prof. Padraig Dunne, Dr. Robert Jeffrey, Dr. Morgan Fraser, Assoc Prof. Luis León-Vintró, Assoc Prof. John Quinn, Dr. Antonio Martin-Carrillo, Bairbre Fox and Angela Dunne O'Toole. I acknowledge funding from Science Foundation Ireland for this work under grant number 17/CDA/4723.

Finally, I would like to thank those who have supported me over the course of this work and who I have greatly missed over its duration, my friends and family, my Mother, Sister, Brother and my late Father. I would also like to express my heartfelt thanks to my good friend Milena Corcos who has made the years since we met all the more special.

List of Figures

List of Tables

Index of Acronyms

EGRET Energetic Gamma-Ray Experiment Telescope 27, 28

EGSE electrical ground support equipment 104, 106, 107, 110, 118, 158

EIRSAT-1 Educational Irish Research Satellite-1 12, 25, 32, 34–36, 47, 51, 55, 72, 73, 75, 97, 100, 102–105, 108, 110, 121, 125–127, 152, 156, 158, 159

EMC electromagnetic interference 126, 127

EMI electromagnetic compatibility 126, 127

EMOD ENBIO Module 33, 57

EPS electrical power supply 33

EQM engineering qualification model 37, 38, 46, 51, 104, 105, 115, 117, 125, 126, 128, 130, 131, 133, 149, 153, 157

ESA European Space Agency 32, 33, 75, 104, 106, 125, 127, 150

ETC environmental test campaign 32, 36, 38, 46, 55, 103, 104, 124, 128, 152, 155, 157, 158

eUSCI enhanced universal serial communication interface 49, 55, 57, 70

FE finite element 108, 110

FIFO first in first out 52, 56, 65

FITS Flexible Image Transport System 135, 138

FM flight model 34, 36, 47, 51, 56, 73, 104, 105, 109, 128, 153, 157–159, 161

FPGA field programmable gate array 51, 159

FRAM ferroelectric random access memory 49, 56, 60, 69–71

FRED fast rise and exponential decay 3

FSSC The Fermi Science Support Center 135

FTDI Future Technology Devices International 129, 154, 155

FTP File Transfer Protocol 135

FWHM full width half maximum 33, 37, 94, 96

FYS Fly Your Satellite! 32, 75, 125, 127, 150

G-APD geiger-mode avalanche photodiodes 23, 24

GBM Gamma-Ray Burst Monitor 1, 2, 4–8, 10, 11, 20, 24, 26, 30, 37, 51, 130, 133–139, 146–149, 158

GCN Gamma-ray Coordination Network 29, 31

Geant4 GEometry ANd Tracking 4 toolkit 30, 33, 73, 98

GECAM Gravitational Wave High-Energy Electromagnetic Counterpart All-Sky Monitor 12

GIFTS Gamma-Ray Investigation of the Full Transient Sky 30, 149, 159

GIOC GBM Instrument Operations Center 135

GM Geiger-Müller 15

GMOD Gamma-Ray Module x, 12, 23, 25, 33–58, 60–65, 67, 68, 70–73, 75–77, 96, 102–110, 112–119, 121, 122, 124–126, 128–130, 132–139, 142, 143, 145, 147–150, 152–159, 162–168

GMoDem Gamma-Ray Module Demonstration 77, 79–85, 87–96, 157

GNSS Global Navigation Satellite System 81

GPIO general purpose input output 64, 82, 129

GPS Global Positioning System 81–83

GRB gamma-ray burst 1–12, 15, 20, 21, 24, 25, 29–39, 49, 51, 56, 58, 60, 61, 67, 71, 72, 77, 102, 128, 130, 131, 133–141, 143–145, 147–149, 157–159, 161

GRD Gamma-Ray Detector 73–75, 77–79, 103, 157

GRIPS Gamma-Ray Imaging, Polarimetry and Spectroscopy 73, 75

GRM Gamma-Ray Monitor 73

GSE ground support equipment 106, 152

GTRB GMOD Top Reinforcement Bracket 46, 47, 105, 109, 124, 126
GW gravitational wave 1, 10–12, 159

HDL hardware description language 52, 106
HITL hardware–in–the–loop 35, 36, 55, 133, 149, 158, 161
HPGe high purity germanium 107, 108
HTV H-II Transfer Vehicle 110

I^2C Inter-Integrated Circuit 48, 54, 57, 64, 70, 71, 106, 143, 147–149, 153, 155
IBIS Imager on Board the INTEGRAL Satellite 29
IC integrated circuit 41, 75
IDE integrated development environment 51, 152, 155
InSight Interior Exploration using Seismic Investigations, Geodesy and Heat Transport 50
INTEGRAL International Gamma-Ray Astrophysics Laboratory 10, 11, 24, 29, 31
IO input output 43, 51, 66
IPA isopropyl alcohol 110, 114, 117
IPN Interplanetary Network 8, 24, 31, 32
IR infrared 115
ISM interstellar medium 9
ISP in-system programming 54
ISR interrupt subroutine 147, 148
ISS International Space Station 33, 97, 98, 100, 102, 110, 115
IUT item under test 105, 106, 116

JTAG Joint Test Action Group 54, 66

$LaBr_3$:Ce cerium doped lanthanum bromide 38–40, 73–76, 157
LAD Large Area Detector 30, 31
LAT Large Area Telescope 17, 27, 28
LED light emitting diode 88
LEO low Earth orbit 31, 33, 36, 48, 52, 54, 61, 63, 96–98, 100, 102, 104, 115
LIDAR light detection and ranging 24
LIGO Laser Interferometer Gravitational-Wave Observatory 10, 11
$LiSO_2$ lithium sulfur dioxide 81
LPM low power mode 49, 67, 132
LUT look up table 30
LVTTL Low Voltage Transistor Transistor Logic 51, 53, 57
LYSO lutetium yttrium oxyorthosilicate 74

MarCO Mars Cube One 50
MCS Mission Control Software 153, 155
MEGA Medium Energy Gamma-Ray Astronomy 28
MEGAlib The Medium-Energy Gamma-Ray Astronomy Library 30, 33
MoS margin of safety 108, 109
MPPC multi-pixel photon counter 20, 41

NaI sodium iodide xi, 2, 6, 17, 18, 30, 137, 138
NaI(Tl) thallium doped sodium iodide 24, 37, 135–138
NASA National Aeronautics and Space Administration 50, 77, 81
NCR non-conformance report 106, 115, 121
NIEL nonionizing energy loss 97, 98, 101, 103
NS neutron star 7, 10, 11
NVM non-volatile memory 52

OBC on-board computer 33, 48, 49, 52–58, 60–67, 70–72, 78, 80–82, 95, 130, 131, 134, 148, 150, 152, 153, 155, 156
op-amp operational amplifier 53, 82, 141, 142

PCB printed circuit board 37, 38, 41, 43, 44, 46–48, 54, 74–76, 78–80, 99, 100, 105, 107–110, 115, 118, 119, 122, 124, 154
PCM pulse code modulation 139
PDE photon detection efficiency 18, 24, 40, 42, 76

PDR preliminary design review 150
PHA pulse height analysis 43–46, 51, 60
PIF Proton Irradiation Facility 97, 99–101
PIN p-type, intrinsic type, n-type diode 21–23
PLA polylactic acid 78, 79, 87, 92, 93
PMT photomultiplier tube 17, 20, 21, 24, 26, 30, 39, 41, 75, 87–90
PPS pulse per-second 52, 54, 142, 143
PSI Paul Scherrer Institute 97, 99, 157
PSU power supply unit 53, 78, 80–83, 95, 102, 106, 130
PTFE polytetrafluoroethylene 36, 38, 46, 110, 113, 117
PTR post test review 106
PVC polyvinyl chloride 82
PWM pulse-width modulation 127

QC charge comparator 45, 46

RBF remove before flight 80–83
RC resistor–capacitor 41, 44, 78
RFT reduced functional test 107
RGA residual gas analyzer 115
RISC reduced instruction set computer 49
RMS root mean square 141
ROIC readout integrated circuit 51, 75, 80, 82, 99
RTD resistance temperature detector 33

S^3 Small Space Simulator 107, 118
SAA South Atlantic anomaly 11, 34, 97
SAP Subsystem Adaptor Plate 109, 110, 113
SAR successive approximation register 45, 49, 55
SBC single-board computer 51, 80, 96
SBW Spy-Bi-Wire 54, 154
SD Spectroscopy Detector 30
SDD silicon drift detector 15, 21, 26, 27
SDK software development kit 33
SEL single–event–latch–up 41
SER soft error rate 49
SEU single–event–upset 41
SIP Shaker Interface Plate 109, 110
SIPHRA Silicon Photomultiplier Readout ASIC 36, 37, 41, 43–46, 48, 49, 51–56, 58–60, 64–67, 75–80, 82, 87–89, 96, 99–101, 112, 119, 122, 124, 128–130, 133–135, 138–144, 149
SiPM silicon photomultiplier 17, 20, 21, 23–26, 33, 36–48, 52–56, 60, 73–82, 85–91, 93–103, 107, 110, 112, 115, 116, 121–124, 129, 130, 133, 142, 147, 157
SIRI Strontium Iodide Radiation Instrument 20
SN supernova 10
SoC system-on-chip 159
SPAD single photon avalanche diode 23
SPENVIS SPace ENVironment Information System 98
SPI Spectrometer on INTEGRAL 24, 29
SPI Serial Peripheral Interface 41, 43, 45, 46, 53, 69, 70, 82, 143, 155
SPI-ACS anti-coincidence system of SPI 10, 24, 25
SRAM static random access memory 49, 56, 60, 69
SSO Sun Synchronous Orbit 32, 33, 98, 102, 103
SVF Serial Vector Format 66
SVOM Space-based multi-band astronomical Variable Objects Monitor 12, 29

TAP Test Access Port 66
TDD test driven development 156
TH track and hold 43, 45
TI Texas Instruments 48–51, 53, 152, 154, 155
TPRO test procedure 106
TQCM thermoelectric quartz crystal microbalance 115
TRB test review board 106
TRL technology readiness level 12, 20, 25, 34, 36, 38, 159
TRP temperature reference point 116–121

TRPT test report 106
TRR test readiness review 106
TSPE test specification 106
TSTP test specification - test procedure 106
TTE time-tagged event ix, 44, 48, 49, 51–53, 55–65, 67, 69–72, 80, 128–144, 147–149, 152, 161
TTL Transistor–Transistor Logic 141, 142
TVAC thermal-vacuum chamber 107, 114, 115, 117–124, 126, 158

UART Universal Asynchronous Receiver/Transmitter 52, 154
UCD University College Dublin 32, 34, 75, 100, 101, 125
UI user interface 107, 118
UNH University of New Hampshire, Durham, USA 81, 84
USB Universal Serial Bus 81, 106, 155
UTC Coordinated Universal Time 80
UV Ultraviolet 17, 18
UVOT Ultraviolet Optical Telescope 29

VHDL Very High Speed Integrated Circuit Hardware Description Language 129

WAV Waveform Audio 134, 135, 138–141, 149, 158
WBC Wave-Based Control 33
WFI Wide Field Imager 29

XSVF Xilinx Serial Vector Format 54, 66

Chapter 1

Gamma-Ray Bursts and Instrumentation

1.1. Gamma-Ray Bursts

Gamma-ray bursts (GRBs) are the most luminous events in the universe (Vedrenne et al. 2009), finding their origin in the most extreme and intense environments; the coalescence of massive compact objects like black holes and neutron stars and the core collapse of massive stars through supernova (Burns 2020). These events are characterised by brief and intense flashes of gamma-ray photons which have a binomial distribution in duration (Kouveliotou et al. 1993), where the break between long and short GRBs is approximately 2 s. It has been accepted for quite some time that long GRBs are the result of core collapse supernovae (e.g. Hjorth et al. 2011). On the 17^{th} August 2017, the detection of gravitational wave (GW)170817 and its electromagnetic counterpart GRB170817A confirmed the theory that short GRB events were a result of the merging of massive compact objects, leading to the start of the GW and multi-messenger era of astronomy (Abbott et al. 2017a; Goldstein et al. 2017; Savchenko et al. 2017).

1.1.1. The Characteristics of Prompt Emission from Gamma-Ray Bursts

The initial prompt phase of a GRB is characterised by an intense but brief burst of gamma-ray photons, from which these extreme events derive their name. Early gamma-ray missions such as the Compton Gamma Ray Observatory (CGRO) (Fishman et al. 1992) and BeppoSAX (Boella, G. et al. 1997) sought to classify these events in terms of their spectral and temporal properties, event duration, sky distribution and their evolution in an effort to characterise their features and understand their origin. Missions like the Fermi Gamma-Ray Space Telescope (Meegan et al. 2009; Atwood et al. 2009) and the Neil Gehrels Swift Observatory (Gehrels et al. 2004) continue this work to this day and will soon be supported by CubeSat based instruments like BurstCube (Perkins et al. 2017) and the Cubesats Applied for MEasuring and LOcalising Transients (CAMELOT) mission (Werner et al. 2018). In terms of quantity, the Fermi Gamma-Ray Burst Monitor (GBM) instrument detects ∼240 GRBs per year (von Kienlin et al. 2020), while its predecessor, the CGRO Burst And Transient Source Experiment (BATSE) detected ∼300 GRBs per year (Fishman et al. 1994). A general overview of GRB characteristics are presented in the following sections.

1.1.1.1. Temporal Properties

A GRB light curve describes the variation of intensity of an event over time and is generated by arranging the individual detected gamma-ray photons into a time binned histogram. An example GRB light curve detected by the Fermi GBM instrument, and produced by Mangan et al. 2022a: GRB220527A (bn220527387) is presented in Figure 1.1.

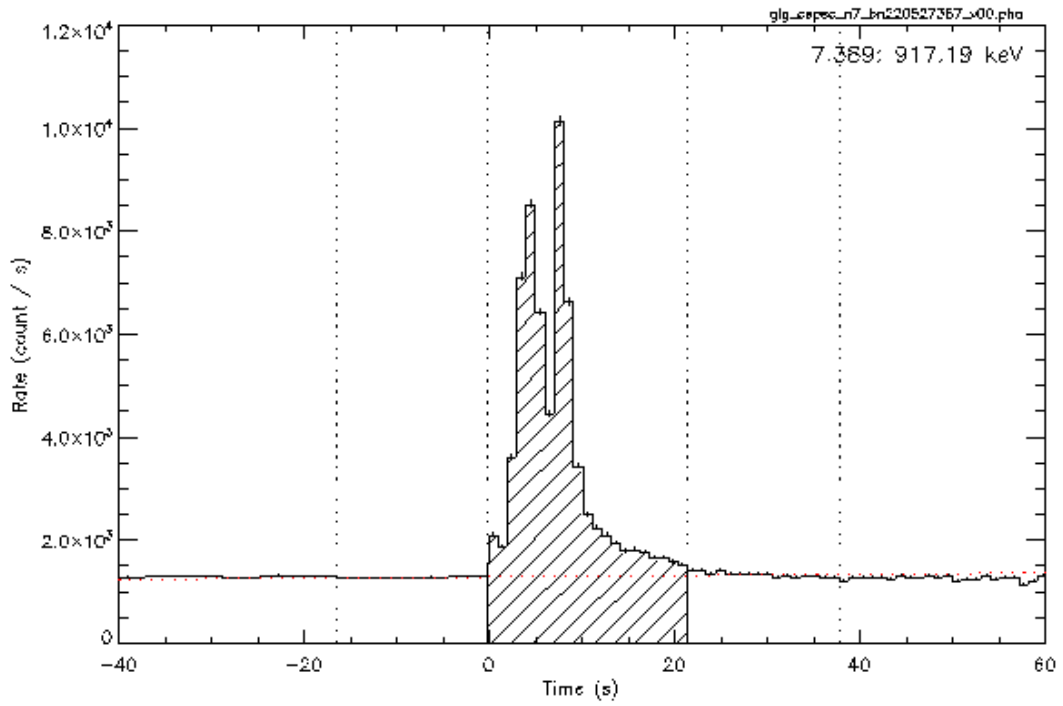

Figure 1.1: An example GRB light curve detected by the Fermi GBM instrument and produced using RMFIT for GRB 220527A (Mangan et al. 2022a) (data accessible from the NASA HEASARC archive). This particularly bright event occured on 02/05/27 at 18:13:27 GMT and features two main emission episodes, what appears to be a minor precursor at T_0 seconds and a relativity flat background which it sits upon. This burst appears to have triggered GBM at T_0 on the precursor pulse, while the main emissions occur $\sim T_{+4}$ and $\sim T_{+7}$ seconds, respectively. Finally a decaying exponential tail is also evident, extending from $\sim T_{+10}$ to $\sim T_{+20}$ seconds. The burst source selection is shown as the hatched region, while the background selection is shown as the two dashed intervals pre and post burst. This light curve includes photon energies from 8 KeV – 900 keV, the full operating range of the sodium iodide (NaI) GBM instrument. GCN 32133 - GRB 220527A - 2/05/27 18:13:27 GMT.

The temporal properties of these GRB light curves are highly diverse, complex and distinct from one event to another and as such, there is no one predictable GRB profile template. This is exemplified in Figure 1.2, showing a collection of GRB light curve profiles collected by the CGRO BATSE instrument. As can be observed from this set (Fishman et al. 1994) and others like it (von Kienlin et al. 2020), GRB light curves can exhibit a wide diversity of morphologies.

For example, some events have a single emission episode, while others can have multiple emissions or fine structures which are separated by relatively short or long time breaks. Some events are strong, while others are weak and are barely distinguishable above background. Certain temporal events or features within events may be composed predominantly of hard (higher energy) gamma-ray photons, while others may be predominantly of soft (lower energy) gamma-rays (or even down to x-ray energies, provided the light curve includes lower energies within the integration). One form which is very common is that of a fast rise component superimposed

against a slower decay component called the fast rise and exponential decay (FRED) burst profile (Yu et al. 2022). Other events have a weak precursor event (Lazzati 2005), heralding a much more intense emission immediately or up to tens of seconds later, while some have long extending tails which evolve spectroscopically over the emission duration. In fact, attention to the distribution of event duration and spectral hardness can be used to infer a classification and probe at two distinct progenitors, as will be discussed in Section 1.1.1.2, Section 1.1.1.3 and Section 1.1.2.

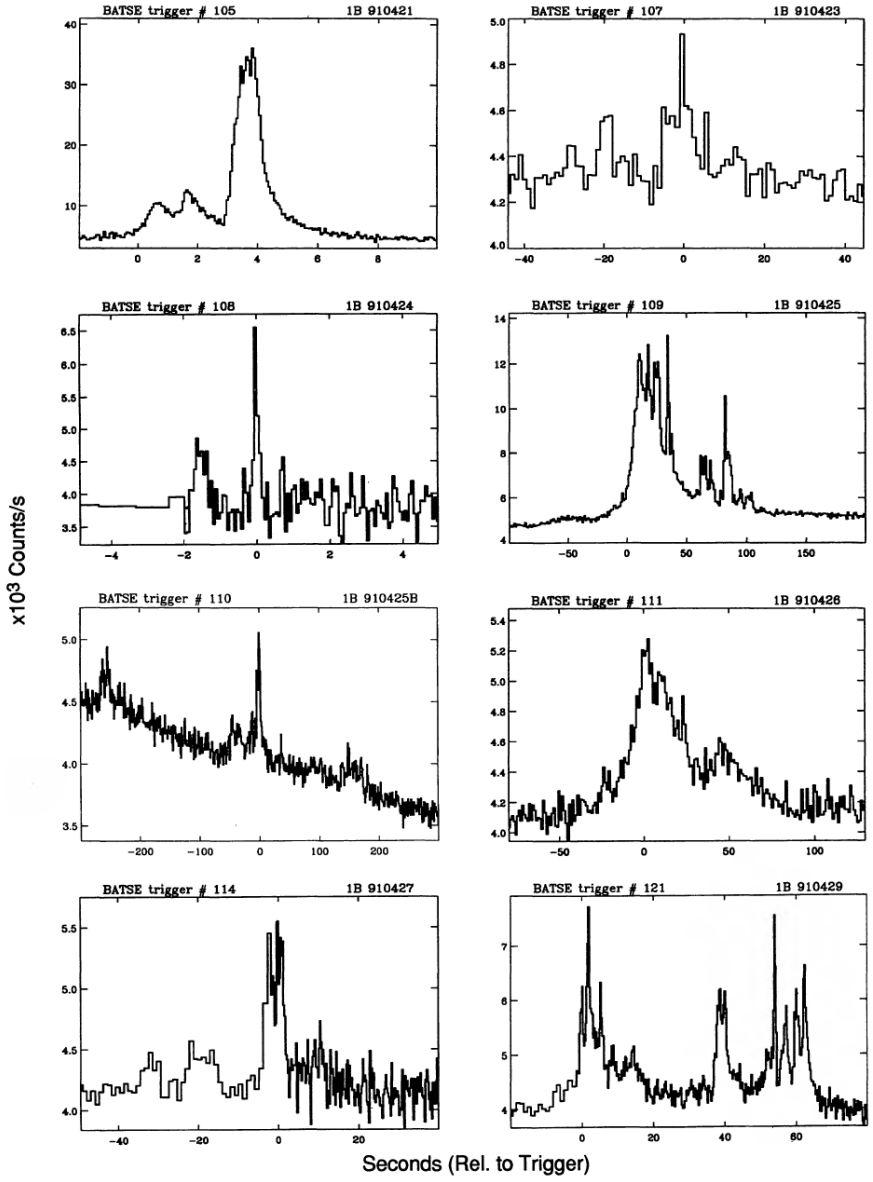

Figure 1.2: A collection of GRB light curves measured by the CGRO BATSE instrument and compiled into the first BATSE GRB catalogue. Adapted from Fishman et al. 1994. As can be seen from this small selection, there is a wide diversity of GRB profile with no single identifiable form common between all.

1.1.1.2. T_{90} Duration and the Bimodal Distribution

Measuring the duration of a GRB can be made difficult by events with multiple emission episodes or for weak bursts which do not present distinctly above the background. For this

reason, a method of duration determination called the T_{90} was developed, which defines the time interval between collection of 5% up to 95% of total fluence over the burst duration. A similar T_{50} can also be defined which is the collection between 25% up to 75% of total fluence, though the T_{90} measurement is more commonly quoted. As mentioned, when observing the distribution of T_{90} duration for a sample of GRB events, a distinction between two populations of dissimilar duration becomes apparent. This classification was first noted by Kouveliotou et al. 1993 and is referred to as the bimodal distribution of GRB events. Essentially it describes a population of short GRBs which have durations approximately $\leq$2 seconds and a population of long GRBs which have durations approximately $>$2 seconds, as recently corroborated by the Fourth Fermi GBM GRB Catalogue (von Kienlin et al. 2020).

This would imply two distinct GRB types, short and long GRBs. As will be discussed in Section 1.1.1.3, a further delineation can be exposed by the spectral hardness of both populations (i.e. short-hard and long-soft). By extension, this would also suggest two separate generation mechanisms or progenitor events, which will be explored further in Section 1.1.2. An additional third, soft-intermediate, classification is sometimes suggested as opposed to just the two component model of the bimodal distribution, however there is limited evidence supporting the existence of a third component (Bhat et al. 2016).

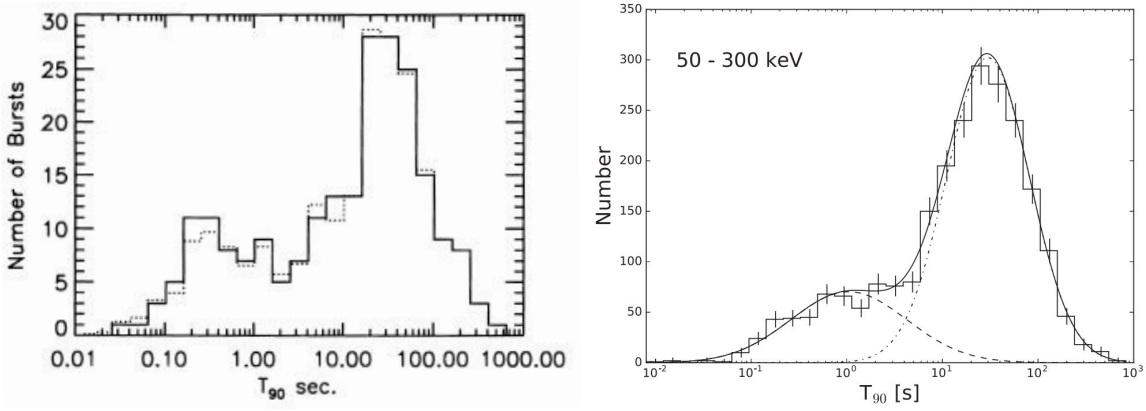

(a) Kouveliotou et al. 1993

(b) von Kienlin et al. 2020

Figure 1.3: The bimodal distribution of GRB events, showing a clear distinction between a population of short ($\leq$2 s) and long ($>$2 s) GRBs. a) The bimodal distribution first noted in Kouveliotou et al. 1993 using CGRO BATSE data. b) The most recent bimodal distribution developed with the Fermi GBM data (von Kienlin et al. 2020).

1.1.1.3. Spectral Properties

An energy binned spectrum, integrated over the duration of a burst can be produced revealing a simple broad continuum which is best fit using a smoothly broken power law, called a Band model (Band et al. 1993a) and which tends to peak within the standard BATSE 50 – 300 keV energy range. This is an empirically derived model, typically suggesting evidence of non-thermal emission (Ghirlanda et al. 2007), proposing an origin involving synchrotron emission or inverse Compton scattering caused by relativistically accelerated electrons (Tavani 1996).

An example GRB spectrum, best fit with a Band model was produced by Mangan et al. 2022a: GRB220527A (bn220527387) and is presented in Figure 1.4.

The Band model, which adequately fits most GRB spectra is defined in Equation (1.1) in terms of photon flux, with units of $[ph\,s^{-1}\,cm^{-2}\,keV^{-1}]$ (Poolakkil et al. 2021), as a function of energy E in keV. The parameters of this model include A, a normalisation constant, α and β as the low and high-energy power law indices respectively, and E_{peak} representing the characteristic break energy correlating with the peak in the differential νf_ν spectrum (Gehrels 1997). A pivot energy parameter is also included and is fixed as 100 keV in the denominator of the main terms of the model. For most GRBs the band model fits with α and β parameters ∼-1 and ∼-2 respectively and E_{peak} ∼200 - 300 keV (Preece et al. 2016; Yu et al. 2022).

$$f_{BAND}(E) = A \begin{cases} \left(\frac{E}{100\,keV}\right)^{\alpha} exp\left[-\frac{(\alpha+2)E}{E_{peak}}\right] & , E < \frac{(\alpha-\beta)E_{peak}}{\alpha+2} \\ \left(\frac{E}{100\,keV}\right)^{\beta} exp(\beta-\alpha)\left[\frac{(\alpha-\beta)E_{peak}}{100\,keV(\alpha+2)}\right]^{\alpha-\beta} & , E \geq \frac{(\alpha-\beta)E_{peak}}{\alpha+2} \end{cases} \tag{1.1}$$

In other circumstances when the detectors energy band is not wide enough, or for fitting weak GRBs (Yu et al. 2022), or in cases where a thermal or quasi-thermal Comptonization element is evident (Ghirlanda et al. 2007), a smoothly broken power law with a high-energy cut off may be used, refereed to as a Comptonised model. This is another empirical model which is usually best fit and considered valid when the β parameter of the Band model is poorly constrained (Li 2021). As can be seen from its expression in Equation (1.2), this is simply the Band model without the high-energy component. Finally, if the Comptonised model does not produce a good fit, a simple power law, like that described in Equation (1.3) may be used, where λ represents the photon index. While these models tend to point towards a non-thermal emission origin, none of these models explicitly describe a physical process at the heart of the GRB emission and in some cases where a thermal blackbody component is presented (i.e. photospheric emission from the fireball (Bhat et al. 2011)) a blackbody model is required to fully describe the spectrum.

$$f_{COMP}(E) = A\left(\frac{E}{100\,keV}\right)^{\alpha} exp\left[-\frac{(\alpha+2)E}{E_{peak}}\right] \tag{1.2}$$

$$f_{PLAW}(E) = A\left(\frac{E}{100\,keV}\right)^{\lambda} \tag{1.3}$$

Another perspective to view the spectral nature of GRBs is in their hardness ratio, defined as the ratio between accumulated counts within a low-energy and a high-energy band. For example, the harness ratio $HR_{50-300\,keV} : HR_{10-50\,keV}$ (Poolakkil et al. 2021), the number of counts within the high band against the low band, would be >1 for a spectrally hard event, and <1 for a spectrally soft event. Comparing the distributions of hard and short GRB events and soft and long GRB events indicates a correlation between the event nature: short GRBs are typically harder and composed of a higher ratio of high-energy gamma-ray photons as compared to long soft GRBs. For instance, Figure 1.5 from the 10 year Fermi GBM catalogue (von Kienlin et al. 2020) shows the relationship between hardness ratio and T_{90} duration, describing

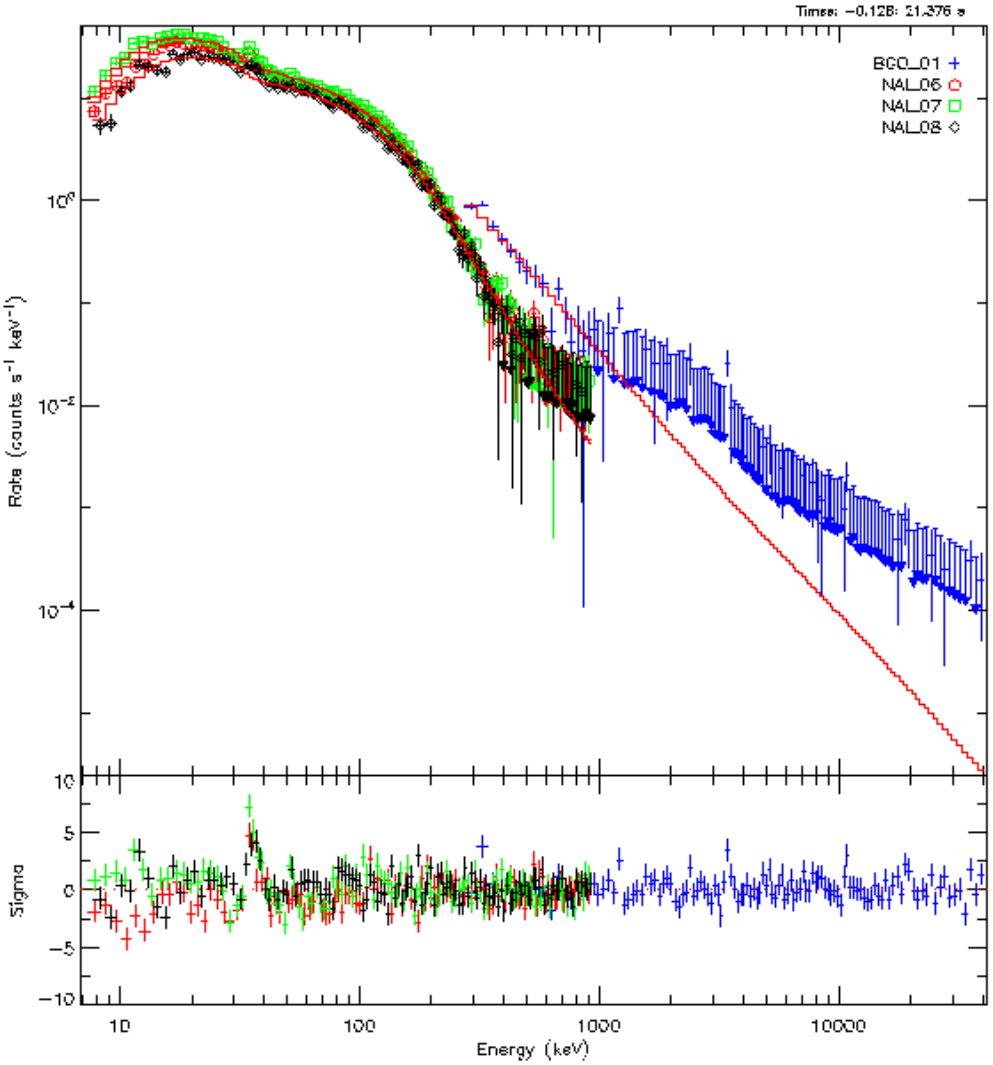

Figure 1.4: An example GRB spectrum measured by the Fermi GBM instrument and produced using RMFIT for GRB 220527A (Mangan et al. 2022a) (data accessible from the NASA HEASARC archive). This spectrum uses data collected from multiple GBM NaI detectors and one of the bismuth germanium oxide (BGO) detectors. The energy range of the NaI and BGO detectors overlap, where the blue crosses represent data derived from the BGO instrument and all others represent a selection of NaI detectors which were chosen due to their optimal orientation with respect to the burst origin. This spectrum is integrated from the period $T_{-0.128s}$: $T_{+21.376s}$ (see Figure 1.1). This figure shows the best fit (according to C-Stat/DOF) for a Band function Equation (1.1) with E_{peak} 151.6 $\pm$ 2.7, α = -0.75 $\pm$ 0.02 and β = -2.55 $\pm$ 0.05. GCN 32133 - GRB 220527A - 2/05/27 18:13:27 GMT.

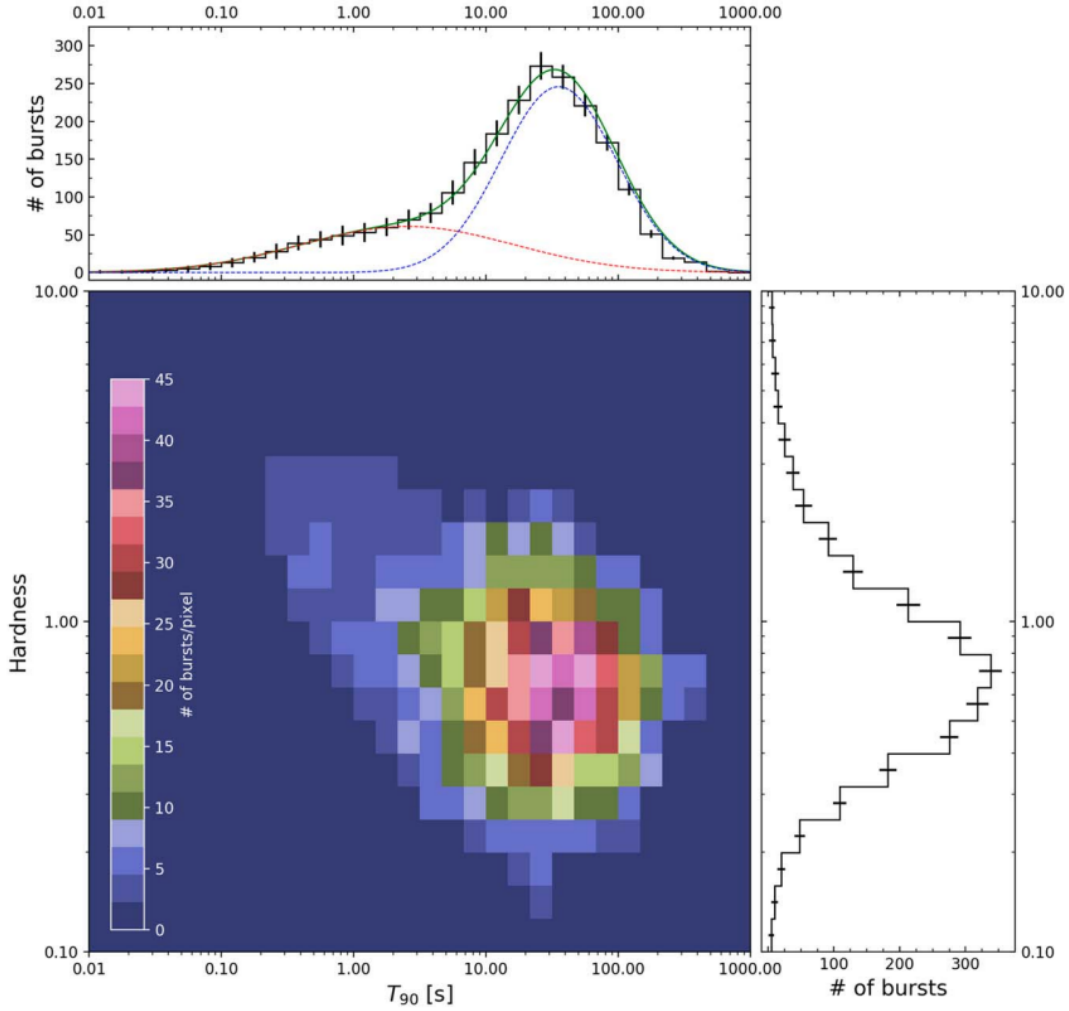

Figure 1.5: A two dimensional probability density plot of both spectral hardness and T_{90} duration, while the top and right most panel correspond to the individual probability density plots of both hardness and duration respectively. This plot describes the relationship between hardness ratio and T_{90} duration and is derived from the Fermi GBM catalogue (von Kienlin et al. 2020).

an apparent population of short hard GRBs distinct from the longer soft GRBs sample. This further indicates a distinction between the GRB types and drives the understanding that two independent astrophysical mechanisms are responsible for these two events.

1.1.1.4. Angular Distribution

The determination of the origin of GRB events must start with the obvious question of where they are originating from, i.e. are they galactic, extra galactic or cosmic in origin? Depending on the distance, this question also feeds into the luminosity and the amount of energy understood to be released during these events. In the beginning of GRB astronomy, it was believed that the origin lay with neutron stars (NSs) within the galactic disk (Atteia et al. 2021). This was for a couple of reasons, firstly measurements of the spectra from GRBs appeared to show evidence of non-thermal emissions, such as the detection of a 400 keV line which was suggested to be as a result of 511 keV annihilation photons (Section 1.2.2.3) generated by the acceleration of electrons within the intense magnetic fields of a NS and which were shifted down due to

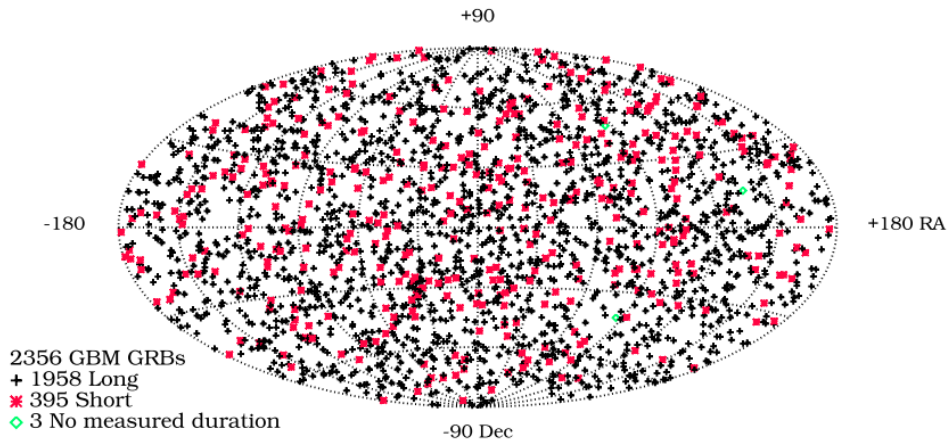

Figure 1.6: The full sky isotropic distribution of GRB events detected by the Fermi GBM instrument using 2356 GRBs as listed in the most recent 4^{th} Fermi GBM catalogue (reproduced from von Kienlin et al. 2020).

the large gravitational influence at the star surface. This would rely on a distribution of GRBs around the galactic plane and a notable anisotropic arrangement across the sky. One of the benefits of this theory was that it allowed a reasonable amount of energy (10^{38} erg) to be involved in the emission.

The first attempts to measure the angular distribution of GRBs came from the Interplanetary Network (IPN) (Hurley et al. 2021) (to be discussed in Section 1.4.2) and the Konus experiment (Mazets et al. 1981) which localised 171 GRBs using both the triangulation and anisotropic response techniques outlined in Section 1.4. These measurements revealed that the distribution was in fact isotropic as opposed to restricted to the galactic disc or any other particular region (i.e. the galactic center or other structures such as the Virgo cluster, Andromeda M31 or the Magellanic Clouds), implying that GRB events were in fact not galactic in origin. Later measurements of a population of 260 GRBs by the CGRO BATSE (Fishman et al. 1994) and most recently the Fermi GBM (von Kienlin et al. 2020) further confirmed the isotropic nature of GRBs (as seen in Figure 1.6). This implies much more energy being involved in GRB events much greater than (10^{38} erg) and often quoted up to and beyond 10^{52} erg (Atteia et al. 2021). The detection of the afterglow of many bursts, and subsequently the redshift measurements of either the afterglow or host galaxy, confirms the extragalactic nature of these events (Atteia et al. 2021), for example as with GRB170817A (Coulter et al. 2017; Drout et al. 2017) and GRB200826A (Ahumada et al. 2021).

1.1.2. The Fireball Model and GRB Progenitors

The fundamental characteristics of GRB events as observed from many mission over the past half-century has been explored from a high level perspective in Section 1.1.1. Although many origin mechanisms have been proposed, the most successful and commonly cited is the Fireball model, introduced first by Cavallo et al. 1978 and encapsulated in Figure 1.7.

This model describes the prompt emission as originating from a central engine, which drives

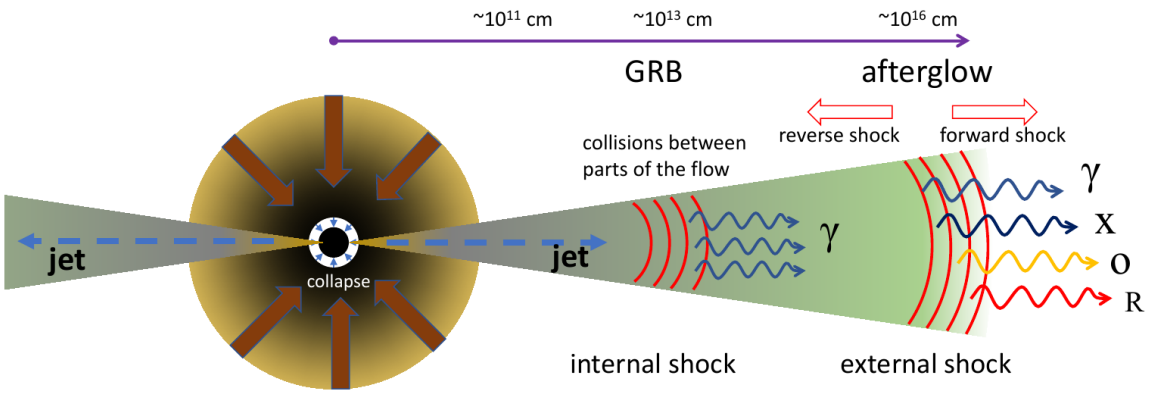

Figure 1.7: The Fireball model, describing the production of a collimated jet of relativistic material driven by the central engine. This material forms shells that propagate at dissimilar velocities and collide, resulting in internal shock events that correspond to the prompt emission of a GRB event. Reproduced from Dado et al. 2022.

the outflow of relativistically accelerated material (composed of electrons, positrons, photons and a small amount of baryons (Bhat et al. 2011)) in collimated jets from either pole of the rotating body (Atteia et al. 2021). As the jet outflow is variable and inhomogeneous, material is accelerated in separated regions of high density called shells which propagate at different rates from the central engine. Eventually, it is possible for some of these shells to collide into slower moving shells in what is called the internal shock. In this phase, ejecta composed of charged particles within the shock region are further accelerated. The electrons undergo synchrotron emission (Longair 2011) as they gyrate within the intense magnetic field producing the gamma-ray photons detected during the prompt phase of the GRB. Each of the separate emission peaks in a binned light curve can be considered to correspond to individual internal shock episodes between different shells propagating at dissimilar velocities (Bhat et al. 2011). According to this model, the duration of the GRB event also corresponds to the duration of activity of the central engine.

As the jet material eventually collides with the interstellar medium (ISM), the deceleration of the ejecta results in what is called an external shock. This has two components: a forward shock which continues its propagation away from the central engine, and a reverse shock which is essentially a reflection of the jet as it rebounds off the ISM. During the external shock phase the relativistic charged particles again undergo synchrotron or inverse Compton scattering (the up scattering of lower energy photons into higher energy photons) which results in the detected afterglow phases of the GRB, detectable in multi-wavelength follow ups to the prompt emission.

In this model, the central engine is created via some form of extremely energetic event. The large distances involved, along with the typical fluences measured by GRB detecting gamma-ray instruments imply an intense amount of isotropic energy must be released during a GRB, on the order of $\sim 10^{50-51}$ erg (Yu et al. 2022). As described by Yu et al. 2022, such a huge release can only be supplied by the gravitational energy produced during the catastrophic contraction

of a massive compact system, from a large size to a few tens of kilometres.

For many decades, the collapsar model has been associated with long GRB events, which describes a compact object whose iron core collapses forming a black hole (BH) (Atteia et al. 2021). The remaining material from the collapsed star is then accreted as a disk around the fast spinning black hole. A relativistic jet of material is then produced as described with the Fireball model. This is supported by observation (Schönfelder 2001), a notable example of this is the coincident detection of SN1998bw which was associated with GRB980425 (Galama et al. 1998). Alternatively, short GRBs have traditionally been strongly associated the coalescence of massive compact objects, like NS-NS mergers, NS-BH mergers or BH-BH mergers (Kochanek et al. 1993). As two massive compact objects orbit each other, they slowly radiate gravitational energy (Burns 2020). Over time the orbit decays with the objects slowly starting to inspiral, while accelerating due to the shrinking of their orbital separation. The increase in acceleration further strengthens the gravitational energy emission, until such a point that both objects coalesce in an extremely energetic event. The remnant object begins to ring down while the remaining material forms a disk which is accreted onto the object, again as before, producing a highly collimated jet as described by the Fireball model. This was most prominently observed for GW170817, along with the electromagnetic counterpart GRB170817A, starting the era of multi-messenger astronomy.

1.1.3. Gravitational Waves and Multi-Messenger Astronomy

To date, there have only been three coincident detections which could be described as being observed through multi-messenger astronomy (Burns 2020), the most notable being the coincident detection of GRB170817A and GW170817 (Abbott et al. 2017a). However, messengers from objects other than GRB related events have been detected, including the well known detection of neutrinos in coincidence with photons from the core collapse of supernova (SN)1987A (Hirata et al. 1987) and the flaring blazar, TXS 0506+056 (IceCube Collaboration et al. 2018).

On the 17^{th} August 2017, the Advanced Laser Interferometer Gravitational-Wave Observatory (LIGO) and the Virgo gravitational wave facility network detected a GW event originating from the coalescence of a binary NS pair (Abbott et al. 2017b). Approximately 1.7 s later the Fermi GBM (Goldstein et al. 2017) and the International Gamma-Ray Astrophysics Laboratory (INTEGRAL) anti-coincidence system of SPI (SPI-ACS) (Savchenko et al. 2017) triggered on a weak short GRB, the first ever coincident detection of a GW with an electromagnetic counterpart. Hours later, an optical transient (Coulter et al. 2017; Drout et al. 2017) and kilonova (Smartt et al. 2017) were detected in the region localised by the joint contribution for LIGO/Virgo and GBM/SPI-ACS, providing the multi-wavelength component and redshift measurements.

The consequences of this event were profound. In practical terms, the combined data produced by LIGO and Virgo along with INTEGRAL SPI-ACS and the Fermi GBM allowed a precise localisation and subsequent follow up campaign. This coincident detection also meant cross corroboration of the classification of the event. As the gravitational signal detected by the

LIGO/Virgo collaboration was capable of determining the combined mass of the progenitor object (Abbott et al. 2017b), the progenitor could be narrowed down to a NS-NS binary system. For the first time this confirmed the long held theory that short GRB events were produced by the inspiral of massive compact objects like NS-NS mergers. With respect to the implication of this discovery, this provides a confirmation of the progenitor of some short GRB events. But also more fundamentally (Bailes et al. 2021) it provides constraints on the speed of gravity and the Hubble constant as it may be used as a form of cosmological standard candle reference. It also presents a window into the the remnant object after the merging and the physics behind these extreme events.

The future of GW detection will see upgrades to the existing interferometry based instruments and the completion of further ground based detectors, like the Einstein Telescope (Maggiore et al. 2020). However to continue extracting the benefits of the new era of multi-messenger astronomy, a full sky coverage of the high-energy regime is required (Perkins et al. 2017). At the time of detection of the first recorded electromagnetic counterpart to a GW, only two of the main flagship missions detected the prompt transient. This is due to the fact that other GRB detecting instruments were at the time occulted by the Earth or were not available to observe the event. Furthermore, the Fermi GBM instrument triggered on GRB170817A just before it reached the cusp of the South Atlantic anomaly (SAA), a region where detectors are disabled due to the concentration of high-energy particles. Therefore, to achieve the most scientific return from these instruments and this new era of astronomy, it is essential that the total sky at any given time is being observed, such that short transient events are not missed and coincident detections can be measured. A promising solution to this is the drive towards CubeSats and nano satellites, developed to test new technology, utilize miniaturised high performance instrumentation and to contribute to the monitoring of the full transient sky.

1.1.4. CubeSats in the Era of Multi-Messenger Astronomy

CubeSats are miniaturised satellites whose standard dimensions are in units of "U", where 1U describes a spacecraft of up to 2 kg which is $10\,\text{cm} \times 10\,\text{cm} \times 10\,\text{cm}$ in cubic volume, as defined by the CalPoly CubeSat Design Specification (Johnstone 2021). This is a scalable system where CubeSats may be built in multiples of U such as 1U, 1.5U, 2U, 3U, 6U and 12U. CubeSats from 1U–3U scale in terms of their length, morphing from a cube to a cuboid, where the base remains $10\,\text{cm}^2$ (i.e. ranging from length of 10 cm to 30 cm). CubeSats with larger dimensions, like 6U and 12U remain the same length, but instead scale from their width and depth by adding two 3U and four 3U CubeSats together respectively. Naturally the mass allocation also scales with increasing volume up to 24 kg for 12U spacecraft.

One aspect that makes CubeSats so advantageous is their low risk, minimal cost, fast development time and when considering these factors, their ability to take advantage of technology which has limited flight heritage. These qualities are also attractive for gamma-ray astronomy. The current fleet of GRB detecting spacecraft (Fermi (Meegan et al. 2009; Atwood et al. 2009), INTEGRAL (Winkler et al. 2003), the Neil Gehrels Swift Observatory (Gehrels et al. 2004))

have exceeded expectation, operated far longer than anticipated and will continue to perform in their respective missions. However, with this ageing comes the possibility of loss of capabilities or eventual wind down of operations.

The prospect of this in the early stages of the multi-messenger era and when GW detectors are becoming more sensitive will mean a loss of scientific return. There will simply not be enough GRB detecting instruments, with the required sensitivity or unocculted view of the sky which will be available to contribute to localisation, measurements of fluence, duration and spectral characterisation. Further exacerbating this situation is the fact that, with the exception of mission like the Gravitational Wave High-Energy Electromagnetic Counterpart All-Sky Monitor (GECAM) (Zhang et al. 2019) and the Space-based multi-band astronomical Variable Objects Monitor (SVOM) (Atteia et al. 2021), there are currently no new large scale dedicated GRB detecting mission or missions currently under development by any major space agency other than those which are still classified as mission concepts.

CubeSats offer a new way of performing gamma-ray astronomy. While their dimensions, mass and power requirements may pose some limits (Arneodo et al. 2021), for the most part the platform provides numerous advantages. This includes being able to use modern, compact low technology readiness level (TRL) equipment, the low risks associated with the minimal costs to develop, launch and operate these spacecraft and the ability to produce multiple instruments ultimately granting the ability for a true unocculted view of the gamma-ray/transient sky (Perkins et al. 2017). The Educational Irish Research Satellite-1 (EIRSAT-1) mission (Murphy et al. 2018) (see Section 1.5) is one such CubeSat which can contribute to this future. The following sections will lay the technical groundwork and context to the Gamma-Ray Module (GMOD), a CubeSat compatible GRB detecting instrument and the primary science payload on EIRSAT-1.

1.2. Detectors and Material Interactions in Gamma-Ray Instruments

1.2.1. Photons, Electromagnetic Waves and Ionising Radiation

For the purposes of this discussion, ionising radiation can be subdivided into two groups, particle radiation (e.g. α, β particles), consisting of high-energy and relativistically accelerated particles and photonic radiation (e.g. x-ray, gamma-ray particles), which consists of energetic photons with sufficient energy to ionise atoms through a number of interactions mechanisms (Section 1.2.2). High-energy photons are of particular interest in the detection of GRBs simply due to the prompt emission of these events being characterised by a sudden intense flash of gamma-ray photons (though other messengers do exist (Section 1.1.3). The boundary distinguishing x-ray photons from gamma-ray photons in terms of either photon energy or wavelength is not well defined (as seen in Figure 1.8) and is often chosen based on the convention and circumstances of the field in which they are discussed. In the context of the material discussed in this thesis, the boundary for classification will be such that energies $>$30 keV are considered the domain of gamma-rays. As the following section will discuss the interaction mechanisms between matter and gamma-rays, it is mostly convenient to frame light in terms of photons with

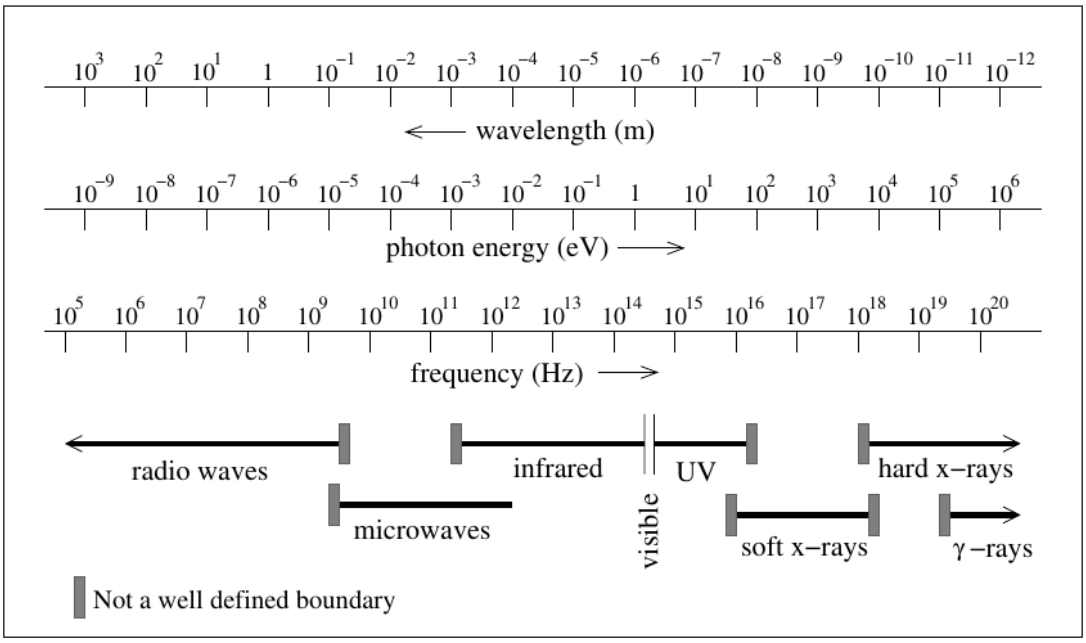

Figure 1.8: The electromagnetic spectrum and corresponding scale of photon energy, showing the undefined boundary between x-ray and gamma-ray energy photons. Reproduced from Ahmed 2017.

quantised energy, as opposed to waves with respect to wave-particle duality.

1.2.2. Material Interactions

The penetrating nature of high-energy photons makes it difficult to measure them in ways which are analogous to low-energy photons. X-rays and gamma-rays cannot be collected using the same means as are exploited on other telescopes via focusing or reflection (though depending on the energy it is possible to reflect at shallow grazing angles). Instead, to measure an x-ray or gamma-ray photon, it is necessary to absorb the photon energy and proportionally reproduce the quantised energy into some means which can be measured using an electronic front end system. For this reason, the following main modes of photon interactions of gamma-ray photons are discussed below, these being photoelectric absorption, Compton scattering and pair production.

1.2.2.1. Photoelectric Absorption

Photoelectric absorption (Gilmore et al. 1995) describes the process where a single photon interacts with an atom of an absorbing material, is completely absorbed and produces an energetic electron as a result. The mechanism behind this phenomena is called the photoelectric effect which was first described in 1905 (A.Einstein 1905), in which the interacting photon has sufficient or greater energy to liberate an electron, most likely, from the inner K shell of the atom. The ejected electron then has energy equal to the difference between the incident photon ($h\nu$) and the binding energy (E_b) (Equation (1.4)) which the interacting electron was initially subjected to. The ejection of the inner K electron causes an instability in the ionised atom, which is equalised by a weaker bound electron from an outer shell descending and filling the vacancy. In the process the descending photon emits an x-ray photon, referred to as x-ray florescence,

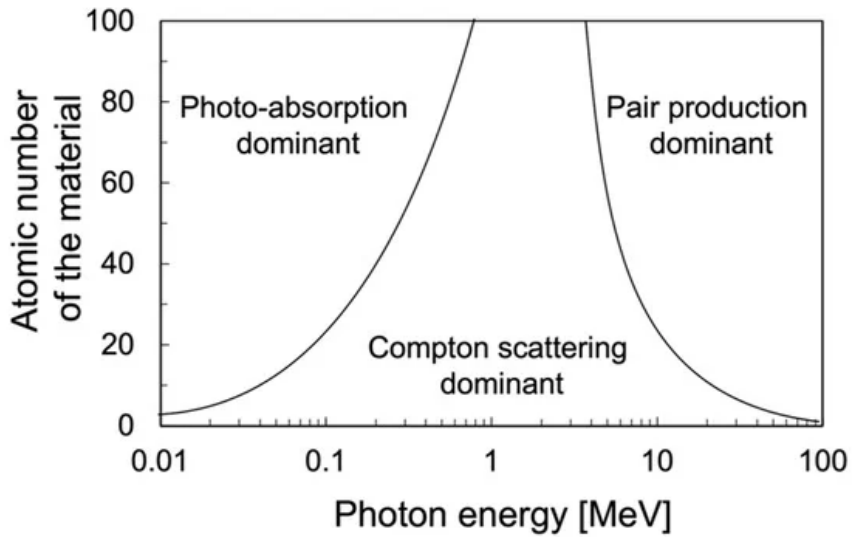

Figure 1.9: A diagram describing the likelihood of each of the interaction methods discussed in this section and their respective region of dominance as a function of photon energy for the material atomic number. Reproduced from Parajuli et al. 2022.

where the energy is the difference between the two corresponding shell binding energies. This process is visually depicted in Figure 1.10. This is a conversion of a single photon into an electron, with excess energy being retained by the ejected electron. In other words this is a complete absorption of the photon energy into the absorbing material. As will be discussed, in Section 1.2.3, this is most desirable as it allows a complete measurement of the photon energy, resulting in a photopeak in the integrated spectrum.

$$E_e = h\nu - E_b \tag{1.4}$$

1.2.2.2. Compton Scattering

Compton scattering contrasts against photoelectric absorption as a partial absorption of the incident photon energy. First described in 1923 (Compton 1923), Compton scattering describes the inelastic scattering of a photon through interaction with an electron from a weakly bound shell of an atom. When a photon with energy sufficiently greater than the outer shell binding energy of a material interacts with an "almost" free electron (Ahmed 2017), both the electron and photon are scattered. The photon is deflected at an angle θ and transfers a portion of its energy to the liberation of the electron, where the energy exchanged is a function of the angle θ, according to Equation (1.5).

$$E_\gamma = E_{\gamma 0}\left[1 + \frac{E_{\gamma 0}}{m_0 c^2}(1 - cos\,(\theta))\right]^{-1} \tag{1.5}$$

Where $E_{\gamma 0}$ represents the incident photon, $m_0 c^2$ is the rest-mass energy of the electron, θ is the scattering angle of the scattered photon and E_γ is the scattered photon. This is also illustrated with θ shown in Figure 1.11.

The energy transfer is dependent on the angle of scattering of the photon; according to Equation (1.5), low angle scattering results in low-energy transfers (the incident photon loses little energy), while scattering angles approaching π have the highest energy transfer (the incident photon loses most of its energy). For example, a photon with a scattering angle near 0° will transfer the least amount of energy to the material while retaining the maximum amount, and vice versa for large angles approaching 180°.

As all angles of scattering are possible, this effect consequently produces a spectral continuum starting from the Compton edge, the photopeak energy minus half the rest energy of the electron (E_γ - 255 keV) extending down to lower energies. This is particularly evident in the spectra of mono-energetic sources or those with gamma-ray emissions with energies separated by hundreds of keV across the spectral continuum, for example as seen in Figure 5.9.

1.2.2.3. Pair Production

Pair production is the conversion of a gamma-ray photon into an electron positron pair upon interaction with an atoms Coulomb field (Knoll 2012). This is in contrast with the photoelectric effect and Compton scattering which interact with electrons in the atomic shells. Pair production conversely interacts with the atom as a whole. As a result of the interaction, the photon is completely converted into mass, implying that the photon energy must atleast be the combined rest mass of the electron and positron pair (1022 keV) (Gilmore et al. 1995). As such, the excess energy is equally imparted to the electron and positron as an increase in kinetic energy. These two newly created particles transit through the absorption medium, with the positron inevitably annihilating with an electron producing a pair of 511 keV gamma-ray photons. The process of annihilation is described in Figure 1.12.

1.2.3. Scintillators

As discussed in Section 1.2.2, to measure a high-energy photon, it is preferable to fully absorb the photon. The change as a result of the transfer of energy to the absorbing material, can then be quantised and measured providing information on the interacting photon energy. There are a wide variety of gamma-ray detecting media including gas filled detectors (Geiger-Müller (GM) counters, spark chambers), liquid filled detectors (Cherenkov detectors), silicon detectors (silicon drift detectors (SDDs)), however for the purposes of GRB detecting CubeSat instruments, scintillation based detectors are predominantly employed.

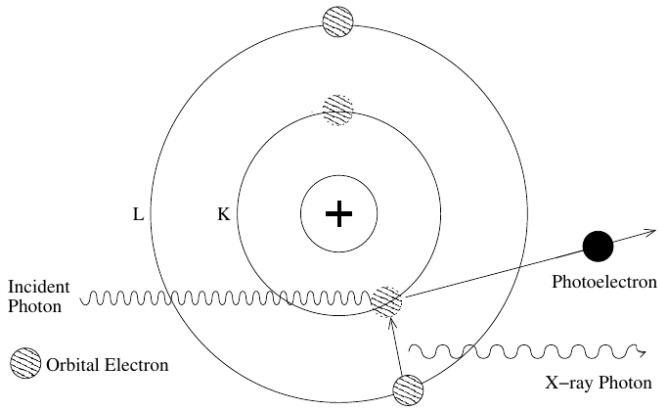

Figure 1.10: The photoelectric effect: An incident photon with enough energy liberates an electron causing complete photon absorption and photoelectron. A weaker bound electron from an outer shell of the ionised atom may descend and fill the vacancy, emitting x-ray florescence in the process. Reproduced from Ahmed 2017.

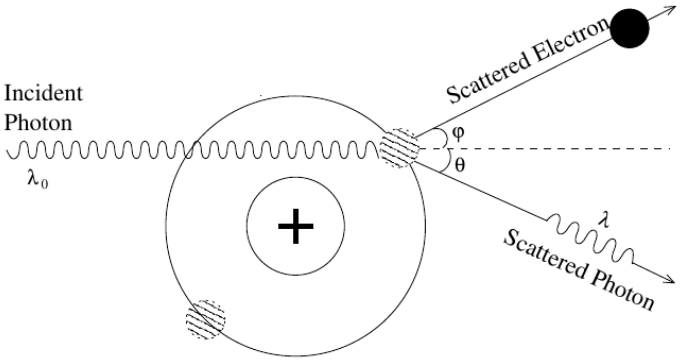

Figure 1.11: Compton scattering: An incident high-energy photon inelastically scatters off a bound electron. The photon deflected at an angle θ and transfers a portion of its energy in the liberation of the electron. Reproduced from Ahmed 2017.

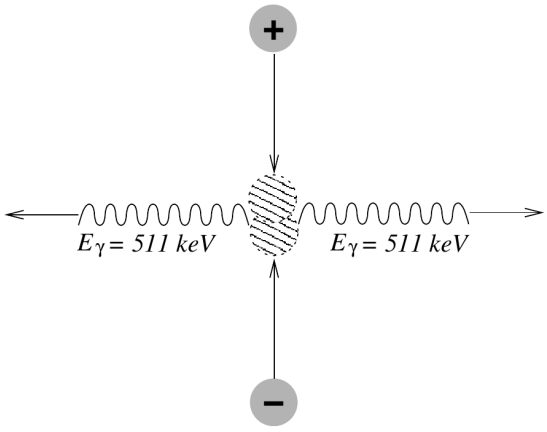

Figure 1.12: Pair production: The mass-energy conversion of a gamma-ray photon into an electron positron pair eventually leading to the inevitable electron-positron annihilation (shown here) in the medium producing a pair of 511 keV gamma-ray photons. Reproduced from Ahmed 2017.

Scintillators come in two main forms: organic and inorganic. Organic scintillators are formed from hydrocarbons and rely on florescence produced by transitions from a number of singlet energy states within the molecule (Knoll 2012) each with their own excited and ground states. The elevation of an electron to a higher singlet state and subsequent descent to the corresponding lower singlet state is through a radiationless emission. The latter descent to the lower singlet energy state produces florescence photons usually within the Ultraviolet (UV) wavelength. Organic scintillators include liquid scintillators which have a number of advantages over inorganic scintillators, including stability and easy machinability into complex geometries. However their disadvantages include their low density, making them incapable of stopping high-energy photons as well as their susceptibility to radiation damage (Ahmed 2017). One area where they have seen continued use is in anti-coincidence shields (ACSs), used to detect and veto charged particles on instruments like on the Fermi Large Area Telescope (LAT) Anticoincidence Detector (ACD).

Inorganic scintillators on the other hand are particularly dense and crystalline in structure, where the energy states are defined by the lattice of the material (Knoll 2012). These crystals have a large forbidden region band gap separating the conduction and valence bands and are typically doped with activator impurities to improve the scintillator parameters. Due to their density, they have high stopping power and can be radiation resistant depending on the material. However some have an intrinsic background radiation and are hygroscopic requiring hermetic sealing adding to the scintillator mass and dimensions.

Scintillation detectors work by providing a sensitive volume in which the absorption of high-energy photons (i.e. x-rays, gamma-rays) can take place. For a single high-energy photon, the scintillator then responds by producing a proportional quantity of photons of a longer wave length in which the quantity produced is proportional to the incident photon energy. This is effectively a translation of high-energy photon energy, into low-energy photon quantity. The advantage being that traditional photomultiplier tube (PMT) and modern photon counting devices like silicon photomultipliers (SiPMs) are sensitive to this longer wavelength of light and more fundamentally, are transparent to high-energy photons given their high penetrative nature and the low density of the detector materials. Common photodetectors are discussed later in Section 1.2.4.

The scintillation mechanism operates as described in Figure 1.13. The general process is excitation by a high-energy photon which as a consequence produces an electron hole pair in the conduction and valence band respectively. The de-excitation, the descent of the electron from the conduction band back to the valence band and recombination, results in the emission of a photon. However, given that the scintillator is an insulator, the band gap would be so large (in the case of NaI for instance (Gilmore et al. 1995)) that the resulting photon emitted would not be in the acceptable wavelength range for common photodetectors sensitivity. Furthermore it is possible that some quantity of this produced light would end up being reabsorbed by the medium. It is thus necessary to selectively “implant” lattice defects by doping the scintillator

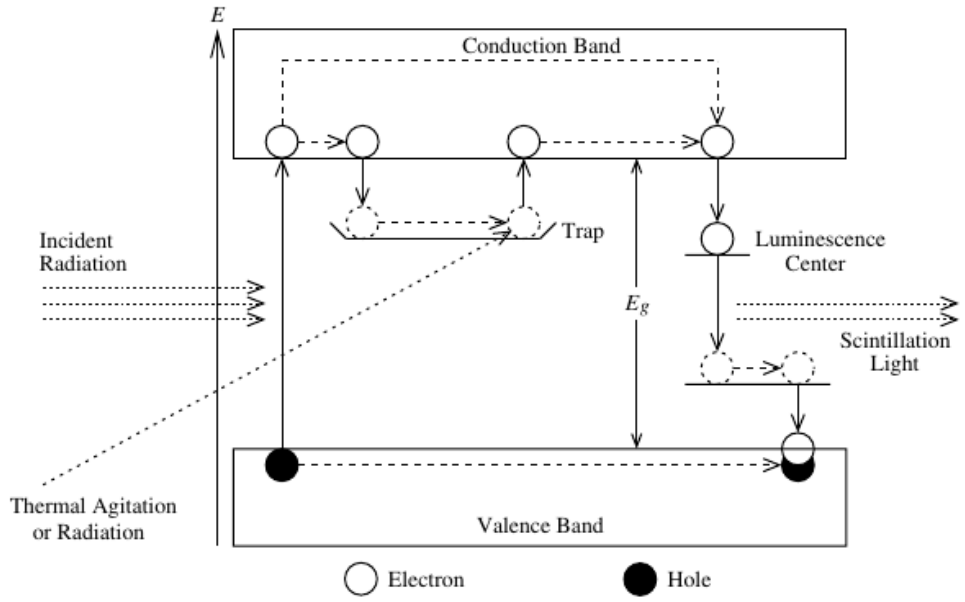

Figure 1.13: A graphical description of scintillation, where electron-hole pairs are generated by incident radiation interacting with the material. The scintillator is doped such that luminescence centres are added in the forbidden region, just below and above the conduction and valence bands of the material. During electron-hole recombination, the electron in this case recombines by de-exciting from the upper luminescence centre, rather than the conduction band, releasing a photon within a specific wavelength of light. Reproduced from Ahmed 2017.

crystal with an activator (thallium in the case of NaI), producing a number of energy levels within the bandgap called luminescence centres (Ahmed 2017). Two centres are produced, an upper and a lower luminescence centre. Depending on the scintillator and its intended application, these luminescence centres may be separated such that the decent of a electron from the upper to the lower results in an emission of a photon in the visible to UV wavelengths where most photon detectors peak photon detection efficiency (PDE) resides and are most sensitive.

As a high-energy photon interacts with the material, as shown in Figure 1.13, the photon deposits a portion of its energy into the material, creating an electron hole pair. Depending on the energy imparted to the pair, the electron may become excited and enter the conduction band (and vice versa for the hole) or in the case that a lower energy transfer took place, the electron enters an energy level just below the conduction band and both are electrostatically bound. This pair is referred to as an exciton and may transverse and become trapped within the luminescence centre. Upon descent from the upper to the lower luminescent center, a photon is released. A list of common scintillators which have space heritage are listed in Table 1.1.

1.2.4. Single Photon Detectors and Multi Pixel Photon Counters

The ability to detect individual photons is essential in scintillation based detectors. As discussed in Section 1.2.3, the quantity of photons produced by a scintillator is proportional to the energy of the incident photon energy. And therefore the measurement of the number of photons produced is necessary to accurately measure the incident photon energy. Single photon detectors

Table 1.1: A table of common scintillator properties. Derived values are from a variety of sources and some variation may be present depending on scintillator manufacturer processes, doping and crystal dimensions.

Scintillator Properties									
Parameter	**NaI(Tl)**	**BGO**	**CsI(Tl)**	**CsI(Na)**	**SrI_2(Eu)**	**LaBr(Ce)**	**$CeBr_3$**	**GAGG(Ce)**	**LYSO(Ce)**
Light yield $[photons/keV]$	38*	8-10*	52*	41*	115§§	63*	60††	60‡	33*
Decay constant $[ns]$	250*	300*	1000*	630*	>1200§§	16*	18†	88‡	36*
Peak scintillation wavelength $[nm]$	415*	480*	550*	420*	435§§	380*	370†	520‡	420*
Refractive index $[at\,emission\,max]$	1.85*	2.15*	1.79*	1.84*	2.05§§	1.9*	1.9†	1.91§	1.81*
Density $[g/cm3]$	3.67*	7.13*	4.51*	4.51*	4.5§§	5.08*	5.23†	6.63‡	7.1*
Hygroscopic	Yes*	No*	Slight*	Yes*	Yes§§	Yes*	Yes†	No§	No*
Atomic number	51‡	74‡	54‡	54##	49§§	46.9◇	45.9††	54‡	-
Energy resolution $[\%\ fwhm\,at\,662\,KeV]$	∼7–8**	∼11–12**	∼5–6**	9##	4§§§	∼3**	∼4–5**	6.1‡	∼8–9**
Melting point $[K]$	924#	1323#	894#	894¶	538§§	1441‡‡	995††	1850§	2320♣
Hardness $[Mho]$	2#	5#	2#	2##	-	3‡‡	-	8§	5.8♣
Cleavage Planes	(100)#	None¶	None#	None¶	-	-	-	None§	None♣
Intrinsic Radioactivity	None	None	None	None	None	Yes	Slight	None	Yes

* Saint-Gobain Crystals: Physical Properties of Common Inorganic Scintillators

** Arneodo et al. 2021

† Scionix Scintillation Crystals: Mechanical, Optical and Scintillation Properties.

†† Advatech: CeBr3 - Cerium Bromide Scintillator Crystal

‡ Nobashi et al. 2021

‡‡ $LaBr_3$ Crystal Bromide Crystal Halide Crylink

§ Values derived from Crylink: GAGG:Ce Scintillator Crystals

§§ Advatech: SrI2(Eu) - Strontium Iodide (Eu) Scintillator Crystal

§§§ Mitchell et al. 2019

¶ Hilger Crystals: Crystal Materials Index

Saint Gobain: Crystal Scintillators

Epic Crystal CsI(Na) Scintillator

♣ Epic Crystal LYSO(Ce) Scintillator

◇ Mizushima et al. 2020

and multi-pixel photon counters (MPPCs) produce a known charge output per single photon detection and as such produce a net charge output for all photons detected during scintillation. The net charge output can then be processed by front end electronics, to measure the photon energy. For many years PMTs were the primary choice for photon counting experiments both terrestrial and spaceborne (i.e. Fermi GBM, CGRO BATSE). However in recent years, SiPM and silicon based photon detectors have approached the TRL and maturity to be considered for their use in space applications, such as on Glowbug (Woolf et al. 2022), BurstCube (Perkins et al. 2017), the Strontium Iodide Radiation Instrument (SIRI) (Mitchell et al. 2019) and the enhanced ASTROGAM (e–ASTROGAM) mission (De Angelis et al. 2017). For this reason, the operating principles of the traditional and the modern detectors will be explored in this section.

1.2.4.1. Photomultiplier Tubes

PMTs take advantage of the photoelectric effect (Section 1.2.2.1); a photon (in this case emitted by a scintillator in the 350 – 500 nm wavelength band) interacts with a photocathode, a type of material which is specially designed with a low work function to encourage the emission of photoelectrons. The liberated electron is then electrostatically focused onto an electrode structure called a dynode, a stage which is used to amplify the signal by creating secondary electron cascades. Depending on the PMT there can be anywhere from 5 up to 10 dynode stages, each amplifying the single electron signal down the chain. The gain applied to the signal is dependent on the potential difference between each dynode in the chain, thus the applied voltages for operation of a PMT can be as high as 1 kV. Finally, the last element of the dynode chain is a gridded anode in front of a final dynode. The grid strucure allows electrons to pass and incident on the final dynode, while the charge build up is collected by the anode grid. This process is described in Figure 1.14.

PMTs have many favourable attributes including high gain, sensitivity, radiation resilience, fast response and good signal to noise ratio. Furthermore they have extensive heritage in numerous experiments in particle physics and high-energy astronomy. However, there are some drawbacks, evident in the practical limitations implemented by space based GRB detecting instruments. For example, PMTs are large and comparatively heavier than silicon based alternatives. This means particular attention to the design parameters of an instrument, and with the exception of miniature PMTs (i.e. 3UCubed (Mehta et al. 2020)), for the most part rules them out as eligible for use in payloads on CubeSats. Furthermore, PMTs are particularly sensitive to shock and vibration given their delicate construction. This adds risk to a mission in that during launch and separation stages, high-g loads can be placed on the spacecraft payload. While PMTs have a high gain characteristic, this is obtained by having a high voltage operating requirement, as discussed above. PMTs are also known to suffer from magnetic field interference which can disrupt the normal operation of the device. In conclusion, these devices have a large heritage in space experimentation and while they have a number of drawbacks, their advantages continues to be exploited in instruments used in terrestrial, balloon and spaceborne experiments.

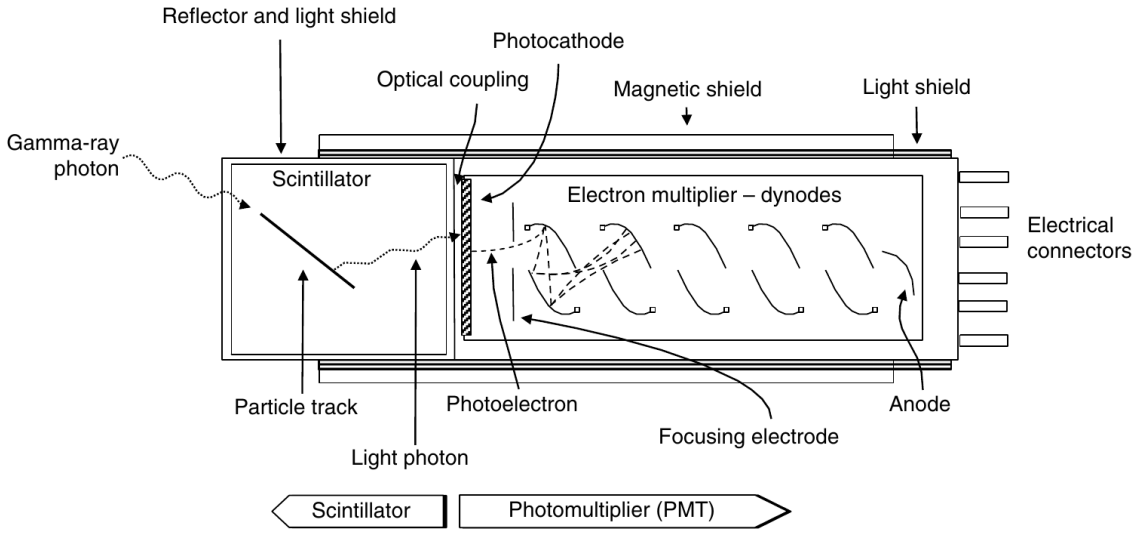

Figure 1.14: A standard PMT, describing the internal structure and coupling with a crystal scintillator. The PMT dynodes are used to amplify the signal from a photoelectron generated by gamma-ray interaction with the scintillator, to provide the capability of single photon counting. Reproduced from Gilmore et al. 1995.

1.2.4.2. The P-N Junction

An alternative to PMT technology are photodiodes, silicon based photodetectors which have seen use in terrestrial experiments like particle accelerators (ALICE, ATLAS, CMS and LHCb) (Renker et al. 2009), but are only in recent years coming to the forefront of space applications due to their relatively recent maturity. There are numerous photodiode devices available, in fact really any diode consisting of a p-n junction can operate as a photodetector, though limited by typically small bandgap regions and low bias voltage. However devices such as p-type, intrinsic type, n-type diodes (PINs), avalanche photodiodes (APDs), SDDs and SiPMs are specifically designed to enhance this effect to provide low leakage current, noise and faster responses. In fact there are numerous advantages to using silicon based detectors over the traditional PMT devices which make them particularly favourable for spaceborne GRB detectors.

A p-n junction (shown in Figure 1.15) is created by the joining of p-type doped silicon with n-type doped silicon. Silicon (like germanium and gallium-arsenide) is a semiconducting material, meaning in its pure state its level of conductivity falls somewhere between a conductor and an insulator. The conductive properties of a semiconductor can be altered by doping, a process where impurities are intentionally added to increase the number of positive or negative charge carriers in the lattice structure and by effect increase the number of energy levels in the band gap between the valence and conduction bands. A semiconductor doped to produce a material with a greater number of positive charge carriers (holes) and energy levels near the valence band is referred to as a “p-type material”, while a material doped for a greater number of negative charge carriers (electrons) and energy levels near the conduction band is referred to as a “n-type material”. The joining of these two materials creates the p-n junction which immediately forms

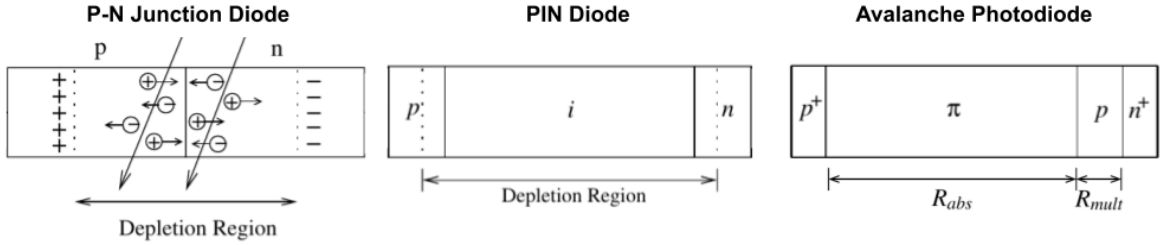

Figure 1.15: Diagrams of the p-n junction, PIN diode and APD. *Left*) The p-n junction with widened depletion region by applied reverse bias potential (not shown). As a high-energy photon is incident within the depletion region, electron hole pairs are generated and flow in opposite directions forming a current. This is a very basic form of photodetector. *Center*) The PIN diode is designed such that a permanently wide depletion region is formed by sandwiching an undoped intrinsic material between a pair of p and n doped semiconductor material. This means that a lower reverse bias voltage is required to produce a wider depletion region for photon absorption without the risk of breakdown of the crystal structure occurring. *Right*) The APD uses a similar structure with an intrinsic material sandwiched between other doped materials (noted as π in this figure). However in this case a heavily doped p and n material are used and a lighter doped p material is placed between the intrinsic and the heavily doped material. The intrinsic is used again as before to generate electron-hole pairs, however electrons are accelerated in the lightly doped p material due to the strong electric fields. This allows the electron to produce multiple secondary and tertiary electrons due to impact ionisation. Adapted from Ahmed 2017.

a depletion region caused by the cross transfer of charge carriers from the n-type (electrons) material combining with the charge carriers from the p-type (holes) material and vice versa. As a result the depletion region becomes deprived of mobile charge carriers and an electric field is established by the concentration of donor and acceptor ions on either side of the junction, resisting the flow of carriers from either side. This is the construction of a basic diode. Application of a forward bias potential (i.e. a positive voltage applied to p-type material with respect to the n-type material) can be used to reduce the width of the depletion region and encourage a greater number of opposing charge carriers on either side of the junction, to the point where the electric field can be overcome and a current can begin to flow. Conversely a reverse bias (i.e. a negative voltage applied to p-type material with respect to the n-type material) can increase the internal electric field and the depletion region width. It is the p-n junction depletion region, when broadened by an applied reverse bias, that acts as the photon absorption medium. As a photon crosses the junction, it produces electron hole pairs in its wake and the widening of the depletion region makes this more likely and reduces leakage current (induced by imperfections in the silicon) thus improving the signal to noise ratio. This is described in Figure 1.15.

1.2.4.3. PIN Diodes

As mentioned previously (Section 1.2.4.2), the p-n junction can be used for single photon detection by applying a large reverse bias voltage to increase the width of the depletion region. However the standard diode structure has a limited tolerance to excessive reverse bias poten-

tial; at a certain point the semiconductor crystal structure breakdown is exceeded allowing a high reverse current to flow which can potentially destroy the diode. This is as opposed to Zener diodes which are specially designed for reverse breakdown at low voltages and without damage. To overcome this limitation, PIN diodes are designed with an intrinsic material (e.g. silicon) sandwiched (Renker et al. 2009) between the p-type and n-type material. This allows a fixed depletion region to exist according to the intrinsic material thickness even without applied reverse bias potential. This structure is shown in Figure 1.15. These devices can be made as either blue or red sensitive for the corresponding scintillators to be used and are characterised by being able to detect low light output and their successful operation in high magnetic field experiments. However their major drawback is the lack of internal gain, something which is addressed by APDs.

1.2.4.4. Avalanche Photodiodes

APDs exploit the process of impact ionisation, whereby an electron which is highly accelerated within a crystal structure can impact and ionise additional atoms within the lattice thus producing secondary and tertiary free electrons within the conduction band. The APD is constructed with multiple doped semiconductor layers. Like the PIN diode, the cross section consists of a intrinsic material sandwiched between a p-type and n-type semiconductor, which in this case are both heavily doped. An additional p-type semiconductor is layered between the intrinsic and n-type material. This is where the acceleration of elections and multiplication through impact ionisation occurs in the diode. A photon interacts with the large intrinsic material absorption medium much like the PIN diode and creates charge pairs which are accelerated by the internal electric field. The electron travelling through the diode toward the p-type multiplication region is then accelerated by the high electric field and the high reverse bias voltage. As a result, the initial single electron produced from the photon ionisation is accelerated and through multiple cascaded generations of impact ionisation, can result in a large net charge output substantially increasing the signal according to the device gain. This gain is typically in the area of ~ 50 – 100 and can be higher (10^4) but the device stability is dependent on external environmental factors making this difficult to maintain (Renker et al. 2009). Depending on the requirements these devices can be produced as P on N for blue sensitive devices (i.e. like the J series SiPM devices used on GMOD) or N on P for red sensitive applications (i.e. the no longer produced MicroRB Series by SensL[1]). This structure is shown in Figure 1.15. The most immediate advantage of APDs are their high gain output, increasing the signal to noise and substantially improving the capability of low light signal detection.

1.2.4.5. Geiger-Mode Avalanche Photodiodes and Silicon Photomultipliers

APDs may be operated such that a positive feedback loop can cause impact ionisation and a self sustaining avalanche multiplication of charge carriers in the diode, providing the reverse bias applied is high enough. These are called geiger-mode avalanche photodiodess (G-APDs) or sometimes single photon avalanche diodes (SPADs). Once started and operating in the so called

[1] SensL RB-Series Datasheet

Geiger-mode, the avalanche output continues and must be quenched for subsequent detections by reducing the applied bias voltage below breakdown across the device using a series quench resistor. As the avalanche current increases, it causes a voltage drop in response across the quench resistor, dropping to around the device reverse breakdown voltage, ceasing the avalanche and allowing the G-APD to recover. For an APD to operate in Geiger-mode, the applied bias must be so high that the avalanche can occur allowing both negative (electrons) and positive (holes) charge carriers to participate in impact ionisation. This is contrasted by an APD operated in a lower reverse bias regime and standard APD mode (as described in Section 1.2.4.4), where only electrons participate in the ionisation and as a result quenching is not necessary (Gundacker et al. 2020). Holes do not contribute in this standard mode as they require a greater electric field due to their larger effective mass.

These devices are the building blocks of SiPMs, which are composed of an array of many thousands of G-APDs called microcells. Each microcell consists of a G-APD with its own quench resistor with a common parallel readout. The accumulated charge output of the SiPM device corresponds to the sum of all G-APDs which have been fired and in this way allows the counting of individual photons, where the output signal magnitude is proportional to the number of single photon detections. SiPMs have found particular use in light detection and ranging (LIDAR) sensing applications but also most promisingly in upcoming space applications. What makes SiPM so advantageous against PMTs is their light and small form factor, low power requirements and magnetic field immunity. Their disadvantages include breakdown voltage temperature dependence (which effects PDE and gain) as well as their susceptibility to radiation damage (Garutti et al. 2019).

1.3. Instrument Configurations for Gamma-Ray Missions

1.3.1. Monolithic Scintillator Instruments

Probably the most basic configuration for a scintillation based GRB detector is a conventional monolithic detector. This is essentially a scintillator coupled to a photodetector with single or multichannel readout, or a single instrument consisting of multiple detectors. For instance, the Fermi GBM (Meegan et al. 2009) consists of a set of 12 thallium doped sodium iodide (NaI(Tl)) scintillation detectors and 2 BGO detectors, each of which is a scintillator (either BGO as seen in Figure 1.17 or NaI(Tl)) coupled to a PMT with associated electronic readout. Furthermore, many monolithic detectors are composed of an array of photodetectors or have scintillators which are subdivided, allowing position sensitive localisation of the photon interaction site (Ulyanov et al. 2017b) and can therefore be extended for use as calorimeters in Compton telescopes (Laviron et al. 2021; Greiner et al. 2012). In fact, even support ACS elements for more complex instruments, can be extended for GRB detection and contribution to the IPN (Hurley et al. 2021) through localisation by time of flight. For example the INTEGRALs (Winkler et al. 2003) SPI-ACS (Rau, A. et al. 2005), which uses a series of 91 BGO with PMT readout, configured as a column of rings around the Spectrometer on INTEGRAL (SPI) instrument. While the SPI-ACS GRB detecting capacity is limited due to its intended design parameters

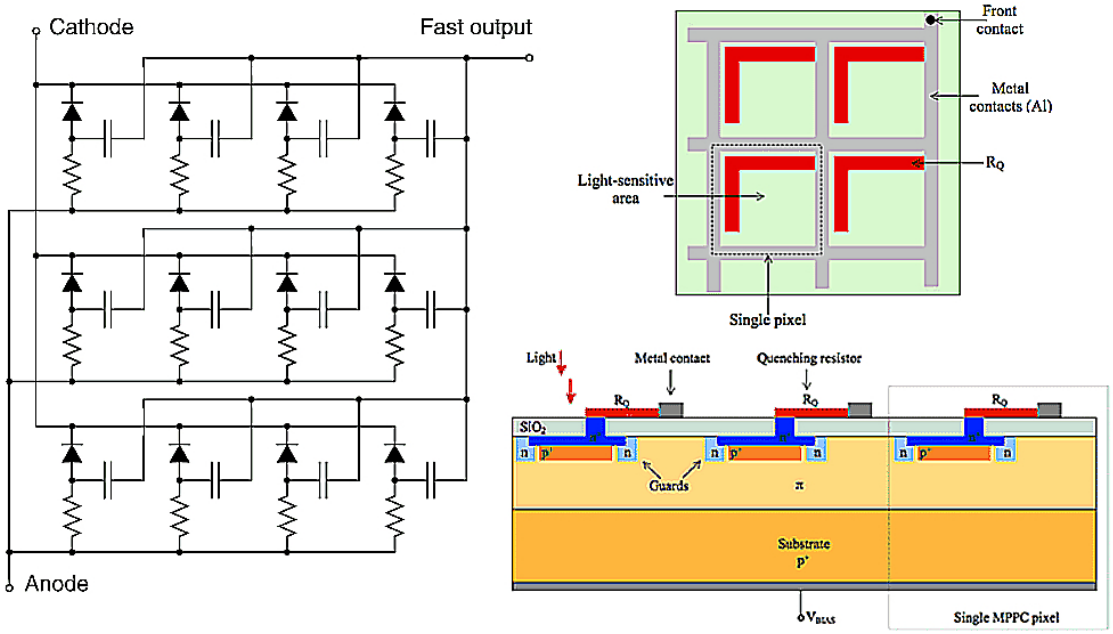

Figure 1.16: An SiPM microcell simplified schematic and a pair of architecture diagrams adapted from both OnSemi Silicon Photomultipliers(SiPM) J-Series SiPM Sensors and Hamamatsu: Physics and operation of the MPPC silicon photomultiplier. The SiPM is composed of an APD with quench resistor. J-Series SiPMs developed by OnSemi also provide an additional "fast output", which acts as a capacitively coupled readout of the entire network of microcells. The architecture diagrams describe the layout of the APD (as described in Figure 1.15) and the corresponding quench resistor.

(i.e. the weak spatial resolution or the lack of spectral information, neither of which are needed for its intended vetoing purpose), the SPI-ACS has still contributed immensely (Savchenko et al. 2017) to GRB detections, localisations and afterglow follow up campaigns. This format of instrument is also popular for GRB detecting instruments for demonstration payloads (i.e. for increasing SiPM, scintillator, readout TRL), where science data collection is also a key mission parameter. For example many GRB detecting CubeSats have adopted the monolithic format such as BurstCube (Perkins et al. 2017) and GMOD (Murphy et al. 2021a; Murphy et al. 2022) on EIRSAT-1 (Murphy et al. 2018).

1.3.2. Compton Imaging Instruments

Compton telescopes take advantage of Compton scattering (Section 1.2.2.2) to produce an imaging and polarimetry instrument which has reasonable interaction cross-section in the 100 keV up to around 10 MeV energy range (see Figure 1.9), something which is otherwise difficult to accomplish due to Compton scattering being the dominant mode of interaction in this range (Parajuli et al. 2022). These telescopes consist of two detector planes one situated above the other, a scattering layer (*D1*) and an absorbing layer (*D2*), where the aim is to track the trajectory and reconstruct the origin of gamma-ray photons as they pass through the detector layers. The scattering layer (*D1*) is designed to provide a scattering medium for gamma-ray photons,

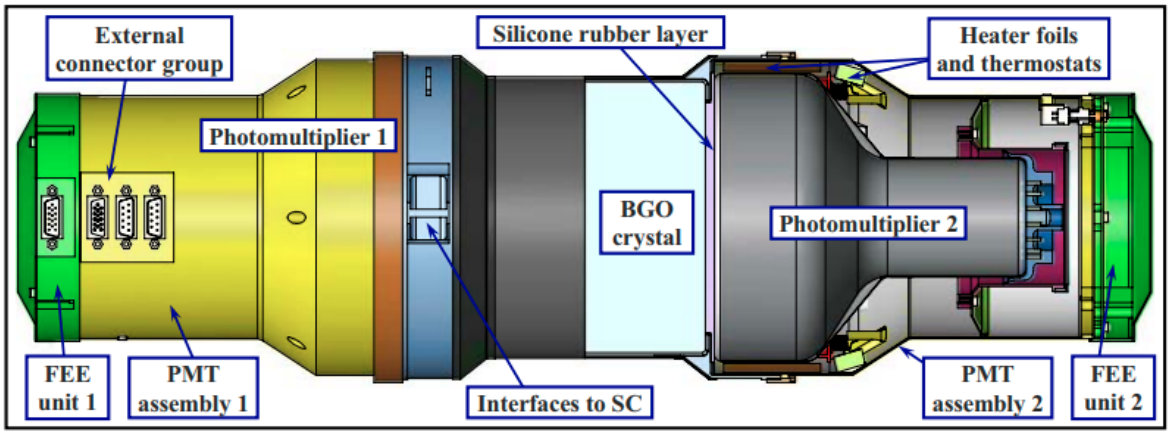

Figure 1.17: The BGO detectors used on Fermi GBM, showing the internal PMT assembly through cutaway, the BGO scintillator and mechanical enclosure. Reproduced from Bissaldi et al. 2009.

typically composed of a low Z material to improve the cross-section for Compton scattering interactions. The final layer (*D2*) is used to absorb the scattered photons after interacting with the scattering layer and is usually made from a high Z material to ensure complete photon absorption via the photoelectric effect (Section 1.2.2.1).

Each detector layer is subdivided such that it is possible to localise the point of interaction and energy deposited by incident photons within the given layer. As the gamma-ray photon interacts with the scattering layer (*D1*) it transfers a portion of its energy ($E_{p-scatter}$) to the medium and is scattered at an angle proportional to the energy exchange according to Equation (1.5). The scattered photon is then absorbed within the absorbing layer (*D2*) depositing the remainder of the photon energy ($E_{p-absorbed}$). The initial incident photon energy is then given as the sum of both ($E_{p-incident} = E_{p-scatter} + E_{p-absorbed}$) and since the interaction location for both scattering and absorption are known, it is possible to determine the original scattering angle (ϕ) as in Equation (1.6) (Schönfelder et al. 2013). This reconstruction projects a "Compton cone" with the tip originating at the scattering location where the cones central axis runs along the scattered photon trajectory and the cone base describing an annulus where any point along the circumference could be the photon source origin. Multiple photon reconstructions are thus required to minimise ambiguity and constrain the exact location. With multiple annuli, the overlapping rings intersect to show the true location origin.

There have been multiple balloon flight demonstrations (e.g. Bloser et al. 2016; Beechert et al. 2022), however to date the CGRO Compton Telescope (COMPTEL) instrument is the only Compton telescope to have flown in space due the material mass required. However with the advent of lighter photodetectors like SDDs and SiPMs it has become more feasible to build and fly these instruments, such as the proposed e–ASTROGAM De Angelis et al. 2017 mission. It has even become possible for this technology to be used on CubeSat mission payloads, for

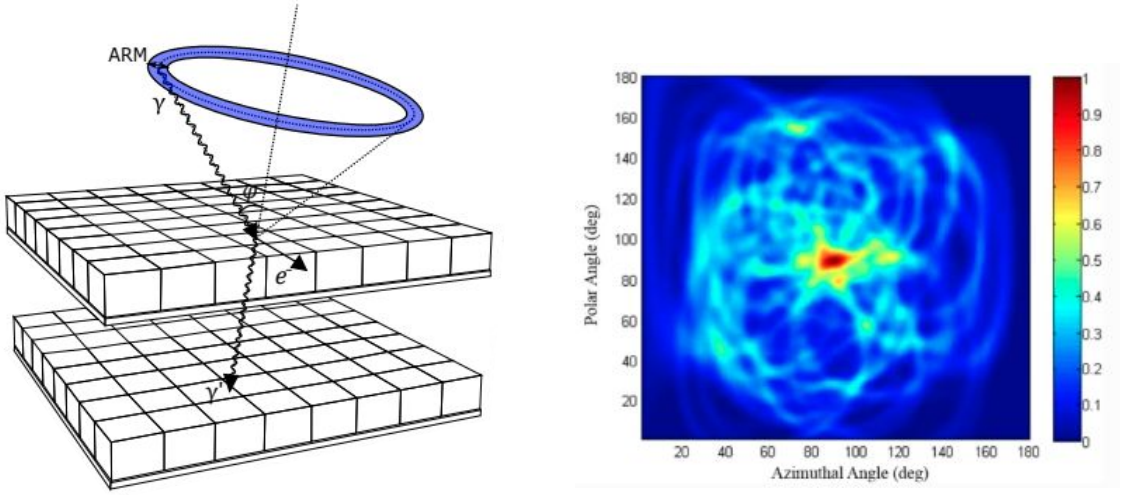

Figure 1.18: *Left*) A diagram showing the operation of a Compton telescope with scattering and absorption layers. Reproduced from Lucchetta 2021. *Right*) A superimposed image from data collected using a Compton telescope as reported in Zhang et al. 2019, showing many annuli intersecting to reveal the source location.

example on the COMCUBE CubeSat mission (Laviron et al. 2021).

$$cos(\phi) = 1 - \frac{m_e c^2}{E_{p-absorbed}} + \frac{m_e c^2}{E_{p-scatter} + E_{p-absorbed}} \tag{1.6}$$

1.3.3. Pair Production Instruments

Pair production telescopes (Schönfelder et al. 2013) similarly use reconstruction techniques for imaging higher energy photons >10 MeV, providing a window into the very high-energy universe by exploiting the effect of pair production Section 1.2.2.3. A pair production telescope is constructed from multiple stacked layers of conversion and tracking stages. The conversion stage within each layer is selected to be a hi-Z material as these have the greatest cross-section for pair production interactions of photons at energies >10 MeV. Once the electron positron pair have been created in the conversion layer, their trajectory and energy deposition into the subsequent tracking layers are recorded. The tracking layer may for example be a gas filled spark chamber with gridded mesh (as on the CGRO Energetic Gamma-Ray Experiment Telescope (EGRET)), where as a particle transverses the medium, it ionises the gas producing a current signal indicating the path of the electron positron pair. Modern SDDs provide a lighter alternative for example the silicon tracking layers on the Fermi LAT (Atwood et al. 2009). Finally a calorimeter (scintillator and photodetector pair) at the base of the stack is used to absorb any remaining energy from the interaction, such that the total energy can be calculated and the path of the products of interaction can be reconstructed. It is essential that the stack is collimated to the direction of the sky which the instrument is observing from, as it is otherwise inevitable that the isotropic cosmic ray background in space could easily saturate the instrument. For this reason a set of ACS plastic scintillator detectors are arranged around each side of the stack for

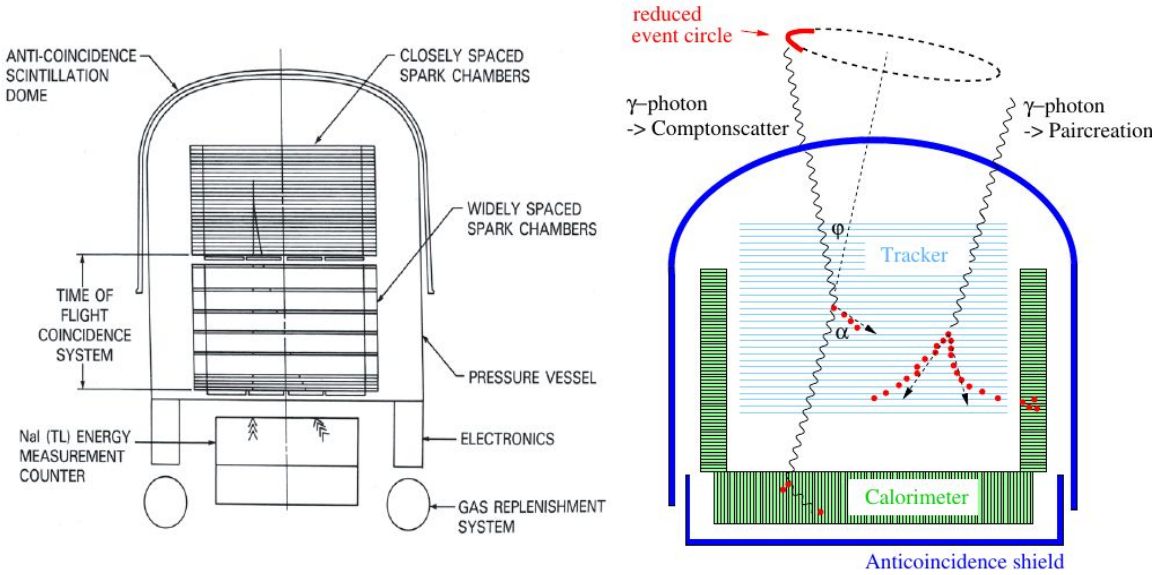

Figure 1.19: The EGRET pair production telescope (Hartman et al. 1999) on CGRO and the proposed MEGA instrument (Kanbach et al. 2005). The proposed MEGA instrument can be operated for tracking the products of both Compton scattering and pair production interactions.

side rejection and vetoing of cosmic rays and high-energy photons outside the field of view of the instrument (for example the Fermi LAT ACD). In addition to this it is also necessary to correlate each stage of the photon/electron positron pair trajectory through the instrument in terms of the expected energy, direction and expected time sequence to further exclude background events. As mentioned pair production instruments have been flown on many missions, including the Fermi LAT and the CGRO EGRET, with some instruments operating as both Compton and pair production telescopes, such as the proposed Medium Energy Gamma-Ray Astronomy (MEGA) (Kanbach et al. 2005), the Astro-Rivelatore Gamma a Immagini Leggero (AGILE) (Tavani et al. 2003), All-sky Medium Energy Gamma-ray Observatory (AMEGO) (McEnery et al. 2020), e–ASTROGAM (Rando et al. 2019) and COMPAIR (Moiseev et al. 2015).

1.3.4. Coded Aperture Mask Instruments

A coded aperture mask uses the concept of a pinhole camera for imaging (Cieślak et al. 2016). A single pin hole camera technique for gamma-ray imaging was developed and presented in Mortimer et al. 1954, with a segmented detection plane and perforated mask plate. However as the camera has an inherent trade-off dictated by the pin hole size, a compromise between large angular resolution and improved signal to noise ratio occurs. For small hold diameters, better angular resolution is achieved, for large hole diameters improved signal to noise ratios are achieved. To circumvent this, many multiple holes can be used in scatter-hole cameras which have holes of small diameter randomly distributed on the perforated mask plate (Dicke 1968). This creates another problem as the number of randomly placed holes make reconstruction very difficult. By creation of a known and particularly designed arrangement code for the placement of holes in a mask the image reconstruction can be performed using deconvolution (Fenimore et al. 1978). The mask is a plane with a grid arrangement of obstructing lead, tungsten or tan-

talum tiles specifically placed according to a mask code to absorb high-energy photons, where an x-ray or gamma-ray source produces a shadow on the detection plane, typically either a charge-coupled device (CCD) array, or cadmium zinc telluride (CdZTe) solid state detector in conjunction with scintillators or gas filled tubes. The use of coded aperture mask systems is quite common in space based instruments, for example the Imager on Board the INTEGRAL Satellite (IBIS) and SPI on INTEGRAL (Winkler et al. 2003), the Neil Gehrels Swift Observatory Burst Alert Telescope (BAT) (Gehrels et al. 2004), the SVOM ECLAIRs (Atteia et al. 2021) and the BeppoSAX Wide Field Imager (WFI) (Boella, G. et al. 1997).

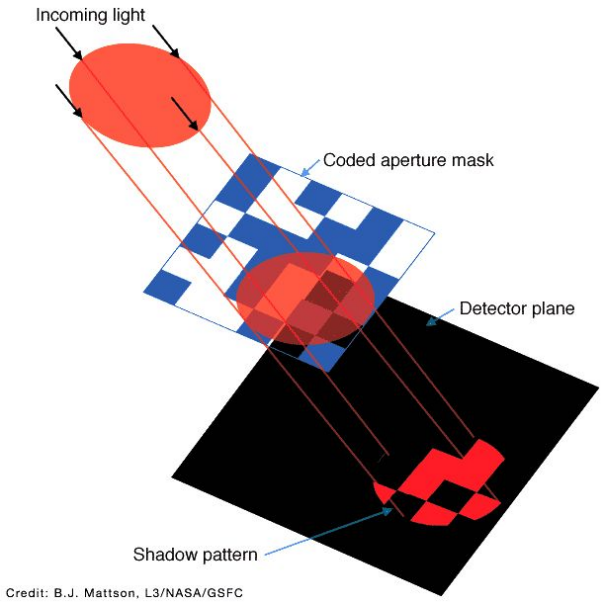

Figure 1.20: A diagram describing the coded aperture mask. The mask tiles produce a shadow pattern on the detector plane which can be used to distinguish multiple present sources. Reproduced from Rau, A. et al. 2005.

1.4. Gamma-Ray Burst Localisation Techniques

Localisation of GRBs is important as it provides the opportunity to measure the complete spectral and temporal evolution of the event through time and energy. Furthermore, in the era of multi-messeger astronomy, low latency reporting of localisations for gravitational wave, multi-wavelength and sub-threshold events is essential to extract the maximum amount of science from these instruments. For example, this allows follow up observations from terrestrial observatories (e.g. the Zwicky Transient Facility (Bellm 2014), the Watcher robotic telescope (Topinka et al. 2014)), such that redshift distance measurements can be made. GRB detecting spacecraft are typically only capable of observing the electromagnetic spectrum within the gamma-ray regime and cannot do multi-wavelength observations (the Neil Gehrels Swift Observatory is one such exception with its Ultraviolet Optical Telescope (UVOT) (Oates et al. 2021)) and so it is necessary to alert the community as soon as possible, for example through Gamma-ray Coordination Network (GCN) notices (Barthelmy et al. 1998). It is not possible to localise with just monolithic detectors as these can only provide limited if any localisation information. Localisation using imaging telescopes is possible for serendipitous GRB events

that fall within the field of view of the instrument. However as GRBs are unpredictable and occur isotropically across the observable sky (i.e. as opposed to being constrained to a given portion of the sky like the galactic plane), it is not an effective method of localisation. Instead a full sky approach must be considered.

1.4.1. Relative Rates and Anisotropic Instrument Responses

The exploitation of the anisotropic response from a cluster of detectors mounted in specific orientation with respect to the spacecraft structure can be used to determine the statistically likely direction which a GRB arrived from, using the relative rates in each detector and comparing this to the expected response from all directions. This was used on the CGRO BATSE experiment, as seen in Figure 1.21, which used an arrangement of 8 detectors called the Large Area Detectors (LADs) (Fishman et al. 1992) composed of a 20 inch NaI scintillator and PMT coupled readout (a Spectroscopy Detector (SD) also accompanied each LAD for energy optimised measurements). Other instruments like the detectors on the 6U CubeSat BurstCube, Gamma-Ray Investigation of the Full Transient Sky (GIFTS) and the Fermi GBM detectors use a similar technique for localisation. This requires a complete knowledge of the instruments (the detector cluster) angular and energy response (Bissaldi et al. 2009). A Monte Carlo simulation[1] of the response is performed across the spacecraft coordinate system. For GBM (Connaughton et al. 2015) this includes photon energies from 5 keV – ∼50 MeV across 272 positions around the spacecraft which are interpolated to give a 1° resolution grid about the coordinate reference frame (CRF) forming 41168 reference points in the sky. Scattering of high-energy photons from the spacecraft instruments and components (e.g. solar panels, radiators etc.) as well as the contribution of scattering from Earths atmosphere may also be incorporated and subtracted from the observed data. The responses are then compared to a look up table (LUT) onboard Fermi which records three tables containing detector responses in the 50 keV – 300 keV range for three source spectra; soft, medium and hard spectra modelled using a Band model (Equation (1.1) (Band et al. 1993b)) with parameters α = -1.9, β = -3.7 and E_{peak} = 70 keV for the soft spectra and [-1, -2.3, 230 keV] and [0, -1.5, 1 MeV] for medium and hard spectra respectively. Finally the simulated responses for all three spectra with the closest match to the observed data is determined by χ^2 minimisation.

1.4.2. Time of Flight and Triangulation

The propagation of light in a vacuum is finite and at long distances the time of arrival of gamma-ray photons originating from a GRB can be used to determine a localisation (Hurley et al. 2013). When two GRB detecting instruments (S_1 S_2) detect a GRB, both being positioned at a distance of D_{12}, a time delay of δT can be identified in both the resulting observed light curve features. From this, an annulus region of origin can be constructed, indicating an ambiguous ring of possible source positions with a half angle θ with respect to the vector joining both

[1] For example using the GEometry ANd Tracking 4 toolkit (Geant4) based The Medium-Energy Gamma-Ray Astronomy Library (MEGAlib) (Zoglauer, A. and Andritschke, R. and Schopper, F. 2006) suite of simulation tools for high-energy instruments.

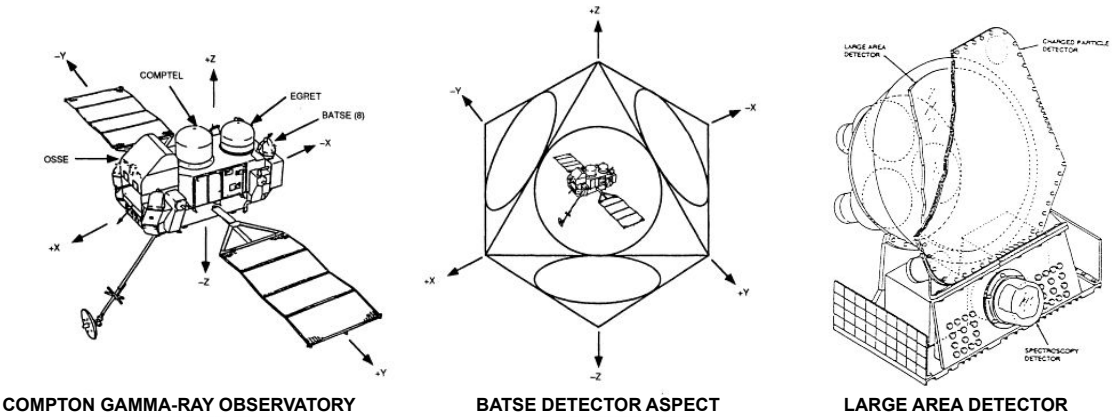

Figure 1.21: The CGRO spacecraft observatory, the directionality of the LAD detectors and a schematic of the LAD detector. Adapted from Fishman et al. 1992.

spacecraft, as described in Equation (1.7) with c representing the speed of light. The width of the annulus, representing the uncertainty of the localisation is given as $d\theta$ and is also expressed in Equation (1.7), where $\sigma(\delta T)$ indicates the uncertainty in the time delay measurement. The addition of a third (or more) spacecraft reduces the ambiguity of the exact location along the annulus, by providing a second annulus which intersects the first at two points, thus the more spacecraft observations, the greater the certainty of localisation. This is shown in Figure 1.22 with similar notation.

$$cos(\theta) = \frac{c\delta T}{D_{12}}; d\theta = \frac{c\sigma(\delta T)}{Dsin(\theta)} \tag{1.7}$$

This method was exploited most notably by the IPN (Hurley et al. 2021), a collaboration of many internationally developed GRB detecting instruments on a variety of spacecraft, both in low Earth orbit (LEO) (Fermi (Meegan et al. 2009)), higher orbits (INTEGRAL Winkler et al. 2003) and even interplanetary missions (the Martian, Mars Odyssey (Hurley et al. 2006)), dating from the mid 70s to present day in the current IPN 3. As with other localisation forms, it is essential that an alert as soon as possible is distributed to the community as afterglow emissions can begin to fade immediately in different wavelengths for follow up campaigns after the prompt phase. The early IPN collaborations missions were in some ways hampered by the international politics of the time, restrictions on the sharing of scientific data, as well as the technology which was often physically distributed. This made immediate follow up impractical. Today, international coordination is key as well as the ability to near instantaneously distribute GCN notices and share data across the world making this a more practical method of localisation. Additionally, the future prospect of a number of GRB detecting CubeSats makes time of flight realisable, especially considering the age and operating life time of the flagship observatories, as well as the anticipation of true full sky coverage (Perkins et al. 2017).

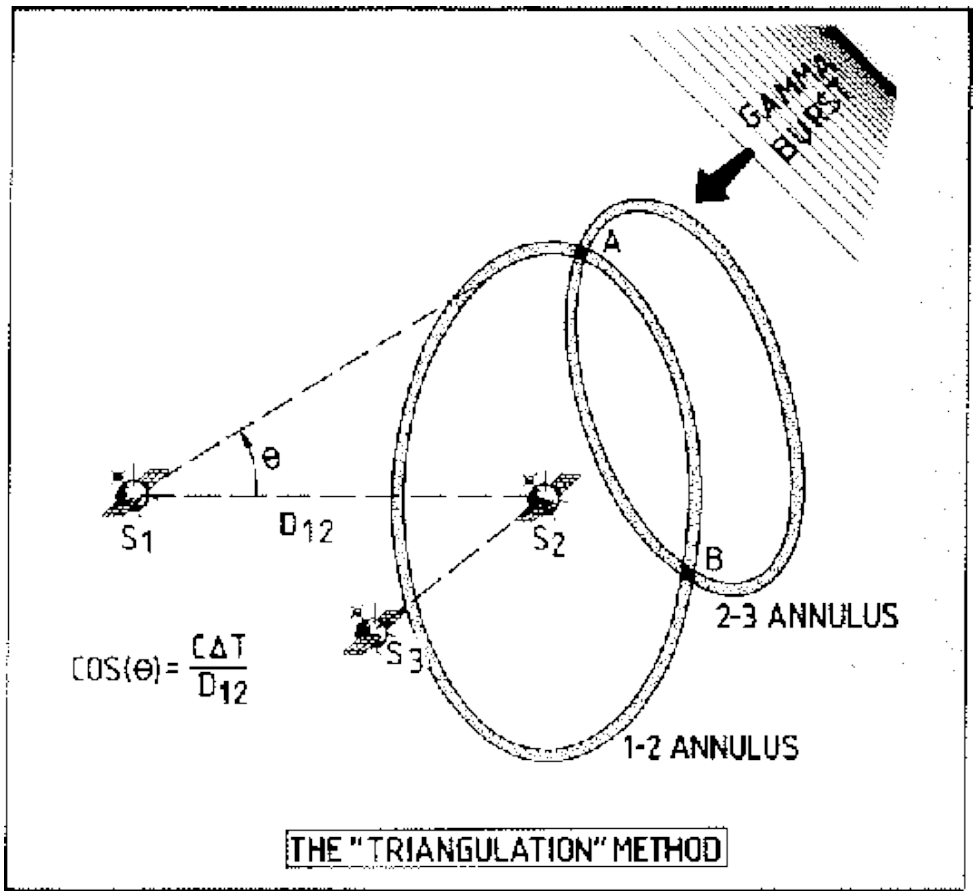

Figure 1.22: The principle of triangulation using multiple satellites for GRB localisation. Spacecraft *S1* and *S2* provide the first annulus, while a third spacecraft *S3* provides the second, reducing the localisation ambiguity. Reproduced from the IPN website.

1.5. EIRSAT-1: The Education Irish Research Satellite-1

The Educational Irish Research Satellite-1 (EIRSAT-1) (Murphy et al. 2018) is a 2U CubeSat satellite and participant in the European Space Agency (ESA) Fly Your Satellite! (FYS) programme. EIRSAT-1 was originally proposed in 2017 and developed by a team of PhD and Masters students from the Schools of Physics and the College of Engineering at University College Dublin (UCD). One of the core aims of EIRSAT-1 is to provide the opportunity for third level students to learn about space mission and technology development, to engage with space in a practical and meaningful way, and finally to spur the Irish space industry such that it can flourish in an academic setting while encouraging the involvement of a younger generation. As a participant in the ESA FYS programme[1], the EIRSAT-1 team has been supported by ESA experts and has been guided over the course of the standard mission lifecycle, from critical design review (CDR), the environmental test campaign (ETC) to launch and early operations. The spacecraft, shown in Figure 1.23, consists of a number of custom experiment payloads and commercial off-the-shelf (CoTS) components. Much of this is elaborated on in Chapter 4 and Chapter 5. The EIRSAT-1 launch window opens in 2023, where upon the spacecraft will be delivered into a Sun Synchronous Orbit (SSO) at an altitude of 520 km onboard the Vega-C

[1] https://www.esa.intEducationCubeSats__Fly_Your_Satellite

launch vehicle by the Arianespace[1] launch service provider.

The primary scientific payload is the Gamma-Ray Module (GMOD), a <1U CubeSat compatible scintillation based gamma-ray detector. GMOD was developed to demonstrate novel detector technology while performing GRB science in LEO. The ENBIO Module (EMOD) is an experiment to test the SolarWhite and SolarBlack thermal coating materials (Doherty et al. 2016) developed by ENBIO and used on the ESA Solar Orbiter mission (Müller et al. 2020). The EMOD thermal coupons which are coated in the SolarWhite and SolarBlack material are mounted on the +Z axis of the spacecraft on a custom endcap, while their temperature profiles are monitored via resistance temperature detectors (RTDs) through the EMOD motherboard. Wave-Based Control (WBC) (Sherwin et al. 2018) is a novel control algorithm for flexible systems developed in house, particularity for spacecraft equipped with long boom structures and solar panels in microgravity. The WBC software payload will be used as a demonstrator for this control algorithm and during demonstrations will be configured to take over the role of the BDOT algorithm which is normally ran on the attitude determination and control system (ADCS). These science payloads are all custom and developed in house. However, the CubeSat also consists of CoTS components developed by AAC Clyde Space[2], comprising the basic essentials of the spacecraft like the structure, ADCS, electrical power supply (EPS), radio, battery and the on-board computer (OBC). While the OBC hardware is CoTS, the software (Doyle et al. 2022a) is custom and has been developed based on a software development kit (SDK) provided by Bright Ascension[3].

The development of the GMOD hardware and firmware is the topic of this thesis and is discussed in detail in Chapter 2 and Chapter 3. The GMOD development hardware has been tested over numerous campaigns including a high altitude balloon flight from Palestine Texas and a 101.4 MeV proton irradiation test of the SiPM array (Chapter 4). Additionally, the instrument hardware and firmware performance was tested during environmental qualification at both subsystem (Chapter 5, Chapter 6) and system level (Dunwoody et al. 2022c) tests. During these tests, instrument energy calibration revealed that the energy resolution was $\sim$4% full width half maximum (FWHM) at 662 keV. Monte Carlo simulations (Murphy et al. 2021a) using the MEGAlib Geant4 suite of simulating tools were used to determine the effective area at $\sim$10 cm^2 at 120 keV, and the expected background gamma-ray trigger rate at around $\sim$50 Hz within the 50 - 300 keV energy range (possibly closer to $\sim$100 Hz in a wider energy band). GMOD is expected to detect between 11 and 14 GRBs[4] over a one year period at a significance of 10 σ, depending on spacecraft pointing. This corresponds to a trigger rate of around $\sim$120 Hz over a single 1024 ms binned light curve record. It is not expected that GMOD will see GRBs which generate over 500 counts per second and the vast majority of GRB triggers will be less than

[1] https://www.arianespace.com/

[2] https://www.aac-clyde.space/

[3] https://brightascension.com/

[4] The was originally simulated for a one year mission in International Space Station (ISS) orbit, which has since changed to an SSO orbit.

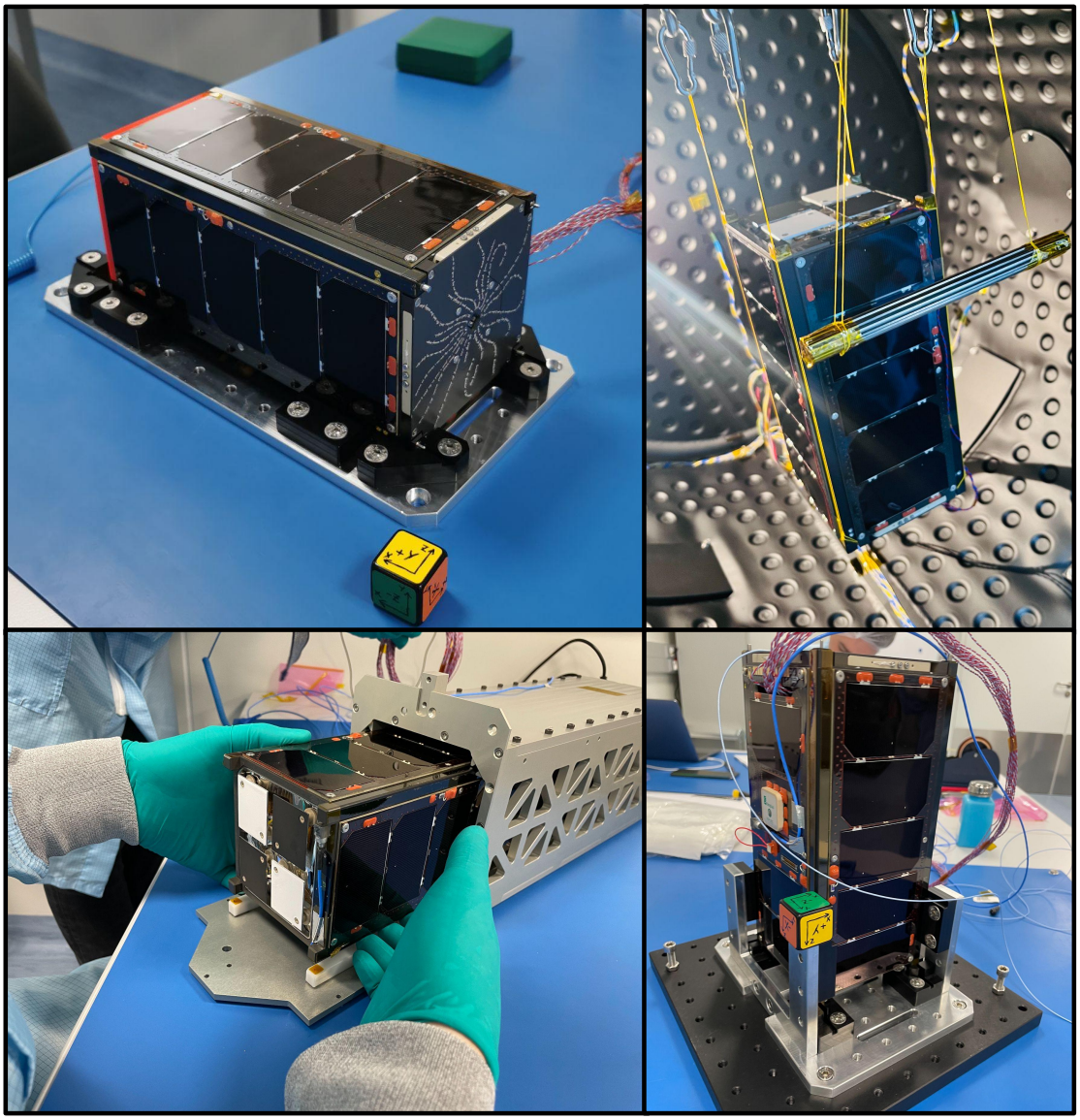

Figure 1.23: The Educational Irish Research Satellite-1 (EIRSAT-1), a 2U CubeSat developed by students at University College Dublin (UCD), pictured during flight model (FM) environmental testing.

$10\,\sigma$. An event at such high rates for any long duration is not expected, however high rates are expected while transiting the SAA (due to the concentration of high-energy protons) or if passing through high latitude regions (due to the concentration of high-energy electrons). In these circumstances the instrument experiment will be disabled to prevent excessive triggering. Once in orbit, GMOD will contribute to the progression of the TRL of novel detector technology and contribute to the field of high-energy astronomy and GRB science as the main payload on EIRSAT-1, Ireland's first satellite.

1.6. Summary

This chapter presents an overview of GRBs, their common characteristics, the most widely accepted theory of origin and their place in the context of multi-messenger astronomy. Furthermore, the types of instruments used were explored, starting with the fundamentals of gamma-

rays interactions, scintillators and photodetectors. Following on from this a discussion on instrument configurations for the measurement of spectra, gamma-ray imaging and localisation techniques for GRB events was presented. Finally a brief overview of the EIRSAT-1 mission was presented, describing the the CoTS components and main science payloads, with a focus on GMOD. This thesis will continue by providing a more detailed overview of the GMOD instrument hardware (Chapter 2), the firmware (Chapter 3) and instrument origin and early development (Chapter 4). This is intended to lay the groundwork for the final chapters, including an overview on the initial subsystem level environmental test campaign of GMOD (Chapter 5), firmware hardware–in–the–loop (HITL) testing (Chapter 6) and finally a breakdown of the lessons learned during firmware development (Chapter 7). A conclusion (Chapter 8) will also be presented, summarising the main findings from the development of GMOD, general lessons learned and the future prospects.

Chapter 2

The Gamma-Ray Module Hardware

The Gamma-Ray Module (GMOD) (Murphy et al. 2021a; Murphy et al. 2022) is a novel, CubeSat compatible instrument built for the detection of high-energy transient events and GRBs (Vedrenne et al. 2009) as a demonstrator for larger instruments in the era of multi-messenger astronomy. As the main science payload on EIRSAT-1, GMOD will contribute to GRB science research and help further the TRL of the detector hardware, including compact and low power SiPMs and its fast high light yield cerium bromide ($CeBr_3$) scintillator, for use in future space-borne instruments. This chapter will describe in detail the FM hardware of GMOD, followed by an overview on the FM instrument firmware in Chapter 3. The origin of GMOD, the initial design and testing will be further discussed in Chapter 4. Finally, the subsystem level ETC and the firmware HITL testing will be discussed Chapter 5 and Chapter 6 respectively.

2.1. The GMOD Detector Assembly

The design of the GMOD detector is based on a development heritage for gamma-ray detecting instruments (Ulyanov 2013; Ulyanov et al. 2016; Ulyanov et al. 2017b; Ulyanov et al. 2017a) and a number of extensive test campaigns, focusing on GMOD (Murphy et al. 2021b; Ulyanov et al. 2020; Mangan et al. 2021f) and EIRSAT-1 (Dunwoody et al. 2022c). The key enabler of the design is the use of modern detector technology, using a tiled array of SiPMs coupled to a high light yield $CeBr_3$ scintillator. GMOD consists of a 25mm×25mm×40mm Scionix $CeBr_3$ crystal, coupled to a 4×4 tiled array of 16 MicroFJ-60035-TSV On Semiconductor SiPMs, with frontend readout performed by the 16-channel IDE3380 Silicon Photomultiplier Readout ASIC (SIPHRA) (Meier et al. 2016), as shown in Figure 2.1 and Figure 2.2. The detector electronics are contained within a machined light-tight aluminium housing and are electronically interfaced to the GMOD motherboard supplying power, readout and control for LEO instrument operation.

2.1.1. The $CeBr_3$ Scintillator

GMOD uses scintillation as the mechanism for measuring single high-energy photons, utilising a monolithic 25 mm×25 mm×40 mm Scionix[1] $CeBr_3$ crystal. As $CeBr_3$ is hygroscopic, the crystal is hermetically encased within an aluminium housing with a 2 mm thick quartz window for optical transmission on its shortest face[2]. The aluminium housing is 4 mm thick on each of the longest sizes of the scintillator and 0.8 mm thick on the rear case end (enclosing dimensions of 33 mm×33 mm×43.8 mm in total) where the crystal is inserted and hermetically sealed with epoxy, after being wrapped in a reflective polytetrafluoroethylene (PTFE) material

[1] Scionix Application Note: High resolution low background $CeBr_3$ scintillators

[2] The optical window is slightly larger in area than the crystal face at 28.7 mm×28.7mm.

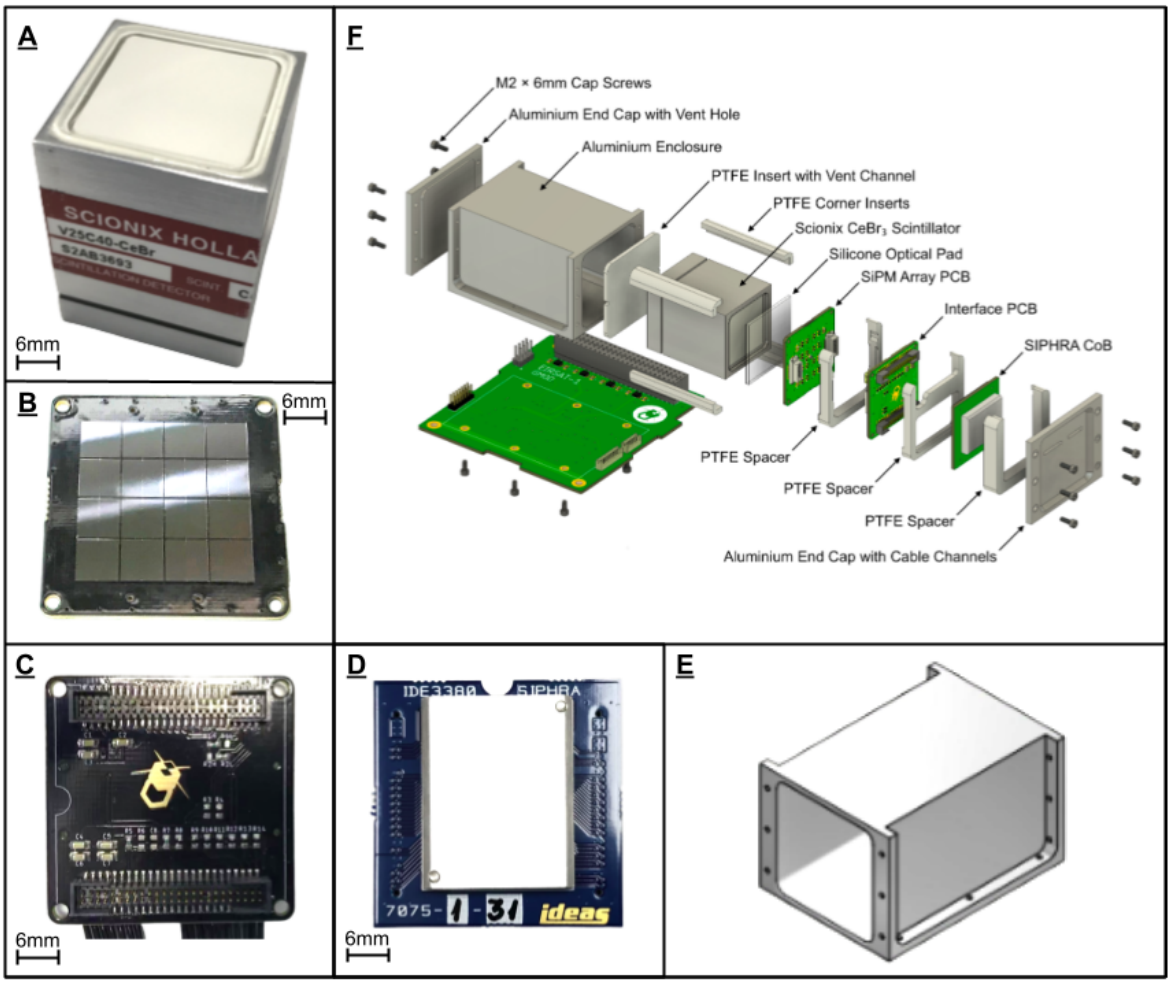

Figure 2.1: The Gamma-Ray Module (GMOD). The main instrument components are arranged in side panels with an exploded diagram in the upper right describing their configuration within the GMOD detector. From the upper left: A) the $CeBr_3$ 25mm×25mm×40mm Scionix $CeBr_3$ scintillator, B) the 4×4 tiled MicroFJ-60035-TSV SiPMs array, C) the custom SIPHRA/SiPM interface printed circuit board (PCB), D) the IDE3380 SIPHRA application specific integrated circuit (ASIC) frontend readout encapsulated within a chip on board (CoB) package, E) the aluminium light-tight detector housing, F) an exploded computer aided design (CAD) diagram showing the arrangement of the instrument components. A figure showing an assembled configuration with cutouts is also shown in Figure 2.2 for the engineering qualification model (EQM) version of GMOD, while Figure 2.6 shows the FM version integrated with the spacecraft. Dimensions are approximate.

to help improve scintillation light collection. The $CeBr_3$ scintillator is presented in Figure 2.1A and Figure 2.2. Some key parameters of $CeBr_3$ are presented in Table 2.1, most notably its high light yield at 60 photons keV^{-1}, fast decay at 18 ns and exceptional resolution of $\sim 4\%$ at FWHM at 662 keV (see Section 1.2.3 for a comparison with other standard scintillators).

For the purposes of GRB triggering, high spectral resolution is not a necessity; instruments such as the Fermi GBM detectors which use NaI(Tl) (Meegan et al. 2009) and BurstCube (Perkins et al. 2017) which uses thallium doped caesium iodide (CsI(Tl)) are both more than adequate scin-

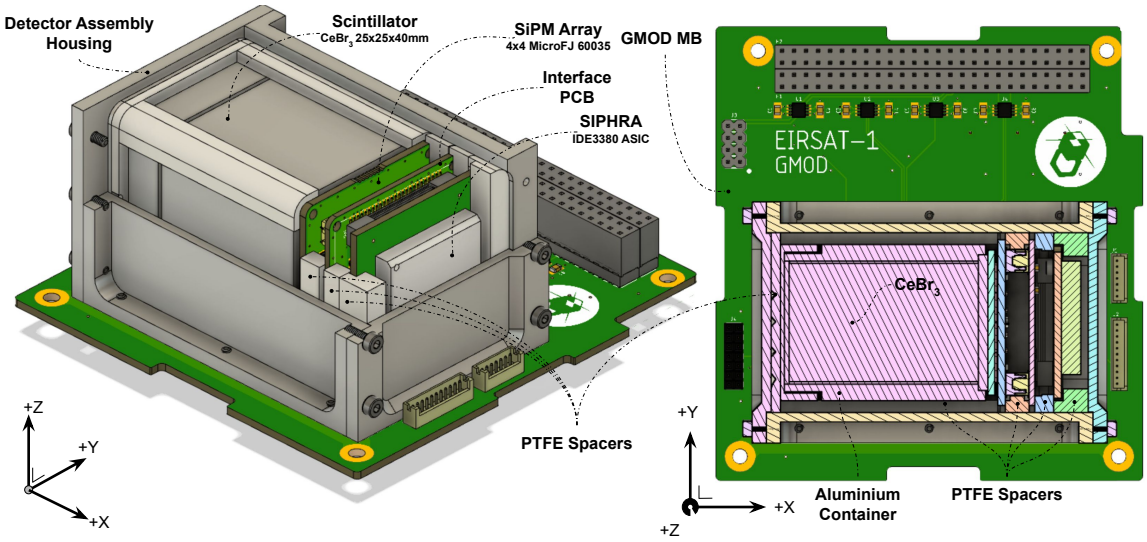

Figure 2.2: *Left*) A pealed back view of GMOD's internal electronics assembly, supported by PTFE spacers, showing the exposed $CeBr_3$ scintillator, SiPM array PCB, interface PCB and ASIC chip on board (CoB). *Right*) A top-down, +Z-axis view, with detector assembly cutaway showing internal assembly components. As described in Section 2.1.4, this figure shows the original mounting configuration used during the EQM subsystem and system level ETC (i.e. direct mounting to the motherboard). This configuration was later changed to as seen in Figure 2.6.

tillators for this task. For GRB triggering, it is the timing, light curve measurement and broad spectral properties, typically within the 50 keV–300 keV energy band that are most important. However CubeSats can provide an invaluable opportunity to both demonstrate technology and perform GRB science with low cost, low risk and short development timescales while maximizing the capability to develop clusters or constellation configurations for true full sky coverage. For example, while GMOD is a science payload which is expected to produce a scientific return, it is also a means to demonstrate future gamma-ray detector technology, such as high performance scintillators and SiPMs.

Cerium doped lanthanum bromide ($LaBr_3$:Ce) as a scintillation material was investigated and proposed (Mitrofanov et al. 2010; Greiner et al. 2012) for use with many up coming instruments during development of what would eventually become the GMOD detector (see Section 4.1). This made $LaBr_3$:Ce a scintillator of interest for a CubeSat instrument demonstration to progress its TRL, however for the purposes of GMOD it was deemed unsuitable. This is due to its relative expense but also in part because of a general pivot away from the use of $LaBr_3$:Ce for position sensitive calorimeters, towards $CeBr_3$ which has a lower internal background emission.

The presence of the naturally occurring ^{138}La radioisotope in $LaBr_3$:Ce produces an internal beta continuum background below 255 keV and a corresponding Compton continua from gamma emissions at 788 keV and 1.436 MeV extending down to around 200 keV (Quarati et al. 2012; Camp et al. 2016). This is not necessarily problematic for GRB triggering in the 50 keV – 300 keV energy range as a background would be persistent and can be subtracted, but it may

become more pronounced due to activation while in orbit and poses an unnecessary layer of complication regarding post processing of the spectral data. $CeBr_3$ at the time represented an alternative to missions using $LaBr_3$:Ce and was selected for GMOD as it features many comparable properties to $LaBr_3$:Ce (see Table 2.1) while being more affordable and having a lower internal background from α emissions occurring at energies >1 MeV by the decay of ^{227}Ac impurities (Quarati et al. 2013). The significance of the low background is apparent during long duration background integrations as demonstrated during the 2018 balloon flight test (see Section 4.3), where peaks from internal excitation can be see in Figure 4.13. These peaks may be used in a similar way in flight, as in that campaign, to inform the state of calibration while in orbit without contributing excessively to the relevant GRB spectral bands.

Table 2.1: Table of $CeBr_3$ properties. Equivalent measurements for $LaBr_3$:Ce are shown for comparison. The high light yield, fast decay and high resolution performance are notable when compared to other scintillators (see Table 1.1 for a more complete list of scintillators).

$CeBr_3$ Parameters		
Parameter	**$CeBr_3$**	**$LaBr_3$:Ce**
Light yield $[photons/keV]$	60	63
Decay constant $[ns]$	18	16
Peak scintillation wavelength $[nm]$	370	380
Refractive index $[at\,emission\,max]$	1.9	1.9
Energy resolution $[\%\,FWHM\,at\,662\,KeV]$	∼4	∼3
Density $[g/cm3]$	5.23	5.08
Hygroscopic	Yes	Yes
Intrinsic Radioactivity $[counts\,s^{-1}\,cm^{-3}]$	0.022±0.002*	1.185±0.006*

* Measured between 20 keV – 3 MeV for a 1"× 1" cylinder (Quarati et al. 2013).
Note: values derived from sources listed in Table 1.1

2.1.2. The MicroFJ-60035 Silicon Photomultiplier Array

SiPMs are a relatively new technology for photodetection in scintillation based instruments, providing a low voltage, compact and mechanically rugged alternative to PMTs. Given the scale of GMOD and the fact that it is a CubeSat instrument intended to perform science operations and demonstrate new technology, SiPMs were an ideal option from a technical perspective, while at the same time allowing an opportunity to demonstrate the initial calorimeter concept that GMOD was based on (see Section 4.1). A tiled 4×4 array of 16 MicroFJ-60035-TSV SiPMs supplied by OnSemi are used on GMOD providing collection of the scintillator light output. These devices were chosen primarily as they were inherited from the original calorimeter concept which used B-Series SiPMs, produced by SensL, later acquired by OnSemi. SensL was at the time an Irish based silicon photodetector company and a spin off from the Tyndall National Institute in Co. Cork. SensL SiPMs were in part selected to coordinate with the Irish photonics

and space industry. Even more fundamental to the instrument design though, the J-Series SiPMs match many of the parameters required for the GMOD instrument including the bias supply requirements, spectral and dimensional parameters of the $CeBr_3$ scintillator and also having good operating specifications including high microcell count, gain and PDE (see Table 2.2).

The J-Series SiPMs are available in 3 mm, 4 mm and 6 mm packages, denoted as FJ-30020, FJ-30035, FJ-40035 and FJ-60035 with incrementally larger numbers of microcells with increasing device dimensions. The 6 mm Micro FJ-60035 devices contain 22,292 microcells, each being a single APD with quench resistor and optional capacitive coupled fast output. They have a breakdown voltage of $\sim$24.5 V and an operating range above breakdown of $\sim$5 V, bias supply parameters which are easily accessible for standard low noise inverting boost converter circuits. The standard operation bias during testing was typically $\sim$-27.5 V or 2–3 V overvoltage applied above breakdown, however this may be adjusted during in flight operation as required in response to increased dark current as a result of radiation exposure over its long duration life time. The J-Series devices from OnSemi are blue sensitive with the spectral range matching most common scintillator types and the peak PDE between 400–450 nm. This provides a good spectral match to $CeBr_3$ and as it happens $LaBr_3$:Ce, making interchange possible. The silicon substrate is covered in glass (refractive index $\sim$1.5) which makes index matching between the optical window on the scintillator, gel/pad media and SiPM transmission as efficient as possible.

The 6 mm Micro FJ-60035 SiPMs, with physical dimensions of $6.13\times6.13\,mm^2$ have a fill factor of 75%, an active area of $6.07\times6.07\,mm^2$ and are tiled such that the minimum space between each is 200 μm depending on the assembly accuracy. This gives the physical dimensions of the SiPM array at $25.12\times25.12\,mm^2$ (including 200 μm spacing) with a sensitive area spanning $25.06\times25.06\,mm^2$, about 6% of which is dead space between each active area[1]. This is an excellent match to the $CeBr_3$ scintillator at 25 mm$\times$25 mm, ensuring maximum light collection by the array surface. To further improve the optical coupling an Eljen EJ-560[2] silicone rubber interface was cut and placed between the interface (refractive index $\sim$1.43). This is a non fluid interface pad which is capable of compression, (i.e. during assembly, shock or vibration) but which does not deform irreversibly. No other form of optical coupling, like optical grease for example, was considered as this can leak and become extruded from between the interface gap during compression, under heavy vibration or during long duration operation. Furthermore, optical grease can be difficult to remove once applied, making it difficult to refurbish non-flight

[1] Assuming the SiPM active area is geometrically centred on the SiPM device, each SiPM package will have a 30 μm thick dead space boarder. Assembly placement adds an additional 200 μm between each adjacent array pixel. Each adjacent pixel active area is thus separated by 260 μm. In total, the active area span of the array is then sum of the active area width (6.07 mm $\times$ 4) for each pixel plus the sum of the dead space width between each active area (260 μm $\times$ 3). This excludes the dead space around the perimeter of the array. The perimeter dead space is the difference between the total array area (631.01 mm^2) and the area spanned by the active area (including the dead space between pixels) across all SiPMs (628.00 mm^2), which is approximately 3.01 mm^2. The total array active area (excluding dead space) is 589.52 mm^2, thus the dead space between each active area in the array totals 38.49 mm^2, approximately 6 % of the active area span.

[2] Eljen - Silicon rubber optical interface EJ-560

models of GMOD before and after testing.

The SiPMs are mounted via ball grid array (BGA) interface to a custom built 35 mm×35 mm PCB, fabricated by Litho Circuits[1], Co. Limerick and assembled by Realtime Technologies Ltd.[2], Co. Dublin. The array signal and bias voltage interface is provided on the underside of the PCB using a pair of 30 pin Hirose DF17s. Each SiPM is supplied bias voltage in common anode configuration through a low pass resistor–capacitor (RC) filter with cut off frequency of $\sim 300\,\text{kHz}$[3]. This is to minimise noise from transient spikes generated by the switched power supply used, as suggested in the provided datasheet[4]. A PT100 is present on the underside of the PCB along with the filtering components such that the temperature may be recorded by the ASIC readout per each gamma-ray event measurement. A fast output option, is available as a readout with fast pulse timing, but this is not used on GMOD, instead SiPM channel readout is performed on the cathode where each SiPM is directly coupled to one of sixteen SIPHRA channel inputs. The GMOD detector SiPM array is shown in Figure 2.1B and the placement within the detector is shown in Figure 2.2.

2.1.3. The IDE3380 SIPHRA ASIC

SiPM front end readout is performed using the 16-channel IDE3380 SIPHRA (Meier et al. 2016) ASIC which is supplied as a wire bonded die (shown in Figure 2.4) to a carrier chip on board (CoB) PCB[5], as shown in Figure 2.1D and Figure 2.2. SIPHRA is a low power, compact front end readout integrated circuit (IC) for SiPM, PMT and MPPCs which was designed specifically for gamma-ray detectors in high radiation environments, with high resilience to single–event–upsets (SEUs) and single–event–latch–ups (SELs) (Stein et al. 2019). In the event that the internal registers do experience a single bit flip event, unintentionally altering the ASIC configuration, a parity error circuit logs the error status for each register which is accessible over Serial Peripheral Interface (SPI) and flags the error using a dedicated output pin.

The CoB implementation allows modularity to the design of instruments as well as reducing time and complexity in the design and assembly. The die is covered with a removable aluminium cap and contains a series of 100 nF decoupling capacitors situated close to the power terminals of the ASIC to minimise noise contribution from the supply. A PT100 is also included, however this is not read by the ASIC but is instead intended to be supported externally and as the harnessing interface between the ASIC and the motherboard had already been defined, it remains unused in GMOD. The ASIC is interfaced to the SiPM array and feeds the required regulated voltages and constant current via a pair of 50 pin Samtec CLM-125-02-L-D-A connectors. The final element of the detector electronics assembly is a custom built SiPM-to-ASIC PCB interface (shown in Figure 2.1C and Figure 2.2). This is a passive interface with additional decoupling components that connects the SiPM array outputs to the ASIC and the detector elec-

[1] Litho Circuits

[2] Realtime Technologies Ltd.

[3] $f_c = \frac{1}{2\pi RC} = \frac{1}{2\pi \times 50 \times 10 \times 10^{-9}} = 312\,\text{kHz}$

[4] OnSemi: AND9782/D - Biasing and Readout of ON Semiconductor SiPM Sensors

[5] IDEAS - The IDE3380 ASIC Carrier Board

Table 2.2: A table of the most relevant parameters for MicroFJ-60035 SiPMs. The parameters associated with an overvoltage of +2.5 V is most applicable as the standard bias configuration on GMOD. Some parameters vary between similar series devices (FJ-30035, FJ-40035, FJ-60035), but are mostly the same with variation due to different microcell counts.

J-Series MicroFJ-60035 Silicon Photomultiplier Parameters		
Physical Parameters		
Active area $[mm^2]$	6.07 × 6.07	
No. of microcells	22292	
Microcell fill factor $[\%]$	75	
Package Dimensions $[mm^2]$	6.13×6.13	
Operating Temperature Range $[^\circ C]$	-40 – +85	
Cover Refractive Index [at 436 nm]	1.53	
Peak PDE wavelength $[nm]$	420	
Temperature dependence of Vbr $[mV/^\circ C]$	21.5	
Operating Parameters	**Minimum**	**Maximum**
Breakdown voltage $[V]$	24.2	24.7
Overvoltage $[V]$	1	6
Operating voltage (Vop = Vbr + Ov))	25.2	30.7
Spectral range*$[nm]$	200	900
Performance Parameters	**Ov = +2.5 V**	**Ov = +6 V**
PDE $[\%]$	38	50
Dark count rate $[kHz/mm^2]$	50	150
Gain (anode-cathode)	2.9×10^6	6.3×10^6
Dark Current - typical $[\mu A]$	0.9	7.5
Dark Current - maximum $[\mu A]$	1.25	12.0
Rise Time*- anode-cathode output $[ps]$	180	250
Crosstalk $[\%]$	8	25
Afterpulsing $[\%]$	0.75	5.0
Microcell Recharge Time Constant $[ns]$	50	
Capacitance (anode output) $[pF]$	4140	
Capacitance (fast output) $[pF]$	160	
Fast Output Pulse Width (FWHM) $[ns]$	3.0	

* The range where PDE 2.0% at Vbr +6.0 V

† Measured as time to go from 10% to 90% of the peak amplitude and measured over a 1 Ω series output resistor.

Note: values derived from OnSemi Silicon Photomultipliers(SiPM), High PDE and Timing Resolution Sensors in a TSV Package J-Series SiPM Sensors

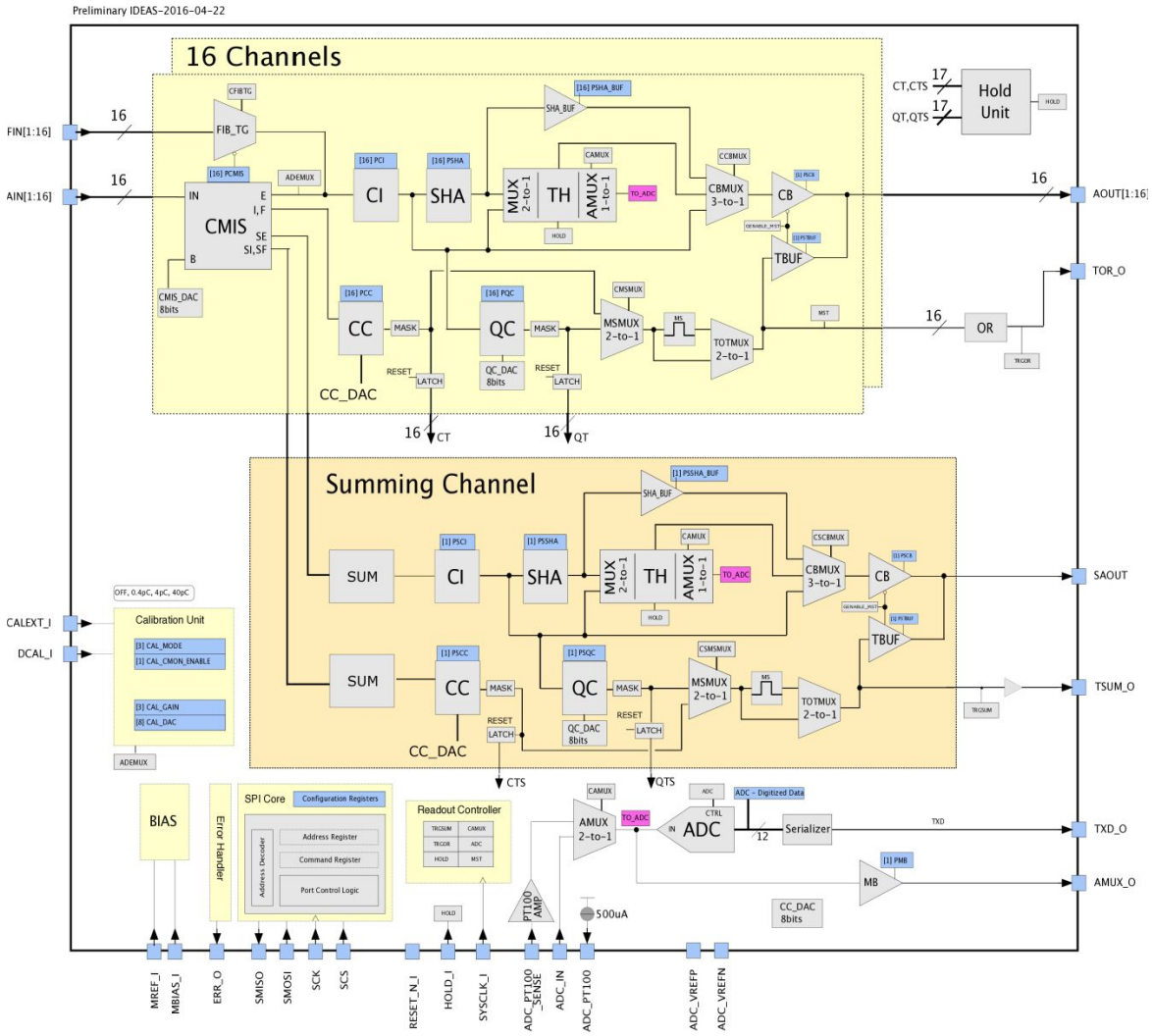

Figure 2.3: The IDE3380 SIPHRA block diagram showing the internal stages for individual SiPM and summed channel readout (Meier et al. 2016).

tronics to the GMOD motherboard. On one side of the PCB are the corresponding connectors for the CoB ASIC and on the other are the corresponding DF17 connectors for the SiPM array along with a pair of Hirose DF13 connectors (7 pin and 11 pin) for the power and digital data interface to the motherboard. Through the 7 pin DF13 connector, the necessary 3.3 V regulated voltages are supplied for analog, digital and input output (IO) supplies (AVDD, DVDD, VDDIO), along with an 80μA constant current source for internal circuit biasing. The 11 pin DF13 supplies the ASIC with digital signals, including the SPI register control, serial event readout, error and reset IO, the external trigger pin and finally a 1 MHz system clock supplied by the complex programmable logic device (CPLD). The SIPHRA block diagram showing internal functionality is illustrated in Figure 2.3 and operates as follows:

SIPHRA is capable of processing the analogue signals from the SiPM array by use of a per-channel current integrator (CI) circuit with adjustable trigger threshold, gain, shaping and a track and hold (TH) system, enabling measurements for pulse height analysis (PHA) spectroscopy and 16-channel SiPM readout. The combined signal of the individual active channels

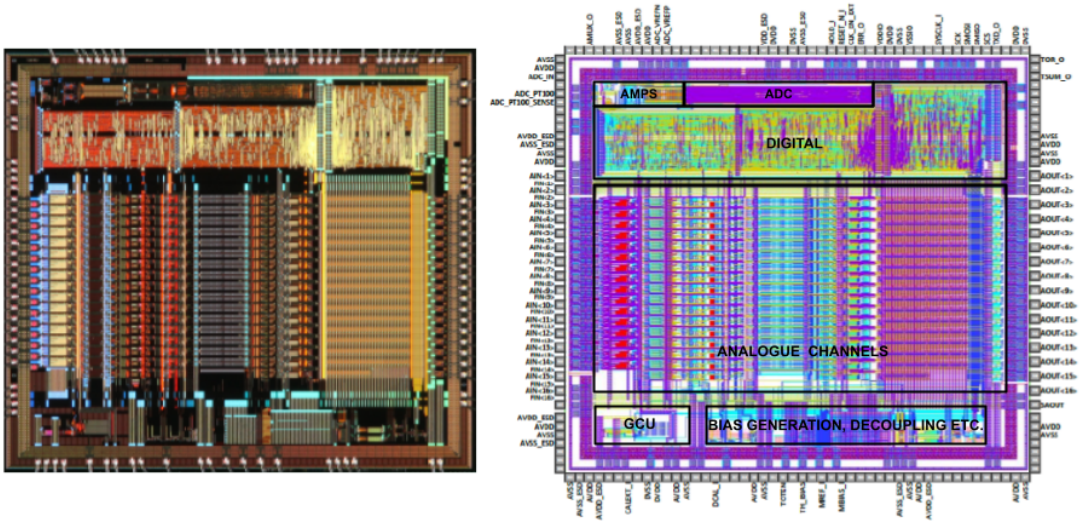

Figure 2.4: *Left*) An image of an exposed SIPHRA die from beneath the CoB aluminium cover. *Right*) The SIPHRA die floorplan (Meier et al. 2016).

can be used to produce a summed measurement output, while the SiPM array temperature may also be measured using the PT100 sensor mounted on the underside of the array PCB and sampled by SIPHRA at trigger time. Upon triggering a gamma-ray event, SIPHRA samples the peak heights and outputs a serialised data stream of 12 bit digitised 16-channel and summed PHA measurements with PT100 channel readout. This event data is the basis for GMOD time-tagged event (TTE) data products (discussed in more detail in Section 3.1.4).

The individual SiPM channels are buffered internally by SIPHRA with a current mode input stage (CMIS), one per input channel. This is used to downscale the input SiPM current as the required space on the silicon die is limited and to implement a capacitor large enough to integrate these signals would be non-viably large. This also allows the coupling of a photodetector with large output current signals with a gradation of input attenuations as follows: $\frac{1}{10}$, $\frac{1}{100}$, $\frac{1}{200}$ and $\frac{1}{400}$. In addition to this, the CMIS provides an 8 bit digital to analogue converter (DAC) which is adjustable over a range of 1 V to fine tune the applied overvoltage to account for minor variations in the breakdown voltage of each pixel in the array. In the event that any individual SiPM becomes damaged (i.e. during launch or as a result of radiation damage), the CMIS channel input may be powered down preventing the contribution of unnecessary noise from the damaged pixel.

The SiPM signal is then integrated, where again each input channel is provided its own CI circuit. The integrator stage essentially collects the charge signal from the SiPM and CMIS inputs and converts them to a voltage proportional to the integrated charge. The gain of this integrator output and the decay of the output signal (which is necessary for subsequent event integrations) is controlled by the circuit RC feedback components and can be configured in the SIPHRA registers to match a variety of instrument configurations (i.e. balancing for slow/high rate applications, complete charge collection and pile-up minimisation).

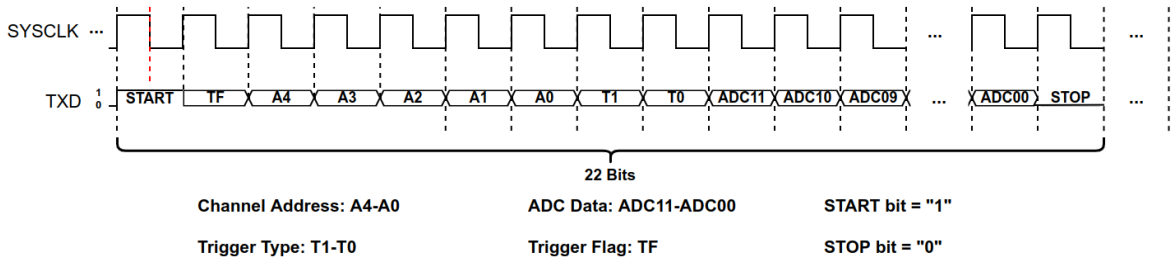

Figure 2.5: The format of the 20 bit byte readout from SIPHRA for each SiPM channel, which at 1 MBaud takes up to 22 μs per channel plus a further 22 μs deadtime between each channel readout and before re-triggering can occur.

To allow accurate measurement of the peak heights integrated by the CI stage, a semi-Gaussian shaper is provided for each channel following integration. As the CI output is similar to a delta function with decaying exponential, it is very difficult to accurately measure the peak height. The shaper stage increases the rise time of the signal by broadening and rounding the peak into a semi-Gaussian waveform with voltage magnitude proportional to the CI input. The peak rounding provides a broader and smoother signal with a more stable maximum which can be accurately sampled improving the instrument resolution by ensuring accurate measurements. The shaping time can be configured for the instrument parameters, including 200 ns, 400 ns, 800 ns and 1600 ns shaping times, essentially defining the pulse width.

An internal TH unit tracks the shaper output and holds the signal for digitisation as a PHA measurement. The hold action can be initiated internally via a current comparator (CC) or charge comparator (QC) which compares the input against a configurable threshold, or externally by supplying a logic high signal to the external trigger input (either via SPI command or pulsed pin input). In normal operation, internal triggering is used with SiPM channel input signals (i.e. in the detection of gamma-ray photons), while external triggering can be used to determine noise background and for other testing. Once held, the tracker output matching the rounded shaper signal remains constant with a configurable hold delay (69 ns–4.7 μs), during which the tracked signal is then digitised by a 12 bit successive approximation register (SAR) analogue to digital converter (ADC) at a rate of 50 ksps. Each channel track signal is multiplexed to the input of the DAC allowing digitisation and PHA measurements for all channel inputs.

The PHA measurements are then output over 1 MBaud asynchronous serial along with trigger information, including the trigger type and channel number. SIPHRA also provides a summing channel which integrates the analogue input from all 16 SiPMs which can be used for triggering. This is a separate internal channel but which has the same stages of CI, shaper, TH and PHA as on other channels. This can be used to provide a single PHA measurement for the detector when using a multichannel SiPM array along with a monolithic scintillator as on GMOD. The PT100 channel input which can give temperature measurement is readout at trigger time, allowing external monitoring of the SiPM array temperature and for bias compensation. Many of these stages and internal modules have parameters which may be configured using an inter-

nally implemented SPI core controller to program configuration inputs as required at clock rates nominally 1 MHz and up to 5 MHz.

SIPHRA readout is performed channel by channel, with each channel output amounting to 20 bits (excluding start and stop bits) as shown in Figure 2.5. For a single channel, the serial transfer consists of a 1 bit trigger flag, a 5 bit channel address (channel ID), a 2 bit trigger type flag and 12 bits for the individual SiPM channel PHAs ADC measurements and the PT100. The trigger flag bit is used to indicate if a given channel was the one which triggered the HOLD signal for the SIPHRA track and hold unit and which subsequently began the SIPHRA readout. The channel address is used to signify which channel the readout corresponds to (0 – PT100, 1,2..16 – individual SiPM channel readout from 1 – 16, 17 – summed channel, 18 – ADC_IN an auxiliary ADC input unused on GMOD). The trigger type indicates what type of trigger event caused the SIPHRA readout (i.e. internal QC, internal CC or external trigger forced by raising the HOLD_I input or via the SPI interface command). Regardless of which channels are active and enabled for readout, SIPHRA will readout enabled channels in this order.

2.1.4. The Detector Light–Tight Enclosure and Electronic Interface

The detector electronics assembly is loaded into a light-tight aluminium enclosure along the X-axis of the GMOD CRF (as seen in Figure 2.1E and Figure 2.2, which is sealed at both ends with aluminium end-caps. Within the aluminium housing the scintillator and electronics assembly are secured using a set of PTFE spacers which support and prevent compression of the SiPM array and electronics components. PTFE inserts are placed about each corner of the scintillator with a final spacer being placed between the scintillator and the -X-axis end-cap. This aluminium end-cap features a 1 mm venting hole while the associated PTFE spacer has a serpentine venting channel to mitigate stray light ingress and release any trapped air while in vacuum conditions. As seen in Figure 2.1, the original design had the detector assembly mounted onto the +Z face of the motherboard using a set of 6 M2 threaded cap screws. This is the configuration used by design during the EQM ETC. However, during vibration testing of the CubeSat integrated EQM spacecraft (which had larger test margins), this configuration was found to cause cracking in some of the solder joints just beneath the edge of the detector assembly footprint, which runs laterally along the X-axis of the PCB. It is understood that due to the mass of the detector assembly mounted to the motherboard PCB, the vibration caused flexing in the PCB around the X-axis with enough displacement to strain and crack the solder joints of the components which were mounted just beneath the detector assembly on the underside of the board. This solder cracking affected a pair of capacitors used by the bias supply which may have also been internally damaged by the flexing, causing unexpected behaviour in the GMOD readout[1]. As a solution, the damaged capacitors were replaced with capacitors which have metal framed tabs on either side which are used to raise the capacitor from the surface of the PCB and allow a level of flexibility along the solder joints. Additionally to mitigate any further risk to the PCB, a new structural bracket, the GMOD Top Reinforcement Bracket (GTRB),

[1] To be discussed in a later publication in prep

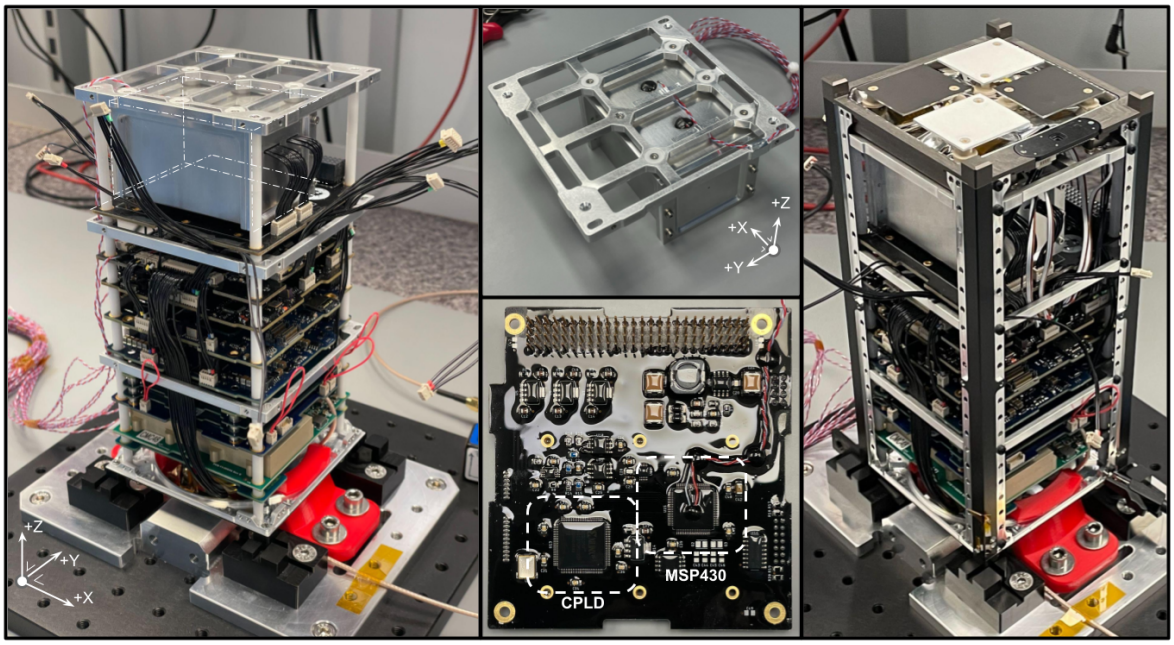

Figure 2.6: The GMOD and EIRSAT-1 FM hardware. *Left*) EIRSAT-1 during FM integration. GMOD is visible as the top most (+Z) subsystem identifiable by the light-tight aluminium detector housing (partially highlighted). *Centre Top*) The detector assembly enclosed within the aluminium housing and mounted to the GMOD Top Reinforcement Bracket (GTRB) *Centre Lower*) The GMOD motherboard PCB (-Z) showing the Xilinx CoolRunnerII CPLD and the TI MSP430FR5994 microcontroller *Right*) EIRSAT-1 close to full integration just before the solar panel installation.

was developed to mount the detector assembly above, instead of to the motherboard PCB. The GTRB (shown in Figure 2.6) is part of the spacecraft structure and interfaces thorough the 4 support rods as with other structural brackets and the PCB stack. The GTRB has a ribbed grid structure which provides rigidity and a mounting point to connect the detector assembly. The same M2 threaded cap screws are used to bolt the detector in what would have been its original inverted position, while all but one of the mounting points are thermally and electrically isolated using Delrin spacers. This is shown in Figure 2.6 with the mounting configuration in the CubeSat stack. The detector assembly is electronically mated with the GMOD motherboard by a set of DF13 connectors which connect to the SiPM-to-ASIC interface PCB and which are routed to the exterior of the detector assembly through slots in the +X-axis aluminium end-cap (Figure 2.2 harnessing and slots not shown, and Figure 2.6). These connections supply the detector assembly with power and provide a two way channel for configuration and transmission of event readout for processing by the motherboard.

2.2. The GMOD Motherboard

As GMOD is the primary payload on the EIRSAT-1 CubeSat, power consumption is at a premium. The GMOD motherboard was designed to be a low power, but capable readout and support solution for the GMOD detector. The motherboard supports the instrument operation

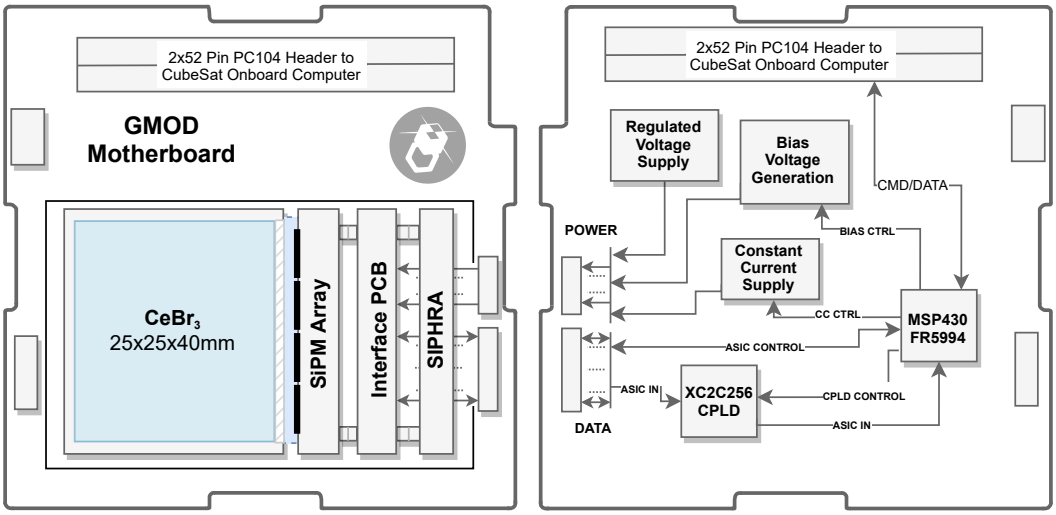

Figure 2.7: *Left*) Schematic operational layout diagram of GMOD, including scintillator and SiPM arrangements on the top of the motherboard. *Right*) The principal components for readout and control with flow of operation.

through generation of regulated power and bias supply, TTE data preprocessing, readout and storage, ASIC and general configuration of the instrument for LEO operation. The motherboard is a PC/104 compatible PCB and includes a Texas Instruments (TI) MSP430FR5994 microcontroller for main operating tasks, a Xilinx XC2C256 CoolrunnerII CPLD for detector readout preprocessing into TTE packets and a Winbond 128 MBit NOR flash device for external TTE storage. The motherboard features circuits for bias voltage generation and feedback which include the use of a TI DAC7562T dual channel 12 Bit DAC for bias voltage adjustment and a Analog Devices (AD) MAX629ESA inverting DC-DC boost converter for bias generation. Managing the instrument operation is the MSP430 which is programmed with a custom C/C++ firmware. The GMOD firmware design is covered in greater detail in Chapter 3, however the relevant details of the experiment operation are discussed as follows.

From a high-level perspective, the spacecraft OBC configures the MSP430 over Inter-Integrated Circuit (I^2C) for the intended instrument operation. This includes SiPM bias voltage and constant current configuration (for the ASIC), ASIC register configuration and preparation of the flash memory for subsequent writes upon firmware mode change into experiment mode. The transition into experiment mode enables the detector readout operation and TTE generation[1]. SIPHRA does not provide timing or timestamp information, thus to produce TTE data and to format the TTE packets with as little overhead as possible the CoolRunnerII CPLD was included for the dedicated task of TTE generation. The CPLD receives the 20 bit byte data (as in Figure 2.5) from SIPHRA for each active channel being readout and produces two TTE packet types corresponding to the two separate modes of operation: Summed TTEs (generated in Experiment Mode from summed and PT100 channel data) and full Channel TTEs (generated in Experiment16 Mode from all 16 channels, the summed and PT100 channel readout). The

[1]The general principles of operation are the same for experiment 16 mode, which allows individual SiPM readout.

summed TTE packet format takes the original SIPHRA summed and PT100 channel readout and packs it into 4 bytes. A 2 byte attached synchronous marker (ASM) used to identify the type/start of the TTE and a 4 byte fine timestamp with μs precision are then prepended completing the TTE packet. These packets are then transmitted over 1 MBaud asynchronous serial to the MSP430 which receives the TTEs, process them, caches them in the external flash memory and when requested, transmits them to the OBC to be used for GRB triggering and the generation of light curves and spectra.

2.2.1. The TI MSP430FR5994 Microcontroller

At the core of this system is the TI MSP430FR5994[1][2], a 16 MHz mixed signal microcontroller based on a reduced instruction set computer (RISC) architecture (shown in Figure 2.6 and Figure 2.7). This device was selected for numerous reasons: its low power optimisation, 256 kB of high speed ferroelectric random access memory (FRAM), a variety of integrated peripheral modules, past family space heritage (Schoolcraft et al. 2017) and ease of accessibility. The MSP430 can be placed into an number of operational states called "low power modes", effectively a set of predefined states of activity which selectively enable or disable the central processing unit (CPU), peripheral modules and their relevant clock sources. The current consumption of any digital device is in general related to the rate at which it is clocked; the MSP430 clock system can produce three independently configurable clock signals for the CPU and peripherals. By varying the low power mode (LPM) settings, certain clock sources and peripheral resources may be placed into a low power state while others remain active. This allows the user to develop a firmware which can optimise the current consumption of the device depending on the stage of operation. The combined use of LPM states and internal FRAM storage helps to reduce the power requirements of the MSP430. FRAM is equivalent to flash memory in terms of its interface and non-volatility, but superior in terms of read/write access (close to 8 MBps compared to flash at 14 kBps), read/write endurance (10^{15} write/erase cycles compared to 10^5 for flash)[3], and ultra low power requirements (requiring just 1.5V compared to 10-14V for the flash charge pump). It has even been shown to have some level of radiation resilience (Guertin et al. 2015) and a reduced soft error rate (SER)[4] as compared to static random access memory (SRAM), 8 kB of which is available on the MSP430FR5994[5]. The device has a large selection of internal peripheral modules: six 16-bit timers with multiple capture compare registers, two enhanced universal serial communication interface (eUSCI) modules (eUSCI_A supporting up to 4 channels independently configurable as either UART/SPI and eUSCI_B supporting up to 4 channels independently configurable as either I2C/SPI), a 6 channel direct memory access (DMA) controller, a 12-bit SAR ADC with multiplexed inputs and 68 multiplexed

[1] MSP430FR58xx, MSP430FR59xx, and MSP430FR6xx Family User's Guide (SLAU367P 2012, Rev:2020)

[2] MSP430FR599x, MSP430FR596x Mixed-Signal Microcontrollers Data Sheet (SLASE54D 2016, Rev:2021)

[3] Maximizing Write Speed on the MSP430™ FRAM (SLAA498B 2011, Rev:2014)

[4] MSP430™ FRAM Quality and Reliability (SLAA526A 2012, Rev:2014)

[5] This is partitioned in the default linker file provided by TI in Code Composer Studio (CCS), into 4 kB blocks, half allocated to common use by the CPU and stack, while the other reserved for the Low-Energy Accelerator module. As this is unused on GMOD, this has been merged into a single 8 kB block.

general purpose input/outputs. A brief list of some of the internal peripheral devices on the MSP430FR5994 microcontroller and GMOD in general are summarised in Table 2.3.

Table 2.3: A component list of the GMOD instrument, including a high-level overview of the detector and the GMOD motherboard hardware and a list of the most relevant MSP430FR5994 internal peripheral modules.

Detector			
Crystal	Scionix $CeBr_3$ 25×25×40mm		
SiPM	OnSemiconductor MicroFJ60035-TSV		
Array	Custom 4x4 (16×) tiled SiPM array		
Front-end	SIPHRA IDE3380 ASIC (Carrier Board)		
Motherboard			
μC	16-bit, Texas Instruments MSP430FR5994		
CPLD	Xilinx CoolRunnerII XC2C256		
Storage	128-Mbit (16 MB) temporary flash storage		
DAC	12-bit DAC7562T (bias/CC supply adjustment)		
MSP430FR5994 Peripherals			
CPU	16 MHz, 16-bit RISC architecture	Clk Sys	3× independent clocks (MCLK, SMCLK, ACLK)
FRAM	256 kB storage	ADC	12-bit SAR
SRAM	8 kB storage	GPIO	68 multiplexed I/O
DMA	6 channels	CRC	32-bit & 16-bit CRC
Timer	6× 16-bit timers with 7× CCRs	eUSCI	eUSCI_A (4×SPI/UART), eUSCI_B (4×SPI/I2C)

This combination of peripherals make the MSP430 a versatile option for the multiple requirements of GMOD and the general use of it in a variety of space applications. For example, the 430 platform of the MSP family has seen frequent use within CubeSat Kits[1], small satellites (Ubbels et al. 2005) (Klesh et al. 2013) and CubeSat subsystems (Aslan et al. 2014). It was most notably used on the Mars Cube One (MarCO) (Schoolcraft et al. 2017) CubeSats, companions to the National Aeronautics and Space Administration (NASA) Interior Exploration using Seismic Investigations, Geodesy and Heat Transport (InSight) lander during its 2018 Martian arrival. Finally, a large resource of example code[2] has been made available by TI for the MSP family of devices, including the MSP430FR5994, which hosts both register level and driver level examples. A wealth of documentation and application notes are also available with detailed information on all aspects of the register configuration settings for device operation. This

[1] http://www.cubesatkit.com/, https://www.gaussteam.com
[2] https://www.ti.com/product/MSP430FR5994

makes writing and testing firmware on the MSP430 an approachable task for CubeSat teams, many of which are composed of university level students, as is the case for EIRSAT-1. Much of this is discussed in greater detail in Chapter 7. A firmware specifically designed to take advantage of all of these qualities can provide high performance with a low power optimised operation. A C/C++ firmware has been developed for GMOD using the Eclipse based, TI CCS[1] integrated development environment (IDE). To date, the firmware has been verified in a series of experiments testing its response over a range of detector trigger frequencies and a simulation of GRB events using Fermi GBM data, which is discussed in detail in Chapter 3 and Chapter 6.

2.2.2. The Xilinx XC2C256 CoolRunnerII CPLD

As mentioned, SIPHRA outputs the individual channel PHA measurements in 20 bit bytes over Low Voltage Transistor Transistor Logic (LVTTL) serial without timing information. This format of serial data is unusual and is not typically supported by generic microcontroller serial module peripherals. Similarly, while high resolution timing is capable on the MSP430, its possible that the firmware may be incapable of balancing its numerous main tasks during experiment operation while at the same time providing accurate timestamping for consistent TTE readout. For these reasons a dedicated Xilinx XC2C256 CoolRunnerII CPLD[2] was used to provide the functionality of generating TTE packets from received SIPHRA channel readout, while also appending fine timestamp detection information.

The CoolRunnerII family of devices are produced with each member having a power of 2 scaled number of microcells, from the XC2C32A to the XC2C512 device. Originally the XC2C64A device was selected for GMOD as on the demonstration model (DM)–1 motherboard as this offered the minimum anticipated amount of resources required. However this was revised for the DM–3 motherboard to the XC2C128 which uses the same VQ100[3] package dimension and footprint as the XC2C256 allowing easy upgrade if necessary. This was eventually superseded by the XC2C256 and replaced on the DM–3 motherboard and added to the EQM and FM designs. The XC2C256 CoolRunnerII has 256 macrocells in total, each being a building block for synthesised logic designs. A series of 16 of these make up a programmable logic array function block which are internally interconnected to each other and to the IO block for external/internal IO. The CPLD is clocked externally using a 20 MHz oscillator which is divided for 1 MHz clock rate, which the CPLD also supplies to the SIPHRA system clock.

A configurable logic device like a CPLD was the ideal solution, providing high speed configurable logic while being a relatively simple solution to the unusual serial format. The choice of a CPLD over, for instance, a field programmable gate array (FPGA) device (i.e. the Xilinx Zynq-7000 as used on the Galao readout integrated circuit (ROIC) evaluation board) or a single-board computer (SBC) which could also incorporate the tasks of the MSP430 microcontroller, again amounted to excess power consumption, something which was limited by the mission

[1] https://www.ti.com/tool/CCSTUDIO

[2] CoolRunner-II CPLD Family Datasheet (DS090 (v3.1) September 11, 2008)

[3] VQFP (Very-small Quad (VQ) 1.0 mm thick in a flat package form with 100 pins

parameters. Furthermore the use of a CPLD in this particular situation offers a number of advantages. They are typically low cost, their memory is internally stored in non-volatile memory (NVM) (i.e. external NVM is not required), they are electronically erasable and in the case of the CoolRunnerII CPLD is in flight reprogrammable (functionality discussed in Section 3.1.9), a massive advantage given its ultimate operation environment in LEO. One downside is the fact that these devices are inherently smaller in programmable complexity and internal resource capacity which means the implementation of a logic based serial Universal Asynchronous Receiver/Transmitter (UART) transmit/receive, first in first out (FIFO) buffer and TTE time tagging system must be conservative in its design.

A source code was developed in the Verilog hardware description language (HDL) with the Xilinx ISE Design Suite[1], which would synthesise a custom logic based serial UART with 20 bit byte transmit/receive capability, a temporary FIFO buffer and a TTE time tagging system. When SIPHRA readout is triggered, the channel data for each active channel is readout in sequence. This readout sequence is predictable, beginning with channel 0 (PT100 channel data), the next being the first SiPM channel data up to the 16^{th} SiPM channel and finally the summed channel data readout. Of course the readout of a given channel by SIPHRA is dictated by which channels are configured to be enabled by the GMOD MSP430, which itself is determined by the configured GMOD state by the OBC (i.e. experiment mode enables summed and PT100 readout, while experiment 16 mode enables full channel readout, summed and PT100 channel readout).

Each bit received from SIPHRA is shifted into the CPLD into a FIFO receive buffer. Upon reception of the first 20 bit byte for a given SIPHRA trigger, a 32 bit counter incrementing at a frequency of 1 MHz is sampled within the CPLD. This represents the fine timestamp for this event. The fine time is essentially a 1μ second record of elapsed time relative to the SIPHRA system clock which is supplied by the CPLD and rolls over every 71.5 minutes[2]. The first channel received will always be Channel 0 (the PT100) regardless of experiment configuration modes as all include readout of the PT100 temperature sensor. Therefore, since the channels enable for SIPHRA readout are dependent on the current GMOD mode, it is ambiguous which channel data will be received next and by consequence, which TTE packet the CPLD must produce. However, once the following channel byte is received it becomes obvious which TTE must be generated based on the channel address ID: if this is Channel 1 (SiPM channel 1) this implies a full 16 channel TTE is to be generated, if it is Channel 17 (summed channel) this implies a summed channel TTE is to be generated.

At this point, the packet transmission begins by placing data into a transmit FIFO buffer. These recieve/transmit FIFOs are used to allow some margin for timing delays between the receive and transmit ends of the CPLD accrued by the logic and the time lost in determining the readout and

[1] ISE Design Suite Website

[2] To relate this to an absolute time frame and avoid ambiguity with respect to the OBCs time record, an additional coarse timestamp is also associated with TTEs packets grouped into pages by the MSP430 which sources a counter with a 1 second time base referenced by the OBC pulse per-second (PPS)

TTE type to produce. Once the TTE type being generated by the CPLD has been established, a 2 byte ASM coded as either a summed channel ASM (0x44, 0x4D) or a 16 channel ASM (0x47, 0x4D) is placed into the transmit buffer along with the fine timestamp and the TTE packet data. This packet structure is discussed in more detail in Chapter 3 and is illustrated in Figure 3.4. As the individual channel bytes from the SIPHRA readout (see Figure 2.5) are received by the CPLD for each active channel, the channel information is packed in such a way to strip redundant information and minimise inefficiency in CPLD resources, transmission time and memory requirements. The channel address and its padding is removed (replaced by a channel enable bit) as this information is implied by the TTE known packed structure established for the instrument. The TTE packet is transmitted over LVTTL serial at 1 Mbaud asynchronous serial to the MSP430 and is further processed as discussed in Section 3.1.4.

2.2.3. The Winbond W25Q128JV 128 MBit NOR External Flash

A Winbond W25Q128JV 128 MBit NOR flash device[1] was selected as external memory for caching large quantities of TTE data while in instrument readout operation. The use of this chip is further explored in Section 3.1.7. While the flash chip has a number of advantageous features (block/sector protect, power supply control, dual and quad SPI communications), the entirety of the addressable space is used simply as a pair of buffers, a circular ring buffer (summed channel TTE storage) and a linear buffer (16 channel TTE storage). The flash device can be read, programmed (written), erased and configured over 16 MHz SPI using an instruction set devised by the manufacturers. The 128 MBit flash memory is organised into 256 individual 64 kB blocks. Each block is composed of 16 sectors of 4 kB, where each sector is divided into 16 pages of 256 bytes.

2.2.4. Bias Voltage Generation and Regulated Voltage Circuits

The SiPM adjustable bias voltage circuit is based around a MAX629ESA inverting DC-DC boost converter[2]. This inverts and boosts the battery supply ($\sim$8 VDC) from the spacecraft power supply unit (PSU) from a voltage between -24.5 V up to $\sim$ -28 V as configured by component selection and with variability set by adjusting the feedback pin between 0 V and 3.3 V using a dual channel 12 bit TI DAC7562T DAC[3]. The DAC is SPI configurable by the MSP430 and its bias voltage can be set through GMOD by the OBC. This device uses an internal 2.5 V reference, which is configured with a gain of 2 (V_{ref} = 5 V)[4] meaning the DAC and the bias voltage output can be adjusted in steps of 1.2 mV per digital increment from 0 – 2^{12} - 1. The second channel of the DAC is used in the generation of a 80μA constant current supply required by SIPHRA for internal biasing, using an instrumentation operational amplifier (op-amp)[5] and a circuit based on a recommended design from TI[6]. A set of three low dropout voltage regula-

[1] Winbond 128 MBit NOR flash Datasheet
[2] MAX629ESA inverting DC-DC boost converter
[3] DAC7562T 12-Bit DAC
[4] As the supply to the DAC is 3.3 VDC the device output is saturated at 3.3 V.
[5] INA326, Precision, Rail-to-Rail I/O Instrumentation Amplifier
[6] TI Precision Designs: Verified Design Low Level (5 µA) V-to-I Converter

tors[1] are used on GMOD to generate the required 3.3 V supply for the voltage sources (DVDD, AVDD, VDDIO) for SIPHRA. A fourth regulator is also included to generate a 1.8 V supply for the CPLD.

2.2.5. The Motherboard PCB

The GMOD motherboard is fabricated from a four layer FR-4 material, two internal ground layers for improved signal integrity and a bottom layer for the majority of GMOD electronic components with the upper layer being dedicated mostly to electrical interfaces. A series of mounting holes are included, which were originally intended for the mounting of the GMOD detector assembly to the motherboard PCB, using a set of M2 bolts. This configuration has been replaced by the more mechanically sound arrangement of a top bracket instead supporting the detector assembly just above the PCB surface (as described in Section 2.1.4). A number of electrical interface points exist on GMOD between the detector and the motherboard, the spacecraft bus and various programming ports. A pair of Samtec ESQ-126-39-G-D socket strips make up the 104 pin spacecraft bus header, the layout of which is similar to other CoTS hardware such as that from the CubeSatKit developed by Pumpkin Inc[2]. This is also coincidentally similar to the form factor outlined by the PC/104 specification (PC/104 Consortium 2015). These headers provide access to GMOD for the OBC (over Spy-Bi-Wire (SBW), I^2C, serial and the PPS signal) and supplies power (over 3.3 V, 5 V, +12 V and +VBatt which is nominally around 8 V) and star configured ground for the spacecraft. A separate pair of DF13 headers, a DF13-1$\times$7 and a DF13-1$\times$11 are used to supply regulated power, a constant current supply and the SiPM bias voltage along with the necessary digital signals required for ASIC configuration, operation and readout. A pair of programming headers are also available for programming both the CPLD and the MSP430 over Joint Test Action Group (JTAG), however these have been mostly phased out in their use in preference of the intended in-system programming (ISP) method. The OBC is capable of reprogramming the MSP430 over SBW using the source code compiled binary, while MSP430 is able to reprogram the CPLD[3] over an Xilinx Serial Vector Format (XSVF) command interface using binary data buffered from the OBC. The motherboard PCB was fabricated by Litho Circuits and the assembly of electronic components was provided by Realtime Technologies Ltd.

2.3. Conclusion

In this chapter, a detailed overview of the GMOD instrument hardware was presented including, describing the detector assembly $CeBr_3$ scintillator, SiPM array, SIPHRA ASIC and the GMOD motherboard readout and supports system. The following chapter (Chapter 3) will address the firmware aspect of the instrument, developed as part of this thesis to operate GMOD in low Earth orbit (LEO).

[1] LP385x 1.5-A Fast Response Ultra-Low Dropout Linear Regulators
[2] www.cubesatkit.com
[3] Xilinx In-System Programming Using an Embedded Microcontroller

Chapter 3

The Gamma-Ray Module Firmware

The GMOD detector is functionally supported by the GMOD motherboard, a custom built readout and support system. A detailed overview of the GMOD hardware is given in Chapter 2. The motherboard will provide a number of operation critical duties, including readout and control of the GMOD detector, instrument configuration, bias voltage generation and service of time tagged and processed TTEs to the EIRSAT-1 OBC. This in-house developed system will accomplish this using a C/C++ firmware running on a Texas Instruments MSP430FR5994 mixed signal processor, a 16-bit, low power, 16 MHz microcontroller. This firmware has been extensively tested over a number of test campaigns at system level (mission testing (Doyle et al. 2022b) and ETC testing (Dunwoody et al. 2022c)) and at subsystem level (fixed trigger rates (Mangan et al. 2021e) and dynamic HITL testing (Mangan et al. 2022d)). The latter is discussed in Chapter 6, while a detailed discussion of the development approach, cycle and versioning employed for the firmware is given in Chapter 7. This section will present an overview of the development of this firmware, the design and functionality. The contents of this chapter are partially derived from a publication in the proceedings of the 8th IEEE International Conference on Space Mission Challenges for Information Technology (SMC-IT, July 26–30, 2021) (Mangan et al. 2021e).

3.1. MSP430 Firmware Structure

3.1.1. High-Level Perspective

The basic operation of the GMOD firmware is the collection of TTE data as generated by SIPHRA and the CPLD in response to a single gamma-ray photon detection (this is described further in Section 2.2.2). Readout of the detector is illustrated in Figure 3.2 and occurs as follows: a gamma-ray is either partially or fully absorbed by the $CeBr_3$ scintillator, which in turn produces a number of photons proportional to the energy of the incident gamma-ray within a wavelength matching the peak photo sensitivity of the J-Series SiPM array. Each SiPM is made up of an array of many thousands of microcells, avalanche photodiodes in Geiger-mode operation with a series quench resistor; photons absorbed by these microcells trigger an avalanche flow releasing a fixed amount of charge which is proportional to the energy of the incident gamma-ray photon. SIPHRA integrates and shapes this current signal, which when surpassing a fixed trigger threshold, triggers digitisation of the pulse height using a 12-bit SAR ADC. The ASIC then outputs the event data as a 20-bit serial stream at 1M Baud for each active SiPM channel, 12-bits for the ADC measurement and the remaining bits allocated to channel trigger information. This is an unusual form of serial transmission which cannot be readily handled by the MSP430 eUSCI module and must first be reduced for efficient bit packing. This is performed by a Xilinx XC2C256 CPLD which directly receives the SIPHRA trigger data

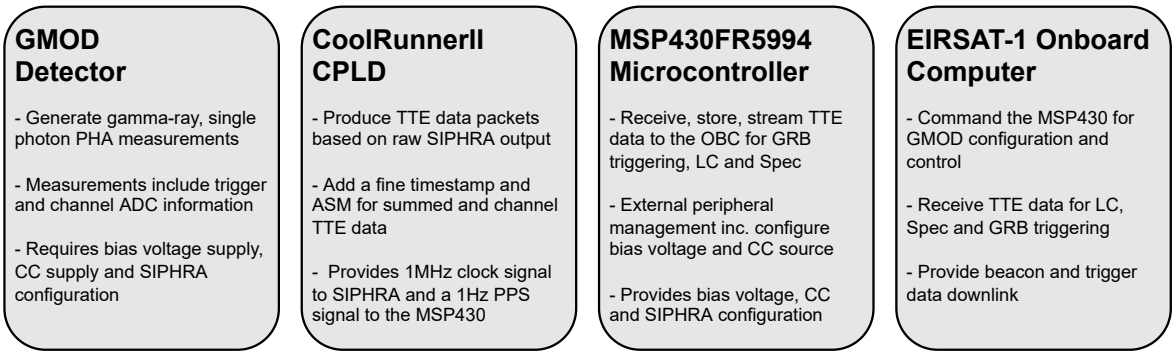

Figure 3.1: Figure showing the high-level breakdown of GMOD's instrument operation. Details of the motherboard hardware are provided in Figure 3.2 and the MSP430 in Figure 3.3.

and produces two types of TTE: 16 channel, containing measurements for each active SiPM channel and summed channel, containing the summed signal measurements from the SiPM array. The CPLD also applies a 4 byte fine-timestamp with a 1 μs time base and an ASM as identification bytes for distinct recognition of the TTE type (as either summed channel or 16 channel data). It is at this point that both summed and 16 channel TTEs, consisting of the pulse height spectroscopic measurements from the detector, are transmitted to the MSP430FR5994 microcontroller over 1 MBaud serial for processing and temporary storage. This collected TTE is grouped within the MSP430 SRAM memory in a 1 kB FIFO buffer which is split into 4 pages (each 256 kB in size), before being written to external flash memory. There are two modes for the OBC to retrieve this data: as each page is written to flash it is also copied to a larger 4 kB FRAM buffer used to stream each page directly from internal memory. Alternatively, streaming from external flash memory may be used when the streaming buffers overflow or upon starting from a page before streaming internally began. This data is retrieved by the OBC and is used in the process of light curve and spectra generation for GRB triggering onboard (Doyle et al. 2022a). The operation of the GMOD firmware is encapsulated in the block diagram, Figure 3.1.

3.1.2. Design Philosophy

The philosophy behind the design of the GMOD firmware on the MSP430 dictates that the firmware has limited autonomy in performing configuration actions outside the knowledge of the OBC or the spacecraft operators. This is to make the system as simple as possible, while ensuring that the state and actions of the firmware are predictable by reducing the complexity of the implementation, thus minimising the likelihood of unintended bugs passing into the FM iteration. As such, the MSP430 acts in many ways as a "slave" device to the OBC, and its authority in configuring the instrument parameters (bias voltage, constant current output, SIPHRA register configuration etc.) is derived from instructions from the OBC, and by extension (in most cases) the spacecraft operator. In other words, the MSP430 firmware must be able to interpret commands from the OBC and implement the given configurations as instructed, but (under this philosophy) cannot configure the instrument independently of the OBC. This is exemplified by the fact that the MSP430 does not perform light curve generation or GRB triggering, however this is also partially due to limitations with the hardware as it is unlikely that in the current

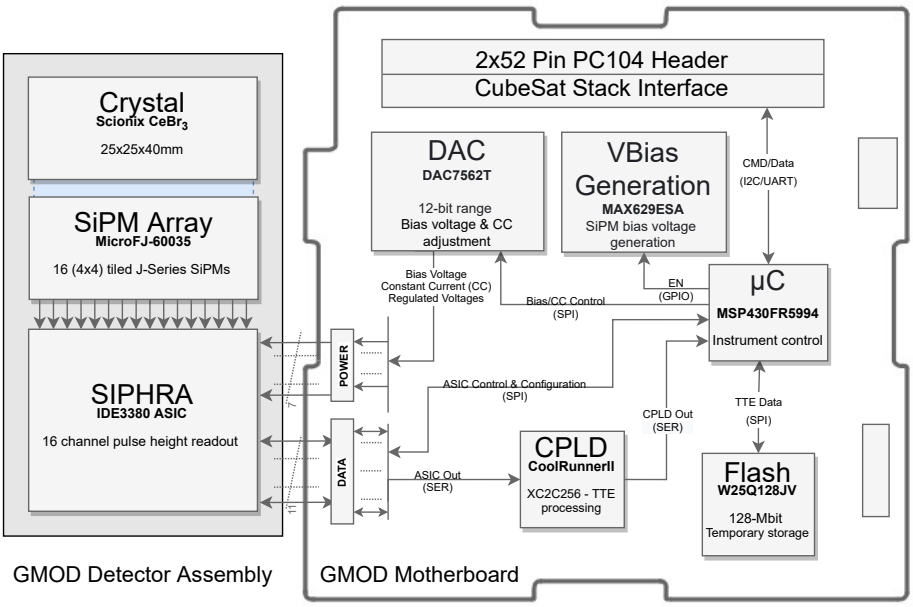

Figure 3.2: The high-level hardware operational diagram of GMOD, including the detector assembly, GMOD motherboard and principal components. For clarity, only the most relevant details are encompassed in this diagram. A complete overview of the instrument hardware is presented in Chapter 2.

bare metal configuration, TTE collection, storage and service of calculated light curve data and triggering could be reliably implemented on a 16 MHz microcontroller, while at the same time serving this trigger related TTE data to the OBC. Performing light curve and spectra generation along with triggering algorithm calculations would add a significant overhead which could compromise the reliability of the essential processes of TTE collection, processing and storage.

3.1.3. Data Transmission, Command and Control

Command and control of the MSP430 is performed exclusively over I^2C interface at a standard 100 kbits/s. The I^2C communication on the MSP430 firmware side is entirely interrupt driven with the MSP430 and GMOD acting as a slave device to the OBC. A generic command structure developed for GMOD has been implemented, with the first byte received by the MSP430 indicating a command type (i.e. firmware mode change), all following received bytes representing data with which to perform the command (i.e. the mode to change to) and a final transmitted byte indicating the command status success/fail (i.e. successful reception of the command).

Transmission of TTE data in 264 byte page based packets is carried out over 128 kBaud LVTTL serial to the OBC. In this way the entirety of the detector experiment data is conveyed over asynchronous serial, while instrument configuration and status can be requested over I^2C. This was done because the I^2C bus GMOD uses is shared with the EMOD payload and high rates of science data transfer end up blocking configuration commands for both payloads. While higher baud rates are available on the MSP430 eUSCI peripherals, the rate of data transfer is limited by the amount of data which the OBC can receive and process in its internal serial buffers within a short amount of time. In order to manage this and to allow the OBC the time needed

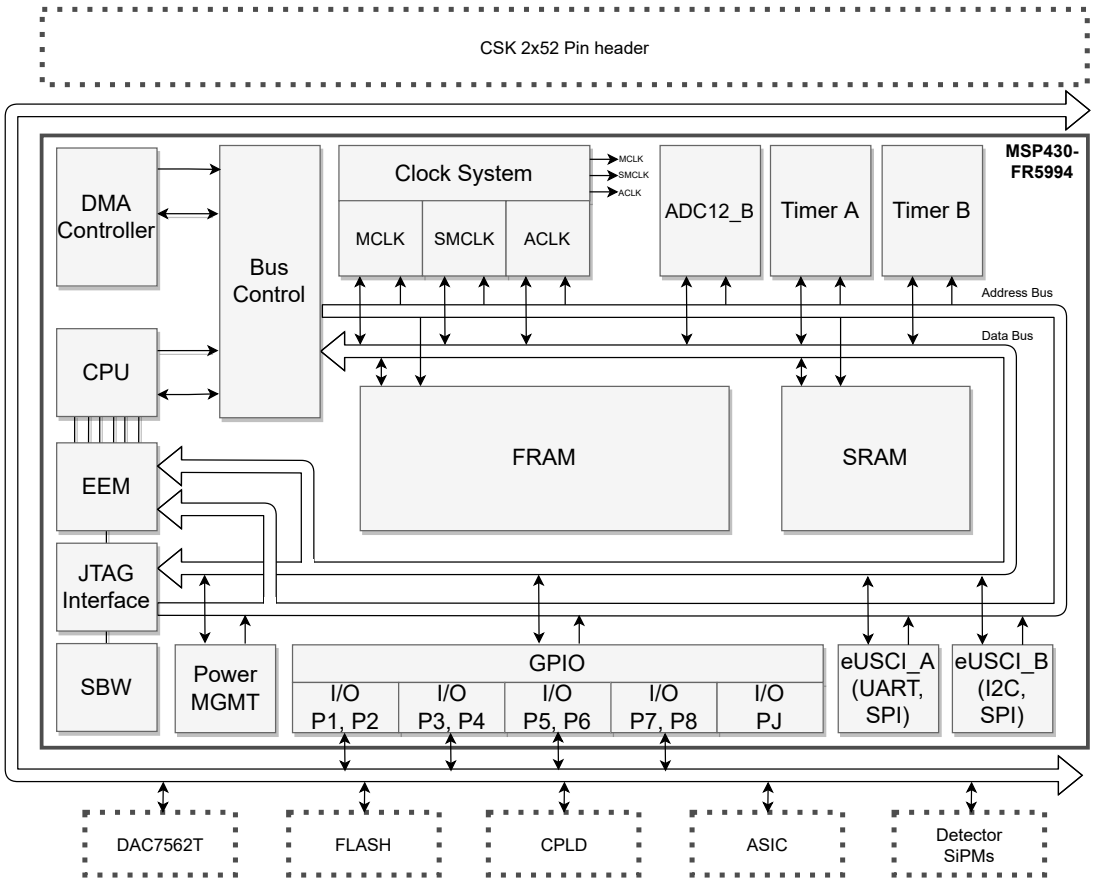

Figure 3.3: Functional block diagram of the MSP430 along with its interface to external peripherals on the GMOD motherboard. Based on information from the MSP430FR5994 datasheet - SLASE54D.

to read the transmitted data from its serial buffers, the baud rate was configured as 128 kBaud (which can be modified in flight) while at the same time a set-to-transmit flag on the MSP430 was implemented which must be set by the OBC before the firmware queues the next page of data for service to the OBC. This means that the OBC controls the flow of TTE page data from GMOD which helps to prevent bottlenecking.

3.1.4. Data Products, Packet Structure and Flash Memory Allocation

There are two main data products from the GMOD instrument: summed and 16 channel TTEs. The format of these packets are shown in Figure 3.4 and their storage in external flash memory is described in Figure 3.5. Summed channel TTE data is the main scientific data product and is used for the generation of light curve, spectra and GRB triggering on the OBC. This form of data is generated in both experiment and experiment 16 mode during active operation while 16 channel TTE data is generated only in experiment 16 mode and is supplementary to summed channel, for use during monitoring or health checking of the instrument in flight.

3.1.5. Summed Channel Data

During experiment mode readout, the SIPHRA readout register enable bits for the summed channel output and the PT100 channel output are set. At the time of gamma-ray event trigger-

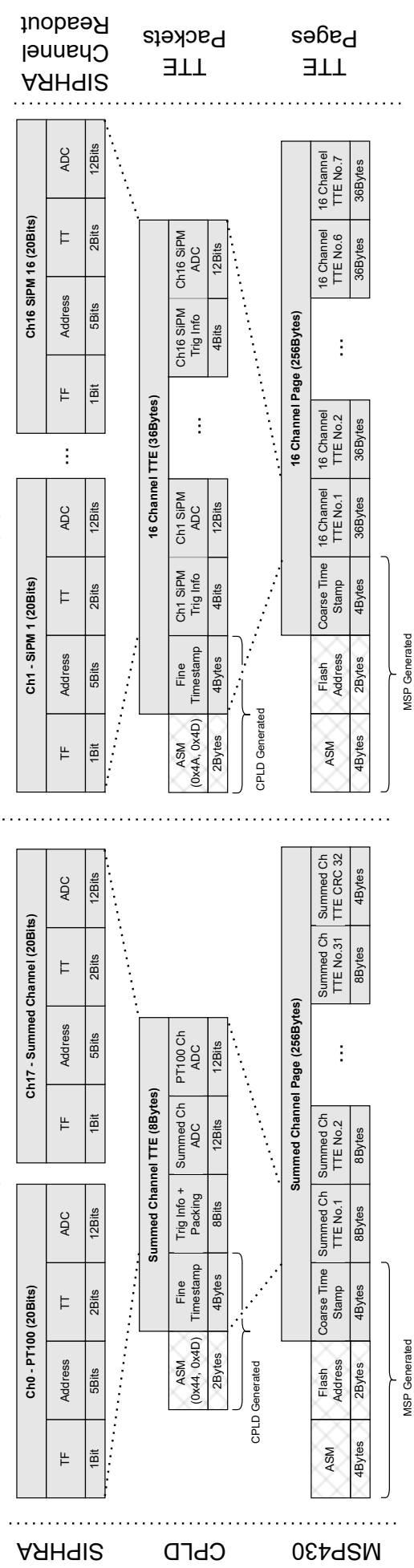

Figure 3.4: The packet structure describing the breakdown of TTE pages into individual TTEs from their source as raw SIPHRA channel readout. The derivation of summed channel TTEs and 16 channel TTEs are shown. Note: the hatching of ASM and flash address bytes for the TTE packets and TTE pages are such as these are stripped when received.

ing, the SIPHRA readout produces 20 bit bytes each for both the summed and PT100 channels (which is extended to all 16 SiPM channels while in experiment 16 mode). Each 20 bit byte is then conformed to the defined TTE packet structure by the CPLD, including the addition of a 2 byte ASM (0x44, 0x4D), a 4 byte fine timestamp (with 1 μs time base), 2 bytes of summed channel data and 2 bytes of PT100 channel data. In total the summed channel TTE packet amounts to 10 bytes, 8 bytes when the ASM is stripped. When received by the MSP430, the firmware groups each of these bytes into pages of 256 bytes, each containing a 4 byte coarse timestamp (1 s time base), 31 summed channel TTEs (with stripped ASM) and a 4 byte cyclical redundancy check (CRC) calculated over the leading 252 bytes of data contents. The packet structure for summed channel readout is shown in Figure 3.4.

3.1.6. 16 Channel Data

Full 16 Channel TTE data which consists of PHA measurements for all 16 SiPMs is also available for readout. This is provided as a secondary scientific data product and is not used for GRB triggering but instead the monitoring and health checking of the SiPM array. This form of data is only generated by the instrument in experiment 16 mode (see Section 3.1.9), but the flash memory partition associated with 16 channel TTE data may be read in idle or experiment mode. To avoid a gap the instrument availability over a long period of time during which a GRB trigger may occur, summed channel readout is also enabled in experiment 16 mode. On entry to experiment 16 mode the SIPHRA channel readout register bits corresponding to all SiPM channels, the summed channel and the PT100 channel are enabled providing full channel readout of the instrument. Each 16 channel TTE is made up of 38 byte packets (36 bytes once the ASM is stripped): a 2 byte ASM (0x4A, 0x4D), a 4 byte fine timestamp (1 μs time base) and 16 2 byte PHA measurements for each individual SiPM (32 bytes in total). As with summed channel data, the 16 channel TTE packets are grouped into a page structure of 256 bytes consisting of a 4 byte coarse timestamp (1 s time base) and 7 36 byte 16 channel TTEs (with stripped ASM). A CRC is not calculated for these pages due to their lack of priority and to ensure efficient bit packing. The packet structure for 16 channel readout is shown in Figure 3.4.

3.1.7. Flash Memory Organisation

The MSP430 has 256 kB of internal FRAM and 8 kB of internal SRAM. Given the large quantity of summed channel TTE data expected while in operation and the TTE feed on request system established between the OBC and GMOD, this memory capacity is insufficient. A circular buffering system with much larger capacity than is available internally on the MSP430 is necessary to ensure complete readout of TTE data collected by GMOD for transmission to the OBC. This is because the rate of TTE generation is highly variable both with respect to a fixed background rate but also the more dynamic rates associated with GRB events and other high-energy phenomena. Furthermore the rate of TTE requests by the OBC, and thus the freeing of memory is also variable as the OBC may request new pages of data (groups of TTE packets) when it sees fit. This means that the rate of reception of TTE data as well and the freeing of used memory for reuse is not predictable. This requires a large buffer space allowing sufficient mar-

gin such that recent historical data can still be accessible but also that the oldest data in memory can be erased and freed for reuse in storing new TTE data. In addition, enough memory must be available for a second linear style buffer for 16 channel TTE data storage.

A 128 MBit NOR flash device (hardware discussed in Section 2.2.3) was selected to provide this buffer space. The flash is split equally into two partitions, the summed channel and 16 channel (each partition containing 8 MB, 32 k pages (of 256 bytes), 256 32 kB blocks and 128 64 kB blocks). Each partition is operated independently of the other, where the address boundary is defined by the most significant bit of the addressing. The address of any byte within the flash memory is represented by a three byte value. The "state" of the most significant bit, being "0" or "1" therefore indexes byte addresses from the lower range (0x000000 – 0x7FFFFF) corresponding to summed channel data, or the higher range (0x800000 – 0xFFFFFF) corresponding to 16 channel data. The division of flash is illustrated in Figure 3.5.

The summed channel partition is operated as a circular ring buffer with a writing pointer tail indicating the next page address to be written. As summed TTE data is written to flash, it overwrites the oldest TTE pages memory, with the "writing pointer" looping continuously around the summed address space. The "writing pointer" is recorded by the MSP430 as an index of the address in flash to be written to next. This is as opposed to the conventional "head" and "tail" used in most circular buffers, which point to the start and end of the stored data respectively. The OBC can read this pointer and determine the amount of unread TTE pages in flash memory. For this reason, a reading pointer is implemented only to the extent to feed out pages to the OBC during streaming, however the conventional concept of a head does not exist on GMOD. It is important that the amount of unread data in flash which has yet to be transmitted to the OBC is kept as close to a minimum as possible to avoid the unlikely event that the circular buffer overflows and TTE data is overwritten. For the expected background rate of 50 Hz in LEO, the summed channel buffer will take $\sim$5.7 hours without reading to fill. As the memory capacity available is so large, particularly in the summed channel buffer memory space (which is to be used for GRB triggering), it is unlikely that the OBC will need to request data from address outside all but a narrow window of address space. Flash data is accessible for single page read or start of streaming from any address in the summed channel space (except for a range greater than a 32 kB block above the writing pointer), while the oldest data is erased ahead of the writing pointer to allow clean writing to the next 32 kB block of memory.

The 16 channel partition is operated as a linear buffer, with similar arrangement for head (reading), tail (writing) pointers and its old data erasing scheme. Once entered into experiment 16 mode, the writing pointer resets to the first address in the space and the first 32 kB block is erased for writing to, with each successive block being preemptively erased ahead of the writing pointer. The difference being that the writing pointer does not loop around the 16 channel address space but instead acts to fill a fixed capacity of memory of 16 channel TTE data. This was done as during a health check or channel monitoring test, the continuous readout of 16 channel and summed channel data can overwhelm both GMOD and the OBC due to its large

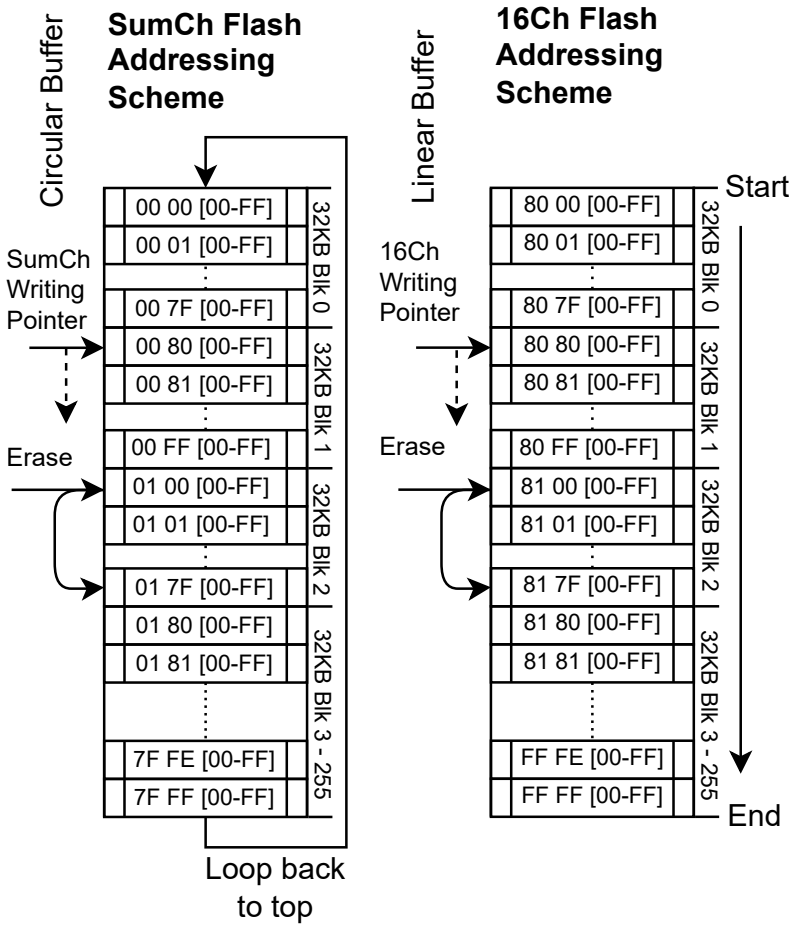

Figure 3.5: The external flash circular buffers used for summed and 16 channel TTE storage. This demonstrates the writing and erase procedure of flash memory. Erasures occur when the writing pointer reaches the start of a previously erased 32 kB block; the next 32 kB block is erased in preparation for the subsequent writing of new TTE data. The OBC has unrestricted access to the flash and may request individual page reads from anywhere in memory or for streaming to begin from any address. The addressing scheme is also shown, where the first half of flash is reserved for summed channel data and the second for 16 channel data.

quantity (see Chapter 6). 16 channel TTE data is comparatively 4× larger than summed channel which can lead to bottlenecking during readout, while at the same time it is conversely less essential. To reduce the amount of bandwidth required by GMOD and the OBC, the partition is instead used as a sort of 8 MB 16 channel sampling buffer; experiment 16 mode can be entered, GMOD can collect a sample of 16 channel data, store it for service to the OBC when convenient and upon filling of the address space automatically cease 16 channel data generation. Once the writing pointer reaches the final address in the 32 KB block of the 16 channel partition, the partition is filled, the firmware ceases 16 channel TTE generation (by mode change) and all recorded 16 channel data must be readout in its entirety before restarting 16 channel readout (otherwise it will be erased on reentry). It is impossible to begin reading 16 channel data ahead of the writing pointer during readout, however it is possible to read from any address before the writing pointer during or after 16 channel readout has begun. For the expected background rate

of 50 Hz in LEO the 16 channel buffer is expected to take $\sim$1.2 hours to fill.

As is standard with flash, it is necessary to erase a memory location before writing to it. A write cycle must be preceded by an erase of the chosen memory location, essentially a write of the memory location to 0s before writing data. Flash memory erase blocks are not on the byte level but instead follow the memory structure as previously outlined in Section 2.2.3 between arranged address boundaries: memory can be completely erased (chip erase), erased in 64 kB, 32 kB blocks or 4 kB sectors. The erase operation takes a significant duration of time to complete as this is essentially a write operation over a large address range, during which the flash chip is in a busy state and cannot be read, written or erased. These durations are 40 s, 150 ms, 120 ms, 45 ms respectively for each erase type and if not managed dynamically can detrimentally impact the performance and the flash availability. To mitigate situations where the flash is essentially blocked during an erase state, a method of suspending flash erase states mid-operation in favour of urgent flash writing of new TTE data was developed, allowing the MSP430 to balance time between erasing old memory locations and writing data to recently cleared memory locations.

The scenario mentioned above is likely to occur during operation. Given the dynamic fashion of storage and retrieval of TTE data from flash during experiment operation (particularly in experiment 16 mode where two independent buffers are active at once), the situation can arise where the flash chip is busy with a location of memory being erased, while at the same time a read/write operation is urgently required in another memory location. To prevent this it is possible to suspend an erase (or write) operation on the flash while another address location may be written to or read from (or erased). As there is only one suspension level, it is not possible to nest suspended operations, i.e. the chip cannot be in a busy state, have that operation placed into a suspended state, be made busy and again have that operation placed into a subsequent suspended state. This technique is used on GMOD to ensure the flash chip availability for constant reliable operation, while 32 kB blocks of flash can be erased to free up previously used and no longer needed flash memory. More detail on the implemented strategy is discussed in Section 3.2.2.

Read and write operations (once the memory is prepared for writing) can be performed on byte level (partial page program/read) or from the start of flash memory to the end of the address space by continuing to hold the chip select low and providing the required stimulus to continue the communication. On GMOD, TTE data (both summed and 16 channel) is grouped and stored in units of pages which are transmitted to the OBC. Each of the TTE pages are contiguously aligned in flash memory and are read/written from the start to the end of their address boundaries.

3.1.8. Page Packet Structure

For both TTE page types, the MSP430 transmits these pages of data to the OBC upon request in packets of 262 bytes referred to as “pages of data”. Each page can hold 31$\times$ summed channel TTEs or 7$\times$ 16 channel TTEs. This difference is due to the larger number of bytes per

16 channel TTE as compared to summed channel TTEs. Before transmitting to the OBC, a header is prepended consisting of a 4 byte ASM (0x47, 0x4D, 0x4F, 0x44) for synchronisation and to distinguish each page start, a 2 byte address (the two most significant bytes of the standard addressing scheme) identifying the page location in flash memory where the page was stored/sourced and finally 256 bytes of TTE page data. This page format was adopted based on the structure of the external flash memory and is shown in Figure 3.4.

3.1.9. GMOD Modes

The GMOD firmware was developed as a bare metal system with multiple modes within a main "super loop" structure. Within this main loop are a set of modes which define the GMOD operating state. The OBC may move GMOD between these different modes, which define certain configurations and the scope that the MSP430 can independently act within. Five distinct modes are defined, these are: idle, experiment, experiment 16, CPLD reprogram and safe mode. Each of these states have intended scopes of functionality, in such a way to allow structured operation and to make distinct the current state of the instrument and its expected behaviour. For example, CPLD reprogramming is performed exclusively in the CPLD reprogram mode, while instrument readout is available in experiment and experiment 16 mode but not in idle mode (however flash readout is permitted in both). Additionally, the transfer from one mode to another is accomplished through a configuration state which performs some minor setting of the instrument parameters without instruction from the OBC, for example, enabling SIPHRA readout when entering experiment or experiment 16 modes, disabling SIPHRA readout when entering idle mode and so forth. Where possible, to allow flexibility and to prevent hard locking the system configuration in situations where in flight debugging is necessary, some of the states defined configurations can be forced, provided the functionality exists within the given mode and permits the action. The available GMOD modes are outlined in Figure 3.6.

Idle Mode:

Idle mode defines the idle state of the GMOD firmware and is the default state upon initialisation for post reprogram and post power cycle actions. Idle mode is intended to be a state in which the experiment (i.e. the instrument) is inactive, SIPHRA readout is disabled and as a platform where the instrument configuration can be performed before entering experiment or experiment 16 mode. Upon entry into idle mode, external interrupts from the SIPHRA/CPLD serial port are disabled to prevent any unexpected serial transmission, SIPHRA is enabled (over general purpose input output (GPIO)) and the SIPHRA channel readout register is configured to disable all channel readout. The serial buffers are cleared in the case that a level transition during the register configuration was unintentionally interpreted as start and stop bits associated with a byte transfer. Finally a check of the status of the flash service register is performed with any suspended/busy states cleared to ensure that the flash is fully available for reading. Within idle mode is a loop state which cycles indefinitely. Through each cycle of the idle loop, the firmware services requests over I^2C from the OBC to read individual pages from flash, stream continuous summed or 16 channel data pages from flash and other peripheral operations for

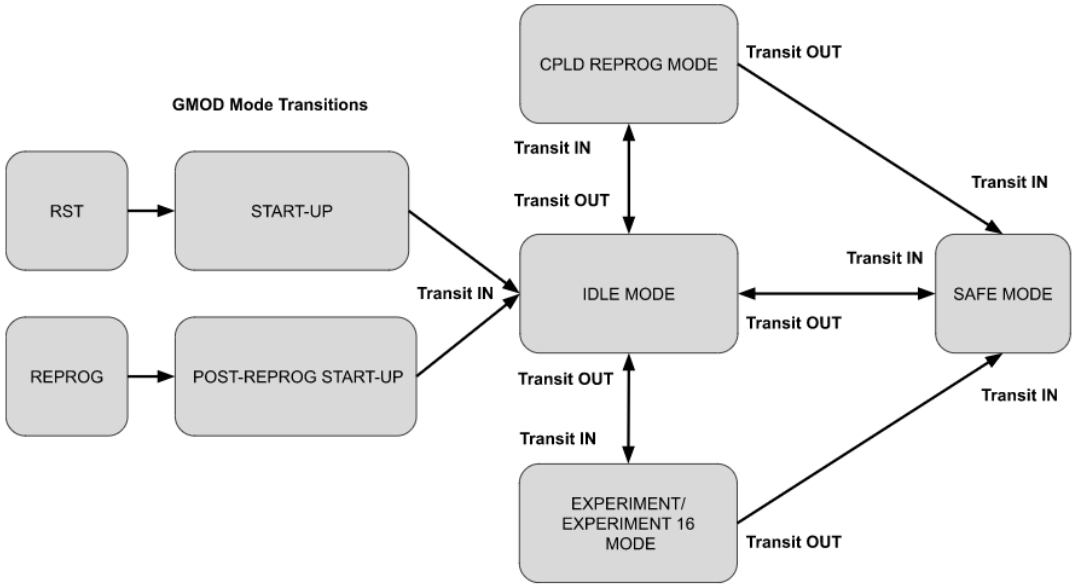

Figure 3.6: Flow diagram describing the transitions between different modes, from power up (or reprogram), through idle mode and then to any of the other available operational modes. Note: the transitions described here are recommended only and the mode change is at the discretion of the spacecraft operator assuming it is a valid mode change selection.

instrument configuration. The spacecraft operator may command GMOD (through the OBC) to retrieve individual pages (256 bytes worth) of data from any flash address location. This is useful in situations of debugging or when looping for pages from a specified block of 32/64 kB of saved TTE data. In the event that the operator requires multiple pages or a continuous stream of data from flash, streaming from either buffer (or both) summed and 16 channel flash buffers is also available from a given starting address. Configuration of the instrument before entry into an experiment mode is the primary intention of the idle mode state. As such peripheral configuration is available here, including configuration of the constant current source supply to the ASIC, bias voltage configuration, SIPHRA register configuration, OBC to GMOD serial baud rate setting and coarse time synchronisation.

Experiment Mode:

Experiment mode permits the instrument operation and enables SIPHRA readout of summed channel data (only), while providing single page and streaming from internal or flash streaming FIFO buffers. Upon entry to experiment mode a specific configuration occurs depending on the previous mode. Generally, the common settings include disabling of the SIPHRA/CPLD serial port interrupts, enabling of SIPHRA, disabling of the SIPHRA register channel readout, preemptively erasing the next 32 kB block of flash in the summed channel buffer partition, flash service register clean up (clearing busy/suspended states) and the clearing of the internal receive side FIFO buffers. Finally the summed channel and PT100 readout registers on SIPHRA and the SIPHRA/CPLD serial port is reenabled. The key distinguishing factor between experiment and experiment 16 mode is the fact that only summed channel TTE data is generated by the

instrument in this state, however streaming from any partition in the flash address space (i.e. summed or 16 channel data) is permitted depending on the configuration by the spacecraft operator. As such, while within experiment mode the same page streaming functionality exists as in idle mode, however the functionality for processing summed channel data generated by SIPHRA and the CPLD is provided.

Experiment 16 Mode:

Experiment 16 mode, which acts similarly deviates by allowing the reception and processing of summed and 16 channel data from SIPHRA and the CPLD. The mode entry configuration for experiment 16 is similar, however due to the fact that the 16 channel flash buffer partition is operated as a linear buffer, the initialisation of the internal and external memory is slightly different. To allow the flash buffer to fill from the first address in the 16 channel buffer partition, the writing pointer for 16 channel flash data is set to the start of the address space and the 32 kB block is erased for the subsequent flash writing. As this memory location is linear, once the partition is filled during readout operation the firmware automatically reverts to experiment mode (summed channel data readout only) disabling further readout of 16 channel data from SIPHRA. Assuming 16 channel streaming is enabled, the 16 channel flash partition will be readout in its entirety until such a time that the complete linear buffer has been readout, whereupon the 16 channel streaming will be automatically disabled. To prevent reentering this mode and unintentionally erasing the first 32 kB block of memory, a protect flag must be reset before entering experiment 16 mode. Both summed and 16 channel readout will be discussed further in Section 3.2.

CPLD Reprogram Mode:

CPLD reprogram mode provides limited functionality with the bare minimum capability to begin the CPLD reprogram operation. Upon entry, serial interrupts from the SIPHRA/CPLD are disabled to prevent unintentional level transitions on the serial port, while the CPLD is placed into an enable state for reprogramming. During reprograming, the MSP430 is fed a compact binary version of Serial Vector Format (SVF) JTAG bus control instructions called XSVF. This XSVF data is interpreted by an XSVF player developed by Xilinx[1] for JTAG programming for over the air and in system programming embedded applications. This player converts the commands and corresponding arguments into the intended JTAG IO stimulus generating the Test Access Port (TAP) signals. While within the CPLD reprogram mode, a loop is entered which incorporates this XSVF player into a custom state machine which handles the reception of chunks of XSVF data and command instructions from the OBC, with interpretation and TAP signalling using the player system.

Safe Mode:

Finally, safe mode was implemented to provide a state which can be entered in the event that the firmware experiences an event which is unfavourable and prevents the normal flow of operation.

[1] Xilinx In-System Programming Using an Embedded Microcontroller (ISE Tools)

For example, on initialisation the MSP430 attempts to initialise the peripheral devices one of which being the flash. If the flash fails in its initialisation (i.e. experiences a communication fail, configuration setting, locked status register), instead of entering idle mode, the MSP430 will be placed into safe mode. There is no entry configuration or settings within safe mode (other than placing the MSP430 in a LPM-3 state) in the attempt to preserve the last condition of the system for debugging.

Low Power Mode Optimisation:

To take full advantage of the low power optimisation on the MSP430, when GMOD is placed into idle mode, the MSP430 returns to a LPM-0 state where the master clock and the CPU which it supplies are deactivated and disabled. Other clock sources remain active like the subsystem master clock and the auxiliary clock, which are used to clock the peripherals and communications modules. Deeper LPM states allow low power operations at the expense of functionality, speed and device wake up time. For instance, placing the MSP430 into LPM-0 while in idle mode has the trade off of slightly higher power draw over other LPM states, while retaining the fast interrupt response and wake up time necessary for TTE collection but while consuming less power than while in active mode. For example, the experiment/experiment 16 modes originally were intended to use a low power state LPM-0, however it was found that the wake up time during TTE reception was insufficient and in many ways was superfluous given the fact that the experiment mode would require the CPU to be active for the majority of the time.

3.2. GMOD Readout Operation

The firmware operation is such that TTE packets are recieved from the CPLD, are processed and then stored in external 128-Mbit flash for service to the OBC. The MSP430 manages this flash storage by dividing it into a pair of circular ring buffers of equal size (a separate partition for summed channel and 16 channel TTEs). Upon request from the OBC, these TTEs are retrieved by the MSP430 and served to the OBC for GRB triggering, light curve and spectra generation. The MSP430 may also "stream" the TTE data directly to the OBC from internal memory for improved data transmission (all TTE data is stored in flash in the event that streaming becomes desynchronised, in this case servicing must restart from the last expected address). This is functionally represented in Figure 3.7, which shows the reception, storage and streaming of TTE data, as discussed in depth in this section.

3.2.1. Reception

The MSP430 receives TTE packets generated by the CPLD based on trigger data from the ASIC. Interrupts are generated by the SIPHRA/CPLD serial port module on the MSP430 at the reception of individual bytes. The MSP430 waits until a recognisable 2 byte ASM sequence has been received which identifies the type of incoming TTE and will determine the specific response actions for summed or 16 channel packets. Both summed and 16 channel data are handled separately within the MSP430 memory and external flash and must be individually requested by the OBC. Once a recognised ASM has been received, the expected number of

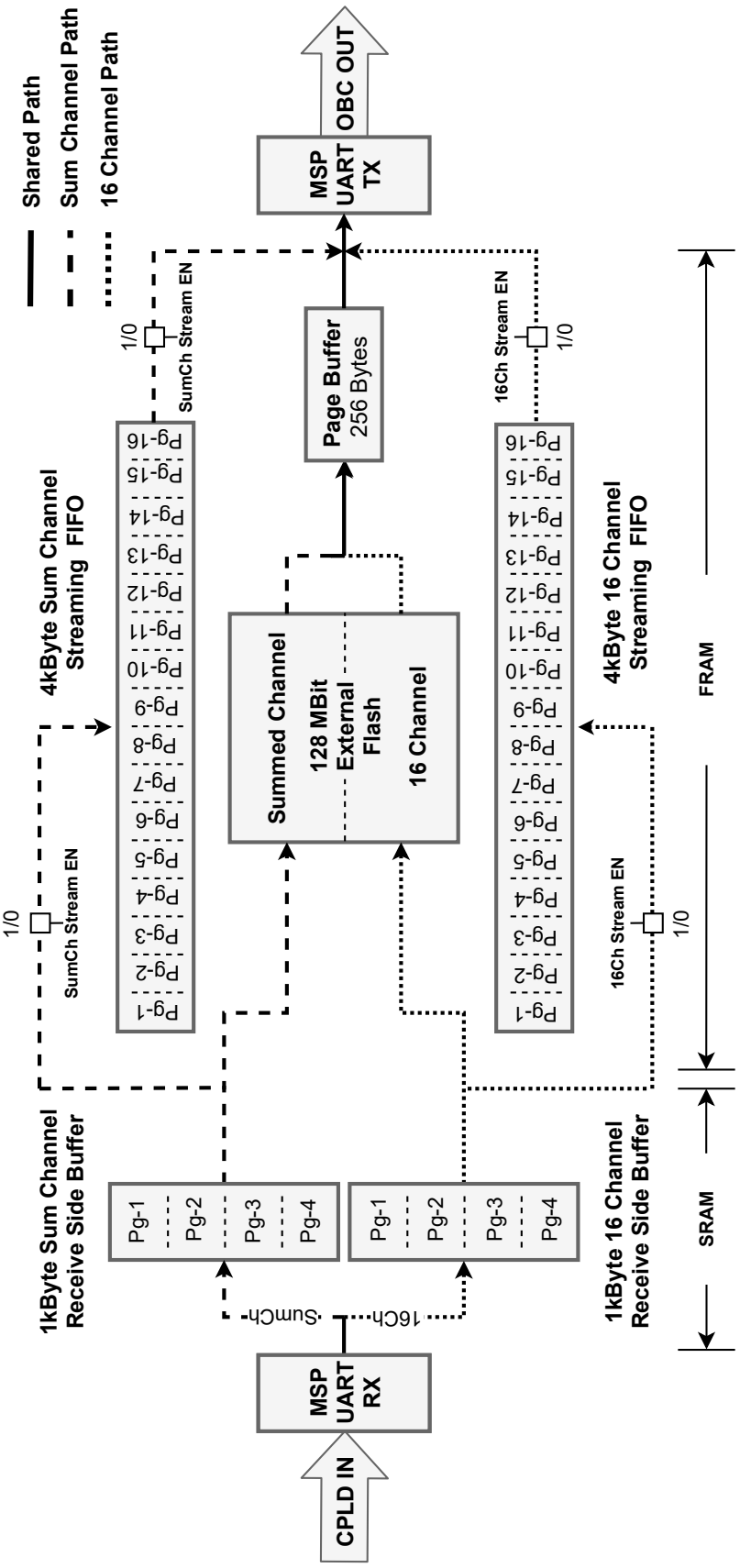

Figure 3.7: The GMOD experiment flow diagram, detailing reception of TTEs from the CPLD, processing and storage and finally service to the EIRSAT-1 on-board computer. TTE packets are received from the CPLD by the MSP430 and placed into the corresponding (summed or 16 channel TTE) receive side buffers. Once a full page of either buffer has been filled, its contents are passed to temporary storage in an external 128-Mbit flash until requested by the on-board computer. If streaming has been enabled, the filled page may also be placed within the corresponding streaming buffer for direct transmission to the on-board computer.

TTE serial bytes are read and stored within a set of "receive-side" circular buffers in MSP430 memory. SRAM memory has been used for the receive-side buffer storage; while FRAM is more abundant on the MSP430FR5994, its read/write cycles are capped at 8 MHz where as SRAM is limited only by the clock source which in the current configuration is set to 16 MHz. The use of SRAM helps to ensure data in the receive-side is transferred to external flash with minimum overhead. The TTEs are temporarily stored here before transmission to flash or before being queued for streaming. There are two of these receive-side buffers on the MSP430, one for summed channel data and one for 16 channel data, both of identical length ($\sim$1 kB). Each circular buffer can contain up to 4 pages (4$\times$256 bytes, where 1 page = 256 bytes) of the given TTE data type. The 16 channel receive-side buffer is $\sim$4 times smaller in terms of the number of TTEs which can be packed within each 256 byte page due to the difference between summed channel and 16 channel data. For this reason, at high data rates, the 16 channel buffers are expected to fill faster than the summed channel buffers. If at any point a receive-side buffers fills completely, TTE data is no longer accepted for the given TTE type, until at least a page worth of the received side buffer has been emptied by transmission to flash storage.

3.2.2. Storage

Once a full page of either TTE type has been received, it may be stored within flash memory. The receive side buffer may continue to be filled during the writing of data to flash. A state within the main loop is entered which primes the page for transmission to flash storage; the flash command and address bytes are prepended to the contiguously arranged TTE page bytes, a 4 byte coarse-timestamp is applied to the page with 1 s time base, and for summed channel a CRC is calculated (as mentioned, this is not done for 16 channel pages). The page is then transmitted to flash over 8 MHz SPI placing each byte from SRAM memory into the SPI module transmit buffer. DMA transfer of data had originally been used extensively in the experiment firmware, in an attempt to optimise the transmission of large amounts of TTE data and to reduce the chance of bottlenecking at high trigger rates. However this was determined to be unreliable and later abandoned. Problems arose with the use of DMA, as block transfers of data (256 bytes in this case) halt the CPU operation. Since reception of TTE ASM bytes is interrupt driven, blocking of the CPU causes the MSP430 to not receive complete TTE ASM and thus drop TTE packets every time a transfer occurs. This would ideally be a viable solution provided that the DMA module on the MSP430 operated in parallel to the CPU. For this reason the transfer of data to and from flash, as well as to and from serial is carried out manually by the firmware.

As with the receive-side buffers on the MSP430, the 128 Mbit flash is partitioned in half, the upper address space being reserved for summed channel data while the lower range being reserved for 16 channel data, as in Figure 3.5. The boundaries between the two TTE data types can be easily identified using a simple bit mask on the most significant bit preventing accidental pointer overflow. Each partition acts independently, similar to the receive-side buffers in the MSP430 SRAM memory, the summed channel partition being a "ring" like buffer and the 16 channel partition like a linear buffer. Once the 16 channel buffer fills in its entirety, no more

data can be added until the complete collection of data is readout, experiment 16 mode is exited automatically by the MSP430 and the complete memory space from lowest to highest address in the range is readout by the OBC.

Once the TTE data has been written to flash and is no longer needed in storage, rewriting to this location requires a pre-erase of the memory location essentially priming it for subsequent write operations. When these erases are staged to occur in the MSP430 firmware, critical read/write operations to/from flash are blocked for this duration. Given these long erase times, it is possible that the receive-side buffers may overflow before the flash is available again for writing. Erases are therefore managed in a dynamic way by suspending flash erase operations to prioritise the writing of new TTE data to flash. Once the write has completed, the erase operation may then be resumed and continued in the background until completion. In the case of GMOD, erase operations are performed on a 32 kB block basis, one block ahead of the "write pointer" location ($\sim$128 ms completion time). Thus the current block will have been cleared previously and be available for writing, while the following block has either been erased or is currently being erased, ensuring that there is always $\geq$32 kB of flash available for writing and only a minimal amount of stored data is erased and recycled for reuse. In this way, the erase of an addressed block of flash memory is triggered by proximity to the current "write pointer" address (i.e. when writing to the start of a 32 kB block boundary, the next block is immediately staged to be cleared by erasing its contents for reuse, as illustrated in Figure 3.5). This strategy strikes a balance between maintaining as much historical TTE data in memory as possible while still ensuring that erases occur in a timely manner to allow new data to be successfully written.

3.2.3. Streaming

When the OBC requests data from a given address it is retrieved from flash in pages and placed within MSP430 FRAM memory. This flash read operation is handled manually to read data from the eUSCI SPI receive buffer and load it into FRAM memory. A frame structure is applied to the page before sending to the OBC, with a header containing a unique 4 byte ASM sequence, identifying the start of the data frame and the flash address bytes from where the page originated (see Section 3.1.8 for more on the packet structure). It is then transmitted to the OBC over 128 kBaud serial. Once the OBC receives the packet and confirms the address bytes are as expected, the next page may then be requested if available.

A 256 byte page buffer (excluding header info bytes) can be used to transfer TTE page data from flash to the OBC, on a page–by–page basis. This is quite slow and requires an I^2C command per page transfer. For a faster throughput of data from GMOD to the OBC, a streaming system has been developed which allows the MSP430 to serve TTE data from internal memory rather than fetching from external flash. It is expected that this will be the primary mode of data transfer from the MSP430 during operation. When the MSP430 transfers the TTE page to flash (and when the streaming mode is enabled), that same page is transferred to a larger $\sim$4 kB circular buffer which can hold 16$\times$ TTE pages. A pair of $\sim$4 kB "streaming" buffers are reserved in FRAM, one for summed channel data and another for 16 channel data. When a page has been

loaded into either streaming buffer, it may be transmitted to the OBC. The OBC may then check the received address bytes in the packet frame to ensure that the correct page was sent by GMOD and that the data has been transmitted in the expected consecutive order according to the incriminating address bytes. If an inconsistency is detected between received TTE pages, the OBC may disable streaming and reenable streaming from the last expected page address in flash. The MSP430 then streams the contents directly from flash up from this address to the current writing pointer and then re-enables the streaming from internal memory at this point, whereupon subsequent pages are transmitted directly from the MSP430 FRAM. If these streaming buffers overflow, the MSP430 can proactively reenable streaming from flash memory to the current writing pointer and then reenable streaming directly from the MSP430 FRAM.

3.3. OBC Operation and GRB Triggering

GRB triggering is performed on the OBC using the data generated by GMOD. This is discussed in detail in (Doyle et al. 2022a) and (Murphy et al. 2022) and is included here to provide context on the instrument operation. Summed channel TTE pages received by the OBC via streaming are parsed into the individual TTEs and associated packet metadata. As described in Section 3.1.3, the OBC controls the reception of TTE data by throttling the rate at which it is transmitted by the MSP430 by use of a configurable timer which toggles an MSP430 internal software flag on the elapse or directly by command over I^2C. This is to minimise bottlenecking and to avoid over flowing the internal buffers on the OBC serial receive ports. The page data is initially checked to ensure its integrity by referring to the flash address in the packet header and ensuring that it corresponds to the correct location (i.e. one page address greater than the page address of the previous data received). A flash device on the OBC is used to store the individual TTE pages onboard for downlink. As with the flash device on the GMOD motherboard, the OBC flash is also arranged into sectors which are composed of 16 pages of 256 bytes each (4 kB per sector). The OBC flash has an allocated capacity of 1.25 GB for GMOD TTE data, amounting to ∼35 – 40 days worth of GMOD data assuming nominal background rates of around 50 Hz.

$$\sigma_{Trigger} = \frac{(N \times \sum Sig.WindowEvents) - \sum Bkgnd.WindowEvents}{\sqrt{(N^2 \times \sum Sig.WindowEvents) + \sum Bkgnd.WindowEvents}} \tag{3.1}$$

The OBC then uses the collected TTE data for the generation of light curves and spectra, for data compression and downlink. These are provided as the spacecraft has a limited ∼30 minute communication window available per day while in orbit and as such it is infeasible to downlink all TTE data given its large quantity, most of which consisting of background. The light curve and spectra are generated by using a pair of buffers which continually accumulates new TTEs and integrates the relevant event data (i.e. the time of arrival and the corresponding ADC quantised energy, for light curves and spectra respectively) into 20 minute records of each. When integration is complete, the filled light curve and spectra buffer contents is framed and stored in flash memory for a compact downlink of the collected data.

A separate triggering light curve buffer accumulates TTE data in parallel to the normal light curve and spectra buffers, as described above. The collected TTE data is used in this case to generate a rolling light curve which is used to detect significance rate changes indicative of a GRB detection, according to the triggering algorithm expression in Equation (3.1). TTE data is stored in a circular buffer which rotates in new TTE data while overwriting old TTE data. The contents of this circular buffer are then used to generate a light curve which is split into three segments: the background, signal and the signal window offset. The background window is the number of counts integrated within the preburst time range, the signal window is the number of counts integrated within the burst time range and the signal window offset is a buffer between both the signal and the background windows. This is added to prevent triggering on preburst fluctuations. The triggering algorithm (Equation (3.1)) then uses the integrated number of counts within the signal and background windows to determine the significance of the detected event; where $\sum Sig.WindowEvents$ is the number of integrated events in the light curve signal window, $\sum Bkgnd.WindowEvents$ is the number of integrated events in the light curve background window and *N* is the ratio between background and signal window integrated counts. Upon triggering, the OBC accumulates a configurable amount of post burst data and transfers the complete TTE collection associated with the trigger event (currently stored in flash) to a secure region in flash dedicated for triggered event TTE data (a capacity of $\sim$40 trigger events) which is protected from overwriting. A basic light curve and spectra are generated with associated metadata (i.e. the peak trigger significance, duration and its location in flash memory), which is logged in flash for initial access and also placed within the spacecraft beacon (transmitted every 1.5 minutes) for rapid alerting of the community and EIRSAT-1 operators.

3.4. Conclusion

A detailed discussion was presented in this chapter on the operation of the GMOD experiment from the perspective of the instrument onboard MSP430 firmware. The processes of instrument readout, storage and streaming of TTE data from the detector were described as well as the overarching firmware structure and design philosophy. To give context to the complete system, the CPLD firmware was discussed in Section 2.2.2, while the use of the generated TTE data by the OBC was highlighted in Section 3.3. This firmware has been extensively tested during system level and subsystem level tests, to be discussed in Chapter 5, Chapter 6 and Chapter 7.

Chapter 4

GMOD Origin, Development and Testing

This chapter will describe the early concept, design and testing of the GMOD hardware up to the final FM iteration. This will begin with the origin of GMOD as the Gamma-Ray Detector (GRD), a prototype detector concept developed to investigate the use of SiPMs and the viability of fast, high-light yield scintillators in calorimeters for combined Compton and pair creation telescopes, such as those proposed for the Gamma-Ray Imaging, Polarimetry and Spectroscopy (GRIPS) (Greiner et al. 2012; Ulyanov 2013) and e–ASTROGAM (De Angelis et al. 2017) missions. The initial design of GMOD, as adapted from the GRD, is then discussed with a focus on the iteration proposed from the EIRSAT-1 CDR. Finally an overview of the initial tests of the prototype detector hardware tested on a high altitude balloon flight from Palestine, Texas (Murphy, Mangan, et al. 2021b) and through a 101.4MeV proton irradiation test of the detector assembly (Ulyanov, Murphy, Mangan, et al. 2020) are presented.

4.1. The GRD: GMOD Origin and Early Concept Development

An initial investigation into the use of SiPMs along with $LaBr_3$:Ce for use as a calorimeter in Compton and pair production telescopes began around the start of the 2010s (Ulyanov 2013) with Geant4 simulations. This study focused the use of these new technologies to produce a calorimeter module which met the minimum design requirements for the GRIPS Gamma-Ray Monitor (GRM) instrument while demonstrating the improved performance provided by these devices with high gain, lower form factor and low mass. These attributes are highly attractive for complex spaceborne instruments like Compton and pair production telescopes, which are made up of multiple detector layers each containing an array of tracker elements and calorimeters. This instrument concept (Figure 4.1) is referred to as the Gamma-Ray Detector (GRD) and is the foundation for the GMOD scientific payload.

This initial study was followed up subsequently by a hardware demonstration of the calorimeter module (Ulyanov et al. 2017a), including the production of a 4×4 tiled array of 16 MicroFB-60035-SMT SiPMs coupled to a $LaBr_3$:Ce scintillator and a custom frontend readout, as shown in Figure 4.1A. A basic design for the light-tight detector assembly housing was also produced which was improved upon and reused during later testing, such as the high altitude balloon flight and the proton irradiation testing. This study demonstrated a simple SiPM non-linearity correction technique (to be later adapted for the balloon flight analysis), SiPM temperature dependence, gain variation as a function of applied overvoltage and the instruments capability for position sensitive localisation of incident gamma-ray photons (specifically relevant to the original instrument design as a calorimeter). A later study published not long after using much of the same hardware (Ulyanov et al. 2017b) compared the position measurement resolution

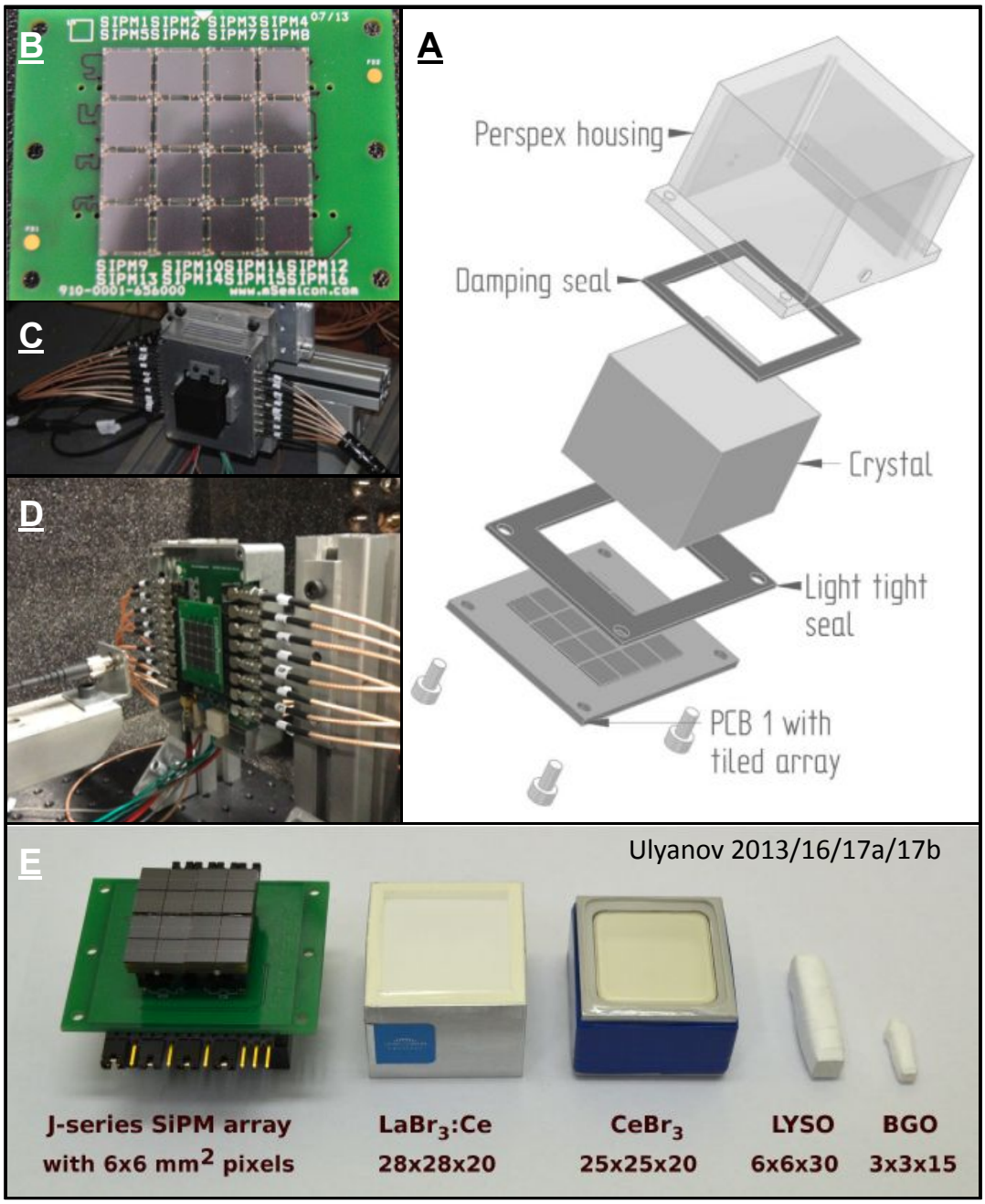

Figure 4.1: A panel of the individual components of the GRD instrument. A) The fully assembled GRD detector showing the SiPM and scintillator enclosed within a custom housing (Ulyanov et al. 2016). The array was assembled with a neoprene light-tight seal between the SiPM PCB and the assembly housing. A damping seal was placed between the housing and the crystal when assembled to ensure a tight coupling but to avoid over compression of the SiPM array surfaces. B) The 4×4 tiled array of 16 MicroFB-60035-SMT SiPMs on a custom array PCB (Ulyanov et al. 2017b). C) The GRD detector mounted on a linear stage within a ^{133}Ba beamline and prepared for XY scanning (Ulyanov et al. 2016). D) The detector assembly disassembled to expose the GRD SiPM array while within the darkbox (EIRSAT-1 2017). E) The GRD detector assembly components, including the solder-less assembly board with an array of J-Series SiPMs, and $LaBr_3$:Ce, $CeBr_3$, lutetium yttrium oxyorthosilicate (LYSO) and BGO scintillators of various sizes (Ulyanov et al. 2017a).

of a number of scintillators which included $CeBr_3$, a scintillator which is favourable due to its relatively low internal radiation emission and its comparative lower expense to $LaBr_3$:Ce (see Section 1.2.3 and Section 2.1.1 for further context).

A compact, low power and radiation tolerant SiPM frontend readout was required for pulse height measurement of the numerous SiPM channel signals, especially if the GRD calorimeter module was to be used as the basis for a larger array in a combined Compton pair production telescope, such as on GRIPS. The SIPHRA (Meier et al. 2016) ASIC frontend IC was developed based on the requirements of instruments like GRIPS, e–ASTROGAM and others, which are capable of polarimetry, spectrocopy and gamma-ray imaging. SIPHRA is specifically designed to operate at low power, in high radiation environments, can accommodate multichannel and summing readout and can be configured for a variety of SiPM/PMT coupling and scintillator shaping characteristics. A study to investigate the performance of SIPHRA was conducted (Ulyanov et al. 2017a) with a selection of scintillators (Figure 4.1E) and similar hardware as before, along with the SIPHRA ASIC test board and Galao (IDEAS 2022) ROIC evaluation kit for readout and configuration. SIPHRA is discussed in further detail in Section 2.1.3.

For this purpose a custom SiPM array was formed using a PCB with sockets for solder-less assembly of arrays of SiPM evaluation boards. In this case the 2×2 ArrayJ-60035-4P-EVB evaluation boards were used, each carrying a tiled array of 4 MicroFJ-60035-SMT SiPMs, in total an array of 16 SiPMs as with other iterations of the same form. This particular configuration was adapted for the detector used during the July 2018 balloon flight campaign (Section 4.3) and the 101.4 MeV proton irradiation testing of the J-Series SiPMs (Section 4.4). The results from this test confirmed that the SIPHRA could be used in a number of SiPM channel coupling configurations, with various scintillator types and with individual or summed channel readout while matching the resolution performance of a generic bench waveform digitiser.

4.2. GMOD Proposal and CDR

In 2017, a proposal to the ESA FYS programme was submitted (EIRSAT-1 2017) detailing EIRSAT-1 and its main scientific payload, GMOD. The initial design of the GMOD detector was based on the GRD concept, featuring a similar form and use of modern detector technology for an in-orbit demonstration of the heritage developed at UCD. The proposed concept has for the most part remained the same, however some technical details have varied over the program lifecycle. The initial proposal featured a Saint Gobain 28mm×28mm×40mm BrilLanCe 380 $LaBr_3$:Ce scintillator (Gobain 2021), coupled to a 4×4 SensL (now On Semiconductor) $36mm^2$ SiPM array, similar to the GRD design outlined in (Ulyanov et al. 2016). This proposed design used SIPHRA as a compact frontend SiPM readout solution. In this iteration, both SIPHRA and the SiPM array are mounted external to the aluminium housing interior. This housing contains the scintillator in a light-tight enclosure while providing a purchase for secure mounting of the detector electronics and for good optical coupling. The detector readout, support and configuration, previously provided by the Galao evaluation kit during bench testing, is handled by a custom GMOD motherboard (Section 2.2), which is also used as a mounting point for the

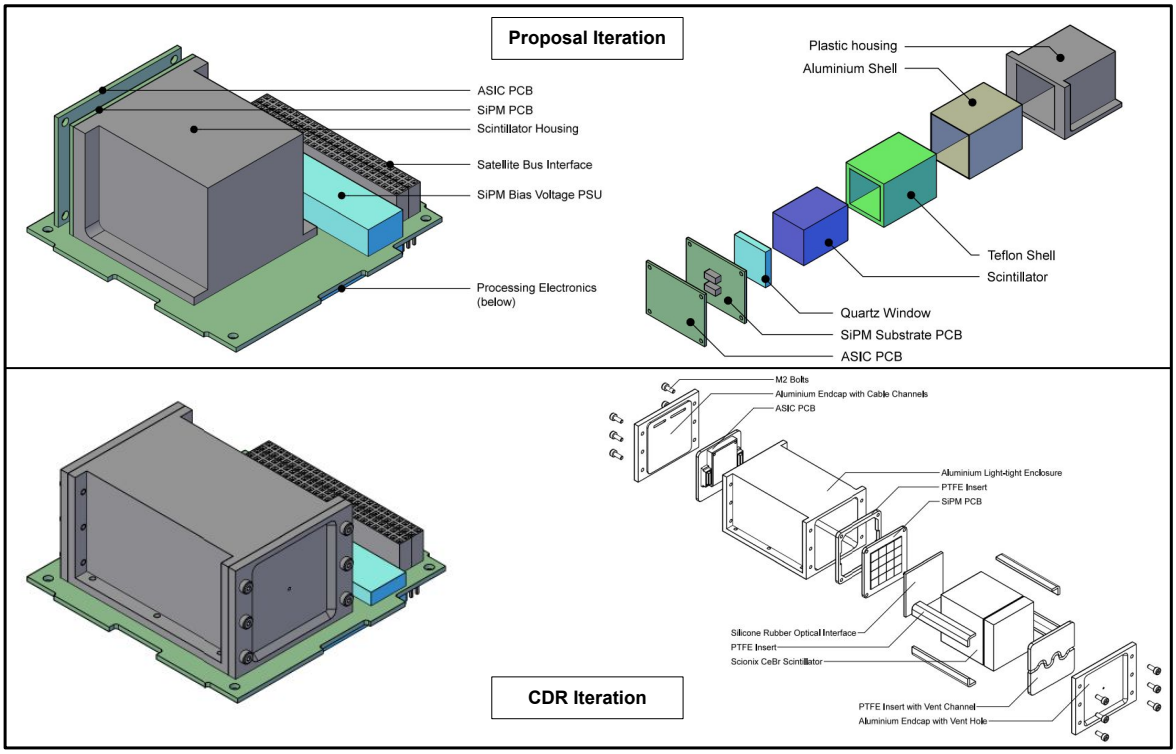

Figure 4.2: CAD figures describing the initial proposed design (Wall et al. 2017) of GMOD and the eventual CDR design (Erkal et al. 2017) of GMOD.

detector assembly. This initial design is rendered in Figure 4.2 as the *proposed iteration*.

Towards the programme CDR, the technical design choices were refined further into the design submitted during the CDR phase of the project lifecycle. For instance, the scintillator type was changed from $LaBr_3$:Ce to a 25mm$\times$25mm$\times$40mm Scionix $CeBr_3$ scintillator as $CeBr_3$ offers similar resolution, timing characteristics and light yield but low intrinsic radioactivity and at the time was more affordable. A tiled array of 16 J-Series MicroFJ-60035 SiPMs were also chosen over the B-Series equivalent as at the time the J-Series was relatively new and allowed improved fill factor and PDE, while also facilitating coordination with the Irish space and photonics industry. For SiPM readout, SIPHRA was to be mounted within the detector assembly with the silicon die wire bonded onto a custom PCB connecting directly to the SiPM array, all housed within an aluminium detector mounted to the GMOD motherboard. This choice of encasing the entire detector electronics within the same housing was made to prevent light ingress within and to avoid light passing through the PCB layers and contributing to photocurrent noise in the SiPMs. It also mitigated mechanical strain on the detector electronics as expected during the intense forces experienced during launch. This iteration of the instrument design is shown in Figure 4.2 as the *CDR iteration*. A GMOD motherboard was also designed for the readout and control of the instrument with a number of DM iterations produced over the lifecycle of the project.

4.3. GMoDem and the Balloon Flight Demonstration

The Gamma-Ray Module Demonstration (GMoDem) (Figure 4.3) was developed to demonstrate the GRD and GMOD detector design from a high altitude balloon flight from the NASA Columbia Scientific Balloon Facility (CSBF) on the 5th July, 2018 (Murphy, Mangan, et al. 2021b). The GMoDem instrument featured the main electronic components of the GMOD detector in a configuration similar to the GRD instrument (as shown in Figure 4.4) and progressed the instrument heritage while informing the design of future gamma-ray detectors built for space based observation of transient GRB events. My contribution to this balloon flight campaign was as a participate in the investigation, initial analysis of the data and draft publication, with contributions in particular to the instrument calibration and linearisation (Murphy, Mangan, et al. 2021b).

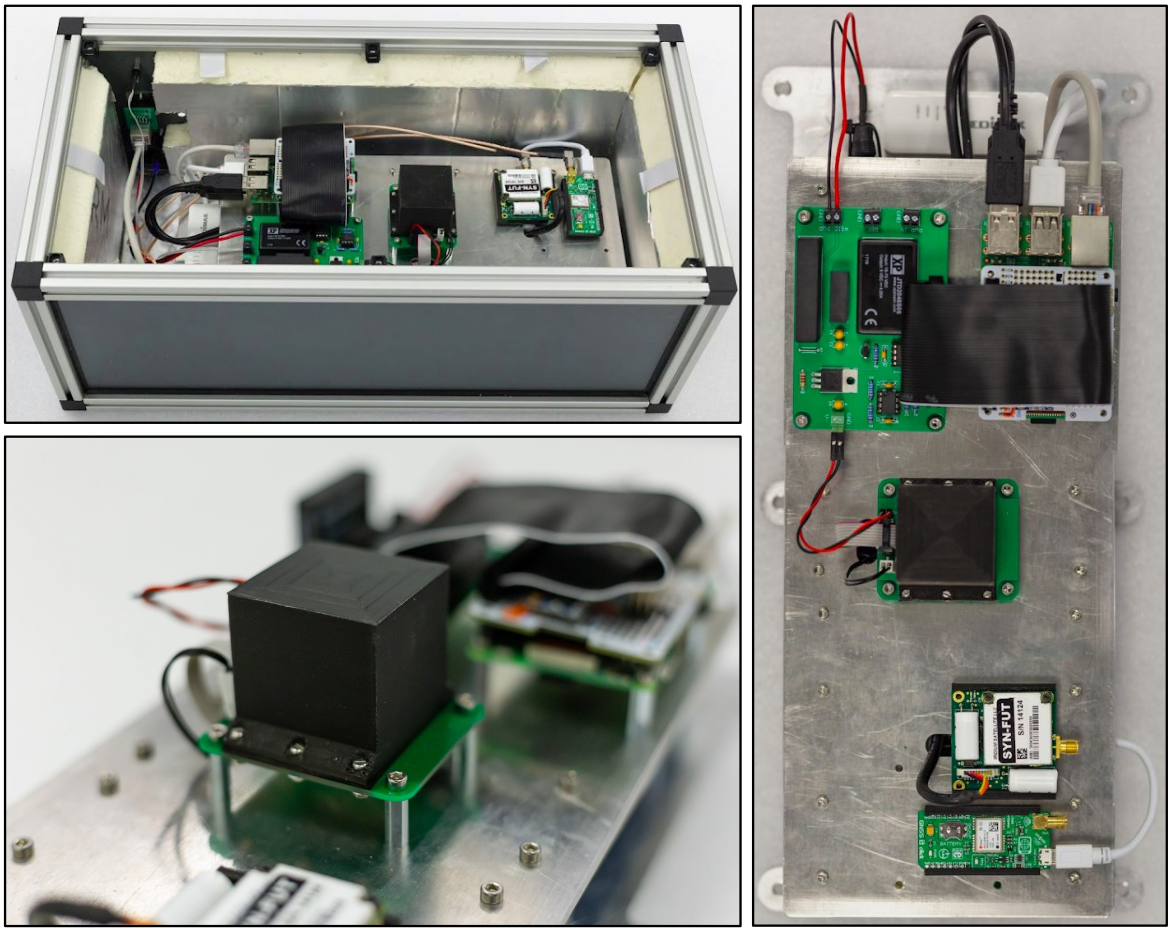

Figure 4.3: The GMoDem detector payload internals.

4.3.1. The GMoDem Detector and Instrument Payload

GMoDem consisted of a Scionix 25mm×25mm×20mm $CeBr_3$ scintillator coupled to a tiled array of 2×2 ArrayJ-60035-4P-EVB SiPMs, readout using the SIPHRA/Galao evaluation board and a custom balloon flight support platform. As is common for hygroscopic scintillators, the $CeBr_3$ crystal was housed in a hermetically sealed aluminium container by the manufacture, with a quartz window aligned with the crystal face to allow the transmission of light. Optical

gel was placed between the crystal window and the SiPM array surface to help couple the crystal to the SiPM array and to aid the transmission of light. The SiPM array featured an array of 16 OnSemiconductor (formally SensL) J-Series MicroFJ-60035 SiPM pre-mounted on the 4 ArrayJ-60035-4P-PCBs. Four of these evaluation boards were mounted on a solder-less carry board PCB via an 8 pin dual in-line (DIL) socket allowing easy mounting and interchange. This was also advantageous as the development of a dedicated SiPM array for the balloon flight would be impractical due to the short development time available before the launch date.

Each of the 2×2 ArrayJ devices (each containing 4 J-series SiPMs) are produced with common cathode configured and with individual anodes for each of the SiPM pixels (individually accessible on the 8-pin DIL header). As the SIPHRA CMIS input requires a negative charge input (and therefore SiPM readout on the cathode), this constrained the SiPM readout to quad channel, one channel per ArrayJ device. As such, readout of the SiPMs was performed on the common cathode of the individual 2×2 ArrayJ devices, providing 4 channels which could be processed by the SIPHRA readout. The anodes of each 2×2 set were commonly connected to a bias voltage supply through a set of RC filters attenuating noise and stabilising the onboard bias supply from the PSU. A PT100 sensor was also installed beneath the SiPM carrier board PCB and was sampled by SIPHRA to determine the bias adjustment required for SiPM temperature compensation.

The SiPM array was operated at a fixed overvoltage above breakdown (∼-24.5 V for J-Series MicroFJ-60035 SiPMs) which itself varies as a function of temperature. As such, variations in temperature can vary the SiPM gain and other operating parameters associated with the device. This temperature dependence was compensated by maintaining a constant overvoltage above breakdown using the onboard PSU, essentially by adjusting the bias in response to temperature measurements. The RaspberryPi OBC received temperature data from a surface mounted PT100 RTD located beneath the SiPM array PCB. This data was then used to determine the appropriate bias voltage to place across the SiPM array according to the measured temperature vs breakdown-voltage relationship.

As seen in Figure 4.4, the crystal/SiPM assembly is enclosed within a black, light-tight housing blocking external light sources. This housing was designed based on previous iterations used with the GRD, 3D printed from black PLA filament and bolted directly to the PCB which holds the SiPM array. A neoprene light-tight seal was trimmed to match the flange face of the housing and was placed between the face and the SiPM PCB, further reducing light ingress. Light which is transmitted beneath the array PCB may also reach the SiPMs causing an increase in photocurrent noise due to the external ambient light. For this reason, an attempt was made to make the internal space of the payload structure as light-tight as possible.

As opposed to developing a dedicated ASIC carrier and readout solution, SiPM readout was handled by the SIPHRA/Galao evaluation boards, which produced single photon energy measurements with timestamp information for each event. The SIPHRA evaluation board was provided by IDEAS and is essentially a SIPHRA breakout PCB with accessible test points for all

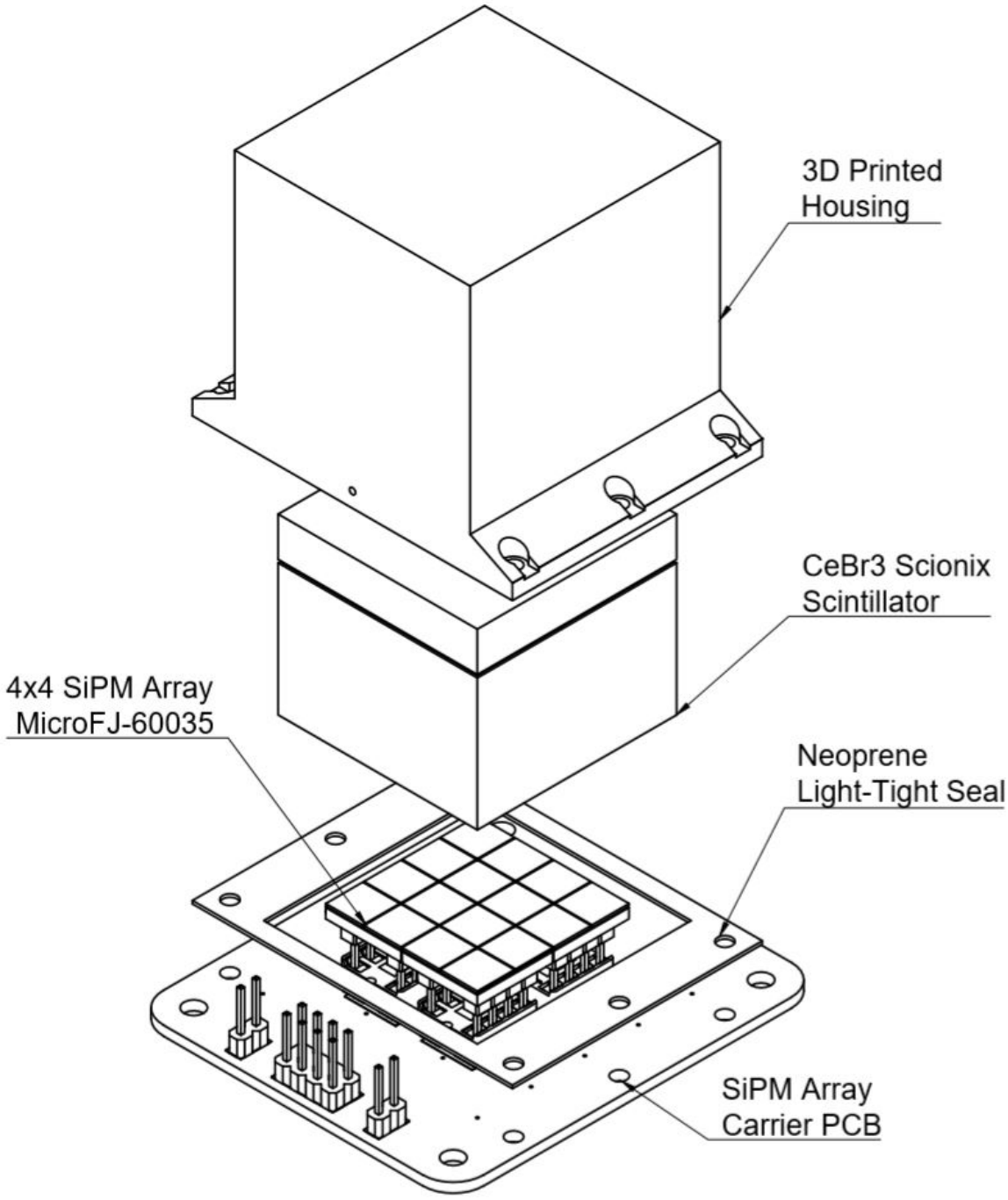

Figure 4.4: The GMoDem detector rendered in CAD. The instrument uses a Scionix 25mm×25mm×20mm $CeBr_3$ scintillator coupled to a tiled array of 2×2 ArrayJ-60035-4P-EVB SiPMs each mounted on a solder-less carry board. While the array is made up of 16 J-Series MicroFJ-60035 SiPMs in total, each of the four ArrayJ modules are readout as a single channel, resulting in quad channel and summed channel readout by SIPHRA (not shown). A similar housing to the one built for the GRD was 3D printed from black polylactic acid (PLA) filament and bolted directly to the PCB which holds the SiPM array. As with the GRD a light-tight seal was placed between the PCB and the housing to prevent light ingress.

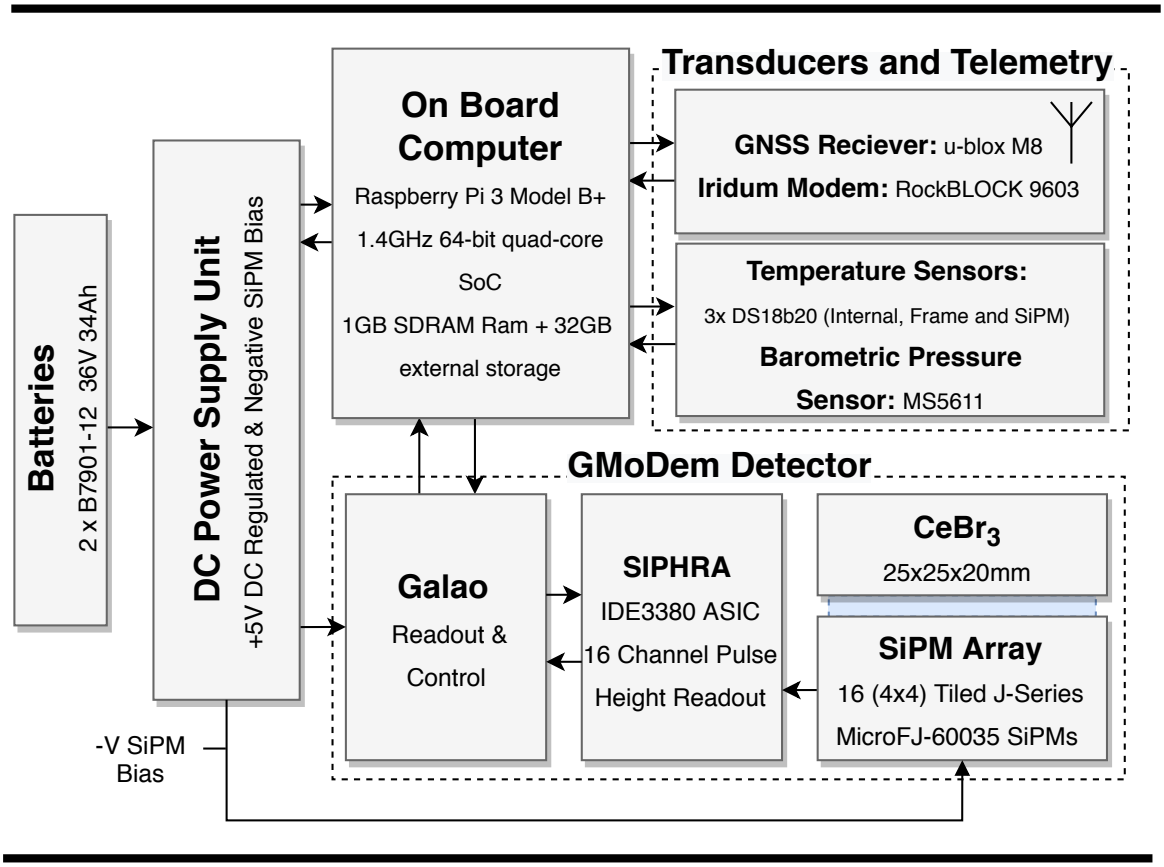

Figure 4.5: The GMoDem functional block diagram, showing the SBC OBC, transducers and telemetry block, PSU and finally the detector payload. The corresponding hardware is shown in Figure 4.3.

the ASIC signals and voltage/current supplies. Both the SIPHRA and Galao ROIC PCB can be interfaced together via a male/female pair of TE 1-1734037-2 board-to-board connectors. Only four of the sixteen available SIPHRA SiPM channels were directly coupled to the SIPHRA inputs due to the SiPM array configuration. Upon gamma-ray triggering, the digitised pulse height measurement signals were clocked out on the serial output of SIPHRA (this included the 4 digitised SiPM channels and the PT100 input channel) to be read by the Galao interface, which supplied the required voltages, constant current, configuration and mediation of communications between the RaspberryPi SBC and the SIPHRA ASIC via Ethernet. The Galao ROIC prepends the number of elapsed clock cycles from SIPHRA from the supplied 2.5 MHz oscillator (a 0.4 μs timebase). Immediately upon receiving every tenth gamma-ray event, the RaspberryPi OBC logs the Coordinated Universal Time (UTC) timestamp along with the TTE data, such that the absolute timestamp (in UTC) can be restabilised for all collected events.

The payload support system is described in a functional block diagram shown in Figure 4.5. A RaspberryPi 3 Model B+ V2 was used for the OBC. A 32GB SD card was loaded with the Linux operating system including the flight software scripts, which were set to run upon boot once the payload was activated by the removal of a remove before flight (RBF) pin. For data

logging, a 62GB Universal Serial Bus (USB) flash drive was selected based on its extreme durability, resistance to water, and impact forces as well as its ability to operate in a wide range of temperatures. This was mounted within the payload enclosure in such a way which made it easily accessible upon recovery. The OBC was used to provide configuration of the experiment payload (via Galao), SiPM bias temperature compensation, telemetry (Global Positioning System (GPS), altitude, temperature and pressure), in-flight communications, and logging of the detector readout.

Communication and telemetry between the balloon payload and the ground segment was handled by technicians at NASAs CSBF, however real-time telemetry from GMoDem was not transmitted. This is because GMoDem was in fact flown as a piggy-back on the flight of the University of New Hampshire, Durham, USA (UNH) Advanced Scintillator Compton Telescope (ASCOT) experiment (Bloser et al. 2016). Instead, a RockBLOCK 9603 Iridium modem was used by the OBC to transmit limited telemetry information, including packets consisting of temperature, pressure, GPS, altitude and the number of counts detected by the GMoDem instrument per packet transmission (a period of $\sim$ 5 minutes).

Pressure and temperature information was recorded using a MS5611-01BA03 barometric pressure sensor. This features an inbuilt temperature sensor which was used to record the internal temperature of the GMoDem payload. External temperature information was recorded using a DS18B20 1-wire temperature sensor. To measure the external temperature the sensor was connected inside of the structure to the aluminium frame as this ensured a good thermal conduction and that no part of the payload was exposed outside the enclosure during the flight. As mentioned an additional PT100 temperature sensor was also mounted beneath the SiPM array board and used to calculate bias voltage temperature compensation. Finally, a u-blox M8 Global Navigation Satellite System (GNSS) receiver, configured in 'airborne' mode, was used to record the positional data during flight. The housekeeping data was recorded every 10 seconds and logged on to the external USB flash drive.

The power for the GMoDem payload was supplied by two parallel B7901-12 battery packs provided by the CSBF. Each B7901-12 pack contains 12 G62 lithium sulfur dioxide ($LiSO_2$) cells in series which supplies an unloaded voltage of 36 V and 34 Ah of capacity. The custom built GMoDem PSU then regulates this voltage powering the onboard computer, telemetry and experiment payload. Mounted to the exterior of the payload structure is a twist lock connector. This connected directly to the B7901-12 battery packs and was internally wired in reverse polarity to the PSU (where the positive terminal was used as the ground reference, such that a negative biasing supply could be easily generated). The twist lock connector was configured in such a way to allow CSBF technicians to safely power down GMoDem by simply plugging the battery supply out once recovered. The payload is activated by a RBF enable/disable pin. The socket for the pin is located on the exterior above the twist lock connector socket. Again, this allows technicians to easily prepare the payload for in flight operation by simply removing the RBF pin.

Once the RBF pin was removed, a switched mode 20W DC/DC converter inverts and drops the voltage from the battery pack (the battery is connected in reversed polarity) outputting 5V to power the onboard computer and the PSU board. The RaspberryPi controls the power delivered to the ASIC via an optically isolated solid state relay. The relay is closed by setting a GPIO pin on the RaspberryPi high, thus supplying the ASIC with 5 volts allowing it to boot (or be rebooted) and begin signal processing. GPS telemetry and other sensors are powered directly from the onboard computer.

The negative bias supply for the SiPM array is generated directly from the battery (the battery is connected in reverse polarity with negative voltage supplied to the PSU). A pair of high voltage op-amps are used to generate a variable bias voltage which can be controlled by the OBC through a DAC over SPI. The first stage is an inverting op-amp with a gain of -6. A 2.5 volt reference voltage is placed on the inverting input (with the non-inverting input connected to ground) generating -15 volts. This is then passed through the second op-amp stage, a non inverting op-amp with a gain of 2, doubling the -15 volts to -30 volts. The ground reference on the inverting input was provided by the DAC which could be varied to lift the reference voltage so that the output could be adjusted between $\sim$-25 V – -30 V.

The breakdown voltage (and gain) of the SiPM array is a function of temperature, therefore variations in the breakdown voltage must be compensated. By maintaining the applied over-voltage (the excess voltage applied to the SiPM array above the variable breakdown) the SiPM gain can be maintained in response to temperature variation. A PT100 located beneath the SiPM array was used to determine the temperature of the array, while the bias voltage to be applied was calculated using a predefined scale based on the known relationship between breakdown voltage and temperature of 21.5 mV/°C. As the temperature varied within GMoDem during the flight, the onboard computer would attempt to compensate the change in breakdown voltage by changing the applied bias and maintaining the SiPM overvoltage.

The GMoDem payload structure was made from 20 mm aluminium T-Slot extrusion and polyvinyl chloride (PVC) plastic panelling. The interior of the structure was made light-tight by sealing the 6 mm thick PVC sheet walls and the aluminium extrusion frame with rubber profile sealing wedged between the interfacing grooves. Each of the walls were then thermally insulated using 1 inch thick polystyrene insulating foam boards, each cut to be flush to the adjacent board edge.

The instrument and payload electronics structure consisted of a pair of aluminium plates. The SIPHRA evaluation board and the Galao ROIC were sandwitched between these plates using M3 stand-offs to fix the boards and plates together rigidly. This ensured that the board to board connection mating SIPHRA and Galao would not be damaged by experiencing any mechanical stressing during flight or landing. The GMoDem instrument and remaining electronics was mounted to the top of the aluminium plate for easy accessibility.

Figure 4.6: The balloon flight payload and gondola, from launch, ascent to landing. *Left*) GMoDem secured to the gondola structure and highlighted for clarity. *Center*) The balloon flight launch showing the zero pressure balloon, flight train and the payload. *Right*) The gondola after landing.

4.3.2. Campaign, Prelaunch Calibration and Flight Characteristics

Once at the CSBF, complete verification of the GMoDem subsystems, onboard Iridium satellite communications system, GPS, PSU and experiment payload was carried out. An on-site calibration of the GMoDem instrument was conducted on the 3rd June, 2018 and the 4th June, 2018 using ^{137}Cs and ^{22}Na calibration sources at the facility. Once assembly and testing of the ASCOT experiment had been complete and both it and GMoDem were securely mounted and restrained to the gondola, the initial schedule for launch indicated a possible launch window for the weekend of the 15th June, 2018 and the 16th June, 2018. It was critical to achieve launch before these dates as CSBF weather briefings indicated that a category 3 hurricane and a disturbance forming in the Gulf of Mexico could produce strong ground winds and some precipitation making launch impossible. Unfortunately all chances of launch were scrubbed due to unfavourable weather conditions. During this time the gondola was both hang tested and flight readiness tested, after which it was given the clear to launch. However, weather problems persisted up to and beyond the end of June. Throughout the first week of July a number of roll-outs of the payload were conducted. This involved the payload transporter "BigBill" (a specialised crane used to hoist and manoeuvre the gondala during launch) carrying the gondola to the CSBF launch pad. Once there, CSBF technicians and any essential personal would lay out the balloon and parachute and perform final preparations before launch. Ultimately, these roll-outs were all cancelled, again due to weather.

Finally, on the 5th July, 2018 ASCOT and GMoDem were given the green light for launch. As before, the gondola was transported to the launch pad and final preparations, including the activation of GMoDem by removal of the RBF pin were complete. At 12:13:09 UTC GMoDem was launched from Palestine Texas into the near space environment.

The entire flight train included a balloon, a parachute and the gondola. This is staged with

an explosive squib between the balloon and the parachute which separates the balloon upon instruction from airborne or ground crews. The balloon flight consists of five stages: launch, ascent, float, descendent and landing (this can be seen in panel 2 of Figure 4.7, where each stage is colour coded). After the balloon is launched it rapidly ascends in altitude for about an hour, after which time it reaches its float altitude. It is at this altitude that the payload has reached the near-space environment and the experiment can be conducted. This is the most lengthy of all the stages. Once ground crew have determined that the experiment has concluded, the balloon is separated from the parachute and payload by the explosive squib. The payload drops, deploying the parachute and allowing a gentle but rapid descent. This is much quicker than the ascent stage. Typically the payload will be travelling at such a high velocity that when it decelerates upon impact it may experience destructive forces or simply topple onto one side. The gondola built by UNH was specially built to accommodate these forces without the frame slipping or warping upon impact.

Table 4.1: Official balloon flight summary (source: Hugo Franco, CSBF Campaign Manager).

Balloon Launch Statistics	
Parameter	**Value**
Flight Number	1600 P
Date/Time Launched	5 July, 2018 12:13:09 UTC
Launch Site	Palestine, TX
Balloon Weight	761 kg
Experiment Weight	585 kg
Float Altitude	37.4 km
Time Reached Float	14:24:28 UTC
Total Float Time	05:08:26 hours
Total Flight Time	08:00:02 hours
Termination Time:	19:32:54 UTC
Impact Time	20:13:11 UTC
Landing coordinates	31°41.45' N, 103°29.76' W
Distance:	735 km

About an hour into the balloon flight, GMoDem reached its float altitude. For the entirety of the flight, all systems were recording telemetry and data including the gamma-ray detector payload. The float period lasted just over 5 hours, after which time ground crews sent the command to separate the balloon and the parachute. GMoDem and ASCOT landed at 19:32:54 UTC, just over 8 hours after launch near the New Mexico Border, close to the town of Pecos (31.41.45N 103.29.76W). Upon recovery by J.Legere of the UNH, the battery was disconnected using the twist lock connector located on the exterior of GMoDem, thus concluding the high altitude experiment.

4.3.3. Flight Analysis

During the flight GMoDem was actively recording events integrating over the duration (see Figure 4.7). The features of the light curve generated during the different stages of the flight are indicative of the high-energy environment at that altitude. It can be seen that just before the flight, a cumulative background was detected at the CSBF, most likely due to the decay of naturally occurring terrestrial radionuclides. This reaches around 600 counts/min (time: 0 seconds to 2.5 k seconds). A similar phenomenon is also observed after landing (time: 31.5 k seconds to 35.9 k seconds) near the New Mexico state border (31°41.45' N, 103°29.76' W) with a higher count rate of around 730 counts/min.

Once launched there is a drastic drop in background exposure. This is expected as the terrestrial background radiation cannot penetrate the higher altitudes, reaching as low as 120 counts/min (time: 2.8 k seconds). From there the count rate increases to around 6790 counts/min, the maximum recorded during the flight which corresponds to an altitude of around 18 km (time: 2.5 k seconds to 5.9 k seconds). This increase in counts occurs because of the interaction of the high-energy cosmic ray particles with the upper atmosphere which produce a cascade of particle showers creating a variety of elementary particles which can go on to produce 511 keV annihilation photons and a spectral continuum via Bremsstrahlung and synchrotron processes. The feature produced is called the Pfotzer maximum, the point of maximum radiation intensity in the atmosphere as a function of altitude . The majority of ionising particles created through these showers (including 511 keV annihilation photons) will be directed towards the Earth, thus the intensity of radiation will vary with altitude depending on the altitude of the site of cosmic ray interaction. Beyond this point, fewer cosmic ray interactions occur and so the intensity of radiation drops. This results in a drop in exposure beyond the altitude corresponding to the Pfotzer Maximum and indeed the float altitude at around 37 km where the count rate is seen to drop to 2317 counts/min. This comprises the ascent stage.

Once at float, a near constant count rate is observed at 2317 counts/min (time: 10.5 k seconds to 28.9 k seconds). This comprises the float stage of the flight. Once descent has began (time: 28.9 k seconds to 35,9 k seconds), the count rate again increases towards the Pfotzer Maximum altitude peaking at around 6190 counts/min with a sharp decline in counts towards terrestrial background at the landing site. Due to the high velocity on descent, not much can be gathered from this phase of the flight as the integration time is not satisfactory to form any real commentary. This comprises the descent stage of the flight.

The internal temperature profile of GMoDem is shown in figure 4.7. This shows the SiPM temperature (recorded with the PT100 located beneath the SiPM array), the internal temperature (recorded with the MS5611-01BA03 barometric temperature sensor) and the external temperature (recorded using a DS18B20 digital thermometer). The maximum internal temperature recorded during the flight was around 49°C with a low of 35°C. As preparations for the balloon launch were taking place the payload was parked on the launch pad for a number of hours. Because of this the payload remained sitting in the sun as the internal temperature rose higher and

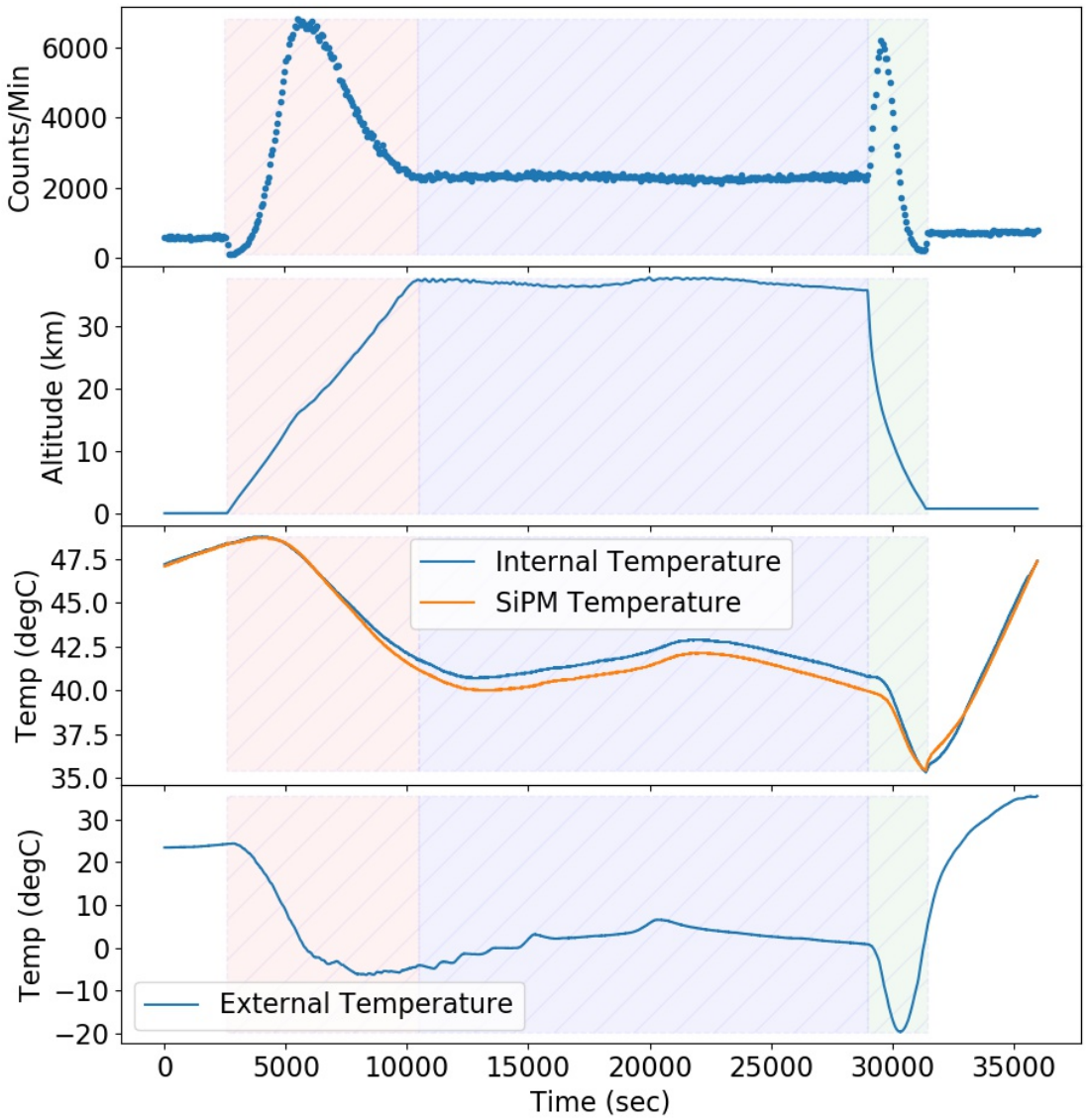

Figure 4.7: Balloon flight telemetry recorded throughout the flight. The different stages of the flight are highlighted as ascent (red), float period (blue) and descent (green). This shows the counts/min (panel 1), the altitude (panel 2), internal/SiPM temperature (panel 3) and external temperature (panel 4).

higher. Further compounding the problem was the foam insulation padding the payload walls intended to maintain the internal temperature of the experiment during the flight. It was later found during disassembly of the detector after flight that the 3D printed housing had warped trapping the crystal within. This is likely due to the high temperatures melting and setting the PLA during the many roll-outs and the balloon flight itself.

As expected, the internal temperature begins to drop during the ascent reaching a sort of steady state at 40°C to 43°C during the 5 hour float period. Interestingly, it can be seen that the internal temperature begins to slowly increase during the first half of the float period. If this increase in internal temperature is reflective of the temperature of the helium within the balloon, it could have resulted in the expansion of the helium gas, increasing the balloon volume and displacing more atmosphere thus increasing the crafts buoyancy. The increase in buoyancy leads to a (relatively) slight increase in altitude which can be seen in Figure 4.7. The cooler air then causes the helium temperature to drop, reducing the volume causing the balloon to become slightly less buoyant and dropping the altitude slightly again. This increase and decrease in altitude is also seen in the altitude plot of Figure 4.7. Finally once descent begins, the internal temperature drops further to 35°C until the payload lands. This drop in temperature is of course due to the high volume of flowing air cooling down the payload.

The external temperature sensor was physically bonded to the aluminium payload structure as it was impossible to fit the device on the exterior. Thermal equilibrium between the ambient atmospheric temperature and the payload structure should then be achieved relatively quickly given the thermal conductivity of aluminium, thus the temperature of the structure should be a near accurate reflection of the actual external temperature. A similar in flight temperature change is seen on the external temperature sensor measurements, however given that the exterior was not insulated, a lower temperature profile with significantly lower temperature drops was experienced. During float, the highest external temperature was 6°C with a low of -4°C (the external temperature dropped as low as -20°C on the decent stage). This is shown in the lower panel of Figure 4.7.

4.3.3.1. SiPM Linearisation

The SIPHRA ASIC used for the detector front-end is known to become heavily saturated for larger signals (Meier et al. 2016), in the case of GMoDem beyond approximately 3800 – 3900 ADC channels (the higher extent of the SIPHRA 12 bit ADC). This saturation leads to a non-linearity in the detector which is caused predominantly by SIPHRA and to a lesser extent by SiPM non-linearity ((Ulyanov et al. 2016), (Ulyanov et al. 2017b)). To account for this non-linearity, a set of measurements were made on the 30th October, 2018 to develop a linearisation correction. This correction compares the response of the GMoDem detector to a PMT whose response is linear within the required range.

Given that the ArrayJ devices were flown in a four quadrant summed configuration, a correction for each quadrant was developed. The SiPM array flown on the GMoDem balloon flight (four ArrayJ-60035-4P-BGA SiPM devices) were placed within a light-tight dark box with a Hama-

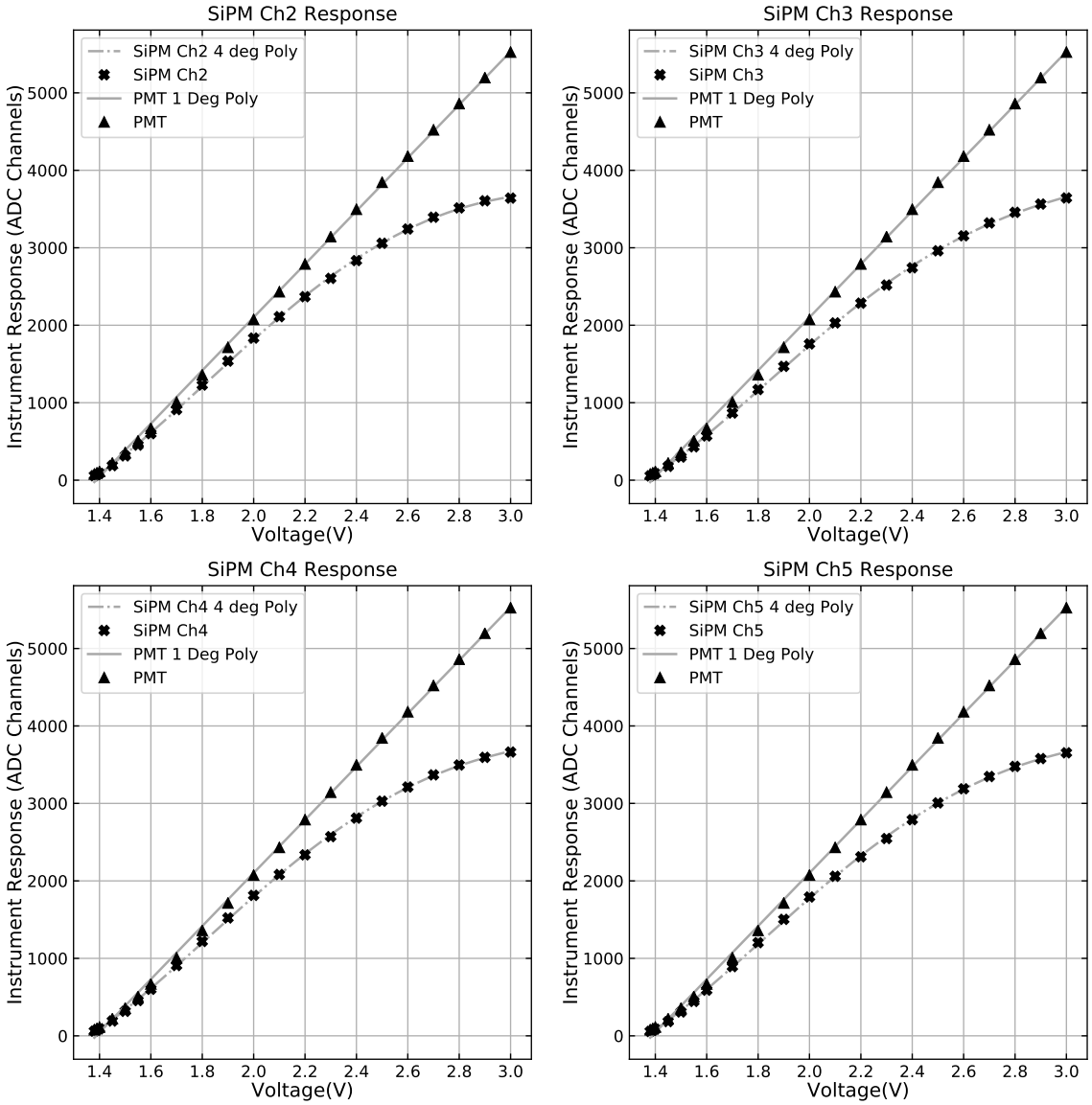

Figure 4.8: Plots of digitised ADC channel response as a function of voltage for both the GMoDem detector (Ch2 – Ch5) and PMT. The saturation of each individual channel is clearly shown against the linear response (within the given range) of the PMT.

matsu R6233-100 (3-inch, 8-stage) PMT, while cables for biasing and readout were accessed via a side feed-through panel. The SiPM array was placed at a distance of 40 cm opposite a 430 nm blue light emitting diode (LED) which was equipped with a light diffuser to provide uniform illumination on the SiPM array surface. The SiPM array was biased and the LED was pulsed with 40 ns square pulses generated by a Aim-TTi TG5011 function generator with 2 kHz frequency. The PMT was biased to 1000 V and positioned such that the reflected light from the SiPM array could be directed towards the PMT, thereby reducing the amount of light detected and preventing PMT response non-linearity.

By varying the LED pulsed amplitude between 1.38 V – 3.00 V, the light intensity would increase and the GMoDem detector and PMT responses could be measured. The SIPHRA ASIC

and SiPM biasing was configured as during the balloon flight. The PMT was equipped with a tapered voltage divider to improve pulse linearity while being sampled and digitally integrated using a CAEN V1720 waveform digitiser (12 bit, 250 MS/s). The SiPM and PMT responses were recorded in terms of pulse-height digitised ADC channels as shown in Figure 4.8.

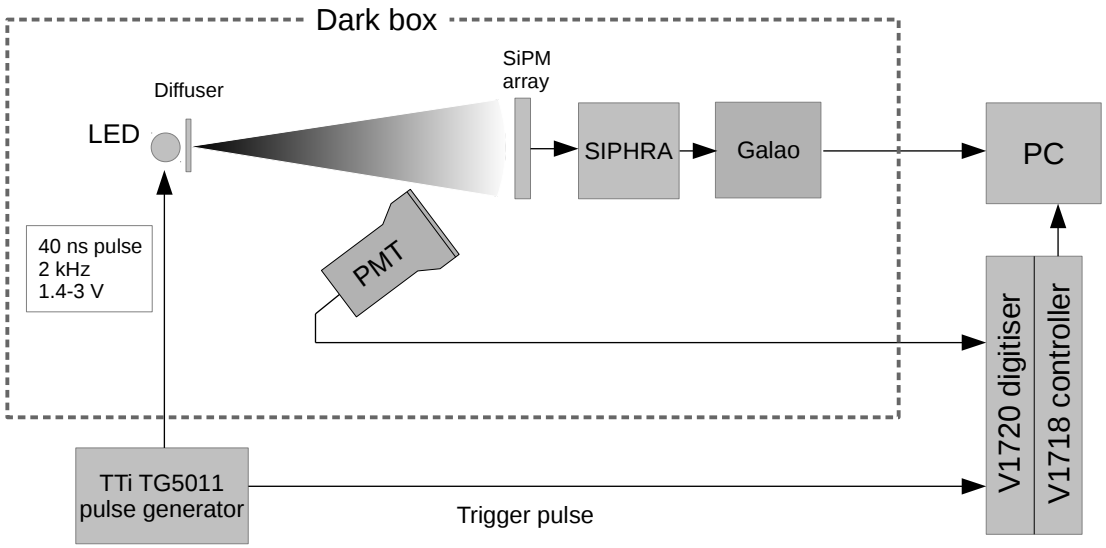

Figure 4.9: A diagram representing the arrangement of equipment for the SiPM linearisation. Reproduced from Murphy, Mangan, et al. 2021b.

The responses of the GMoDem SiPMs shows saturation toward higher signal intensities with some non-linearity evident for lower signal intensities. By relating the GMoDem detector response to the linear response of the PMT, a linearisation correction was generated across the range of ADC channels. A plot of the relationship between PMT and GMoDem detector response is shown in Figure 4.10 for all SiPM channels. This response was generated by cubic spline interpolation between the SiPM and PMT response data.

The correction is curved but relatively smooth between 500 – 3600 ADC channels with a large deviation between 0 – 500 ADC channels. Measurements within these lower signal ranges are expected to be affected to some degree by time walk effects, that is to say that the time at which SIPHRA samples a signal is dependent on the pulse height and the trigger threshold and may possibly contribute in some part to the non-linearity observed in the lower ADC range of the detector. SIPHRA uses a track and hold circuit for pulse height spectroscopy which operates by matching the shaped output signal and holding the voltage after trigger to be sampled using the internal 12 bit ADC. The "HOLD" signal can be generated either externally or in this case internally using an internal comparator with configurable trigger threshold. SIPHRA is triggered once the comparator threshold has been exceeded, and after elapse of a configurable hold delay (69 ns to 4.7 μs) the "HOLD" assertion signal is applied, the voltage is then held and digitised by the 12 bit ADC. Depending on the pulse height, the time that the comparator trigger occurs may vary. By extension, the "HOLD" signal is then asserted at a time after the elapse of the hold delay duration and offset by the influence of the time walk effect as a function

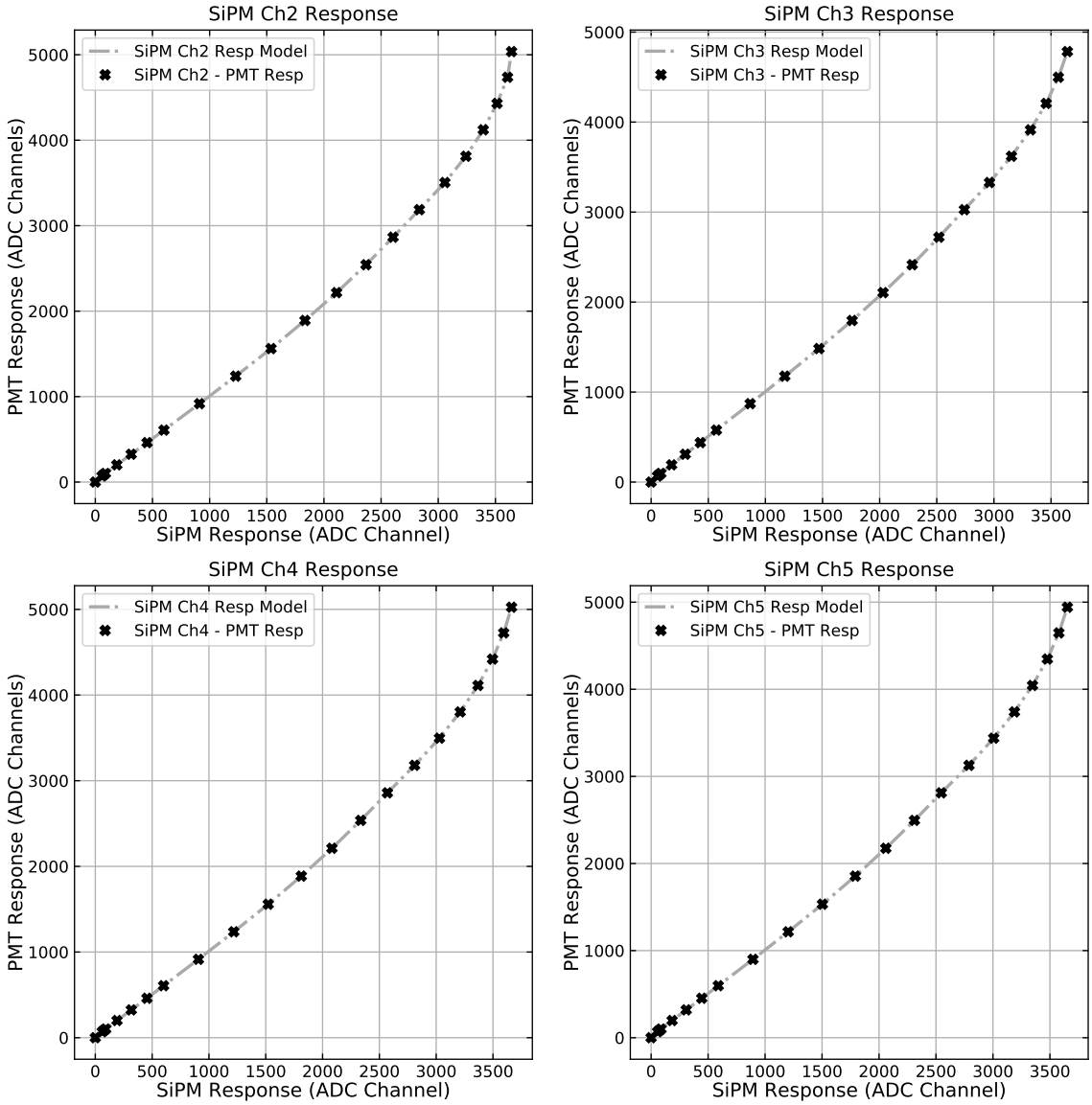

Figure 4.10: The PMT/GMoDem detector response which was used to produce the linearisation correction. As noted, the GMoDem detector saturation causes an overestimation of the correction in the range of approximately >3600 ADC channels. The PMT response data has had a re-scale factor applied (individual to each SiPM channel) to give a near match of the GMoDem detector response data. The response model is a cubic spline interpolation between the respective SiPM channel and PMT response data.

of the shaped pulse height. This ultimately affects the time during the evolution of the pulse that the voltage is held and effectively the measurement of the pulse height for shorter pulses. Furthermore, it is difficult to rule out any contribution to the correction in the lower ADC range due to potential bias in the PMT responses for lower signals. Unfortunately, this could not be further investigated due to the fact that the same set of SiPM ArrayJ devices were to be used in a later SiPM radiation damage study beginning on the 6th November, 2018 (Ulyanov, Murphy, Mangan, et al. 2020).

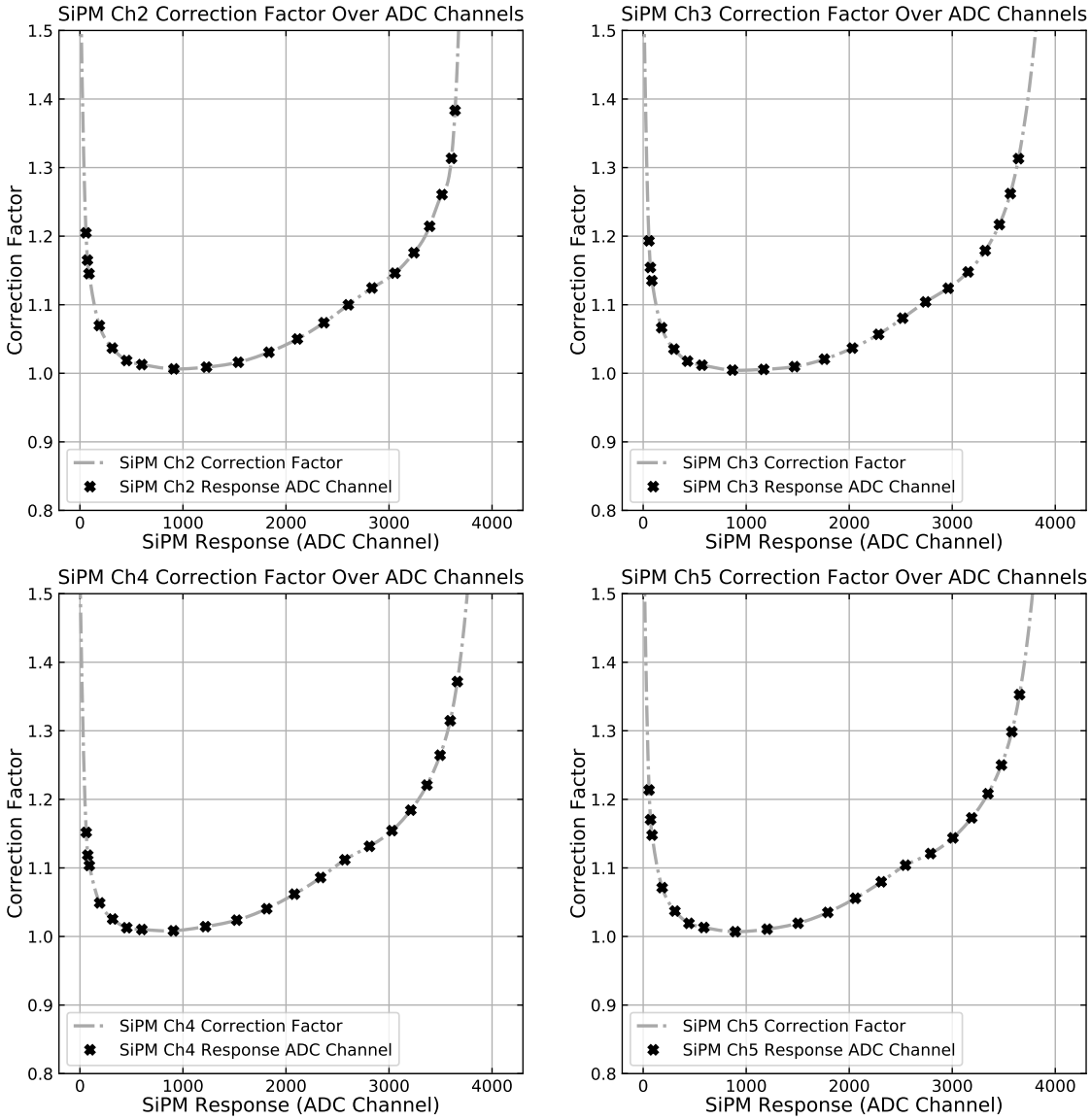

Figure 4.11: The GMoDem detector correction factor as a function of ADC channel. This describes the correction across ADC channel space with larger corrections applied to the lower (approximately < 500 ADC channels) and upper bounds of the detector channels. Note the apparent overestimation of the correction factor beyond 3600 ADC channels.

Above 3600 ADC channels the GMoDem response becomes saturated and cannot be reliably corrected, as a small error in the measured SiPM response corresponds to a large change in the linearised signal. At this point it is only possible to determine the lower limit for the linearised signal. The GMoDem detector correction factor as a function of ADC channel is shown in Figure 4.11. This further highlights the non-linearity of the detector response measured across the channel space with significant saturation of the response beyond 3600 ADC channels. The extent of the correction applied to lower response range (approximately < 500 ADC channels) is also shown. For each received event, the correction functions are individually applied to the baseline-subtracted signals from the four arrays. The total detector signal is then calculated by

adding the four linearised signals.

4.3.3.2. Calibration

As previously mentioned, a preflight calibration of the detector was conducted on the 3rd June, 2018 and the 4th June, 2018 (roughly one month prior to the eventual launch of GMoDem). To calibrate the detector a number of gamma-ray emitting radioactive isotopes were used to produce distinct peaks in the spectrum. The sources used and their gamma-ray emission energy are recorded in Table 4.2. A Gaussian with quadratic model was then used to model these peaks and background contribution in the gamma-ray spectrum. An example of such a fitting is shown in Figure 4.12 showing the fitting for the 662 keV photopeak, with a resolution of 5.4%. It was later discovered that this calibration became invalid just before launch, likely due to some displacement of the crystal coupling during roll-out between the 2nd July, 2018 and the 3rd July, 2018.

$CeBr_3$ is known to contain impurities which contribute to an intrinsic background emission in long duration spectral integrations. For instance, α emissions from the decay of ^{227}Ac can be found around 1.35 MeV, 1.55 MeV, and 1.8 MeV (Quarati et al. 2013). This contamination may be used as a simple verification of the energy calibration and as such any large deviations could be used to inform the validity of the calibration. The energy of these emission lines when measured against the preflight calibration were found to be shifted down by a factor of $\sim$2. Similarly, a 511 keV annihilation line due to the cosmic ray triggered particle showers in the upper atmosphere was also expected, and while identifiable, this was also shifted based on the original calibration. This is illustrated in Figure 4.13 which shows a series of 30 minute integrations during roll-out and launch preparation between the 13^{th} June – 5^{th} July. This represents the calibration with respect to the intrinsic emission lines just after preflight calibration and just up to before the balloon launch. The intrinsic emission lines from ^{227}Ac can be easily seen as the three peaked features in the higher energy channels beyond 1.25 MeV (between the 13^{th} June – 2^{nd} July). By comparison, the spectrum taken the following day on the 3^{rd} July shows clearly that the lines have shifted by $\sim 2\times$ suggesting that the calibration had become invalid sometime between the 2^{nd} – 3^{rd} July, and remained that way (5^{th} July) during the launch. This calibration disturbance is very likely due to the warping of the PLA detector housing. During

Table 4.2: Positions and widths of the different gamma-ray lines (with corresponding isotopes) measured one month before the flight (Murphy, Mangan, et al. 2021b). This analysis includes baseline subtraction and linearisation of the measured photons.

Energy (keV)	Isotope	Mean (ADC channel)	FWHM (%)
511	^{22}Na	1558.96 ± 0.07	6.2 ± 0.02
662	^{137}Cs	2018.35 ± 0.25	5.4 ± 0.02
1274	^{22}Na	3883.02 ± 0.24	4.0 ± 0.02

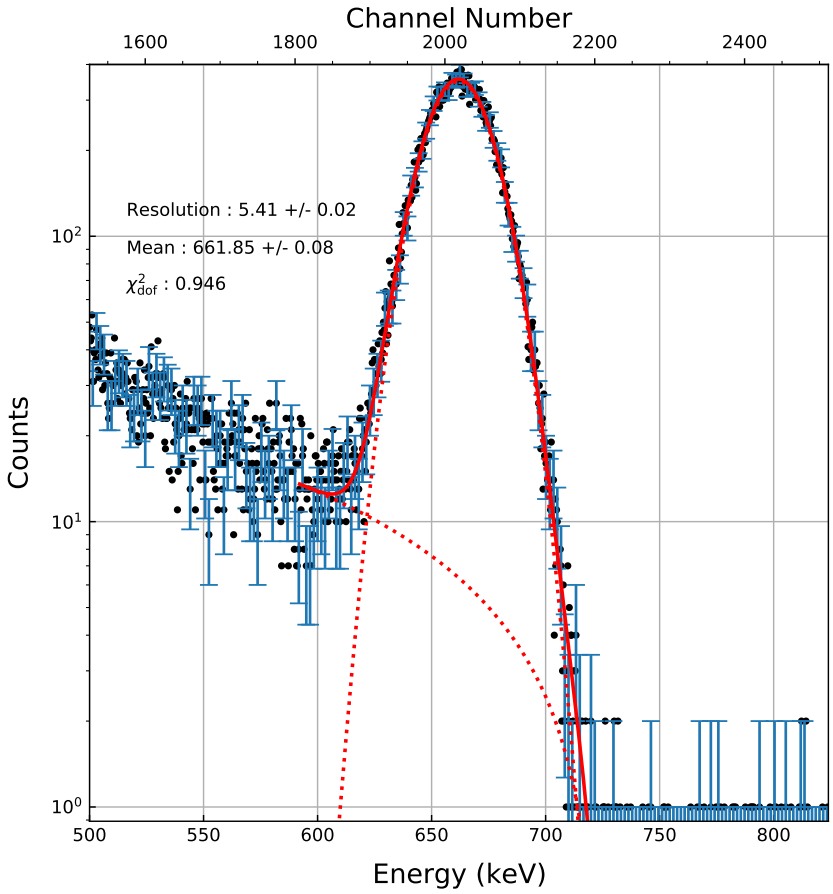

Figure 4.12: Spectrum of ^{137}Cs showing 662 keV line measured by GMoDem. A Gaussian and linear background model fitting is shown.

disassembly the housing was shown to have moulded itself around the $CeBr_3$ crystal aluminium housing and possibly decoupling the scintillator from the SiPMs array face, thus resulting in a loss of light signal reducing the scale of pulse height amplitude measurement for a given photon and invalidating the calibration. This is also shown to have impacted the measured resolution (at 511 keV) while in flight, when compared to annihilation photons from a ^{22}Na calibration source. From a mechanical perspective, this is expected to have been caused by the persistent heat during the numerous roll-out and launch attempts exacerbated by the fact that the GMoDem payload interior was heavily insulated to protect it from the cold near-space environment while in flight. After continuous hot and cool cycling of the detector housing, the PLA would have contracted and expanded, at some point moulding itself around the scintillator housing and during an expansion lifting the scintillator away from the SiPM array. Unfortunately, the $CeBr_3$ intrinsic emissions cannot be used for calibration as their peaks are not prominent enough to accurately determine their channel mean. However an alternate means of calibration of GMoDem postflight is the 511 keV annihilation line which was very clearly identifiable from the continuous integrated flight spectrum.

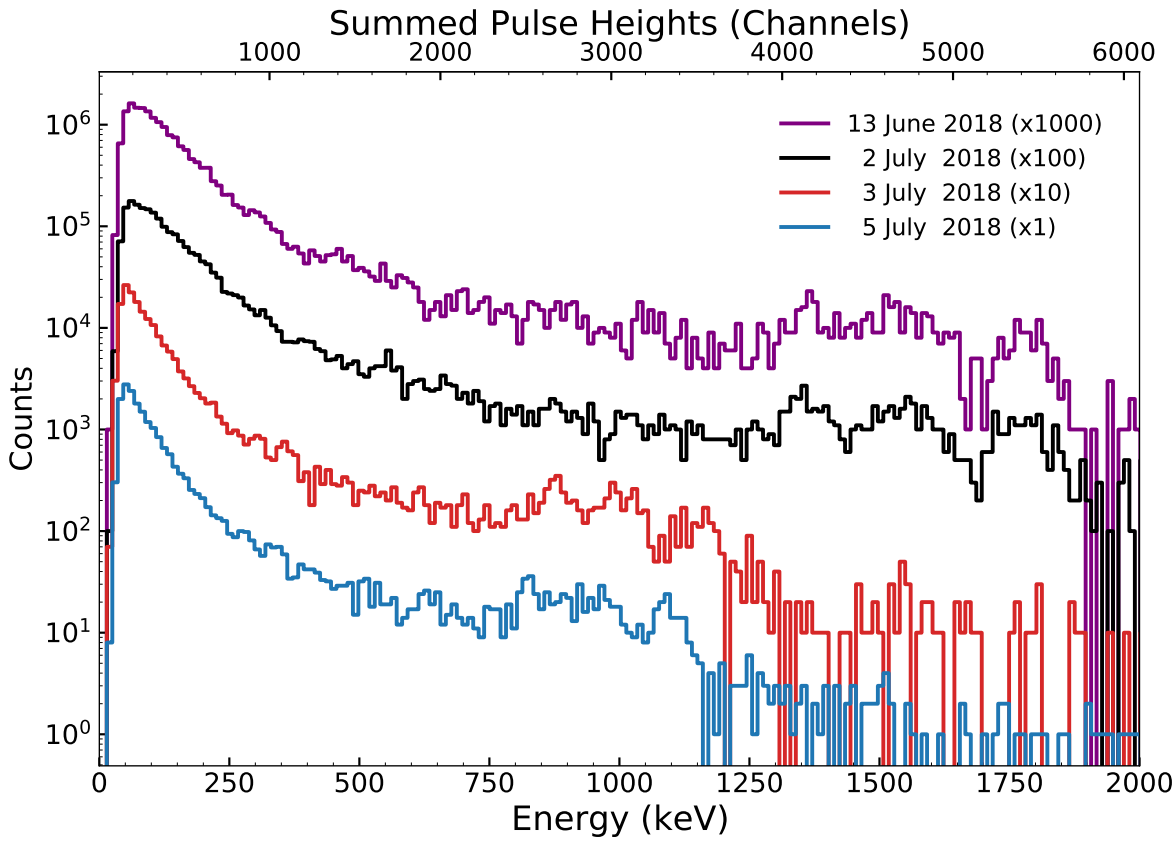

Figure 4.13: Background spectra taken by GMoDem on different dates using an acquisition time of 30 minutes. For visual separation the counts are multiplied by different scale factors given in the legend. All spectra were measured under similar temperature conditions, with the SiPM temperature rising during the measurements from 30°C to 36°C. The energy scale is from the calibration performed on 3 June 2018

4.3.3.3. Spectral Analysis

The flight integrated spectrum is shown in Figure 4.14. As mentioned, a linear correction has been applied to the data after baseline subtraction with a self calibration based on the position of the 511 keV annihilation line. This spectrum does indeed feature a prominent 511 keV peak along with a broad continuum, with the three intrinsic α emissions clearly visible at roughly the expected energies >1 MeV. The resolution of the 511 keV peak is measured at 6.5% – 7.5%, over the duration of the flight. Slightly larger than the resolution measured during the preflight calibration (6.2% at 511keV). This is due to the decoupling reducing the light signal but also temperature variation effects on the SiPM, which were not fully mitigated by the adjusted bias voltage compensation during the balloon flight. As discussed, the SiPM breakdown voltage is a function of temperature and the overvoltage (voltage above breakdown) must be maintained as this dictates the SiPM signal gain. Any variation in gain during long duration integrations as a result of temperature variation results in a smearing of spectral features. For this reason, as the temperature varies, the 511 keV annihilation peak centroid (with its photopeak count distribution describing Gaussian statistics) also varies, and so too does the integrated line FWHM. This temperature dependence was intended to be compensated by the variable bias power supply

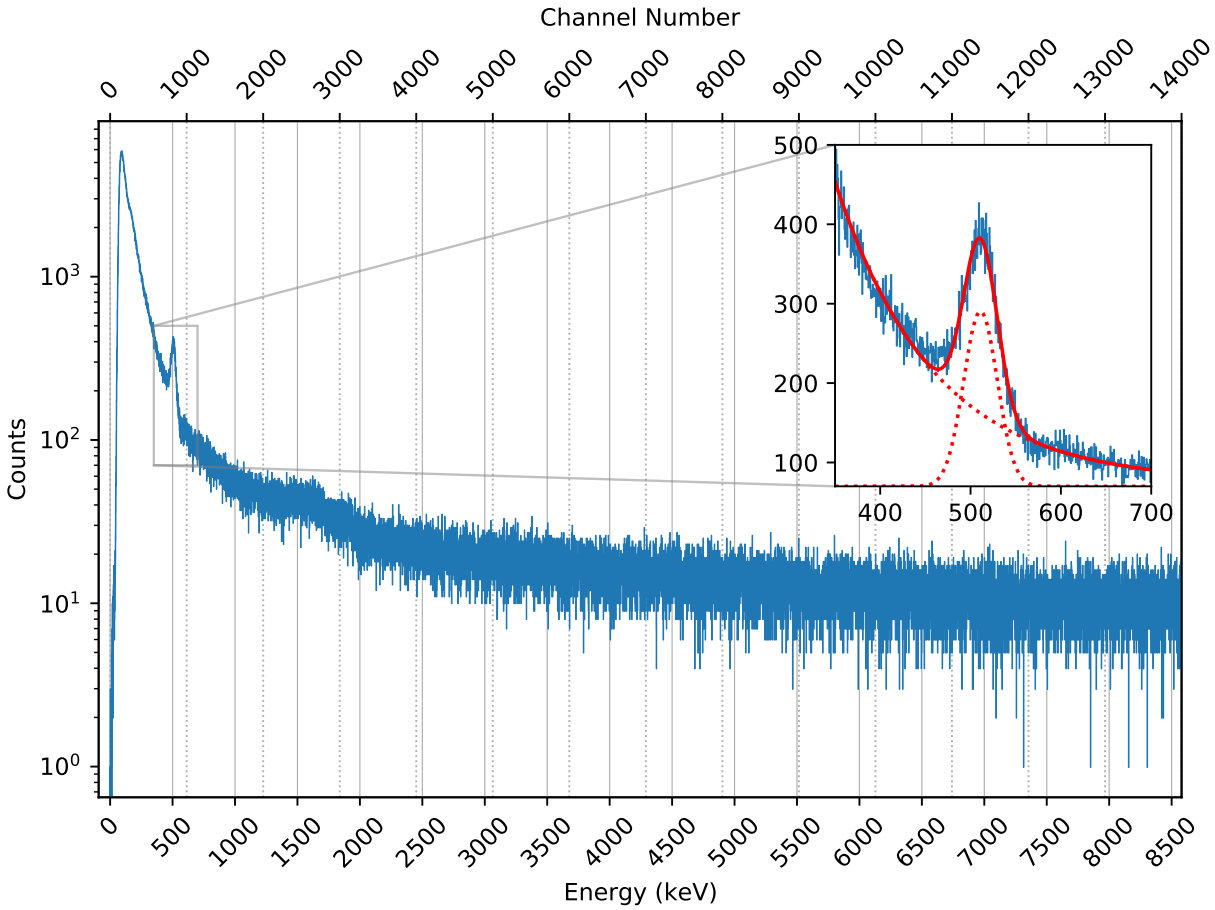

Figure 4.14: Recorded spectrum for the entire flight after baseline subtraction and linearisation (reproduced from Murphy, Mangan, et al. 2021b). The low-energy cut-off corresponds to a trigger threshold of about 100 keV. A fit to the 511 keV is shown in inset. The overall fit is indicated in red, with the constituent components of the fit model shown as dotted lines.

from the OBC, using PT100 temperature measurements of the SiPM array and the known temperature/breakdown relation (of 2.5mV/°C). However it can be observed that the 511 keV peak centroid did indeed vary as a function of SiPM and GMoDem internal temperature, suggesting that the temperature compensation technique either did not compensate aggressively enough or was imprecise in its adjustments. It was later noted that the PSU bias supply was sensitive to temperature variations and this is expected to have been the main source of the observed issues.

It is possible to correct these effects by producing a time dependent calibration, effectively a series of calibrations based on the recorded temperature and the 511 keV peak centroid. The first method uses the linear relationship between the recorded 511 keV peak centroid for binned data and the recorded SiPM temperature for each recorded photon. Each individual event is then calibrated in energy based on this relationship, i.e. for a given event with a recorded temperature the corresponding 511 keV peak centroid is used as the reference to calibrate the recorded energy of the photon. The second method simply bins the total flight integrated spectrum into 15 minute time resolved bins and determines a scale correction based on the 511 keV peak position during the float period when the temperature was most stable during the flight. The scale

Table 4.3: Width of the 511 keV peak at various periods throughout the flight (table contents derived from Murphy, Mangan, et al. 2021b). The peak width is given as recorded by GMoDem and after both bias voltage correction methods have been applied.

	Start	End	Peak FWHM (%)		
			Recorded	Scale Event	Scale Bin
Pfotzer Max (Up)	12:30	14:00	7.31	7.19	7.11
Float All	14:15	19:30	6.73	6.64	6.65
Float Hour 1	14:15	15:15	6.82	6.72	6.78
Float Hour 2	15:15	16:15	6.59	6.54	6.55
Float Hour 3	16:15	17:15	6.91	6.86	6.87
Float Hour 4	17:15	18:15	6.07	6.11	5.98
Float Hour 5	18:15	19:15	6.63	6.72	6.70
Pfotzer Max (Down)	19:30	20:00	7.01	6.87	6.69
Total	12:30	20:00	7.83	6.83	6.78

correction is then applied to each of the time binned spectra calibrations. The resulting interval and 511 keV line FWHM resolution measurements are recorded in Table 4.3. In these measurements, the contribution to the peak FWHM widening due to temperature effects is mostly corrected for and the remaining contribution of the scintillator decoupling is the source of the deviation between the 511 keV line measured from the calibration source (6.2% at 511 keV).

In conclusion, the GMoDem balloon flight successfully demonstrated the prototype design for GMOD by successfully providing continuous spectral integration and functioning without fail in the harsh near space environment. The spectrum showed the expected features (i.e. change of background rate as a function of altitude and the Pfotzer maximum) while the payload subsystem transmitted and logged environmental telemetry. Unfortunately, the performance was affected by the scintillator decoupling and the inability of the SBC to fully compensate for SiPM temperature dependency, however while this is undesirable, the effects could be mostly accounted for in the analysis. This balloon flight provided a test heritage and confidence in the prototype design, while directly testing the instrument components including SIPHRA and the SiPM array, to be further tested in a 101.4 MeV proton irradiation beam line (Section 4.4).

4.4. Radiation Damage Study on J-Series SiPMs

An opportunity arose to further assess the J-Series SiPMs in terms of their radiation tolerance to determine the extent of damage these new devices would sustain in a LEO environment. The J-Series SiPM were at the time of testing relativity new with no published measurements on the device resilience, while at the same time, many up coming spaceborne instruments were considering their use (Mitchell et al. 2019; Moiseev 2017; Mitchell et al. 2017). The same set

of ArrayJ-60035-4P-EVB evaluation boards used during the balloon flight campaign were again used in this study and placed with an assembled detector in a 101.4 MeV proton beam line at the Proton Irradiation Facility (PIF) at the Paul Scherrer Institute (PSI), Switzerland on the 6 November 2018. The detector was irradiated in increasing fluence levels, with the cumulative fluence corresponding to a 6 years in LEO. The following chapter is adapted from Ulyanov, Murphy, Mangan, et al. 2020, where my contribution was as a participant in the experiment investigation at the PSI, specifically the set-up, testing and transport.

4.4.1. The Radiation Environment

The LEO space environment is known to be dominated by a concentration on high-energy trapped particles within Earth's magnetic field. This consists of high-energy protons in the region of the SAA and high-energy electrons at higher latitudes near the poles. In the case of a standard ISS like orbit (which at the time was expected for EIRSAT-1) the primary contributor to radiation damage of silicon based electronics, which SiPMs are generally known to be susceptible to (Garutti et al. 2019), are trapped protons within the SAA.

As these high-energy particles transit through the silicon material, they produce dislocation and interstitial defects by displacing atoms within the silicon lattice structure of the SiPM, creating additional energy levels in the APD band gap of the microcells. These new energy levels can interfere with the expected promotion of electrons from the valence to the conduction band and can manifest as a degradation of the SiPM performance depending on where the defect occurs. For instance, the addition of energy levels in the middle of the band gap can encourage thermally excited transitions of electron-hole pairs increasing the device dark current and dark count rate. Because of the increase in dark count rate, at any given time the number of discharged and recovering microcells is increased and larger than it would be normally. As recovering microcells take a fixed amount to time reset they cannot fully contribute to summed charge output, saturating or reducing the SiPM signal gain (Ulyanov, Murphy, Mangan, et al. 2020). Energy levels close to the conduction or valence bands can contribute by trapping electron-hole pairs and delaying their release, further reducing the signal magnitude. Fundamentally, dislocation of silicon atoms also change the doping characteristics and as such can modify the device breakdown voltage after irradiation.

According to the nonionizing energy loss (NIEL) hypothesis (Garutti et al. 2019), the extent of damage by high-energy particles can be inferred intuitively as being proportional to the NIEL of the penetrating particles for a given material, essentially the amount of energy deposited into the material by the dislocation of lattice atoms. The NIEL is a function of energy and differs for particles, therefore to reference displacement damage regardless of the particle in question, the NIEL energy is normalised to that of 1 MeV neutrons and the equivalent fluence to that of 1 MeV neutron fluence. This is shown in silicon material for protons, electrons neutrons and pions in Figure 4.15. As can be seen, protons with energies such as those found concentrated in the SAA, have a relatively greater NIEL than that of electrons of equivalent energy. As such, given the LEO ISS orbit predominance of high-energy protons and the fact that displacement

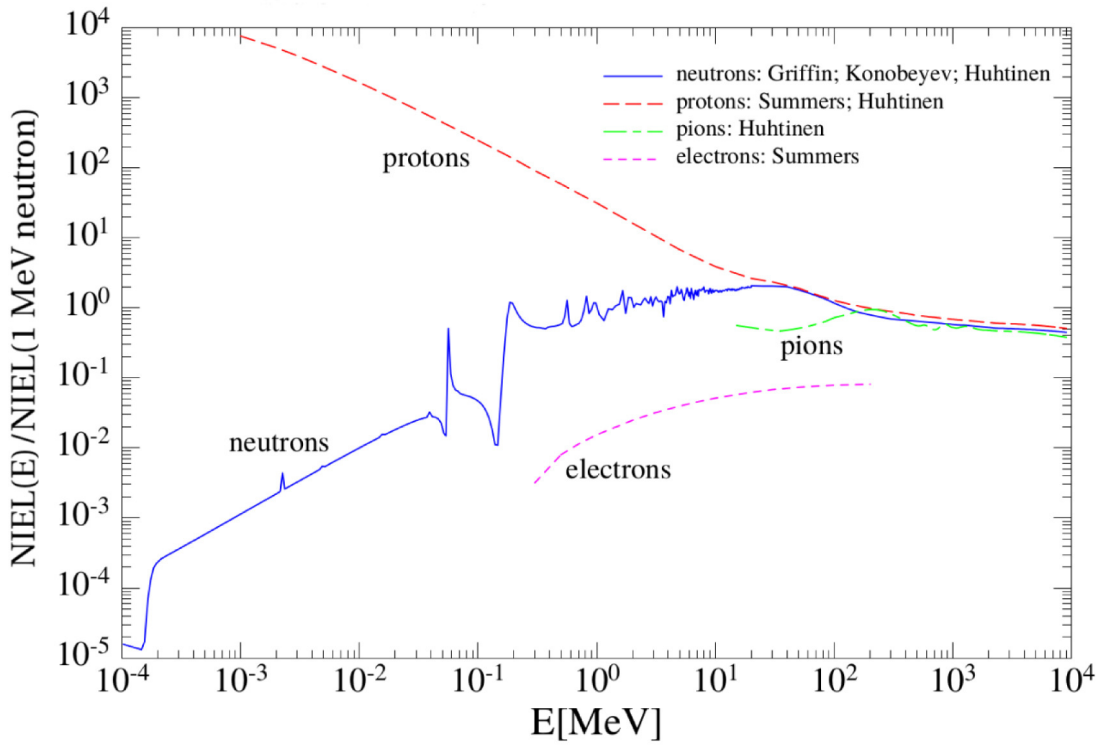

Figure 4.15: The NIEL of a range of particles in silicon (Lindström 2003).

damage is dominated by high-energy protons (according to the proportionality of its NIEL), the contribution of high-energy electrons were not included in this study.

Table 4.4: The proton fluences which the detector was incrementally exposed to over the course of the investigation, simulating a number of orbit configurations and durations. Table contents derived from Ulyanov, Murphy, Mangan, et al. 2020.

Orbit Config.	**Altitude (km)**	**Inclination (°)**	**Proton Fluence (p/cm^2)**	**1 MeV Neutron Equv. Fluence (n$_{eq}$/cm^2)**
ISS	405	51.6	2.6×10^8	4.3×10^8
LEO	550	40.0	1.3×10^9	2.1×10^9
SSO	750	98.5	2.0×10^9	3.1×10^9

The radiation environment for a number of orbits was simulated prior to this study to determine the required proton fluence with which to irradiate the SiPMs to simulate the chosen configurations, including ISS, LEO and SSO. These simulations were performed using the SPace ENVironment Information System (SPENVIS)[1] using the AP-8 MIN (solar minimum) model (Řípa et al. 2020). Geant4 simulations were then used to characterise the extent of shielding attenuation by the spacecraft structure and to determine the proton spectrum and flunce that traverse through the SiPM array for a one year orbit, the results of which are shown in Table 4.4. The average energy of protons impinging on the SiPMs was determined to be 120 MeV with

[1] https://www.spenvis.oma.be/

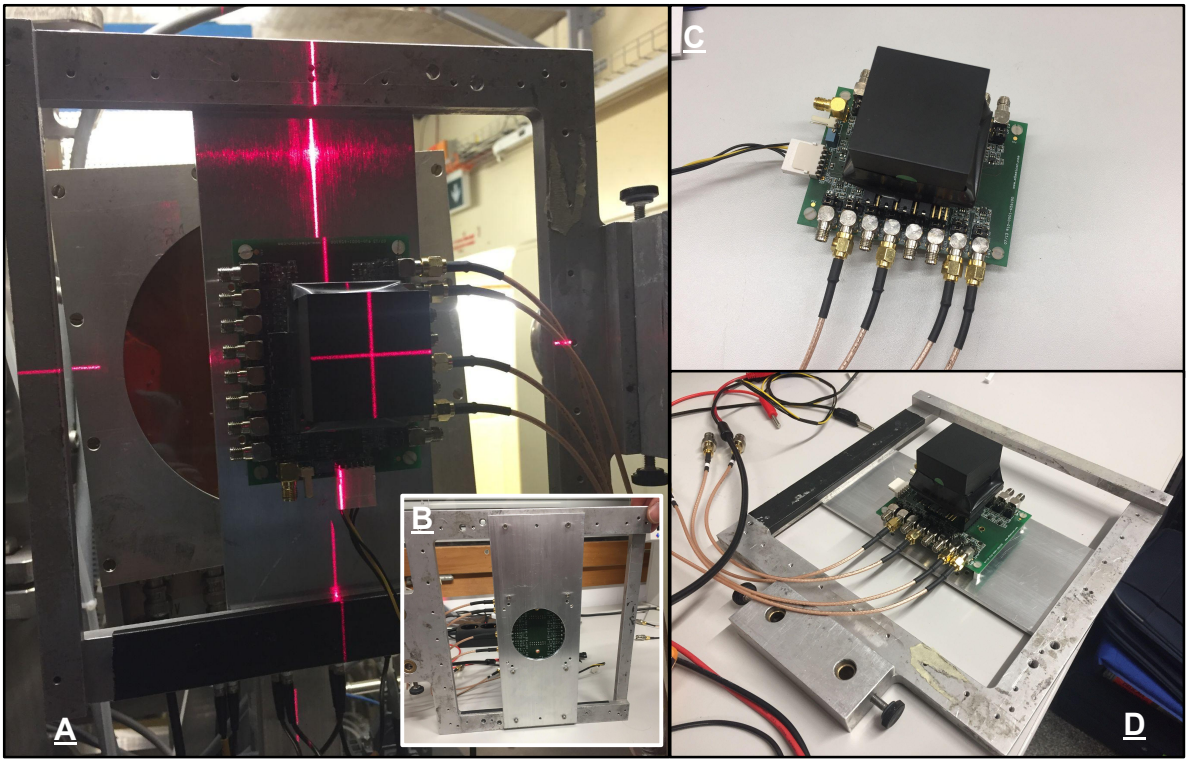

Figure 4.16: The detector used during the proton irradiation testing. A) The detector and aluminum frame mounted to the XY plate before beam exposure. B) The rear of the plate showing the cut out for the beam passage. C) The detector dismounted. D) The detector being prepared for spectral and baseline measurement.

an omnidirectional fluence of 2.6×10^8 p/cm^2, corresponding to a 1 MeV neutron equivalent fluence of 4.3×10^8 n_{eq}/cm.

4.4.2. Test Setup

Proton irradiation of the SiPM array and assembled detector began on 6 November 2018 at the PIF beam line operated by the PSI, Switzerland. The SiPM array used the same ArrayJ-60035-4P-EVB evaluation boards containing 4 MicroFJ-60035 J-Series devices use on the July 2018 balloon flight (Section 4.3), which were coupled to a 25 mm$\times$25 mm$\times$10 mm $CeBr_3$ scintillator in a similar configuration to that shown in Figure 4.4. A second set of bare SiPMs were also separately irradiated in the beam line in this study on a later date, the results of which are discussed in detail in Ulyanov, Murphy, Mangan, et al. 2020.

An initial baseline spectrum was taken to characterise the SiPM array and detector as a whole before irradiation. The entire detector was fixed to an aluminium frame with a hole cut to expose the back of the assembly PCB where the SiPMs were socketed to the board. A set of BNC cables electronically interfaced the detector with the SIPHRA/Galao ROIC readout board, which could be easily disconnect completely separating SIPHRA/Galao from the detector. During each irradiation run the detector would be disconnect from the SIPHRA/Galao readout board (which would remain outside the shielded beam chamber), placed in the beam line, irradiated, removed from the beam line and reconnected to SIPHRA for a performance, spectrum and noise measurement. This characterisation would take place between 10–30 minutes after irradiation

Table 4.5: The radiation environment in terms of proton fluence simulated for EIRSAT-1 placed into a range of orbit configurations with varying duration. Table contents derived from Ulyanov, Murphy, Mangan, et al. 2020.

Exposure №	**Flux (p/cm^2/s)**	**Duration (s)**	**Fluence (p/cm^2)**	**Cml. Flnce. (p/cm^2)**	**Cml. Flnce. (n$_{eq}$/cm^2)**	**Equv. Orbit -**
1	2.56×10^6	40	1.02×10^8	1.02×10^8	1.35×10^8	ISS – 4 Mths
2	2.54×10^6	79	2.00×10^8	3.02×10^8	3.99×10^8	ISS – 1 Yr
3	2.66×10^7	339	9.01×10^9	9.31×10^9	1.23×10^{10}	LEO – 6 Yrs

at the PIF, while a final characterisation took place 86 days after a deactivation period had elapsed such that the detector could be safely shipped back to UCD.

The 101.4 MeV proton beam line, which was collimated to 6.4 mm in diameter, would penetrate perpendicular to the plane of the SiPM array from the back of the assembly, passing through the frame cut out minimising attenuation of the beam and unwanted activation of the aluminium frame. Since the detector was tested in an assembled state, the beam would have to pass through the SiPM adaptor PCB which was made of standard multilayer FR-4 material. As a consequence the beam line was attenuated to 94 MeV. The aluminium frame with the assembly was mounted to an XY table infront of the beam line chamber which could be linearly positioned from an external control room in such a way that the frame cut out lined up with the proton beam. The detector was irradiated, unbiased and disconnected from SIPHRA/Galao over a series of three increasing levels of fluence, each roughly corresponding to an equivalent orbit configuration for a set duration period, as shown in Table 4.5. This includes ISS for four months, ISS for 1 year and LEO for 6 years, where the orbit specifics are described Table 4.4.

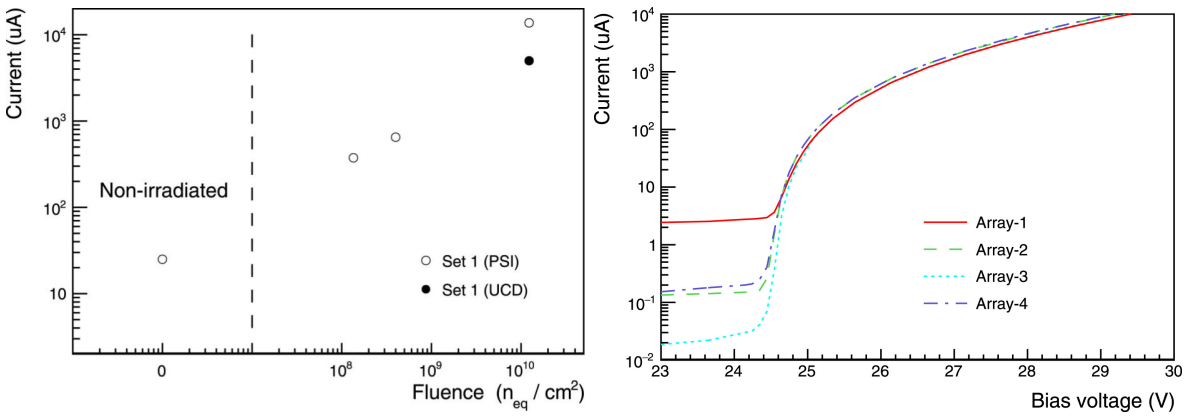

(a) Current vs proton irradiation fluence.

(b) Current voltage curve post deactivation.

Figure 4.17: Measurements on the detector performance during and after the proton irradiation. Reproduced from Ulyanov, Murphy, Mangan, et al. 2020.

4.4.3. Results

As a result of the proton irradiation testing, a noticeable increase in dark current and dark noise was found, and as a necessity the trigger threshold of the detector had to be increased, raising the low-energy cut off to around 40 keV in an effort to minimise the noise effects on the instrument performance.

Before irradiation at the PIF, the SiPM dark current was measured to be 100 μA. After each proton beam exposure (listed Table 4.5) the dark current increased up to 1.5 mA after the first exposure and then up to 2.6 mA after the second exposure. A minor reduction in dark current by around 100–150 μA was noticed within 30 minutes after both first and second exposures, indicating a possible recovery of the SiPM. However after the final exposure at a cumulative fluence level of 1.23×10^{10} n_{eq}/cm^2, the dark current reached 55 mA immediately when biased and continued to rise as a result of self-heating. Once the detector was shipped back to UCD 86 days later, the dark current was measured again. This time the current was measured as 20 mA suggesting again recovery over the interim and deactivation period. The dark current continued to increase to around 35 mA over a duration of around 2 hours. This is summarised in Figure 4.17a, which shows the dark current measurements after 101.4 MeV proton irritation, confirming the NIEL hypothesis where damage is proportion to the NIEL of the particle. An I–V measurement of the SiPMs was also performed at UCD, shown in Figure 4.17b. All four of the ArrayJ devices show a large and similar increase in current once a bias greater than the breakdown voltage is applied, however each device differed below breakdown suggesting possible mechanical damage sustained during prior test campaigns (i.e. the July 2018 balloon flight test from which these SiPMs were used).

As a result of the increased dark current observed prior to the first and second proton irradiations, the contribution of dark noise in the SiPM signal began to surpass the initially set trigger threshold. To account for this during spectral integration tests using a ^{137}Cs calibration source supplied by the PIF operators, the trigger threshold was adjusted just above the noise floor of the SiPM signals to prevent triggering on the increasing noise background. The increase in trigger threshold meant that the lower energy gamma-ray cut off threshold for the instrument increased from 12 keV to $\sim$40 keV after the final exposure. After the final exposure of 1.23×10^{10} n_{eq}/cm^2 1 MeV neutron equivalent fluence, the dark current surpassed the maximum trigger threshold setting available on SIPHRA, such that any spectrum generated was saturation by noise and yielded no other information about the instrument performance. Spectra generated after the 86 day interim period post irradiation testing showed similar results, however it was possible to reconfigure the SiPM readout to the summing channel, which by design scales the input signal by a factor of 16, with still a high trigger threshold applied. These spectra are presented in Figure 4.18, each showing a progressive increase in the low-energy range of the detector as a result of being forced to increase the trigger threshold to counter the increased dark noise contribution to the SiPM signal. The resolution of the detector was also found to have degraded, most notably for lower energies, however the 662 keV peak position did shift due to the increasing

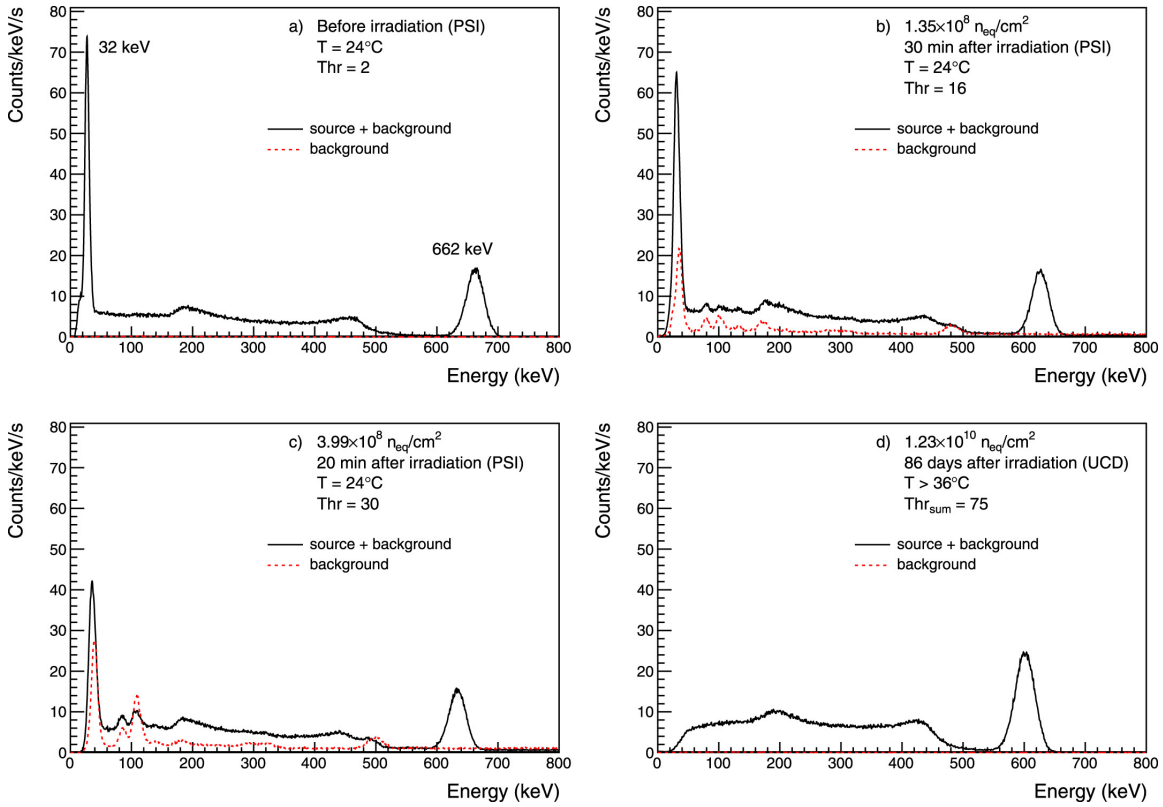

Figure 4.18: Spectra generated during and after the proton irradiation testing. Reproduced from Ulyanov, Murphy, Mangan, et al. 2020

temperature (from increased dark current) and by the increasing of the trigger threshold setting after each irradiation. A number of peaks are also present after irradiation as a result of activation of the instrument material, which were no longer detected after deactivation.

The consequences of these findings in the context of SiPMs for spaceborne gamma-ray detectors suggest eventual degradation of the instrument performance. The increase in dark current contribution to the signal results in both a necessary increase in trigger threshold and an increase in power draw by the SiPM array over a gradation of proton irradiation exposures. In the case of GMOD, the increase in trigger threshold is undesirable but not a major problem, given that the energy range of interest for GRB triggering is 50 keV–300 keV. From this study, over a 6 year LEO operation (which was much longer that originally intended for GMOD), the trigger threshold would only ever increase up to ∼40 keV. The increase in dark current and the resulting power consumption could potentially be problematic for longer missions. At the time of investigation, GMOD was intended for a 1 year maximum ISS orbit. As such it was unlikely that the SiPMs would be irradiated to the extent of straining capabilities of the spacecraft PSU, which can only supply a limited amount of power, before deorbiting occurred. However, given the finally determined SSO orbit of EIRSAT-1, it is possible that the instrument would experience some issues with the increased dark current.

The effect of increased leakage current as a result of irradiation is expected to eventually exceed the capabilities of the GMOD bias PSU during its expected 5 year lifetime (originally 1 year). For example the MAX629 inverting boost converter is configured for a 250 mA current

output limit (selected primarily as it allows a smaller inductor to be used). For a 6 year lifetime in a 550 km orbit, the increase in power consumption of an array of J-Series SiPM devices is estimated to be 3.4 mA/cm^2, based on this study, for a cumulative proton fluence of 1.23 $\times 10^{10}$ n$_{eq}$/cm^2 and an overvoltage of 3.65 V. This corresponds to a total current of 215 mA for the entire SiPM array, while any increase in bias voltage will increase the current draw approximately proportionally to the square root of the overvoltage. However, since the destined orbit of EIRSAT-1 has since changed to a SSO at 520 km altitude, these orbital parameters (inclination and altitude) mean that the spacecraft will be exposed to lower proton fluences and as a result will not be irradiated to the same extent. It is estimated the expected fluence of high energy protons would be 10^9 n$_{eq}$/cm^2/year (this is approximately half that of the LEO orbit at 2.05×10^9 n$_{eq}$/cm^2/year. It is therefore expected that the bias voltage supply will be capable of handling the effects of leakage current due to radiation damage. However, the issues with increased current draw remain and will progressively deteriorate the instrument performance over its extended operating lifetime. It is not expected that the orbit transitions through high latitude regions would contribute a significant amount to the irradiation of the SiPM array, due to the prevalence of high energy electrons in these regions and their lower NIEL value as compared to high energy protons.

To conclude this section, this study, and works by other groups (Mitchell et al. 2019; Mitchell et al. 2021; Mitchell et al. 2022; Garutti et al. 2019), show that radiation damage is an issue to be considered individually for each mission. Considerations include power, the number of SiPMs used, the orbit, and the minimum acceptable range for the low-energy threshold regarding science objectives.

4.5. Conclusion

This chapter discussed the heritage of GMOD; the origin and development of from the GRD instrument concept, through to the proposal, CDR and testing of the design on a high altitude balloon flight and a proton irradiation in a 101.4 MeV beam line. Chapter 5 will provide a deeper discussion on the subsystem ETC, while testing of the firmware developed for the instrument will be addressed in Chapter 6.

Chapter 5

The Environmental Test Campaign

Chapter 4 discussed the development of prototype hardware for GMOD, the previous testing during the high altitude balloon flight from Palestine, Texas (Murphy, Mangan, et al. 2021b), and a 101.4 MeV proton irradiation test of the detector assembly (Ulyanov, Murphy, Mangan, et al. 2020). Between the 3^{rd} and the 7^{th} of February 2020 the GMOD EQM underwent environmental qualification testing at the ESA CubeSat Support Facility (CSF) in Belgium. The EQM hardware was vibration tested in all three axes, simulating the g-force effects imparted by the launch vehicle during launch ascent, followed by thermal-vacuum testing simulating the LEO environment. This chapter details the standardised space qualification procedures and the environmental tests conducted on the GMOD EQM as presented at the International Conference for Space Optics (ICSO 2021), the proceedings of which have been published under open access by the SPIE International Society for Optics and Photonics (Mangan et al. 2021f). This chapter includes an overview of the GMOD EQM subsystem ETC, the equipment and software used for data acquisition, vibration/thermal-vacuum test levels, results and an analysis of the detector's performance throughout. Mangan et al. 2021f contains a multi disciplinary overview of the campaign, including efforts from the GMOD and EIRSAT-1 team. My contributions include the preparation of the demonstration firmware, production of test documentation, participation during testing and proceedings publication and presentation of the work. As this was a team driven campaign, some aspects of the preparation such as the thermal and vibration simulations, bakeout and development of the electrical ground support equipment (EGSE) were conducted prior to the ETC or were managed by other members of the EIRSAT-1 team.

5.1. Qualification and Environmental Test Approach

The purpose of environmental testing can be clearly understood in the context of the typical mission life cycle adopted by most space projects (Bagagli et al. 2008; Monteiro et al. 2019). These phases, outlined in ECSS-M-ST-10C (2009b), provide a structure which stages the development of a space mission from inception (*Phase A: Feasibility*) to end of life (*Phase F: Disposal*). System level environmental testing of the spacecraft falls under *Phase D: Qualification and Production* operations, concerning the production of EQM and FM hardware and software (depending on mission model philosophy) and the completion of qualification and acceptance activities. However, it is common for subsystem level environmental testing and qualification to occur during *Phase C: Detailed Definition* and *Phase D*, concerning the development and qualification of space/ground segments and their products (ECSS 2009b). In the case of GMOD, the EQM was subsystem level tested, while in September - October 2021 the EQM instrument and spacecraft was later system level tested as integrated in the satellite stack

(Dunwoody et al. 2022c; Doyle et al. 2022b).

The model philosophy (as discussed in ECSS-E-HB-10-02A (2010)) which is adopted by the mission dictates the classification of the various iterations of hardware developed (i.e. demonstration models, engineering-qualification model, proto-flight model, flight spare, flight model), its purpose and the test levels which it may be subjected to during verification. In the case of EIRSAT-1 (Walsh et al. 2020) the "prototype" approach was taken which is tailored to missions developing novel payloads, previously untested and complex in design. Under the prototype philosophy a number of models were produced for the GMOD payload. The DM acts as a functional equivalent of the flight model hardware allowing design feasibility and electrical/functional unit level testing during development. The EQM combines the conventional engineering model and qualification model definitions, describing a model which is representative of the form, fit and function of the flight model with some flexibility on the use of high reliability parts. This may be used for fit and functional testing, validation and environmental testing of the payload hardware. The GMOD EQM is the model which was used during the environmental testing campaign and is subjected to qualification test levels and durations as specified in ECSS-E-ST-10-03 (ECSS 2002; ECSS 2012). This was developed as an exact copy of the FM hardware including the use of the same high reliability components and PCB fabrication and assembly facilities. It is not intended for flight but, according to the prototype model philosophy, may later be used as a flight spare or for ground support testing during the mission life time. Finally, the FM is the final implementation reflecting the complete realised design intended for flight. It should be noted that at the time of testing, the EQM design matched the FM flight hardware. However there have since been changes in the flight configuration after the EQM system level testing (which uses higher test levels), most notably the addition of the GMOD Top Reinforcement Bracket (GTRB), a structural bracket which acts as the mounting point of the detector assembly as opposed to the PCB. This is discussed further in Section 2.1.4 and can be seen in Figure 2.6. In response to this, the post system level EQM testing required a subsystem level requalification of GMOD with this new hardware, however this does not negate the findings of the original qualification. This was successfully completed between the 11^{th}–15^{th} April 2022. This testing and the results are to be detailed in a publication in prep and in EIRSAT-1 documentation (EIR_NCR-36 and EIR_TRTP_019).

In general, verification is the process whereby the item under test (IUT) is tested to prove that it has been designed and produced in agreement with the specifications (including any agreed deviations/wavers), that it is free from workmanship defects and conforms to the specified requirements and performance criteria intended for its mission life cycle (as described in ECSS-E-HB-10-02A (ECSS 2010)). This is performed using a number of methods, with testing being preferred for higher confidence results. During qualification, environmental testing is performed on test articles which are flight representative, this provides confidence in the product's performance during launch and in the harsh conditions of the space environment. Following on from successful qualification, the results of the qualification stage are fed into the acceptance stage to assess whether the flight hardware is free from workmanship or manufacturing errors.

This manner of verification was selected for the qualification of GMOD, independent from the rest of the spacecraft, as it was custom built and not CoTS hardware. Furthermore, it would confirm the design and highlight any non-conformance which may not be apparent prior to the test campaign. The test levels, durations and margins are a function of the verification stage, model philosophy and level of hardware decomposition being tested. In this case, GMOD was tested as "space segment equipment" (ECSS 2012) with appropriate qualification test levels, durations and margins as agreed by ESA test facility coordinators.

A number of documents are produced in the lead up to, during and after testing. These documents are intended to be a guide through the test process as well as a record of the performance at each stage. The test specification (TSPE) and test procedure (TPRO) (ECSS 2012) documents were merged into a single document; the test specification - test procedure (TSTP) which defines the purpose of test, an overview of the IUT, pass/fail requirements, the ground support equipment (GSE) and the step by step procedures for conducting the test. The test readiness review (TRR) report acts as a record of the TRR meeting held just prior to the test activity. This is to confirm that the conditions of the IUT, facility equipment and the program test levels are appropriately set up for the requirements outlined in the TSTP and to determine whether testing is ready to begin. Similarly, the post test review (PTR) reports the PTR meeting and summarises the test operation, confirming whether the test was conducted in accordance with the TSTP and TRR specifications as well as discussing any non-conformances which may have occurred. The test report (TRPT) presents an in-depth discussion on the execution of the test campaign and provides an interpretation and analysis of the data collected. In the case of non-conformance and deviation, a non-conformance report (NCR) (as defined in ECSS-Q-ST-10-09C (2018)) documents the extent and nature of any anomalies observed with the IUT, GSE, test equipment as well as actions of test operators and technicians which were contrary to the specifications outlined in the TSTP and TRR. The NCR includes an overview of the root cause of the investigation and the corrective actions taken (if any). An NCR may lead to a Request for Waiver, if a satisfactory and agreed approach to continue has been found. Once testing and documentation have been complete, a test review board (TRB) is called, a panel of all those involved which meet to close out the test activity and to approve the test report findings.

5.2. Functionality, Firmware and Data Acquisition

The MSP430 firmware used during the environmental tests was a development version which provided the basic capabilities necessary to run the experiment, to check the peripheral devices after vibration and during thermal-vacuum testing and finally to enable communications for data acquisition via I^2C and serial protocols. Similarly, a CPLD HDL firmware was prepared for the environmental tests which was in a comparatively more advanced stage of development.

A custom adaptor for command and data acquisition between GMOD and the EGSE was built for the environmental campaign. The EGSE used included a set of 4 mm banana plugs and a 3 channel RS Pro SPD3303X-E PSU, a Total Phase Aardvark used as a USB to I^2C adaptor and a FTDI LC234X module as a USB to serial interface. Command and data collection was

performed using a laptop running Linux Ubuntu OS and a custom user interface (UI) developed for collection of data from GMOD for spectral integration, SiPM temperature monitoring and telemetry logging. The UI was built using the Tkinter Python toolkit with functionality for command and data handling developed in Python3. The EGSE interfaced with GMOD through a pair of custom adaptor PCBs, one being fabricated for vacuum compatibility and mating directly with GMOD and the other featuring the EGSE breakout connections. This interface was designed such that it could be used for both the vibration and thermal-vacuum chamber (TVAC) reduced functional test (RFT) inspections allowing a D-Sub–37 electrical feedthrough between the DN200 ISO-K flange in the Small Space Simulator (S^3) TVAC wall. The EGSE layout including adaptors can be seen in Figure 5.1.

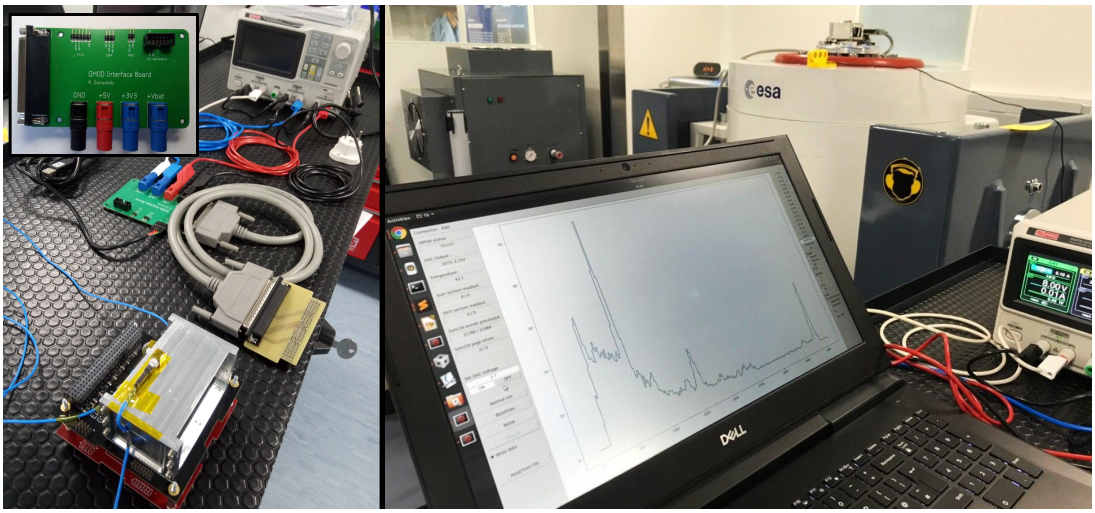

Figure 5.1: *Left*) GMOD and associated EGSE. Shown are the vacuum compatible TVAC boards with power and serial connections prepared for interfacing with GMOD. The EGSE breakout board is shown in the inset. *Right*) The EGSE being used in a functional test to record a spectrum from a set of 2% thoriated tungsten welding rods, which contain the gamma-ray emitting radioisotope ^{232}Th, while GMOD is mounted on the vibration table. Credit: R.Dunwoody.

Standard calibration sources which are normally used during spectral integration and which produce known gamma-ray energy emissions were not available and would likely not be vacuum compatible. These were needed for functional testing, consisting of a ∼10 minute spectral integration used to perform a general health check of the instrument and to roughly gauge any variation in performance. As a substitute, a set of 2% thoriated tungsten welding rods were used, containing the gamma-ray emitting radioisotope thorium–232 in the form of thorium oxide. When ^{232}Th and its daughter isotopes undergo radioactive decay, they produce α and β-ray emissions in addition to a number of known gamma-ray photons, producing a distinct gamma-ray spectrum with prominent peaks. The ^{232}Th spectrum (shown in Figure 5.2) was measured using a high resolution high purity germanium (HPGe) detector with calibrated peak energies (Idaho National Engineering & Environmental Laboratory 1999 (Original 1974)) highlighted for reference. A set of 7 red tipped cylindrical rods (1.6 x 150 mm) were procured, estimated to contain 1.7% – 2.2% radioactive thorium oxide per rod according to ISO standard 6848

(International Organization for Standardization 2004) with a maximum activity of up to ∼7kBq (UK Ministry of Defense and Defense Safety Authority 2020) (0.19μCi) and contact dose rate of ∼1μSv h^{-1} with rapid fall off with inverse distance squared. These rods are particularly convenient as an alternative to standard gamma-ray sources, they are low activity allowing easy transport, relatively safe handling, are cheap and are commercially available.

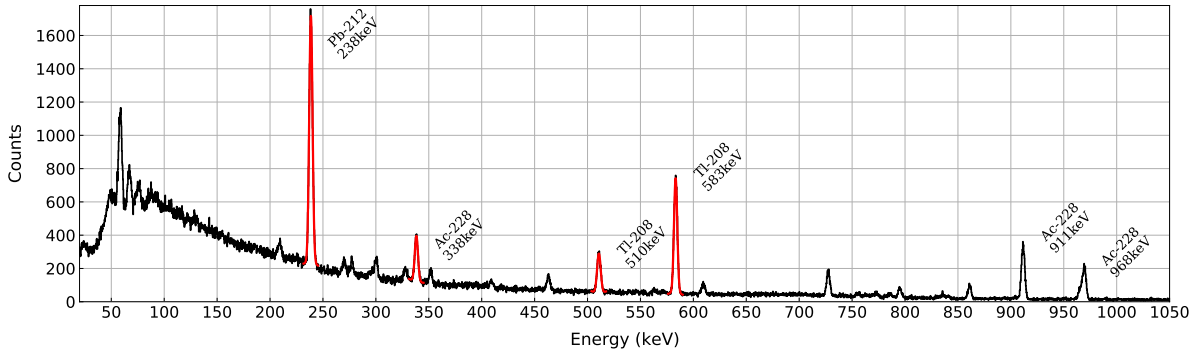

Figure 5.2: HPGe spectrum of the ^{232}Th containing welding rods calibrated with reference to the Idaho National Laboratory (INL) Catalogue https://gammaray.inl.gov/SitePages/Home.aspx of radioisotope spectra measured using Ge(Li) detectors. The four lines in solid red are fittings to the most relatively intense in the GMOD spectra and are readily identified for verification purposes during functional check.

5.3. Vibration Testing

5.3.1. Modelling and Simulations

A finite element analysis was performed on GMOD in order to verify that the structure of the payload can withstand the loads experienced during launch of the satellite. The EIRSAT-1 CAD model was used to develop a finite element (FE) model of the structure with Autodesk Inventor and Autodesk NASTRAN-in-CAD (Autodesk, Inc. 2018). The GMOD model was constrained by the PCB corner holes representing the mounting configuration while integrated within in the EIRSAT-1 stack. Normal Mode Analysis was performed on the GMOD FE model to calculate the natural frequencies and mode shapes of GMOD. For each mode, the modal

Table 5.1: Quasi-static, sine and random vibration Von Mises stress and margin of safety (MoS) calculations for the GMOD motherboard PCB. Note: for the random vibration values the V.M stress values are the 3σ measurements.

Loading Case	**Yield (MPa)**	**Max. V.M. Stress (MPa)**			**Margin of Safety**		
		X Load	Y Load	Z Load	X Load	Y Load	Z Load
Quasi-Static Acc.	262	34.21	27.23	51.62	5.1	6.7	3.1
Sine Vib.	262	5.208	4.204	8.939	39.2	48.9	22.4
Random Vib.	262	42.03	31.78	55.99	4.0	5.6	2.7

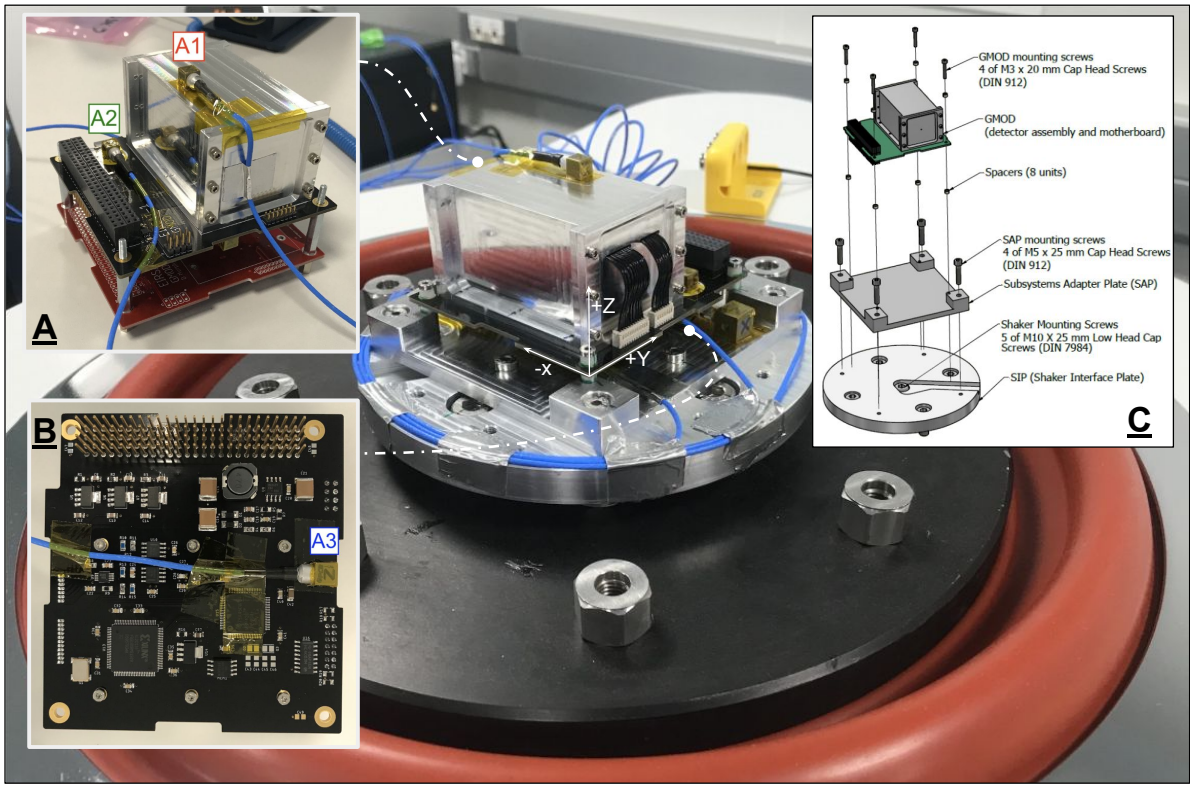

Figure 5.3: GMOD mounted on the shaker for Z-axis vibration. One of the Shaker Interface Plate (SIP) control accelerometers is visible just beneath the motherboard PCB. A) Location of the accelerometers A1 and A2. B) Location of accelerometer A3 on the underside of the motherboard PCB. C) The mounting and orientation of GMOD on the Subsystem Adaptor Plate (SAP) and interface to the shaker using the SIP.

effective masses in each degree of freedom (DOF) was determined, with modes >10% being used to inform the placement of the accelerometers for the vibration campaign. A number of loading cases were then simulated in all three axes, including quasi-static acceleration, sine vibration and random vibration. These were used to determine the MoS with respect to the yield stress calculated using the Von Mises stress in each material for a given loading direction. The MoS was calculated as the ratio between the design allowable stress and the design limit stress scaled by a factor of safety of 1.25 per ECSS-E-ST-32-10C (ECSS 2009a). Simulations show that while positive, the minimum calculated MoS (throughout the spacecraft) of 3.1, 22.4 and 2.7 occurred in the GMOD motherboard along the Z-axis direction during quasi-static, sine vibration and random vibration loading respectively. This reflects the effect of having a large concentrated mass such as the GMOD detector assembly mounted atop the motherboard PCB[1]. The calculated MoS for the motherboard is shown in Table 5.1 for all three axes and loading cases.

[1]As noted in Section 2.1.4 and seen in Figure 2.6, this configuration was later changed for the FM model with the use of a separate structural bracket mounting for the detector, called the GMOD Top Reinforcement Bracket (GTRB).

5.3.2. Test Levels and Set-Up

As the launch vehicle was at the time yet to be determined (ISS orbit was presumed), the vibration test levels were selected based on qualifying the payload for a variety of launch providers such that they cover the minimum requirements for the JAXA H-II Transfer Vehicle (HTV), SpaceX Dragon or Northrop Grumman Orbital Cygnus spacecraft (JAXA 2015; NanoRacks 2013). The levels and durations for the sine (ECSS 2002) and random (ESA Education Office 2018) vibration tests, including tolerances, are detailed in Table 5.2. Prior to any testing at the CSF, GMOD and accompanying EGSE were unpacked and cleaned with isopropyl alcohol (IPA). A visual inspection and functional check was then performed to ensure that no damage had occurred during transport. Three measurement accelerometers were installed on GMOD by the CSF operators. The position of the accelerometers were chosen to detect the primary modes during vibration as determined from the FE analysis described in Section 5.3.1. Accelerometers A1 and A2 were installed on the +Z face of the detector housing and the GMOD motherboard surface respectively (Figure 5.3A), while accelerometer A3 was placed on the -Z face of the motherboard surface (Figure 5.3B). GMOD was mounted to the shaker table via two custom machined aluminium mounting plates: the SIP, which was mounted to the shaker, and the SAP, which mounted on the SIP and which interfaced GMOD to the shaker table (Figure 5.3C). Control accelerometers C1 and C2 were mounted on the SIP as close as possible to the mounting position of the instrument. GMOD was attached to the SIP via the four mounting holes on the motherboard. To replicate the flight configuration of the payload in the EIRSAT-1 PCB stack, 5mm PTFE spacers centred on the motherboard mounting holes were placed above and below the motherboard PCB. The mounting screws for the SAP and GMOD were marked with permanent marker during installation so any rotation could be observed after vibration. The spacers and screw markings can be seen in Figure 5.3 at each corner of the motherboard PCB.

5.3.3. Vibration Test Operation & Results

Sine and random vibration tests were performed for each axis with respect to the instrument's CRF. Sine vibration was conducted as a sinusoidal sweep from 5 up to 100Hz at 2 octaves per minute. The random vibration sequence was comprised of consecutive 10s intervals relative to the specified test levels and then a final interval of 120s at 0 dB. Resonance searches, consisting of a low level sine sweep, were performed before and after each sine and random vibration run. This was used to generate a frequency response of the structure which can be used as comparison pre/post vibration to identify any shift in resonance amplitude or frequency revealing structural changes, including non visible damage, which may have occurred during the test. Visual inspections of the instrument and the screw alignment marks were performed after each sine and random vibration. A functional check was initially scheduled to be performed after completion of the vibration testing, however this was later amended to be performed after completing each axis vibration, to verify that the payload survived without sustaining damage. The functional test involved a basic health check of the instrument which ensured all SiPM channels were still functional; any missing channels would suggest damage to either the SiPM

Table 5.2: Vibration test levels and durations for sine, random and resonance searches. Credit: J.Tompson.

Sine Vibration Tests

Levels			**Duration**	**Tolerances**
Frequency (Hz)	Value	Unit	5-100Hz sweep @ 2 oct/min $\approx$ 130s per axis	Frequency: $\pm$ 2 % / $\pm$ 1 Hz (Whichever is greater) Amplitude: $\pm$ 10 % Sweep rate: $\pm$ 5 %
5 - 21	11	mm		
21 - 60	20	g		
60 - 65	-2.8	g/Hz		
65 - 100	6	g		

Random Vibration Tests

Levels			**Duration**	**Tolerances**
Frequency (Hz)	Value	Unit	10s at -9dB 10s at -6dB 10s at-3dB 120s at full level	Amplitude (10Hz resolution) 20-1000 Hz: -1 dB / +3 dB 1000-2000 Hz: $\pm$ 3 dB RMS acc.: $\pm$ 10 %
20	0.057	g^2/Hz		
20-153	0	dB/oct		
153	0.057	g^2/Hz		
153-190	7.67	dB/oct		
190	0.099	g^2/Hz		
190-250	0	dB/oct		
250	0.099	g^2/Hz		
250-750	-1.61	dB/oct		
750	0.055	g^2/Hz		
750-2000	-3.43	dB/oct		
2000	0.018	g^2/Hz		
RMS acc.	9.47	g		

Resonance Searches

Levels			**Duration**	**Tolerances**
Frequency (Hz)	Value	Unit	5-2000Hz sweep @ 2 oct/min $\approx$ 260s per axis	Same as Sine
5-2000	0.5	g		

Table 5.3: The percentage frequency and amplitude shifts recorded for resonance searches pre/post sine vibration and pre/post random vibration for all accelerometer axes during X-Axis vibration. Any entries highlighted violated the pass/fail criteria. These shifts have been measured from the most prominent resonance peak in both sine and random vibration tests. All other axes passed with shifts less than the predefined limits.

X-Axis Vibration	**Profiles**	**A1X**	**A1Y**	**A1Z**	**A2X**	**A2Y**	**A2Z**	**A3X**	**A3Y**	**A3Z**
Sine % Freq. Shift	(RS1→RS2)	1.0	0.7	1.2	1.0	0.9	0.9	2.1	1.2	0.9
Sine % Amp. Shift	(RS1→RS2)	4.3	2.7	2.4	2.7	4.6	4.8	0.4	11.3	4.4
Rand % Freq. Shift	(RS2→RS3)	11.3	4.8	4.2	5.0	11.5	11.5	5.0	3.9	6.8
Rand % Amp. Shift	(RS2→RS3)	17.0	33.9	11.5	1.0	8.2	20.8	0.8	26.8	1.7

array, or the sensitive wire bonded connections on the CoB SIPHRA. Once the health check was successfully completed, a spectrum was generated using the 2% thoriated welding rods which allowed a rough gauge of the instrument performance; any significant variation in resolution or gain might indicate crystal decoupling as some form of light (signal) loss in the transmission between the scintillator and the SiPM array. The test was considered passed once GMOD successfully produced a spectrum with distinguishable lines from the thoriated welding rods.

To pass the vibration test campaign, a series of pass/fail criteria were defined. Those most relevant are listed below. The vibration test for each axis would be passed if:

1. After comparison of the resonance search before and after each axis vibration, there is less than 5% shift in frequency, and less than 20% shift in amplitude, for modes with an effective mass greater than 10%
2. Visual inspections of GMOD find no damage to the GMOD detector or motherboard and no loosening of mounting screws is observed
3. GMOD successfully produces a gamma-ray spectrum with distinguishable spectral lines

Figure 5.4 shows the pre- and post-resonance search plots for the X-axis vibration. Each column represents resonance data from a single accelerometer (A1, A2, A3) mounted on GMOD, with each row showing acceleration measurements in the X, Y and Z-axis directions with respect to the CRF. Finally, as specified by the legend, each cell is populated by resonance search profiles for pre-sine, post-sine and post-random (RS1, RS2, RS3) tests, relative to the given accelerometer and axis.

While all other tests passed the pass/fail criteria, the X-axis random vibration failed due to a percentage peak shift greater than the predefined limits in amplitude and frequency. The X-axis was the first axis to undergo vibration testing, starting with a pre-sine resonance search, followed by the sine vibration and post-sine resonance search. Sine vibration was completed successfully, seen in Figure 5.4 as the RS1 (blue) and RS2 (red) profiles overlap nearly perfectly with little shift in frequency or amplitude. Following this, a visual inspection was performed with no noticeable change to the instrument or its mounting on the shaker table. Random vi-

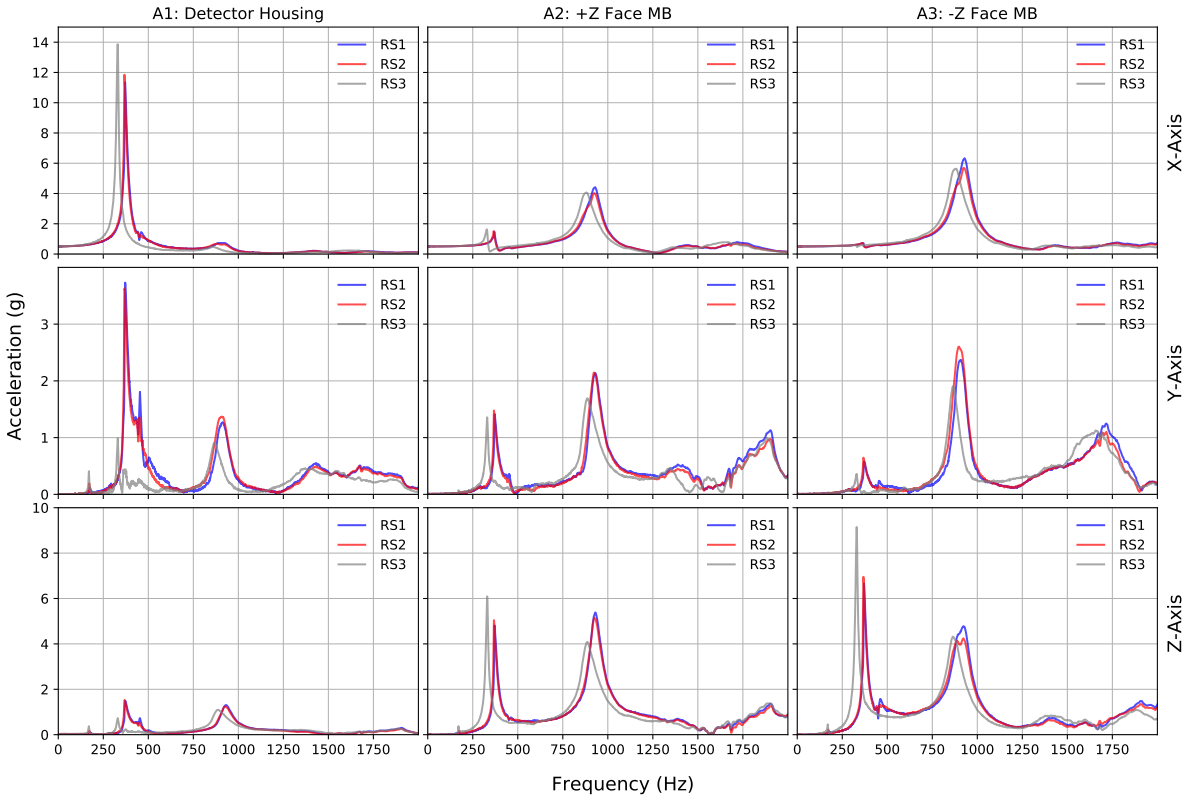

Figure 5.4: X, Y and Z-axis direction resonances (rows) measured during the X-axis vibration testing for each accelerometer (columns) placed on GMOD. Pre/post sine (RS1–blue and RS2–red) and post-random (RS3–grey) resonance searches profiles are shown in each cell whose percentage shifts may be referenced in Table 5.3. Credit: R.Dunwoody.

bration and post-random resonance searches were then conducted. The post-random resonance search profile, RS3 (grey), shows a clear shift in amplitude and frequency after random vibration, as seen in Figure 5.4. For example, a frequency shift of 11.5% was observed for the lowest mode, which violates the first pass/fail criteria stated above. Resonance frequency shifts based on the most prominent resonance peaks for both sine and random vibration tests in the X-axis are shown in Table 5.3 and may be compared to the resonance profiles in Figure 5.4.

A visual inspection of the GMOD motherboard and detector assembly exterior followed, with particular attention paid to PTFE spacers supporting the motherboard for any shifting or rotation about their centres which may have occurred. No visual changes were noticed and none of the marked spacers indicated any such movement. Due to this shift in frequency a functional test was performed after X-axis vibration. GMOD successfully produced a gamma-ray spectrum with evident spectral lines for the ^{232}Th source during the functional test, as shown in Figure 5.5. As GMOD was fully functional, it was deemed appropriate to continue with the Y-axis and Z-axis vibration tests. In the original test procedure, functional testing was foreseen only at the end of the vibration test campaign. After the X-axis anomaly was identified the procedure was modified so that a visual inspection and reduced functional test was carried out after vibration of each axis to monitor the functionality of GMOD throughout the campaign.

Between axes vibration, GMOD was dismounted from the SAP. Between the Y-axis and Z-axis

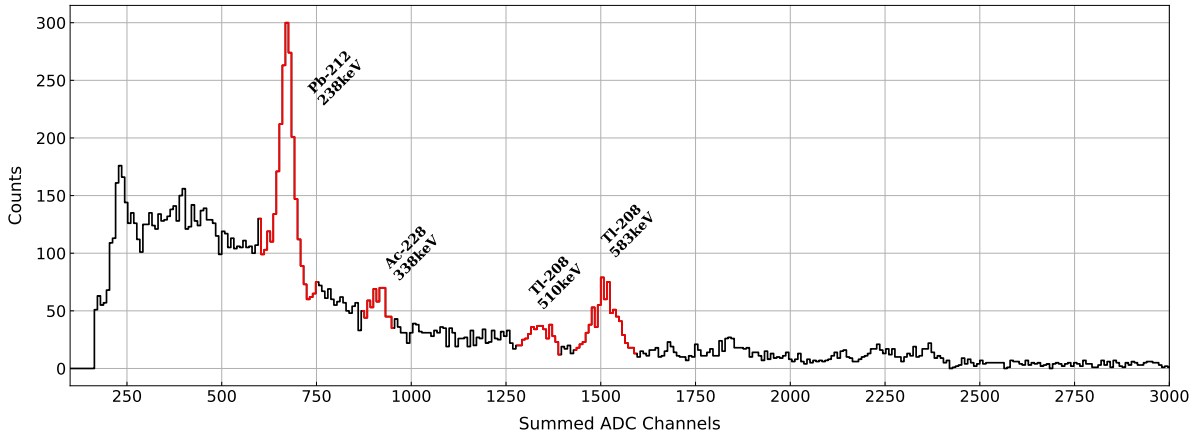

Figure 5.5: Spectrum generated by GMOD using the thoriated welding rods post X-axis vibration indicating no loss in performance. The expected lines (as referenced in Figure 5.2) are observable and have been highlighted. The low number of counts is a result of the short integration time being ∼10 minutes in duration. The spectrum has been re-binned from single bins (ADC channels) to 8 channel wide bins to help distinguish the peaks.

set up, an opportunity to inspect the underside of the motherboard became available; there was no indication of damage found. After vibration in the remaining axes, all pass/fail criteria were passed successfully, no anomalies were detected and GMOD was proven to be fully functional as a gamma-ray spectrum with clear spectral lines was produced in the functional check. GMOD was then removed from the shaker table and disassembled for the mounting of thermocouple sensors for the TVAC testing. This gave a valuable opportunity to visually inspect the electronics assembly hardware post vibration testing to locate any internal structural changes. Each component in the electronics assembly was carefully disassembled, photographed and cleaned using IPA and lint free wipes. No damage was observed. The following are the potential causes of the frequency shift observed during the X-axis vibration which were derived after root-cause analysis, ordered from most to least likely.

1. Movement of GMOD relative to the test fixture - Four M3 bolts secured GMOD to the SAP and SIP plates that were attached to the shaker table. As with possible cause 4, there is a clearance in these mounting holes which could result in a frequency shift. This could not occur at system level as the X-Y constraints in the satellite stack are much tighter.
2. Relief of stresses introduced during assembly - The components of the detector assembly are tightly packed. During insertion of the components, stresses could be introduced that are then relieved as the surface of the spacers shift in the enclosure during vibration. There are no negative effects to GMOD in this scenario.
3. Movement of internal components - Movement of the scintillator could cause additional compression of the silicone optical pad. Compression would improve optical coupling but the effect would likely be undetected as it would be insignificant.
4. Movement of the Detector Assembly relative to the GMOD Motherboard - There is a small amount of clearance in the holes where M2 bolts are used to secure the detector assembly to the motherboard. A shift of ±0.1 mm could explain the frequency shift ob-

served. It should be noted that these bolts were secured using a thread-locking fluid and showed no sign of loosening.

None of these proposed causes pose any issues for GMOD should they occur during the mission. The vibration test campaign was completed successfully and provided confidence in the mechanical design of GMOD. A NCR was issued for the X-axis shift, and the environmental testing continued as planned.

5.4. Thermal-Vacuum Testing

5.4.1. Pre-Environmental Bake-Out

Before being shipped to the CSF, the finished GMOD EQM components were baked out under vacuum to prevent the outgassing of contaminants within the CSF TVAC. During thermal-vacuum testing, neither a residual gas analyzer (RGA) nor a thermoelectric quartz crystal microbalance (TQCM) were used to monitor outgassing, however a cold trap was used to collect any contaminant which may not have already been outgassed during bakeout. Additionally all other equipment (harnessing, adapters etc.) to be used within the components were verified to be vacuum compatible (ECSS 2008b) before transport.

5.4.2. Modelling and Simulations

Simulations were used to determine the expected temperature profile of the satellite while in orbit. A thermal analysis of the spacecraft was performed using the C&RTech package, *Thermal Desktop*[1], an AutoCAD plugin for general thermal response modelling. The spacecraft model was simplified into a set of geometric bodies with curved surfaces approximated by polygonal structures of similar cross-sectional area. This was done to accelerate the computation time. Simplifications include rounded corners being squared, holes being removed from PCBs, the SiPMs being substituted by silicon wafers and bolts being removed. For other simple volume components (like resistors, capacitors etc), these were assimilated into a single lumped mass across the PCB surface. The MSP430 and CoolRunnerII CPLD were retained for their thermal contribution as their profile would vary for operational and non-operational modes. The $CeBr_3$ crystal was modelled as a single block of cerium for a conservative estimate of the thermal properties, as at the time this model was developed $CeBr_3$ had only just began to be used for scintillation and few sources on the thermal properties were available. It was anticipated that the crystal would be heavily insulated due to being wrapped in a number of layers of teflon (as discussed in Section 2.1.1) and hermetically encased within its own aluminium housing. The satellite model was simulated in an ISS-like LEO with an initial temperature of 20 °C over 10 orbits to allow the temperature to stabilise and oscillate about a realistic temperature mean. Sources of radiation within the simulated environment include the Sun, Earth albedo and infrared (IR) re-emission by the planet. A number of mission scenarios were investigated

[1] URL: https://www.crtech.com/products/thermal-desktop

including operational and non-operational modes during nominal, cold, and solstice[1] cases. The results provide an in orbit minimum and maximum temperature range for the SiPM array, CPLD and MSP430. It also verified the high thermal insulation of the scintillation crystal with respect to the rest of the instrument.

Table 5.4: Thermal simulations of GMOD for operational & non-operational modes under a variety of conditions, with a 10 °C simulation uncertainty applied (i.e. 10 °C added to the predicted maximum, subtracted from the predicted minimum). Highlights indicate temperature extremes experienced across all scenarios. Credit: C.O'Toole.

	Nominal		Cold		Solstice	
Operational	**Min**	**Max**	**Min**	**Max**	**Min**	**Max**
SiPM	+10 °C	+44.1 °C	+10 °C	+42.3 °C	+10 °C	+64.6 °C
CPLD	-5.1 °C	+37.8 °C	-8.8 °C	+35.2 °C	+10 °C	+49.7 °C
MSP430	-5.1 °C	+37.8 °C	-8.8 °C	+35.3 °C	+10 °C	+49.7 °C
Non-Operational	**Min**	**Max**	**Min**	**Max**	**Min**	**Max**
SiPM	-9.2 °C	+30.9 °C	-13.6 °C	+30.3 °C	+7.6 °C	+30.0 °C
CPLD	-16.8 °C	+34.9 °C	-20.9 °C	+32.3 °C	+6.6 °C	+30.4 °C
MSP430	-16.8 °C	+34.9 °C	-20.9 °C	+32.3 °C	+6.6 °C	+30.4 °C

5.4.3. Test Levels and Set-Up

Through simulation, the maximum and minimum temperature extremes experienced while in orbit was found to be +64.6 °C and -20.9 °C respectively. For the purposes of qualification testing, an additional ±10 °C qualification margin (ECSS 2012; ECSS 2002) was added to these temperatures. The minimum qualification temperature was therefore defined as -31 °C while the maximum was defined as +75 °C. The vacuum chamber would be pumped down to a target of 10^{-6} mBar with thermal cycling permitted once 10^{-4} mBar had been achieved. Once the temperature reference point (TRP) had surpassed the qualification threshold the instrument was then set to dwell at the qualification temperature for a duration of 60 minutes. The TRP is a physical location on the IUT chosen as a simplified representation of the unit temperature (ECSS 2008a) and is used as a reference when determining if and for how long the IUT had surpassed the qualification thresholds. The dwell period is allocated to allow sufficient time for thermal conduction to stabilise throughout the IUT while at the qualification temperature.

As the temperature differentials used in this test were quite large, along with the high ramp rate, it is possible that the instrument hardware and electronics had been stressed more than necessary to qualify the instrument. However, typically environmental testing is performed with larger margins such that the IUT is fully tested prior to launch and as such, any concerns or risks to the

[1]This is a specialised case representing the duration that the spacecraft is held in a sustained exposure to sunlight due to the yearly solstices and the orbit configuration. The orbit parameters were adjusted to best represent these effects.

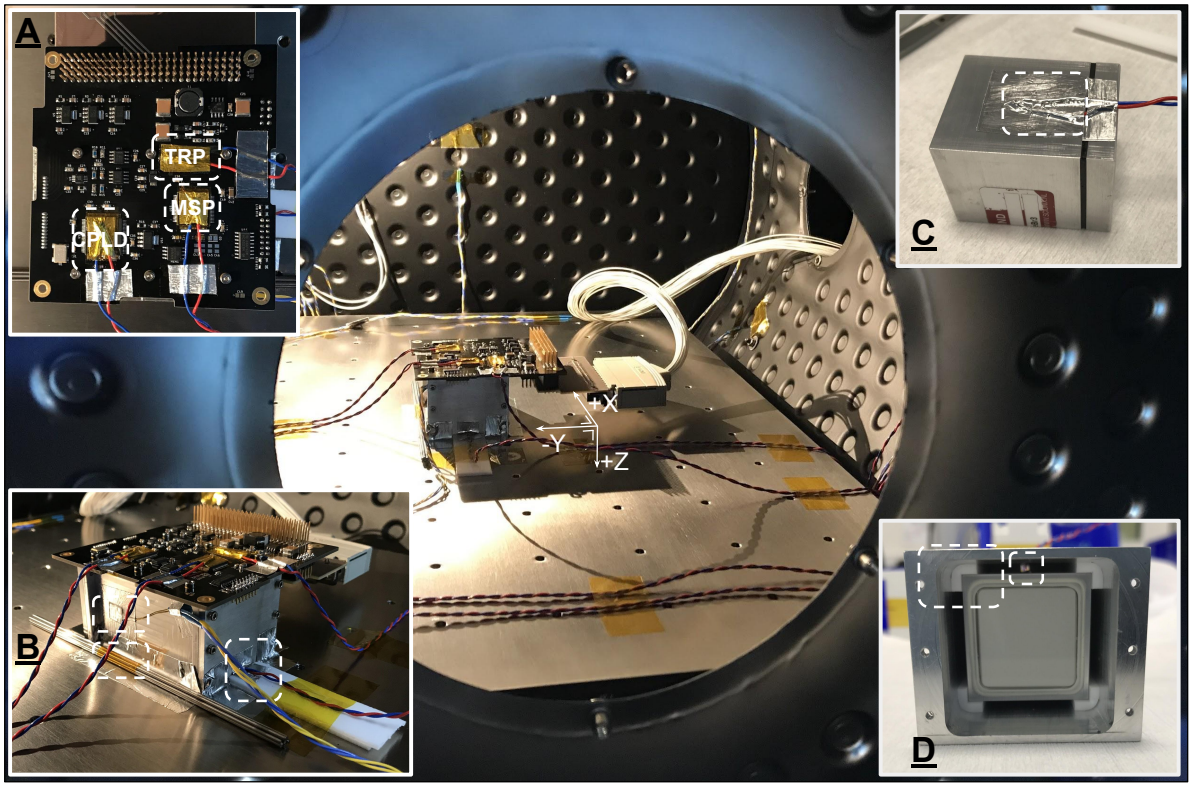

Figure 5.6: GMOD within the TVAC chamber. A) The placement of thermocouples on the MSP430, CPLD and the TRP with kapton tape overlay. B) The placement of GMOD in the TVAC, the throiated welding rods, PT100 mounting and the crystal thermocouple cable. C) The crystal thermocouple mounted on the crystal aluminium container surface. D) The crystal within the detector assembly housing supported with PTFE spacers.

EQM hardware due to high test levels (i.e. the $CeBr_3$ scintillator in particular) were acceptable and necessary to achieve complete confidence. Furthermore at the time of preparation for the tests, there was little information about the scintillator regarding the temperature stability of the crystal itself, the housing or the hermetic seal integrity as a function of pressure or temperature.

Following vibration testing, the disassembled GMOD components were cleaned using IPA and lint free wipes before the PT100 sensor and thermocouples were mounted to the GMOD hardware. These would be used for monitoring the thermal behaviour of the components chosen based on the thermal simulations (Section 5.4.2). The simulations suggested that the crystal would be heavily thermally insulated within the detector assembly; for this reason, it was of interest to monitor its behaviour. A type T thermocouple was installed on the crystal housing while a custom endcap was machined with a channel to allow the thermocouple cable to be routed outside once sealed. The PTFE venting channel was enlarged to allow enough room for the cable cross section to pass through. The spacer and endcap are representational only, with minimal modifications to support the testing. The mounting of the crystal thermocouple is shown in Figure 5.6C and D which shows the PTFE spacers around the scintillator and the raised surface caused by the thermocouple which was mounted using aluminium tape. The rest of the type T thermocouples were mounted onto the motherboard hardware, one on top of the

CoolRunnerII CPLD and the other on top of the MSP430 microcontroller packages. A type T thermocouple to be used as the TRP was also mounted to the motherboard PCB on a region in the center of the board void of components or traces (as seen in Figure 5.6A). This location was chosen such that controlling the temperature at this point would effectively drive the temperature of the instrument as a whole and could be used to infer its mean temperature. This installation was conducted by CSF operators using aluminium tape, while layering a strip of kapton tape atop to attempt to match the emissivity properties of the PCB.

Table 5.5: TVAC test levels and durations, with phase overview and durations spent beyond qualification thresholds below. *Note: for cold cycle durations in *Time Over* T_Q, T_{QMin} is measured as the lower bandwidth threshold of <-30 °C, 1 °C greater than the predefined T_{QMin}.

Parameter	**Level**	**Notes**
T_{QMax}	+75 °C	Bandwidth [+75 °C, +78 °C]
T_{QMin}	-31 °C	Bandwidth [-30 °C, -34 °C]
Pressure	10^{-6} mBar	Cycling permitted beyond 10^{-4} mBar
Dwell	1 hr	Updated to ∼2 hrs after Non-Op
Cycles	4	1 Non-Op 3 Operational (+ 1 half final)

	Non-Op		**Operational**						
Phase	**I**	**II**	**III**	**IV**	**V**	**VI**	**VII**	**VIII**	**IX**
Range	Hot	Cold	Hot	Cold	Hot	Cold	Hot	Cold	Hot
Time $>T_Q^*$	1:06:05	1:45:40	01:40:20	01:02:35	1:33:20	1:03:15	1:35:55	1:03:45	1:07:20

An additional PT100 sensor was mounted on the aluminium housing on the -Y face (with respect to the CRF), kapton tape was not used in this case as the emissivity of the aluminium tape better matched that of the aluminium housing. GMOD was then installed within the S^3 TVAC chamber (Figure 5.6); thermocouple cables were routed through the chamber through a feed through block, while GMOD power and data EGSE were connected using the custom vacuum compatible interface PCB via a D-sub 37 cable. GMOD was inverted within the chamber so the aluminium housing interfaced with the thermal plate, with the addition of aluminium tape to secure good thermal contact. The thoriated welding rods were placed beside the detector assembly along its longest axis as a source of gamma-ray emission for the operational cycle spectral measurements. The PT100 placement, thoriated welding rods and crystal thermocouple sensor cable can be seen in Figure 5.6B. Externally, the thermocouples were routed to the CSF data acquisition hardware, while the GMOD EGSE connected to the external interface board, providing power, command and data readout via the custom UI, discussed in Section 5.2.

5.4.4. Thermal-Vacuum Test Operation & Results

The TVAC was pumped down from ambient pressure to 10^{-6} mbar; after reaching a minimum of 10^{-4} mbar, thermal cycling began with a non-operational thermal cycle later followed by

three operational[1] cycles. The TVAC under vacuum would manage these cycles by varying the temperature at a rate of 2 °C/min (via the thermal interface plate) from ambient temperature to +75 °C with a dwell at that temperature until the instrument reached thermal equilibrium (originally 1 hour duration). The 2 °C/min ramp rate was chosen as an operational requirement as this allowed the TVAC campaign to conclude within the allocated duration. The cycle would then proceed to the cold cycle where the thermal plate would drop in temperature below ambient to -31 °C with another dwell, as before to ensure thermal equilibrium. A final half cycle (from ambient temperature to hot and returning to ambient) was done to allow the detector to return to ambient from a hot cycle phase to prevent any condensation or residual moisture build up within the chamber after repressurisation and to discourage dendritic growth (Zhan et al. 2010) on the SIPHRA silicon die. The TVAC thermal and pressure measurements are shown in Figure 5.7.

To pass the TVAC test campaign, a series of pass/fail criteria were defined. Those most relevant are listed below. The TVAC testing would be passed if:

1. The GMOD instrument completes all functional tests and cycles (operational and non-operational) without sustaining damage due to high or low temperature stresses
2. Detailed visual checks of the GMOD instrument before and after the test campaign show no physical damage to the instruments detector assembly, motherboard, PCB traces or components (i.e. thermal cycling causing cracking, PCB components functionality impaired, any occurrence which results in the GMOD instrument becoming inoperable)
3. The instrument can perform the experiment and successfully generate a spectrum, during the operational cycles

During the non-operational cycle, as expected the crystal was found to be very well thermally isolated from the rest of the instrument, with significant lag between the crystal temperature and the other sensor measurements (Figure 5.7, Phases I & II). The first, non-operational cycle reached its dwell and qualification criteria without incident, after which GMOD was powered up and a serial connection was established while rising from the non-operational cold cycle, into the operational phases (Phases III to IX). A successful health check was performed around 0 °C confirming the instrument had survived the non-operational cycle. GMOD was then commanded to enter operational mode and begin measuring a spectrum leading into the operational cycling stage. The first operational phase (Phase III) demonstrated the crystals extreme thermal insulation; at one point the crystal showed a temperature differential of >70 °C between the crystal and the rest of the instrument (referencing the TRP). An unforeseen effect of this was that the large differential allowed the crystal to act as a heat sink, drawing heat through conduction from the rest of the instrument. While the level of thermal insulation of the crystal was predicted, this behaviour was not. This became problematic during the initial hot dwell of Phase III. Just before the TRP reached +75 °C, the qualification temperature, it was drawn

[1] This involves the power-up of the instrument, a health and functionality check followed by continuous spectral integration using the ^{232}Th containing rods as a gamma-ray emission source.

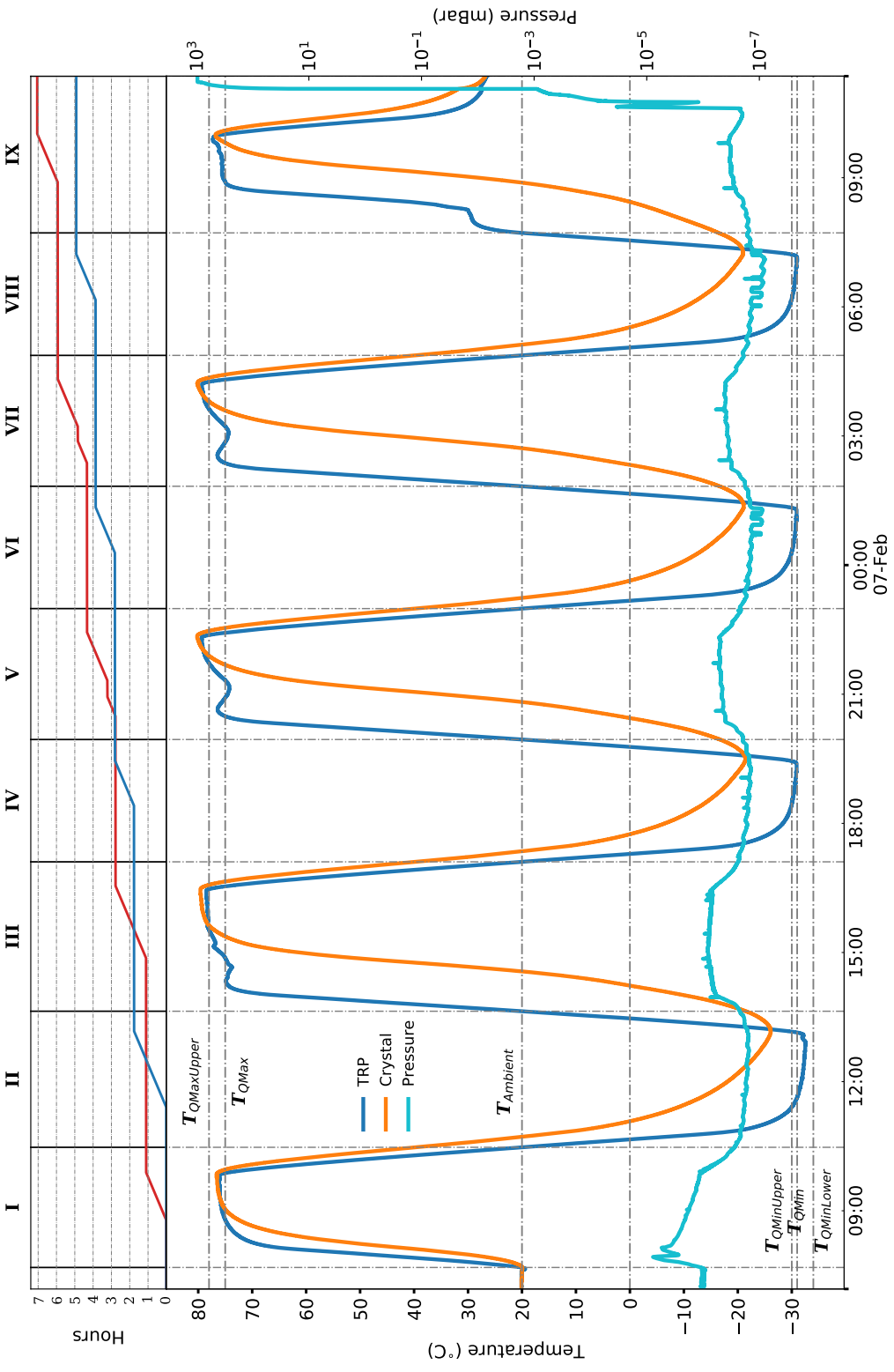

Figure 5.7: TVAC cycling profile with accumulated dwell duration for qualification ranges above in hours. Measurements for the MSP430 and CPLD overlap almost perfectly with the TRP measurements with a maximum difference of $\sim$1.4 °C. For the sake of clarity they have been omitted here. Accumulated durations in hours may be also referenced in Table 5.5 where T_{QMin} is taken as the lower bandwidth threshold of -30°C.

down below this by the crystal's heat sink behaviour, below that required to achieve the pre-defined qualification level. This is seen in Figure 5.7 just beneath the +75 °C mark in Phase III. The CSF operators attempted to mitigate the effects of this by adapting the scripted TVAC control profile resulting in an increased dwell duration from 1 to 2 hours in duration. Despite this, the crystal's behaviour resulted in multiple dwell stabilisation infractions, compounding the matter, it was impossible to manually adjust the thermal plate setpoint for the remaining two cycles (Phases V - VIII) as it would be performed through automation, overnight and without an attending operator. This would cause the TRP to hover just above the cold dwell threshold qualification of -31 °C for all operational cycles (Phase IV, VI, VIII) and exceed at some points the upper limit hot dwell threshold of +78 °C (Phases III, V, VII). Regardless, GMOD continued to function as expected without any impact or impedance to performance. An NCR detailing the non conformance was produced outlining the thermal behaviour of the crystal, but stating that there was sufficient confidence that the instrument was properly stressed for qualification and that the objectives of the test were met. This is due in part to the close proximity of the cold dwell qualification temperature to that which was actually reached, a difference within just 1 °C. Furthermore, it was deemed that the test levels were far more demanding than those defined in the European Cooperation for Space Standardization (ECSS) standards. Additionally, at the time GMOD was yet to undergo system level qualification testing, while integrated with the rest of the EIRSAT-1 payload, which would provide further confidence in the qualification. Upon completion of the fourth and final cycle of the TVAC campaign (Phases VII to VIII), the instrument was returned to ambient from a hot cycle (Phase IX). The instrument was finally removed and disassembled for visual inspection. All thermocouples were removed and components were inspected and photographed. As no observable damage was discovered and GMOD successfully generated a spectrum, all pass/fail criteria were passed successfully. The duration achieved at qualification levels for each phase during the TVAC campaign are shown in Table 5.5.

SiPMs operate above the so-called breakdown voltage, in the case of GMOD this is a negatively applied bias voltage. The overvoltage, the excess voltage above breakdown, defines the internal amplification (gain) of the SiPM. The temperature dependence of SiPM breakdown voltage and the resulting effects on their characteristics are well known (Otte et al. 2017) and were expected to be encountered during the testing. For J-Series SiPMs (OnSemiconductor 2018), the breakdown voltage is known to vary by 21.5 mV/°C. In brief, SiPM gain is defined as the amount of charge released per single photon absorption and is a function of the SiPM overvoltage. Since breakdown voltage is temperature dependent, for a fixed applied bias, any variations in temperature will proportionally vary the overvoltage, and by consequence, the SiPM gain. Thus for a scintillation signal produced by a gamma-ray photon (of a given energy) the amount of charge released by the SiPM array will be either increased or decreased. From a high-level perspective, for a fixed applied bias voltage and variable temperature, this will result in a shifting of spectral features and a smearing of any long duration spectral integration when performing pulse height spectroscopy. Another effect is a strong influence of temperature on the SiPM

dark current and noise, also functions of temperature. SIPHRA readout of the SiPM array is triggered when the current signal from the detector surpasses a fixed trigger threshold level. Normally this threshold is set sufficiently above the thermally generated dark current signal, such that any fluctuations contributed by SiPM noise do not trigger SIPHRA readout. In the event that the average dark current surpasses the trigger threshold due to the strong influence of temperature, SIPHRA will enter a state where it is constantly triggering on dark current signal at its maximum rate, saturating the readout bandwidth with noise events. This can be seen when SIPHRAs output is dominated by successive triggers with low ADC value.

While in orbit, GMOD would counter these effects by compensation using temperature reference measurements and adjusting accordingly the bias voltage or SIPHRA configuration to maintain consistent performance. However, due to the GMOD firmware being in an early stage of development, these compensation mechanisms were not implemented for the TVAC testing, thus the thermal effects and their impacts are shown in Figure 5.8. These effects include temperature induced variations on SiPM gain and dark current fluctuation.

To examine the detector performance as a function of temperature without smearing from temperature induced gain shifting, the plot is arranged in time resolved format binned into 5 minute intervals (along the y-axis), chronologically from the top down. The shade intensity represents counts per pixel for each ADC bin of spectral data (along the x-axis), in other words, each slice along the horizontal is a individual spectrum at a given time interval, where the most prominent peaks generated by the ^{232}Th source can be distinguished by their colour intensity without being smeared or obscured by dark count saturation. A PT100 is present on the underside of the SiPM array PCB which is digitised and read out by SIPHRA upon trigger (as discussed in Section 2.1.2). These measurements are also included for reference with a temperature calibration, where again, the shade intensity represents counts per pixel for each ADC bin of PT100 data. From Figure 5.8, it can be seen that the prominent spectral features (the 238 keV line in particular) are shifted down in ADC channels with increase in temperature and up in ADC channels with decrease in temperature. However this continuous shifting of the features is broken by voids across all but the lowest ADC channels, during the rise up to and descent from the hot dwell. At these times the SiPM array has reached such a temperature, that the intensity of the dark current has exceeded the fixed trigger threshold, producing a spectrum saturated with noise events. The instrument then returns to normal operation when the temperature has reduced below $\sim$40–50 °C, showing standard readout as the dark current level descends below the trigger threshold. It should be noted, there are a number of ways to mitigate the effects of these behaviours, which unfortunately could not be incorporated into the MSP430 firmware at the time of these tests. This includes bias voltage compensation (to maintain a constant overvoltage) as well as adjustment of the trigger threshold. This final method, was actually demonstrated during the final half cycle (Phase IX) towards the end of the TVAC testing with some success. Figure 5.8 shows the spectrum during the last hours of the test to be interrupted by saturation only briefly, while the trace of the 232 keV peak is just clear enough to be seen consistently. That said, this is impractical and quite difficult to perform, particularly if intended to be auto-

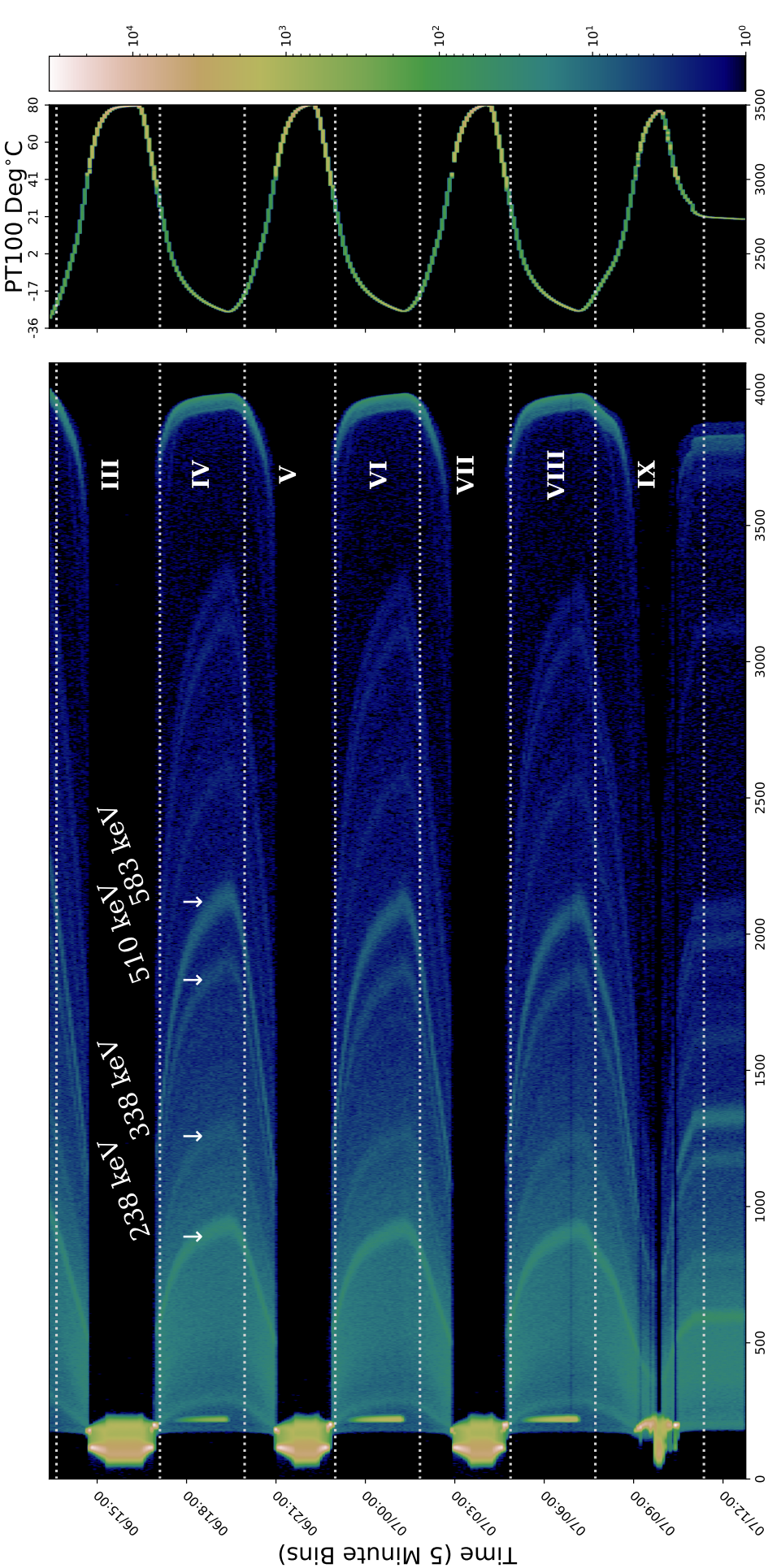

Figure 5.8: The operational cycle spectral measurements in time resolved format obtained during TVAC cycling. Each slice along the horizontal is an individual spectrum, measured over a given time bin interval. The effects of temperature induced gain variation (as described in Section 5.4.4) are apparent, however the required spectral features remain clearly distinguishable, as seen in Figure 5.2 & Figure 5.5. Each phase of the testing has also be labelled as in Figure 5.7, with the SiPM PT100 data included with a calibration applied for temperature reference.

mated while in flight. Certainly this may need to be adjusted during the mission lifetime (for example, due to cumulative irradiation effects on the SiPMs (Ulyanov, Murphy, Mangan, et al. 2020)), however SIPHRA is capable of subtracting the average current before trigger, thus any increase in dark current may be compensated without need of adjusting the threshold level. In the context of the limitations imposed without this being available for the campaign, the instrument performed as expected and was considered to have passed the predefined pass/fail criteria concluding the TVAC campaign.

The thermal effects on the SiPM array overvoltage are the most prominent and clearly observed in Figure 5.8. The effects on the scintillator may be a bit more subtle. Most notably, the scintillation light yield is expected to diminish approximately proportionally with increase in temperature, as reported in Drozdowski et al. 2008. This results in a loss in light signal, again reducing the instrument output gain. The silicon optical pad which is used for optical coupling of the SiPM array and scintillator has an operating range of -40 °C – 70 °C and a minimal expansion coefficient of 3×10^{-4} cm/cm per °C, however it is not known how the refractive index is affected by thermal gradients. It's uncertain what the internal effects of the SIPHRA ASIC are regarding temperature dependence and not much information is provided by IDEAS. Certainly some variation in performance is expected since the device internal references may change with variation in the thermal environment conditions. How this manifests in the instrument performance, and specifically in the thermal vacuum testing and spectra in Figure 5.8 is not clear. However, in the context of this, it should be stressed that the environmental testing simulated the extremes of the operating environment with a large margin applied for qualification. As such, the large thermal gradients, temperature extremes and the corresponding effects that these environmental parameters have on the instrument may in practice contribute less to the performance in orbit than during the ETC.

Other more destructive effects are also possible during environmental testing, even after numerous simulations, however these were not observed in the GMOD subsystem level ETC. Before undertaking environmental testing, it is useful to identify all components which carry a potential risk for damage, one such area noted even at this early stage was the mounting of the detector assembly on the GMOD motherboard PCB, which would later be reconfigured using the GTRB and require a subsystem requalification. Another component which may be susceptible to damage is the scintillator, which houses a fragile $CeBr_3$ crystal within a hermetically sealed aluminium container. If the scintillator had become damaged as a result of the environmental testing (be it through high vibration or the thermal vacuum extremes of the ETC), it would likely be damaged in one of two ways, a cracking of the quartz window or a breaking of the hermetic seal. In either case, the crystal would become exposed to moisture leading to the eventual degradation of performance. If the seal around the window or the encapsulation port is compromised, but the window itself remains intact, degradation of performance may not be instantaneous but instead gradual as the crystal absorbs moisture. This causes the crystal to liquify and become discoloured, reducing its ability to transmit light and thus reducing the signal produced for a given photon received. If the quartz window had become cracked, this will

itself cause a loss of light signal due to the change in the coupling surface and transmissibility of light, while eventually the hydration of the crystal further degrades the performance. This could occur through a physical impact force on the quartz window or by a previous breaking of the housing seal, where the scintillator becomes hydrated and expands within its cavity eventually producing enough outward force to crack the window from within. This is of most concern after environmental testing and during launch in which the instrument is subject to extreme forces, but also during delivery and the waiting period before integration with the launch vehicle, during which a long duration can transpire before any change in instrument performance can be measured.

5.5. Post Environmental Testing

Upon return to Dublin, GMOD was tested one final time to ensure damage had not been sustained during disassembly, reassembly or transport back to UCD. This was also an opportunity to measure the performance using standard calibration sources, in this case ^{22}Na, ^{137}Cs and ^{60}Co which can be more readily used to compare performance as opposed to the ^{232}Th radioisotope found in the welding rods. This test was carried out informally and is considered supplementary to the suite of tests performed for the qualification campaign. The same standards for success were maintained, specifically the criteria that the instrument would function as intended and a spectrum could be successfully measured. The generated spectra indicated favourable performance and a return to nominal operations, with a measured resolution of 4.2% at 662 keV.

Table 5.6: Resolution and ADC channel measurement of peaks from ^{22}Na, ^{137}Cs and ^{60}Co performed at University College Dublin post environmental testing.

Energy (keV)	Resolution (%)	Mean (ADC Channel)
511	4.82 ± 0.02	1229.73 ± 0.11
662	4.21 ± 0.08	1543.48 ± 0.47
1173	2.73 ± 0.15	2525.21 ± 0.99
1274	2.87 ± 0.04	2717.74 ± 0.31
1332	2.58 ± 0.13	2793.11 ± 1.0

5.6. Conclusion

Following the environmental tests described in this chapter and subsequent review by the ESA FYS project team and technical experts, GMOD successfully completed its subsystem level qualification, providing confidence in the instrument's design, construction and performance from launch to operations as a payload onboard EIRSAT-1. The qualification tested GMOD under environmental scenarios which it would need to survive in order to carry out its mission. This testing stressed the instrument based on qualification margins derived from simulations, ECSS standards and in agreement with FYS coordinators. As such, after successful completion of the environmental campaign, the EQM was deemed to have been qualified for launch. While

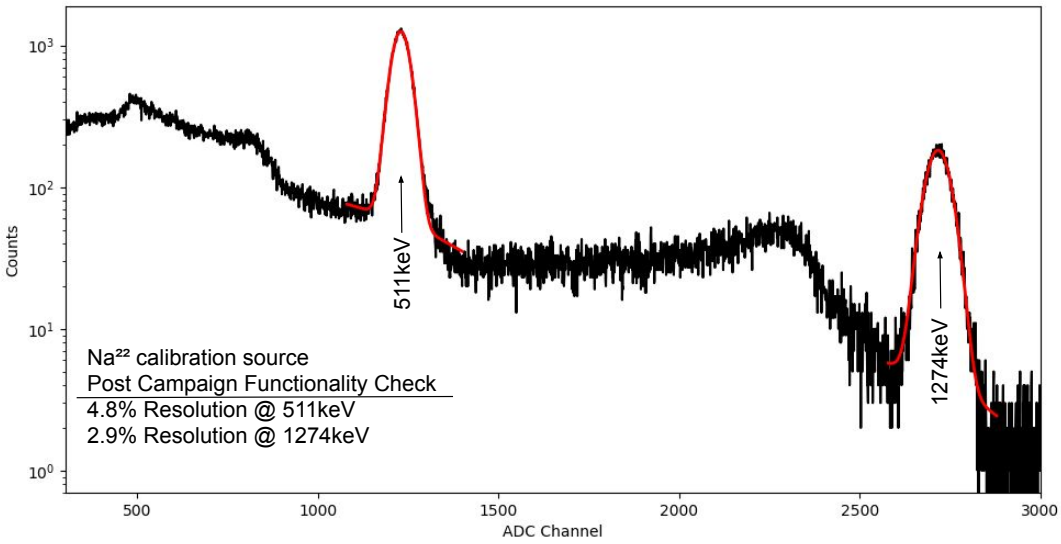

Figure 5.9: The ^{22}Na spectrum taken upon return to Dublin after the environmental campaign completion. The line peaks have been modelled using a composite Gaussian and quadratic function to model the photopeak and background contribution respectively.

the subsystem level qualification had to be repeated due to the change in configuration with the GTRB, that does not negate the success of this campaign as those changes were informed by system level tests which stressed the instrument to a much higher degree (Doyle et al. 2021). The success of this environmental testing, along with other environmental campaigns also meant that we had the confidence to conduct the requalification remotely, in short notice and in quick order to fully qualify the EQM spacecraft.

Regarding the performance of GMOD, the instrument survived the environmental testing and was demonstrated to return to normal operating standards after returning to ambient conditions. This was true for the vibration campaign, which saw a non-conformance and shift after X-axis vibration, and the TVAC campaign which saw the unexpected heat sink behaviour of the $CeBr_3$ scintillator. A number of possible sources of the X-axis vibration shift have been presented in order of most to least likely, none of which pose an issue for the instrument operation or require preventative actions or corrections. Similarly, no corrective actions were deemed necessary regarding the unexpected thermal behaviour of the crystal during the thermal-vacuum testing. The TVAC test in particular tested the instrument's performance far beyond the nominal cycling while in orbit, showing that the instrument could reliably measure gamma-ray spectra up to $\sim$40–50 °C before noise saturation, covering the expected temperature range for normal in-orbit operation. Furthermore, methods to mitigate the effects of temperature dependence have been outlined and will be used while in flight to stabilise the instrument performance. After modifications, including the addition of the GTRB mounting bracket, the GMOD EQM would later be again subsystem level tested and successfully pass its requalification in this new configuration.

Electromagnetic interference (EMC) / electromagnetic compatibility (EMI) testing was not included at system or subsystem level for EIRSAT-1 and at no point was it made mandatory by

ESA FYS to conduct a dedicated campaign of this type. However, ESA FYS do encourage and provide information on how to carry out such a campaign and from our experience this type of test would have been valuable in our early hardware testing. If given a repeat opportunity, EMC/EMI testing would be included early in the EIRSAT-1 testing campaign. Two known cases of EMI related events on EIRSAT-1 have been recorded and investigated. The most recent recorded event was related to radio interference caused by activity of the attitude controlling magnetorquers. The magnetic field generated by the magnetorquers is produced by pulse-width modulation (PWM) switching, whose duty cycle when set to 50 % can produce a signal switched at a frequency of 1 kHz which can become coupled with the spacecraft radio and thus cause interference in communications. An issue like this could potentially have been discovered and addressed earlier if EMC/EMI testing was performed, and for this reason is highly recommended by our team.

Following the discussion of the instrument hardware in Chapter 2 the firmware in Chapter 3 and the hardware development and testing in Chapter 4 and Chapter 5, the firmware testing will be presented in the next chapter, Chapter 6.

Chapter 6

Embedded Firmware Testing

A number of iterations of the GMOD firmware have been developed, including the demonstration version used during the subsystem ETC, the EQM version used during mission tests and the system level ETC, and finally the flight model version used during the FM ETC which is intended for flight. This chapter will discuss the initial baseline testing of the GMOD EQM version of the firmware, leading to the more in depth testing of the FM version. There are many aspects of functionality for which the firmware is responsible, primarily the experiment readout and support. The focus of this chapter is on the ability of the firmware to effectively operate in experiment mode. In particular the testing[1] of the effectiveness of the firmware over a range of fixed trigger rates and simulated rates which mimic the behaviour of a GRB event. This chapter begins with the results of the initial testing for the EQM firmware version, as submitted and presented at the 8th IEEE International Conference on Space Mission Challenges for Information Technology (SMC-IT, July 26–30, 2021) and published in the proceedings (Mangan et al. 2021e). The section continues with a discussion on the testing of the FM version of the firmware, submitted and presented at the SPIE Astronomical + Instrumentation 2022 (17–22 July 2022) and published in the proceedings (Mangan et al. 2022d).

6.1. EQM Firmware Initial Performance Analysis

Initial testing using the EQM version of the firmware, as discussed in Mangan et al. 2021e, indicated that the MSP430 was capable of meeting the requirements of the GMOD instrument in terms of readout and storage, power consumption and data rate handling in the context of GRB detection. The developed firmware must be able to successfully meet the following minimum operating requirements in order to be considered successful:

- Retention of all received TTEs from SIPHRA and the CPLD without loss or corruption.
- Managing trigger rates up to at least $\sim$500 Hz for summed channel data (as this is used for GRB triggering).
- Achieve Low power optimisation with firmware development – power must be less than 181.5 mW (exc. 30% margin) estimated consumption as defined in the spacecraft initial design definition file (DDF) (ECSS 2009b).

[1] Although not presented in detail here, the functional, operation test development, environmental, and mission test campaigns have tested the general functionality of GMOD at system level with respect to bias voltage testing, SIPHRA register configuration, CPLD reprogram and other capabilities ((Walsh et al. 2021; Doyle 2022; Doyle et al. 2022b; Dunwoody et al. 2022c)).

This firmware was tested by externally triggering SIPHRA at a range of fixed trigger rates, intercepting the CPLD output and comparing it against the MSP430 output. This was done in two separate tests, a test where only the summed channel readout was enabled and the other where both the summed and 16 channel readout were enabled. The intention was to investigate the effects of bottlenecking within the MSP430 during high data rates when both 16 channel and summed channel TTE readout was enabled, to determine the trigger rate at which this would begin and to assess how many summed TTEs would be lost as a result. Furthermore, it was expected the power consumption of the MSP430 and GMOD motherboard would increase with both summed and 16 channel readout being processed, as at high data rates the MSP430 is likely being kept in a sustained active state while the flash is being read and written to more often than when just summed channel data is being processed. For this test, it was decided to prioritise the investigation and analysis of summed channel data only, given its higher priority for scientific operations as opposed to 16 channel data, which is only used for health checks and over short durations. As part of the investigation, 16 channel and summed channel readout was processed simultaneously to fully stress the firmware, but it was decided that as only the summed readout would be used for normal operations (light curve, spectra and triggering, see Chapter 3), the analysis would focus on the summed channel data. GMOD is capable of 16 channel readout, but this is reserved for short periods to test SiPM performance or in the event of instrument debugging.

6.1.1. Method

The firmware has been verified by testing the response over a realistic range of input detector trigger frequencies from 50 Hz to 1 kHz for the primary TTE data. The power consumption and ability of the firmware to successfully receive and transmit the packets to the on-board computer was investigated. The experiment demonstrated less than 1% loss of packets up to 1 kHz for the standard transfer mode with the power not exceeding 31 mW. A flow diagram describing the arrangement of hardware and the path of trigger data as it flows through the GMOD motherboard during this test is shown in Figure 6.1.

An external hold input for SIPHRAs track and hold circuit is available, which when asserted, forces a readout which is processed by the CPLD and assigned a fine-timestamp as during normal operation. For this test, the hold signal was generated using the Aim-TTi TG5011 pulse generator, which was configured as a 3.3 V, 25 μs pulse width output, across a frequency range spanning 50 Hz up to 1 kHz. The detector assembly, with the exception of the SIPHRA ASIC, was not needed and was disconnected. A modified version of the CPLD VHDL was used to mirror the serial output to the MSP430 over an easily accessible GPIO pin which could be logged to a PC using an FTDI USB to serial adaptor. GMOD was placed into Experiment Mode and commanded to begin streaming TTE data which was similarly also logged using a second FTDI serial device. It was at this point that the readout configuration was set with streaming enabled (i.e. summed channel readout or both summed and 16 channel readout). During the run, the current draw and voltage of the GMOD motherboard 3.3 V line, supplied by an Aim-

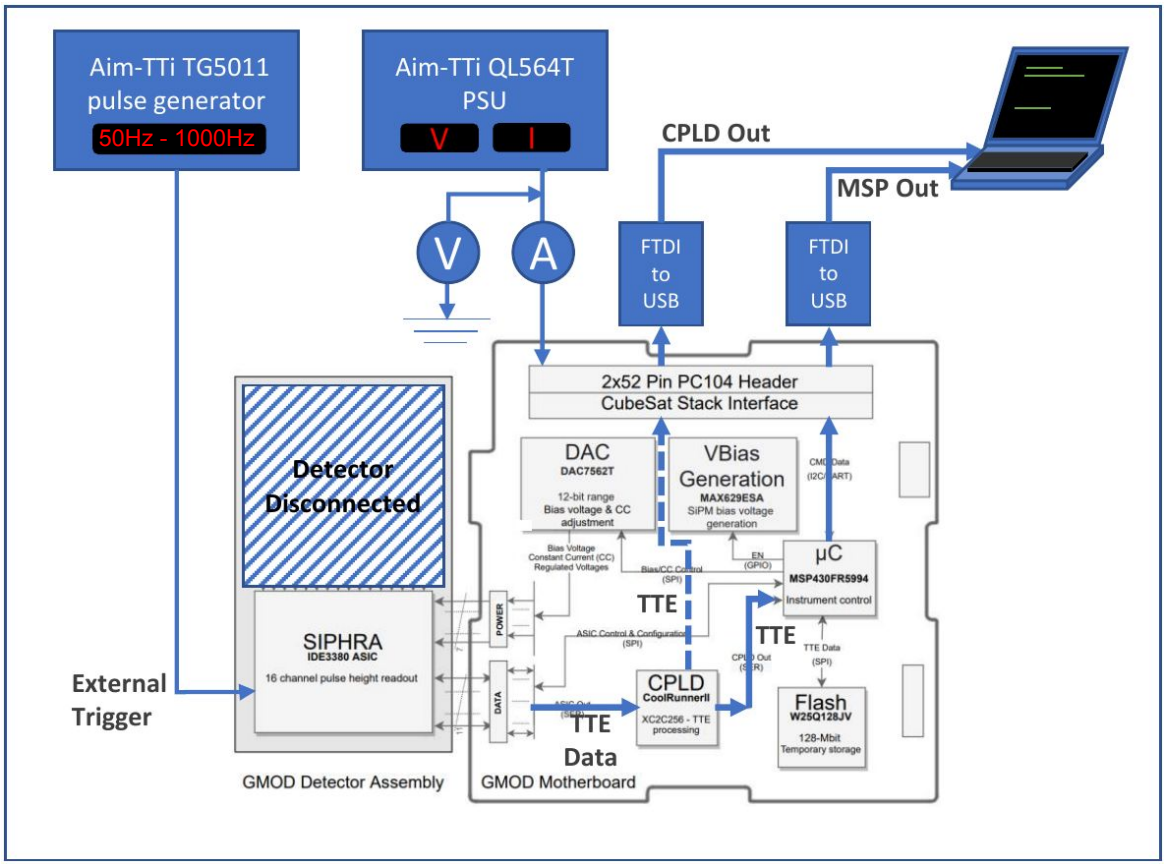

Figure 6.1: A block diagram showing the arrangement of hardware and the path of trigger data as it flows through the GMOD motherboard during the initial testing of the GMOD EQM firmware. The pulse generator is configured to externally trigger SIPHRA at specified rates from 50 Hz – 1000 kHz to force the readout of trigger data and strain test the firmware. The trigger data is used as the basis for the generation of TTEs by the CPLD. The individual TTEs are collected and received over serial by the MSP430, which stores them in external flash, to be retrieved and transmitted to the OBC upon request. For these tests, the CPLD and MSP430 TTE readout is logged and compared to determine the number of TTEs received and transmitted as a measure of the firmware performance and reliability.

TTi QL564T bench top PSU was monitored using a Rigol DM3058 digital multi-meter. The SiPM bias supply was disabled and was not used during this test. The current measurements were sampled 100 times for each run across the frequency range for summed channel only and summed and 16 channel readout cases. The TTE fine-timestamps were used to narrow the range of collected data to a burst of 30 seconds worth of TTEs at a given trigger rate. This was to attempt to simulate a burst from a long GRB, as the mean T_{90} duration for long GRBs, according to the fourth Fermi GBM catalogue is 29.9 seconds (von Kienlin et al. 2020). Each TTE from the CPLD data set was then searched for in the MSP430 received data to confirm that it was successfully processed by the MSP430.

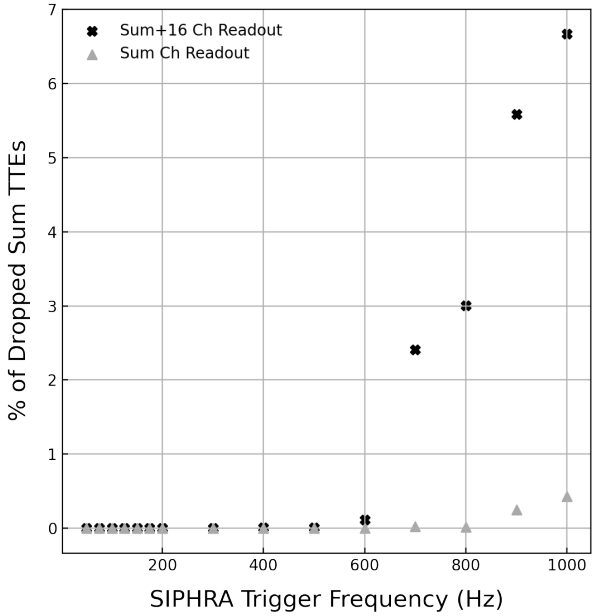

Figure 6.2: The percentage of dropped summed channel TTEs during summed and 16 channel readout and summed only readout, across a range of trigger rates.

6.1.2. Results

The results of this investigation are presented in Figure 6.2 and 6.3. Figure 6.2 shows the percentage number of lost TTEs for both summed channel readout and summed and 16 channel readout, both across the 50–1000 Hz range, in incremented 25 Hz steps below 200 Hz and 100 Hz increments above this range. For both readout configurations, it can seen that the EQM firmware and MSP430 are capable of reliably receiving TTE packets from the CPLD and transmitting them to the OBC without losses up to $\sim$600 Hz. This is well above the $\sim$120 Hz trigger rate expected for a 10 σ significance trigger and the 500 Hz requirement. This suggests that the firmware concept and MSP430 will be capable of reliably processing TTE data from the vast majority of GRBs without losses, even those few well above 10 σ significance. Above 600 Hz, the percentage of lost TTEs begins to increase, showing a large difference between dropped TTEs for both readout configurations. As expected, when summed channel readout is selected with 16 channel readout, more TTEs are dropped as compared to the summed only configuration. This is because of the large quantity of data received especially for summed and 16 channel readout. It is expected that at high data rates, the receive-side buffers will overflow, at these times new TTEs will not be received from the CPLD and will be lost, prioritising already received data and its storage into external flash. The MSP430 may also be in a state in which it cannot react to the reception of serial data from the CPLD, in these cases, it is possible for the ASM bytes to not be read and the TTE cannot be received. As 16 channel and summed channel readout is only used sparingly for health checks and for short durations, operation with low losses up to 600 Hz is acceptable. The MSP430 still shows good performance even at high trigger rates, particularly the summed channel configuration which is consistently below a fraction of a percent, even up to 1000 Hz.

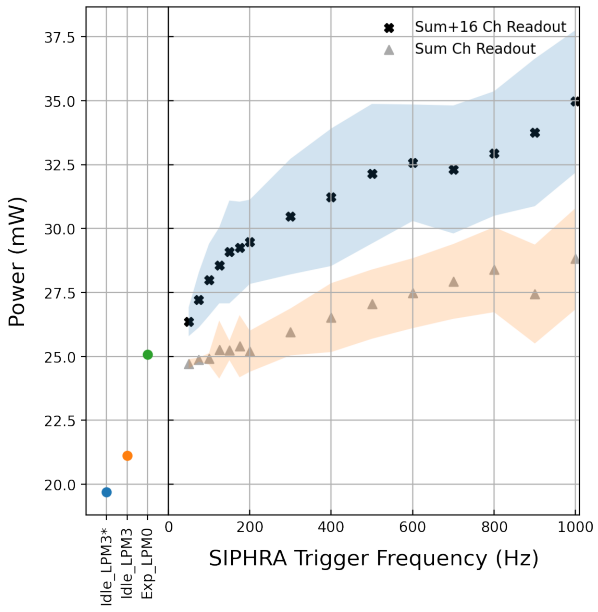

Figure 6.3: The power consumption derived from current measurements on the 3.3 V line during testing. The fill region is the standard deviation calculated from 100 current measurements. The left hand panel shows the power consumption for Idle mode (IDLE_LPM3*) before configuring, Idle mode (IDLE_LPM3) after configuration and finally, Experiment mode (Exp_LPM0) before external triggering.

Figure 6.3 shows the power consumption from the 3.3 V line on the GMOD motherboard for the same range of trigger frequencies. The left hand panel shows the power consumption when GMOD is in Idle mode (IDLE_LPM3*) before the instrument configuration and just after programming, Idle mode (IDLE_LPM3) after configuration and finally Experiment mode (EXP_LPM0) before external triggering has begun. This highlights the use of LPM states as being advantageous, particularly on CubeSat missions where good power management is a must. As expected, summed and 16 channel readout together consume more power, increasing as a function of trigger frequency. In both cases the power consumption is less than the original estimate of 181.5 mW as defined in the DDF. It is interesting to note that the curves both have a set of breaks around trigger frequencies which have been seen in past testing to be the points when the MSP430 streaming buffers overflow and servicing from flash begins. The summed channel streaming buffer was seen to overflow ∼600-700 Hz – a break can be seen in both curves around this range. For the summed and 16 channel configuration, a break is also seen around 200 Hz – previously the 16 channel streaming buffer was seen to overflow ∼200 Hz. This is somewhat unexpected, the reason why these notches appear is not yet known and needs further investigation.

6.1.3. Conclusion

There are a number of caveats and limitations to these initial tests. Firstly, as a fixed duration of 30 seconds of TTE data is being selected across a number of trigger rates, there will be a dissimilar number of TTE samples for each trigger rate data point. Secondly, the use of a

pulse generator which triggers SIPHRA readout at a fixed period is not fully representative of a realistic scenario and does not account for TTEs which have been successively triggered by gamma-ray interactions. During testing, it has been noticed that with the current firmware, the MSP430 has a maximum "dead time" of around 15 μs which is caused by receive-side pointer setup; after receiving a TTE from the CPLD, it is likely that any subsequent TTE whose ASM is received within this 15 μs window will not be registered and will be lost. Thirdly, as the SiPM array and scintillator were not used for this test, the current measurements used to calculate the power consumption exclude any contributions from the bias generation circuit. It is also difficult to isolate the current draw of the MSP430 from the rest of the circuits of the motherboard on the 3.3 V line, circuits whose power consumption may be a function of trigger rate and TTE throughput. Finally, at the time of testing, the CRC and coarse-timestamp were not included in the EQM firmware, an exclusion which may have an influence on TTE throughput to the external flash memory.

6.2. FM Firmware Hardware-In-The-Loop Testing

Initial testing presented in Section 6.1 and in Mangan et al. 2021e indicated that the EQM firmware design was viable and satisfied the broad requirements for the mission. To further qualify the firmware under realistic conditions and to address the caveats and limitations described in the previous test, the readout performance was examined using a HITL simulation of a sample of GRB detections on GMOD using data from the Fermi Space Telescope GBM GRB catalogue. This further quantifies the performance of the firmware in a more realistic operational mode, by accurately simulating the rates expected by GMOD during detection of GRBs and measures performance by comparing the expected output to the actual instrument output. This is done by externally triggering the detector readout to mimic the expected rates for a range of GRB profiles and expected fluxes derived from the 4th Fermi GRB catalogue across a sample of 40 GRBs spanning a range of peak fluxes and durations. The contents of this section are derived from Mangan et al. 2022d.

In order to correctly measure the number and impact of dropped TTEs by the MSP430 firmware, testing was required which would accurately stress the firmware as expected during in flight operation. The previous tests (Mangan et al. 2021e) measured this to a degree by forcing external triggering of the SIPHRA ASIC using a pulse generator set at a range of fixed trigger rates from 50 Hz to 200 Hz in steps of 25 Hz, and up to 1 kHz in steps of 100 Hz. The results proved that the firmware design was capable of meeting the broad requirements for reliable instrument operation. However this initial assessment was limited, as it did not provide information on the effects of dropped TTEs on integrated light curves, nor did it allow any dynamic variation during the trigger rate testing as would be expected during a GRB event. Additionally, the means of testing did not fully stress the MSP430 firmware or its serial readout capability. Externally triggering the detector readout at a fixed rate provides a static period of time between each TTE. This is problematic as the detection of individual gamma-ray photons does not occur at fixed intervals but is instead stochastic and random in nature, resulting in an inaccurate representa-

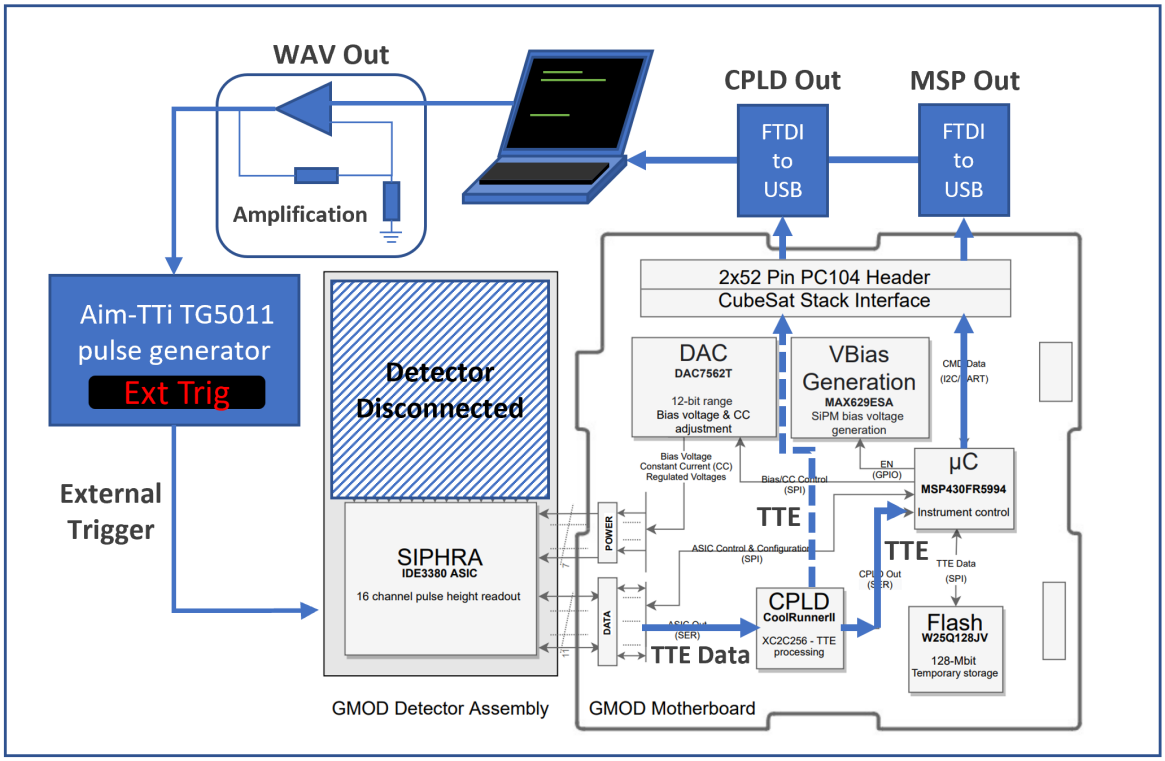

Figure 6.4: The block diagram of the MSP430 firmware testing, showing the path of trigger data as it flows through the GMOD motherboard readout system. The Waveform Audio (WAV) file contents are output using a laptop soundcard and amplified, such that it can trigger the output of a pulse generator. The pulse generator is configured to externally trigger SIPHRA and force the readout of trigger data. The trigger data is used as the basis for the generation of TTEs by the CPLD. The individual TTEs are collected and received over serial by the MSP430, which stores them in external flash, to be retrieved and transmitted to the OBC upon request. For these tests, the CPLD and MSP430 TTE readout is logged and compared to determine the number of TTEs received and transmitted as a measure of the firmware performance and reliability. Not shown here is the logic analyser sampling of the soundcard, pulse generator and SIPHRA output data.

tion of the expected instrument operation. This does not stress the firmware to a realistic degree either, as these static periods make it impossible to simulate the reception of packets arriving in close succession of time at low trigger rates, while also allowing a window of respite with which the firmware operations of reception, storage and transmission of data can recover.

Therefore, the only way to fully stress and ensure the firmware design reliability is to monitor the performance during detection of a simulated GRB event. To achieve this, it is necessary to script the timing of individual external SIPHRA triggers on the μs scale, such that the rate is dynamic and representative of the expected characteristics of a GRB event. This requires a list of timestamps which mimic the random arrival time of gamma-ray photons from a GRB event, a method of scripting these triggers and a means of physically triggering at these times with adequate enough precision to generate TTEs that simulate a GRB event. TTE timestamps were sourced from actual GRB detections by the Fermi Space Telescope GBM (Meegan et al.

2009) instrument and scaled to the expected rate from an equivalent detection by the GMOD detector. Pulses were encoded into WAV audio files at samples according to the photon arrival times from the scaled GRB data. Once these WAV files were played back, the soundcard output would produce electronic pulses at the respective trigger times which could be used to externally trigger SIPHRA and simulate readout of a GRB event. During these simulations, each stage of the summed channel TTE readout was recorded allowing a comprehensive assessment of the performance of GMOD and the instrument firmware. A block diagram describing the layout of the experiment, WAV file output triggering and the flow of TTE data during the experiment is shown in Figure 6.4.

6.2.1. Fermi GBM TTE Data Selection

GRB trigger data from the Fermi GBM Gamma-Ray Burst Catalogue (von Kienlin et al. 2020) was used as the source for the TTE data. Over the ten year period between 12^{th} July 2008 – 11^{th} July 2018, GBM detected 2356 triggers classified as GRBs triggering roughly twice per day. As of the time of writing, there were ∼3300 GRBs in the GBM catalogue. The GBM burst catalogue[1]provides results for location, spectral and duration analysis of all GBM triggers classified as GRB events. For individual bursts, the GBM Instrument Operations Center (GIOC) generate a set of burst data product files accessible over File Transfer Protocol (FTP) from the The Fermi Science Support Center (FSSC). This includes GRB TTE data for the GBM instrument consisting of time and energy information for individual photon events, with at least one TTE file per detector. Each TTE file contains data collected over the burst period, stored in a Flexible Image Transport System (FITS) file format. The 12 individual GBM NaI(Tl) detectors (Meegan et al. 2009), which form the low-energy (8 keV – 1 MeV) portion of the monitor energy regime are the most comparable to GMOD and most simple to scale to mimic an equivalent GMOD GRB detection.

$$F = \frac{\sigma\sqrt{Bt_{bin}}}{A_{GRB\,GMOD}t_{bin}} = \frac{7 \times \sqrt{50 \times 1.024}}{9 \times 1.024} = 5.4\,ph/cm^2/s \tag{6.1}$$

A sample of 40 GRB triggers were selected from the burst catalogue. The full GRB sample list is presented in Table 6.1 along with the broad results from this study. To ensure that only GRBs which could be triggered by GMOD would be included in the sample, a minimum 1024 ms average peak flux threshold of 5.4 ph/cm^2/s in the 50 keV – 300 keV energy range was chosen. This corresponds to a minimum trigger significance of $\sim 7\,\sigma$ on GMOD assuming a nominal background rate of 50 Hz and an approximate GMOD average all–sky effective area (Murphy et al. 2021a) of ∼9 cm^2, per Equation (6.1). Once the catalogue was filtered using this minimum peak flux threshold, all remaining short duration triggers ($T_{90} \leq 2$ s) were included in the final GRB sample. Long duration ($T_{90} > 2$ s) triggers were selected at semi-equally spaced intervals in ascending 1024 ms average peak flux within the 50 keV – 300 keV energy range until a sample of 40 GRB events was created.

[1] FERMIGBRST - Fermi GBM Burst Catalog

6.2.2. Deriving the GMOD/GBM Scale Factor

The scaling process involves downscaling the number of detected TTEs in the GBM TTE file to the expected rates and energy range for an equivalent detection by GMOD. This involves randomly selecting events from the original GBM TTE file using a scale factor which represents an approximation of the ratio between the GMOD:GBM effective area for a GRB (Murphy et al. 2021a). The scale factor was derived by comparing the number of counts detected by GBM to the number of counts which would have been detected by GMOD. This was calculated for a selection of 87 of the brightest GBM triggers in the burst catalogue using the Fermi GBM Data Tools (Goldstein et al. 2022)[1]application programming interface (API) in Python V3.8.10.

For each of the listed bright triggers, the NaI(Tl) detector with the greatest number of counts in the 1024 ms average peak flux interval was found. The corresponding TTE file was then integrated into a 1024 ms binned light curve and a simple background estimation was performed using a 1^{st} order polynomial fitting around the main burst emission time, as shown in Figure 6.5 for GRB130504978[2](pre–burst & post–burst intervals were selected from the catalogue). The number of counts detected by GBM in the 1024 ms average peak flux interval, between 50 keV–300 keV was then calculated. Initially 100 triggers were selected for this calculation, however a list of 12 triggers were omitted from the analysis due to unusual burst profile or due to poor automated background subtraction. A minimum threshold of 1000 counts in the peak flux interval was then set for the GBM number of counts to filter out any triggers which had unexpectedly low signal attributed to incorrect background modelling, removing another trigger from the list.

The estimated equivalent number of counts which GMOD would have detected for this GRB, within the same parameters, was then calculated as expressed in Equation (6.2):

$$\begin{aligned} R =& \frac{N_{signal\ counts\ GMOD}(50-300keV)}{N_{signal\ counts\ GBM}(50-300keV)} \\ =& \frac{Flux\ BATSE\ 1024(ph/cm^2/s) \times A_{GRB\ GMOD}(cm^2) \times t_{bin}(s)}{N_{signal\ counts\ GBM}(50-300keV)} \end{aligned} \tag{6.2}$$

where $Flux\ BATSE\ 1024(ph/cm^2/s)$ is the 1024 ms averaged peak flux in the 50 keV – 300 keV energy range as reported by the Fermi GBM burst catalogue, $A_{GRB\ GMOD}(cm^2)$ is the all–sky averaged effective area of GMOD (Murphy et al. 2021a) for a standard GRB event (modelled using a Band Model (Band et al. 1993a) with spectral parameters α = 1.1, β = -2.3, E_{peak} = 300 keV, as discussed in (Murphy et al. 2021a)), $t_{bin}(s)$ is the interval of each time bin. The mean scale factor from the list of 87 bright GRBs was then calculated to be $R \sim 0.085$.

[1]GBM Data Tools

[2]GCN 14583 - GRB130504C - 13/05/05 23:54:40GMT

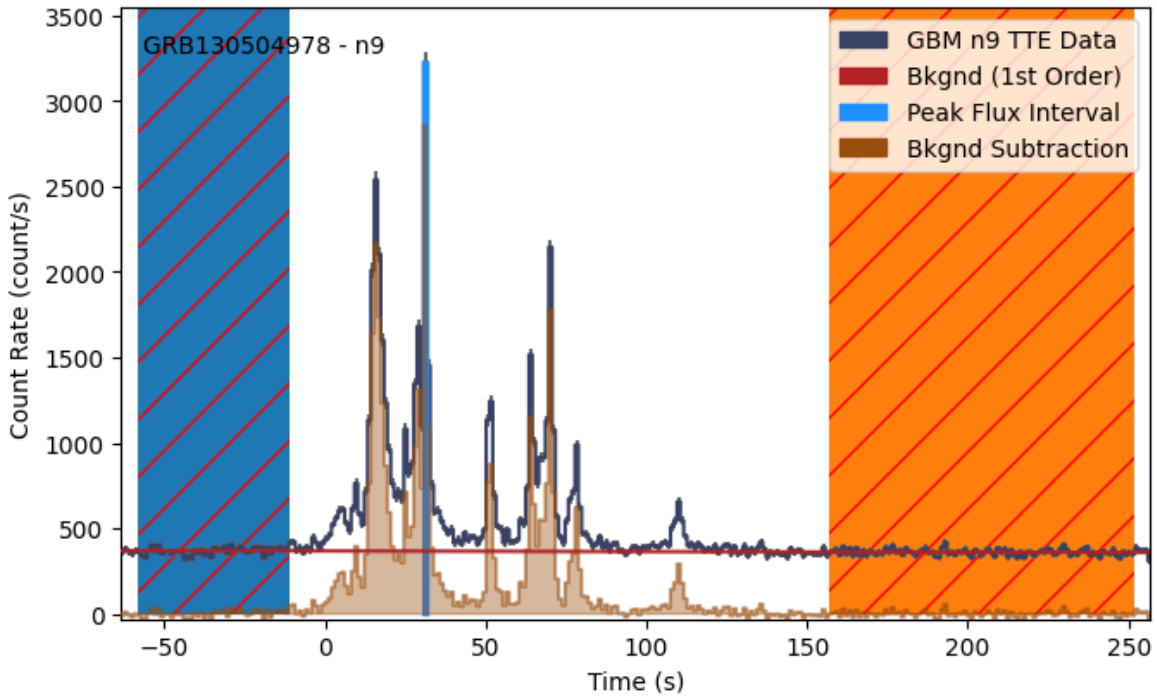

Figure 6.5: An example of the background estimation and subtraction for GRB130504978 NaI–9. A 1^{st} order polynomial was used to estimate the background, while the pre–burst and post–burst intervals were derived from the GBM burst catalogue (indicated by hatched blue and orange highlights). The 1024 ms average peak flux interval bin selection is also shown.

6.2.3. Downscaling GBM TTE Files

Using this scale factor, each of the 40 GRBs from the sample were then scaled down to what would be expected from an equivalent detection by GMOD. First the TTE file was selected by determining which of the 12 GBM detectors had the second most number of counts in the 1024 ms peak flux interval in an attempt to better approximate the geometry of GMOD. If only one detector from the 12 was found to be suitable, this one was selected. A minimum energy threshold was then applied to the chosen TTE data file to match GMOD's energy range. As mentioned previously, each NaI(Tl) detector has an energy range of 8 keV – 1 MeV, while GMOD is closer to ∼30 keV – 2 MeV (Murphy et al. 2022). An energy range of ∼30 keV – 900 keV was selected to match GMODs energy minimum threshold and to exclude contributions from the NaI(Tl) overflow channels. To reduce the amount of file storage required, each TTE file was then trimmed to include all pre–burst and up to 300 s worth of post–burst data.

$$N_{Scaled\,TTEs} = N_{TTEs}(30 - 900\,keV) \times R \tag{6.3}$$

The remaining TTEs in each file were then loaded into an array with unique indexing for each TTE. The number of TTEs to scale down to was then calculated, as in Equation (6.3), where finally a non-repetitive random sampling of up to $N\ Scaled\ TTEs$ from the TTE array was used to generate the scaled TTE list. This list was then integrated into a 1024 ms binned light

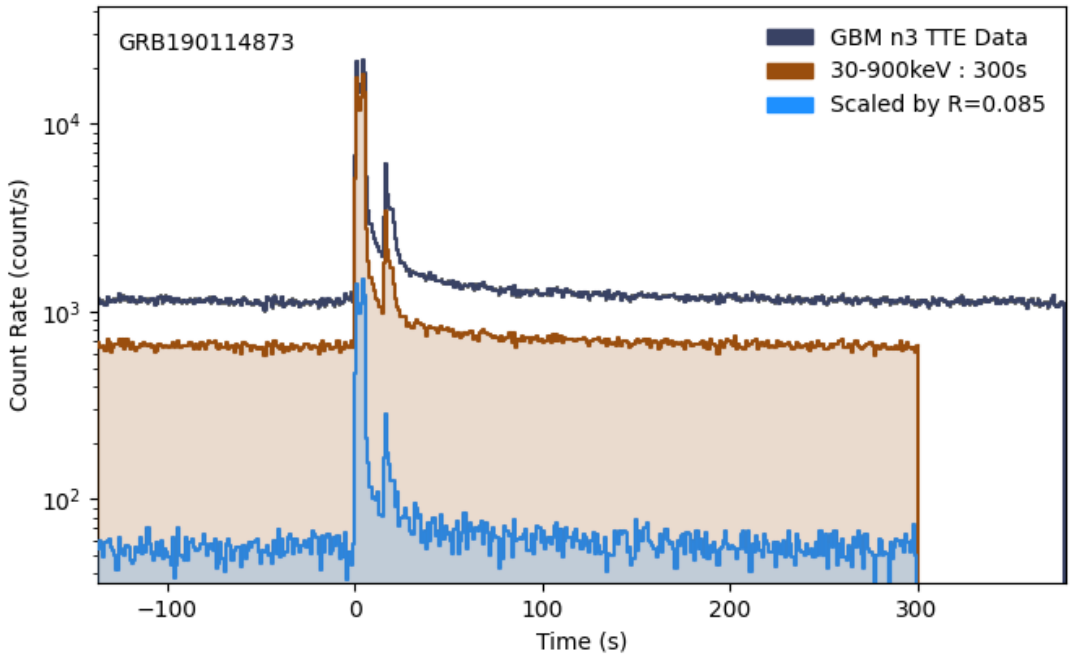

Figure 6.6: An example of the GMOD scaling process for GBM trigger GRB190114873 (detector NaI–3). The TTE file was integrated into 1024 ms binned light curves, showing the original TTE file, energy and time ranged TTE file and finally the scaled TTE file. As can be seen, the broad features of the light curve are maintained across each step of the scaling process.

curve for visual inspection and comparison while the raw TTE data was stored in a FITS format file. An example of the scaling process for GRB190114873[1]is demonstrated in Figure 6.6 which shows the original NaI(Tl) TTE file with an overlay of the application of the energy and time ranging and finally the TTE scaling. This was performed for all 40 of the GRBs in the sample list.

6.2.4. WAV File Generation

The scaled sample of 40 GRBs was used to determine the timing for the external triggering of SIPHRA to simulate detection of a GRB event. As mentioned previously, this provides a realistic representation of the triggering characteristics expected during in–orbit operation. It is then necessary to be able to reliably trigger SIPHRA at the relative photon arrival times for each TTE, with a reasonable standard of time precision such that the characteristics of the scaled TTE files are preserved. It is possible to output timed pulses from a computer soundcard by encoding the individual pulse start time and pulse width as a series of step functions within the bitstream of a WAV audio file. These WAV files can then be used to script the timing of individual external trigger pulses. This method was used in this study to externally trigger SIPHRA according to the scaled TTE timestamps, allowing a simulation of GRB readout. To ensure a standardised pulse profile was presented to SIPHRA and to protect the detector hardware, a pulse generator was used as a buffer between the soundcard output and SIPHRA, such that the soundcard would

[1]GCN 23707 - GRB190114C - 19/01/15 05:59:42GMT

externally trigger the pulse generator and the pulse generator would externally trigger SIPHRA.

The WAV file standard (Microsoft/IBM 1991) is an uncompressed lossless audio format using pulse code modulation (PCM) (Bhagyaveni et al. 2016) for converting continuous signals to discrete digital signals by sampling at fixed intervals (sample periods) and encoding the quantised information into a time series bitstream. The WAV standard supports a range of sample rates, for instance in audio recordings 44.1 kHz is typically used as this best matches the frequency range of human hearing (20 Hz – 20 kHz), roughly twice the maximum required such that the Nyquist frequency, the limiting frequency before aliasing artefacts are introduced, resides just above the highest frequency of audible perception.

In a similar way to ensure that the trigger pulse output from the soundcard could successfully produce the desired pulse shape (a minimum duration rising edge, smooth and flat plateau and minimum duration falling edge) as much frequency content would need to be encoded in the WAV files as possible for each TTE pulse. This required using an ultrasonic sample rate for the sampling to make sure that the desired square wave profile could be produced, while accounting for transition edge ringing due to the inevitable effects of a finite bandwidth by allowing for sufficiently long pulse widths per TTE pulse. Furthermore, since the scaled TTE timestamps are continuous, the placement of the pulse start time will need to be mapped to a discrete range of time values, thus the higher the sample rates, the more samples per second and the greater the time precision available for pulse placement. By consequence it also means more data to store and greater WAV file sizes.

A sample rate of 384 kHz was selected as this allowed a maximum precision of $\pm 2.6\,\mu$s in the mapping of trigger pulses with respect to the scaled TTE file data. The WAV files were chosen to have a bit depth of 8 bits, where each sample amplitude would be represented by a single (mono-channel) 8-bit unsigned integer. This configuration reduces the file size, as only a single channel digital pulse, from logic low to logic high is needed from the soundcard output. In this configuration the bit rate is 3072 kbps – conservatively assuming each GBM TTE file is $\sim$600 s in duration before scaling, each corresponding WAV file would amount to $\sim$1843.2 Mbits or 230.4 MB, excluding WAV header information. A full collection of 40 short and long GRB WAV files would then be approximately 9 GB.

According to the GBM trigger catalogue (von Kienlin et al. 2020), the mean T_{90} duration[1] for long GRB events ($T_{90} > 2$ s) is $\sim$29.9 s. In an attempt to minimise the file storage capacity required, each scaled TTE file was trimmed (as per Section 6.2.3) to include all pre–burst data and up to 300 s of post–burst data. This results in smaller WAV files, between 115.2 MB – 211.2 MB with a total collection of 40 GRBs amounting to between 4.6 GB – 8.5 GB (assuming a maximum pre-burst duration of $\sim$250 s). In practice this was closer to $\sim$6.5 GB. Retaining some pre/post–burst background was necessary to fully test the GMOD firmware as TTE data passing through the MSP430 before and after the sudden rate change associated with the burst event would fully strain the firmware operation of reception, external flash storage and TTE

streaming.

The generation of the WAV files from scaled TTE files is as follows: given a scaled TTE file of example duration 400 s, an array containing byte elements is created whose length is $384000\,Hz \times 400\,s = 153.6\,MB$. Each byte element corresponds to a voltage output at a given sample time where the voltage polarity is indicated by the value of the most significant bit for each byte. Negative voltages are encoded using a most significant bit of 0 (0x00 (- V) – 0x80 (0 V)) while positive voltages have a most significant bit of 1 (0x80 (0 V) – 0xFF (+ V)). Each byte is initialised with a value of 0x80, corresponding to 0 V output from the soundcard. Each TTE timestamp in the scaled file is then re-referenced in time from the first timestamp in the series and rounded to the nearest μs. The pulse start time and the corresponding byte index in the array with which to insert the pulse start is then determined by dividing the TTE timestamp by the sample period (as each sample in the array occurs at a multiple of 2.6 μs). This returns the array index which is rounded to the nearest whole integer and is used as the index of the start of the pulse. The following $N = 30$ samples are then reassigned as 0xFF, corresponding to a + V pulse output at those sample times, where $N/384000 = 78\,\mu$s, the pulse width duration. Finally, once all TTE timestamps have been embedded into the array as pulses, the timestamps are offset by +10 s and a sequence of synchronisation pulses which occur at fixed and predictable times are inserted. These synchronisation pulses generate TTEs at known timestamps, allowing identification of the start of the trigger data. At this point the WAV file is generated using the Python scipy.io.wavfile module[1]. A visualisation of the generated WAV file is presented in Figure 6.7, which shows the waveform display for GRB190114873.

6.2.5. External SIPHRA Triggering and Timing

There are four components in the signal chain when triggering SIPHRA: the soundcard output pulse, the pulse signal amplification, the pulse generator triggering and the SIPHRA triggering and readout. Each of these stages add some amount of time delay which is accrued and propagates from the soundcard output up to the SIPHRA external trigger input. This inaccuracy is expected and acceptable, provided there is minimal impact on the trigger timing characteristics as evident by the resulting integrated light curve.

Soundcard Output:

Even before playback of the WAV file data, there are a number of contributions to imprecision in the timing of the soundcard pulse output. When generating the WAV file, each TTE timestamp is rounded to the nearest μs and then mapped to a discrete time series where each sample is separated by a period of 2.6 μs. There may even be some additional delay added by the soundcard itself through buffering and other latency contributions. Furthermore, the finite bandwidth of the soundcard output adds ringing artefacts before and after the rising edge of the pulse as well

[1] A common method of measuring the duration of a GRB is the T_{90} method, which measures the interval between collection of 5% of the maximum fluence up to the collection of 95% of maximum fluence over the source emission.

[1] SciPy

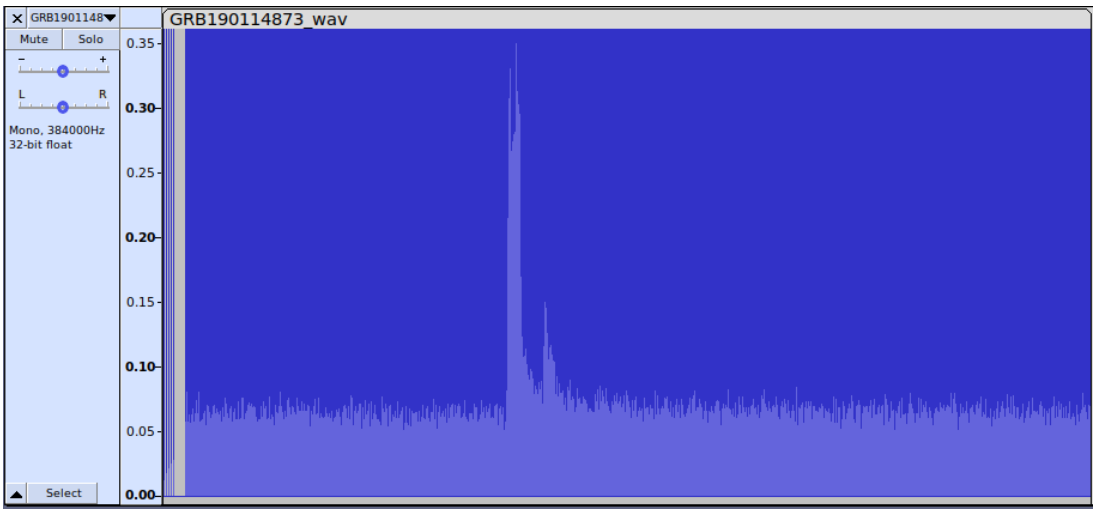

Figure 6.7: The WAV file waveform for GRB190114873 as viewed using the Audacity audio editing software. The GRB light curve is visible though the density of pulses as the average root mean square (RMS) for grouped sets of samples. This is as opposed to the pulse amplitudes contributing to the apparent light curve shape, as all have equivalent magnitudes of 0xFF. The effect of this is particularly visible for the burst interval showing a similar light curve to that in Figure 6.6. The 10 s offset and insertion of the synchronisation pulses can be seen on the left most side of the waveform plot.

as reducing the rate of output slew. The pulse width of the soundcard output was configured for this reason to be 78 μs long, as this was as wide as it could comfortably be set before the SIPHRA summed channel readout duration of $\sim$150 μs had elapsed. This gives a maximum pulse high duration minimising the effects of ringing, while allowing the soundcard output to slew back below the Transistor–Transistor Logic (TTL) logic low state before SIPHRA readout completes. The significance of this last point is that it allows SIPHRA to be triggered as soon as possible after completing readout of the previous trigger. In the case of consecutive TTEs which occur within 78 μs of each other or within the duration for complete SIPHRA readout, the trigger pulses in the WAV file are allowed to overlap but may not necessarily successfully trigger SIPHRA, as this is something which is possible in standard operation.

Amplified Output:

Given the limitation of the soundcard output amplitude and pulse consistency, a simple non-inverting op-amp circuit was built to ensure reliable triggering of the pulse generator. As will be discussed, the minimum requirements to externally trigger the pulse generator are relatively generous, thus a greater reliability could be gained by simply amplifying the soundcard output. A generic 741 op-amp was selected and supplied +5 V to the positive terminal and 0 V to the negative terminal, effectively clamping the circuit output within these rails. A non-inverting feedback circuit was implemented with a gain of $\sim$2.5, driving the amplitude at a maximum up to $\sim$5 VDC when given a maximum +1.8 – 2 VDC pulse input. Note: as the 741 op-amp does not support rail–to–rail operation, the circuit output may never fully reach +5 V during a pulse input, however the intention was simply to surpass +3.3 V at a minimum since the pulse

generator can be triggered on a TTL rising edge above +0.8 V. There may be some delay effects imparted by the slew rate of the op-amp however this contribution is likely negligible.

Pulse Generator Triggering:
The output of the op-amp is simply an amplified version of the soundcard pulse which produces a pulse which is not totally consistent. To protect the detector hardware and ensure a consistent reliable pulse profile is presented to SIPHRA, an Aim-TTi TG5011[1]pulse generator was used as a buffer between the soundcard and the detector electronics. The pulse generator output is capable of being externally triggered using a BNC terminated TTL input within a range of ± 10 V by a configurable positive or negative rising edge. Therefore, so long as the soundcard pulse remains above TTL level high, the pulse generator will not output another pulse, preventing unintentional re-triggering. In this case the positive rising edge trigger mode was selected while the output was set as a 25 μs wide +3.3 V pulse - it is this pulse which would be used to trigger SIPHRA readout. The external trigger of the pulse generator has a latency of $\sim$2 μs before a rising edge is produced.

SIPHRA Triggering and Readout:
Once a rising edge is presented to the SIPHRA external input a pulse height measurement is made on the integrated and shaped signals from the SiPM inputs. Summed channel data (consisting of the summed signals from the SiPM array plus the PT100 temperature sensor data) are the primary science product of GMOD. For this reason only summed channel data is analysed during this test. The readout duration for summed channel and PT100 readout is $\sim$150 μs (from the start of the external trigger input to the first start bit in the SIPHRA readout ($\sim$50 μs), to the completion of readout $\sim$100 μs), during which time triggering is disabled. Only once full readout is completed can SIPHRA be re-triggered. As external triggering forces readout of SIPHRA, the energy information for each TTE can be disregarded as at the time the SiPM bias supply and internal triggering was disabled. Furthermore, the performance of GMOD is independent of the energy and other packed information, but is totally dependent on the rate of TTE data which is being simulated in this test.

6.2.6. Test Setup Configuration

For this test a flight equivalent GMOD motherboard was used and programmed with the latest flight model firmware, V2.0.1. The CPLD was programmed with a debug version of its implementation, which is equivalent in all aspects except that it provides dual output of the generated TTE packets: a standard output to the GMOD serial input and a secondary debug output over the unused PPS input. In this way both the CPLD and MSP430 output were accessible for logging.

The full detector assembly was not necessary for these tests as triggering SIPHRA readout only requires SIPHRA, however for additional spectral integration tests a version of the detector consisting of the demonstration SiPM array coupled to a $CeBr_3$ scintillator was used. During experiment operation, SIPHRA was configured for standard operation and GMOD set to stream

[1] Aim TTI TG251xA/501xA Series

summed TTE data. To prevent readout of internal SIPHRA triggers (which are generated by gamma-ray events) the bias voltage and internal triggering was disabled. To readout the summed channel data from both the MSP430 and the CPLD, a pair of FTDI to USB serial adaptors were connected to the GMOD serial interface and the PPS input pin, repurposed in this test for CPLD readout. For readout and control of GMOD during these tests a series of scripts were written which would provide complete access to command GMOD and to record the serial data output from the MSP430 and CPLD. The control script would interface with GMOD over I^2C using a Total Phase I^2C/SPI Aardvark adaptor[1].

The pulse generator was connected to the SIPHRA external trigger input and configured to be externally triggered to produce a pulse output of width 25 μs and amplitude +3.3 V. The soundcard amplification circuit input was connected to the computer audio out using a standard 3.5mm headphone jack while the amp output was connected to the pulse generator external trigger over BNC cable. To ensure the complete transition of data was traceable from the soundcard to the MSP430, a Saleae Logic 8 logic analyser[2]was connected to the soundcard amplified output, and the pulse generator. During processing of the received data, the start time of the logic analyser recording would be synchronised with the CPLD/MSP430 TTE data using the identifiable synchronisation pulses. Each of the 40 GRBs from the sample were then played in sequence until the TTE data streaming from GMOD was complete. The MSP430 firmware only allows streaming of complete pages (i.e. 31 summed channel TTEs). Due to this, the final page may not be readout during the testing and up to 31 of the final TTEs, consisting of background, may be excluded from the analysis and the calculation of the percentage of dropped TTEs.

6.2.7. Results

The GMOD output from the MSP430 and the CPLD could be readily binned into a light curve and inspected, as these are TTE data products. However, the ultimate aim of the testing was to determine how reliable the MSP430 firmware is at performing its duties and to determine what response, if any, the firmware has on the resulting light curve. For this, it was necessary to compare the collected TTE data before and after each stage, as TTEs propagate throughout GMOD from SIPHRA triggering, the generation of TTEs by the CPLD and the reception, storage and transmission of pages by the MSP430. As discussed in Section 6.2.5, the TTE energy information is not analysed here as SIPHRA was being manually triggered during these tests. However, the successful identification of collected and transmitted TTEs imply that if the energy information was collected and based on internal triggers, the greater the number of successfully received TTEs the better preserved the spectral data would be.

The data collected from the pulse generator and SIPHRA were also integrated into a light curve. Timing information is not provided by SIPHRA and is not available from the output of the pulse generator, this is the responsibility of the CPLD. However, the logic analyser provides timestamps per data point sample and relative timing with respect to the synchronisation pulses,

[1] TotalPhase Aardvark I2C/SPI Host Adapter
[2] Saleae Logic 8

as described in Section 6.2.4, is possible. Each instance of the SIPHRA readout preceded by a pulse generator rising edge (indicating a generated trigger) was matched and both were applied their respective timestamps referenced from the start of the synchronisation pulses and their corresponding sample time. Similarly the equivalent synchronisation pulses were identified in the CPLD and MSP430 TTE data and were used to synchronise the start of the TTE data to the start of the SIPHRA readout and pulse generator data. Finally the original scaled data file, which contains the same synchronisation pulses could also be synchronised to the collected data. Since the scaled data file is referenced from the burst trigger time all of the collected data could then be referenced in seconds from T_0, the start of the trigger. An example of this is shown in Figure 6.8, as 1024 ms binned light curves for the long GRB trigger, GRB190114873.

This set of light curves show the comparison between the previous stage (line histogram in blue) and the current stage (filled histogram in brown). Figure 6.8 a), shows the comparison between the generation of trigger pulses by the soundcard against the original scaled light curve, effectively how well the soundcard managed to trigger the pulse generator at the times corresponding to the original scaled TTE data. The profile of the original light curve has for the most part been preserved with some deviation in bin amplitudes, but for the most part the general pulse amplitude and shape is the same. As mentioned in Section 6.2.5, it is expected and acceptable that the binned light curve from the triggered data does not mirror exactly the original scaled TTE file, provided that there is minimal difference. This is because the exact original light curve profile does not matter, but instead the general shape and rate is what is emphasised, as these pulses are used to trigger SIPHRA to create TTEs. It is then the comparison between the SIPHRA TTE generated light curve and the MSP430 that matters, as this is data which is actually generated by the instrument. In fact the comparison between the CPLD and MSP430 is most important to assessing the MSP430 firmware, as each stage in the readout chain may have its own response imparted onto the collective TTE data, therefore the following stages inherit the effects of the previous stages. Furthermore, it is recognised in Section 6.2.5 that there are numerous inputs to imprecision in the replication of the trigger pulses as they propagate from the original scaled TTE timestamp, thorough the soundcard, pulse generator and eventually to SIPHRA, some of which is constant and some which may be variable, all of which are beyond the scope of this study.

Figure 6.8 b) shows the ability of SIPHRA to produce readout at the instant that a trigger pulse is presented to its external trigger input. In fact it is so capable that the light curve from the pulse generator data and the SIPHRA data are a direct match around the the trigger time (T_{-10} – T_{+50}). The maximum trigger rate of SIPHRA for the summed channel readout configuration has been measured to be just over 10 kHz for fixed rate triggering. This is consistent with the light curves in Figure 6.8 b).

Figure 6.8 c) shows the processing of readout data and generation of TTE packets by the CPLD, as compared to the light curve generated using SIPHRA data. It is evident that some TTEs are not being created by the CPLD and some of the SIPHRA readout is being lost. It is expected

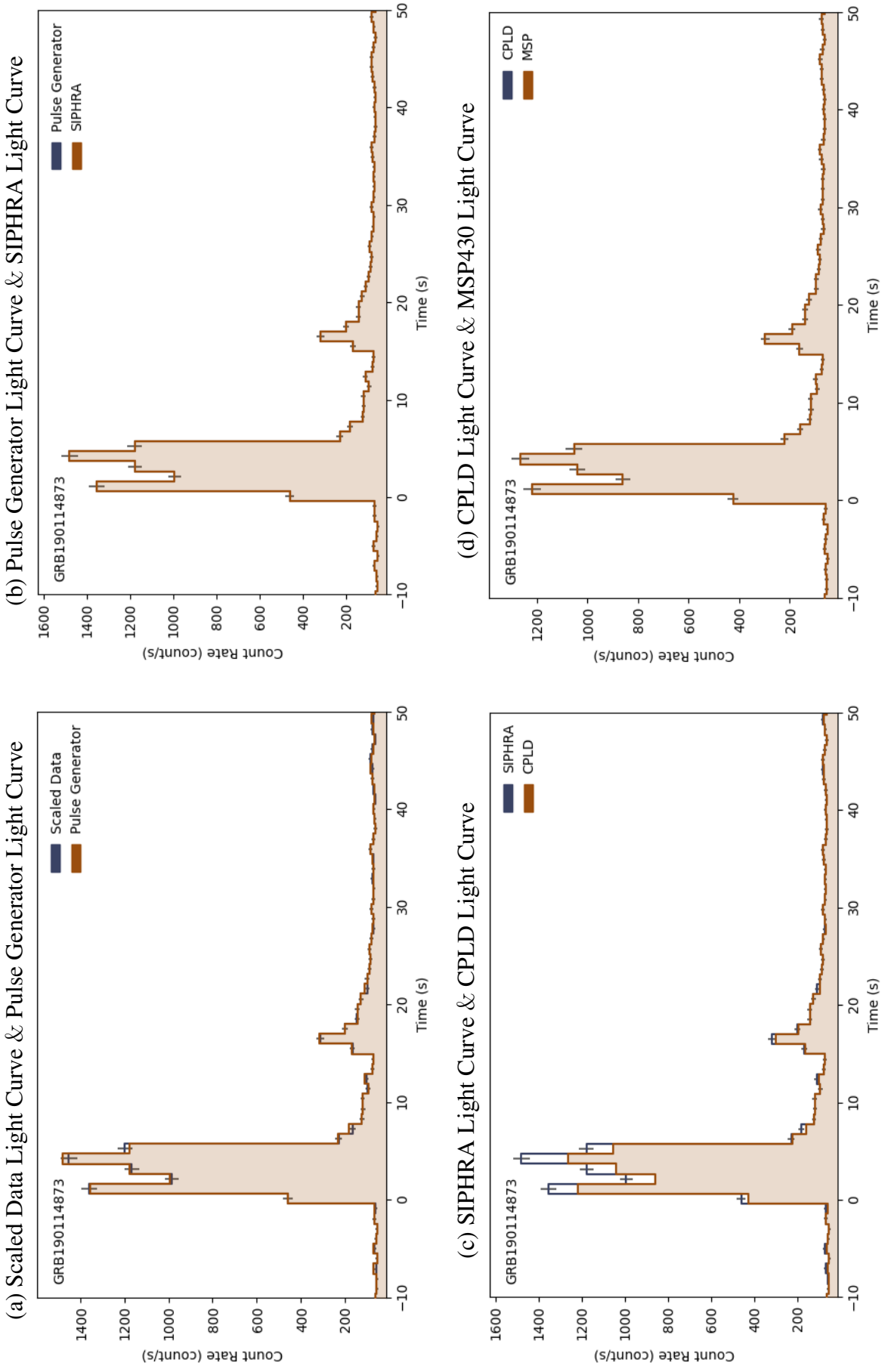

Figure 6.8: Comparison 1024 ms binned light curves for each stage of the GMOD readout for a simulated detection of GRB190114873. Similar figures for select GRBs are available in Appendix A.

Table 6.1: Table of results for the firmware testing, split into short and long triggers and arranged in descending peak flux. Measurements for the peak flux, and T_{90} are derived from the Fermi GBM burst catalogue (von Kienlin et al. 2020).

	GRB Name	Peak Flux (50 keV–300 keV) (ph/cm^2/s)	T_{90} (s)	№ TTEs Received	% TTEs Received	№ TTEs Dropped
Short GRBs ($T_{90} \leqslant 2$ s)	GRB181222841	80.34 ±0.64	0.58 ±0.02	21390	99.991	2
	GRB120323507	34.76 ±0.35	0.38 ±0.04	17143	99.994	1
	GRB140209313	27.09 ±0.36	1.41 ±0.26	21762	99.995	1
	GRB180703949	24.83 ±0.31	1.54 ±0.09	23901	99.992	2
	GRB171126235	22.25 ±0.59	1.47 ±0.14	18352	100.000	0
	GRB170206453	19.74 ±0.28	1.17 ±0.10	20615	99.995	1
	GRB200826187	15.09 ±0.19	1.14 ±0.13	21855	99.991	2
	GRB150819440	14.83 ±0.30	0.96 ±0.09	24025	99.992	2
	GRB210528586	10.88 ±0.25	1.02 ±0.09	23715	99.996	1
	GRB120624309	10.60 ±0.20	0.64 ±0.16	19933	99.990	2
	GRB210909447	8.93 ±0.18	1.41 ±0.09	19685	99.985	3
	GRB101216721	8.00 ±0.18	1.92 ±0.55	16895	100.000	0
	GRB111222619	7.27 ±0.30	0.29 ±0.04	17112	99.988	2
	GRB090228204	7.22 ±0.19	0.45 ±0.14	15810	100.000	0
	GRB190606080	7.09 ±0.17	0.22 ±0.04	19933	99.990	2
	GRB090227772	6.61 ±0.17	0.30 ±0.02	15376	99.993	1
	GRB120222021	6.47 ±0.16	1.09 ±0.14	20212	99.995	1
	GRB130504314	6.22 ±0.22	0.38 ±0.18	22661	99.982	4
	GRB170127067	5.75 ±0.36	0.13 ±0.04	22072	99.982	4

	GRB Name	Peak Flux (50 keV–300 keV) (ph/cm^2/s)	T_{90} (s)	№ TTEs Received	% TTEs Received	№ TTEs Dropped
Long GRBs ($T_{90} \gtrsim 2$ s)	GRB130427324	496.29 ±1.62	138.24 ±3.24	48453	99.992	4
	GRB131014215	174.06 ±0.82	3.20 ±0.09	27342	99.989	3
	GRB211211549	146.95 ±0.94	34.30 ±0.57	34720	99.983	6
	GRB201016019	144.99 ±0.71	2.94 ±0.09	28923	99.993	2
	GRB190114873	122.80 ±0.57	116.35 ±2.56	32178	100.000	0
	GRB210619999	121.26 ±0.85	54.78 ±0.57	30783	99.984	5
	GRB200829582	113.86 ±1.04	6.91 ±0.36	27187	99.996	1
	GRB220426285	98.07 ±0.57	5.63 ±0.36	26412	99.996	1
	GRB120129580	81.16 ±0.63	3.07 ±0.36	19716	99.995	1
	GRB200125864	52.69 ±0.35	5.82 ±0.09	20460	99.995	1
	GRB090424592	45.97 ±0.49	14.14 ±0.26	18786	99.995	1
	GRB160509374	33.30 ±0.31	369.67 ±0.81	25885	99.996	1
	GRB090618353	29.98 ±0.61	112.39 ±1.09	25451	99.996	1
	GRB140102887	25.03 ±0.25	3.65 ±0.09	21948	99.995	1
	GRB140523129	20.50 ±0.28	19.20 ±0.36	24335	99.988	3
	GRB190611950	15.16 ±0.33	100.61 ±0.57	25668	99.992	2
	GRB131108862	9.64 ±0.19	18.18 ±0.57	21731	99.991	2
	GRB210204270	8.85 ±0.16	206.85 ±2.29	26288	99.996	1
	GRB081110601	7.13 ±0.27	11.78 ±2.57	15531	99.994	1
	GRB170825500	6.39 ±0.13	7.17 ±0.57	20522	99.995	1
	GRB180126095	5.66 ±0.16	18.43 ±4.64	21080	99.991	2

that this is due to TTEs, arriving in close succession to one another with the latter being dropped while the former is accepted, causing the CPLD to become overwhelmed during high trigger rate readout as observed within the main burst emission (around $T_0 - T_{+7}$). The root of this is expected to be due to the amount of time the CPLD takes to fully transmit the generated TTE. Regardless, it is unlikely that this can be improved upon as the device internal resources have been expended and the hardware has been fixed at this stage of the mission life cycle. It is also uncertain if these effects make much difference to the overall collection of science data as a whole. Certainly if the impact can be quantified it can be accounted for after downlink from the spacecraft during in-orbit operations. More over, while further testing is needed, it is clear that the effect is minor and does not appear as though there would be any impact on GRB triggering.

Figure 6.8 d) shows the collection of TTEs from the CPLD, the temporary storage and transmission as pages (of 31 TTEs) by the MSP430 firmware. While both the CPLD and MSP430 light curves appear to match for this particular trigger, within this time range ($T_{-10} - T_{+50}$), a complete analysis shows that a minor but non-zero amount of TTEs may be dropped over the entire range of collected data.

The full list of 40 GRB triggers and the results for comparison between the served TTEs from the CPLD and the transmitted TTEs from the MSP430 are presented in Table 6.1. As can be seen, the vast majority of TTEs are successfully processed and transmitted with between 99.98% – 100% TTEs being preserved. These results suggest the majority of TTEs can be successfully processed by the MSP430 firmware with minimal impact on the burst light curve and the spectrum. This figure was calculated as the percentage number of TTEs in the CPLD data that were found in the TTE data transmitted by the MSP430. As mentioned in Section 6.2.6, up to 31 TTEs may not have been read out by the MSP430 due to the format that GMOD serves TTEs, and as such have been excluded from this count. While these results suggest high reliability and good performance by the MSP430, these figures have some caveats which should be acknowledged.

The scaling of GBM TTE data assumes a constant gamma-ray background rate of 50 Hz, however in orbit this will possibly vary over time due to SiPM irradiation (as discussed in (Ulyanov, Murphy, Mangan, et al. 2020)), spacecraft orientation and orbit configuration (i.e. orbit latitude) (as discussed in (Murphy et al. 2021a)). It is possible that higher background rates could put accumulated pressure over time on the MSP430 resources, such that more TTEs will be dropped.

As these tests were intended to determine a baseline for the capability of the MSP430 firmware, I^2C operations were not carried out and no additional functionality other than the core experiment processes were in operation for these tests. It is expected that I^2C operations which occur periodically and at high rates could impact the performance of the MSP430 firmware, specifically the successful collection of TTE packets by the MSP430 from the CPLD. This is because the MSP430 firmware handles I^2C and serial operations using interrupts, which take a finite amount of time to transition to the given interrupt subroutine (ISR) and by definition prevent execution of code in the main loop. For example, an I^2C interrupt can block the execution

of a serial read interrupt potentially preventing the reception of a TTE ASM byte causing the entire byte to be lost or potentially become corrupted. While this requires further testing to fully assess, it has been factored into the firmware design by the addition of interrupt nesting being permitted exclusively in the I^2C ISR for the CPLD serial read operation which has been shown to alleviate the impact of this problem. Furthermore, the way GMOD is interfaced with and the way the firmware transmits TTE pages to the OBC during operation has been influenced by this, as currently the only periodic OBC commands executed mid operation are those concerning housekeeping data on a $\sim$1 s period.

Depending on the GMOD Mode in operation, Experiment Mode or Experiment16 Mode, either summed channel or full 16 channel readout will be performed. Full 16 channel readout requires the reception of 36 bytes of data and naturally this also takes longer to complete, with full readout from the rising edge of external triggering taking $\sim$824 μs. While Experiment16 is only for demonstration purposes and is not the main mode of operation, a GRB event triggered while in this state is possible. It is expected that with the increased level of throughput from the full channel readout and the amount of time it takes to process this quantity of data, that this can impact the MSP430 performance and likely cause some TTEs to be dropped.

Finally, referring back to the TTEs appearing to be dropped by the CPLD, it is possible that the CPLD has effectively filtered out TTEs which would be mutually dropped by both the CPLD and the MSP430, thus misrepresenting the performance of the MSP430. Either way the conclusions prior still stand for both GMOD and the CPLD: it is unlikely that this can be improved upon, it is uncertain that these dropped TTEs make any difference to the science data as a whole, it can be accounted for and it does not appear as though there would be any major impact on GRB triggering.

It can be assumed that at some point the MSP430 will begin to drop TTEs at greater rates due to bottlenecking occurring at the serial input and the transfer of TTE data from internal buffers to external flash memory. It is however difficult to estimate the required amount of flux received which corresponds to a sudden increase in dropped TTEs from this study. This is because of the effect of the CPLD and its inability to produce or its dropping of TTE packets before reaching the MSP430. In other words, the MSP430 can only drop TTEs which are produced and which it received from the CPLD. This filtering of TTEs which would otherwise reach the MSP430 can result in a potential overestimation of the MSP430 capabilities, both in terms of the firmware and the inherent hardware limitations, for example when comparing the flux of the GBM detected event and the corresponding number of TTEs which the MSP430 dropped from the scaled GBM data. However, as a rough estimate, the contribution of dropped TTEs by the MSP430 appears in Table 6.1 to begin to increase above a flux of $\sim$100 ph/cm^2/s, among the brightest GRBs in the GBM catalogue. It must be stressed however, that if the CPLD did not drop or produced all TTE packets, this threshold may be at a lower flux value.

6.3. Conclusion

The results from these tests indicate that the GMOD firmware is capable of meeting the requirements for reliable instrument operation by testing its performance using fixed trigger rate stress tests and a series of HITL simulated GRB events. The initial results from the EQM fixed trigger rate testing (Mangan et al. 2021e) demonstrated the capability of the MSP430 to handle the transfer of data over the range required in orbit (Murphy et al. 2021a) and that the power consumption is within the expected range for a variety of modes and experiment configurations. However as discussed, this test had some limitations which would be addressed in a more realistic study (Mangan et al. 2022d). A sample of 40 GRBs were selected from the Fermi GBM catalogue and scaled down to the equivalent rates expected to be detected by GMOD while in orbit. Each of the scaled TTE files were then used as the source of trigger times, which when used to externally trigger the SIPHRA ASIC reproduced the dynamic rates and quantity of TTEs characteristic of a GRB detection. These trigger signals were generated using WAV files which were embedded with pulses at times corresponding to the scaled TTE timestamps, played from a laptop soundcard, amplified and then used to trigger the output of a pulse generator. The pulse generator output could then trigger SIPHRA and generate TTEs which would then propagate thought the GMOD readout system. This method of hardware in the loop testing can be extended to other instruments to trial the firmware performance in realistic conditions preflight, for example the 6U CubeSat design of GIFTS, likely to use a different readout control system but which relies heavily on the GMOD heritage.

To fully understand the effect that dropped TTEs would have on the collection of science data, the passage of triggers and the corresponding TTEs were recorded at each stage of the readout chain and compared to monitor the performance. The results indicate that a minimal amount of TTE data is dropped by the GMOD firmware, with the firmware successfully receiving, storing and transmitting up to 99.9 $\%$ of all TTEs. The vast majority of TTEs being successfully recorded over the entire burst duration indicates that there would be negligible impact on the triggering of most GRBs above the trigger threshold, as well as confirming that the light curve profile and spectra would be preserved after passing through the MSP430. It also suggests that some amount of TTEs do get dropped by the CPLD and may also be mutually dropped by the MSP430, but that these dropped TTEs can be accounted for in the downlinked data. Additional stress testing of the MSP430 is also necessary. This test and prior testing indicates that certain states of operation can have an impact on the firmware performance, including high rate I^2C interactions, increased background rates and full channel readout. The impact of this will be further examined in the flight model mission test (Doyle et al. 2022b; Doyle 2022). To complement this chapter and Chapter 3, the following chapter will cover a discussion presented at the 4^{th} Symposium on Space Educational Activities (SSEA) Barcelona, April 2022, detailing development tools, our approach and lessons learned through firmware development for the GMOD instrument payload.

Chapter 7

Experiences in Firmware Development

Over the course of this thesis and the development of the firmware described in Chapter 3 and Chapter 6, it became clear that there is a lack of dissemination of firmware development methods for payloads on large missions and CubeSats. This is understandable as there may be legal issues surrounding publication of software for proprietary hardware, or simply that the firmware solutions are seen as too specific to the mission. However, this leads to a gap in the literature and a paucity of references on common techniques when it comes to firmware development and testing. To encourage further sharing of knowledge in this area a discussion on the experiences in developing and testing firmware for GMOD was published in the proceedings of the 4^{th} Symposium on Space Educational Activities (SSEA) Barcelona, April 2022. This publication discussed an overview of GMOD (covered in detail in Chapter 2 and Chapter 3), our firmware development approach, some of the tools used, as well as an overview of some pitfalls and lessons learned throughout its development and testing.

7.1. Firmware Development Approach

The development cycle of the GMOD firmware is presented in Figure 7.1. The process begins with an assessment of the requirements followed by implementation and testing on a subsystem level. If satisfactorily implemented and tested on GMOD as a independent subsystem, testing is then done with the OBC in the loop. If either test fails, the firmware is revised and retested. This approach was selected as it provides a structured approach to development and testing from the perspective of the OBC, payload and the interface between them. This section will describe this process in detail with reference to the procedure outlined in Figure 7.1.

Firmware Requirements:
It is necessary to order the production of firmware in a structured fashion. Typically instrument firmware would be framed around the requirements set out in the preliminary design review (PDR) and CDR products. These are developed as part of phases B/C of the typical project lifecycle and encompass the design specification of the spacecraft and its payloads. For ESA FYS the project structure closely adheres to the ECSS standards set out in ECSS-M-ST-10C as the "Design Your Satellite" phase, which include producing the DDF and design justification file (DJF) documents. These documents form the bedrock of firmware development for the payload and are the fundamental starting point and reference when developing any new functionality.

Outputs From Testing:
Throughout the design and qualification stage of the life cycle, the spacecraft and payloads undergo numerous tests. Environmental testing may be conducted on the subsystem (Mangan

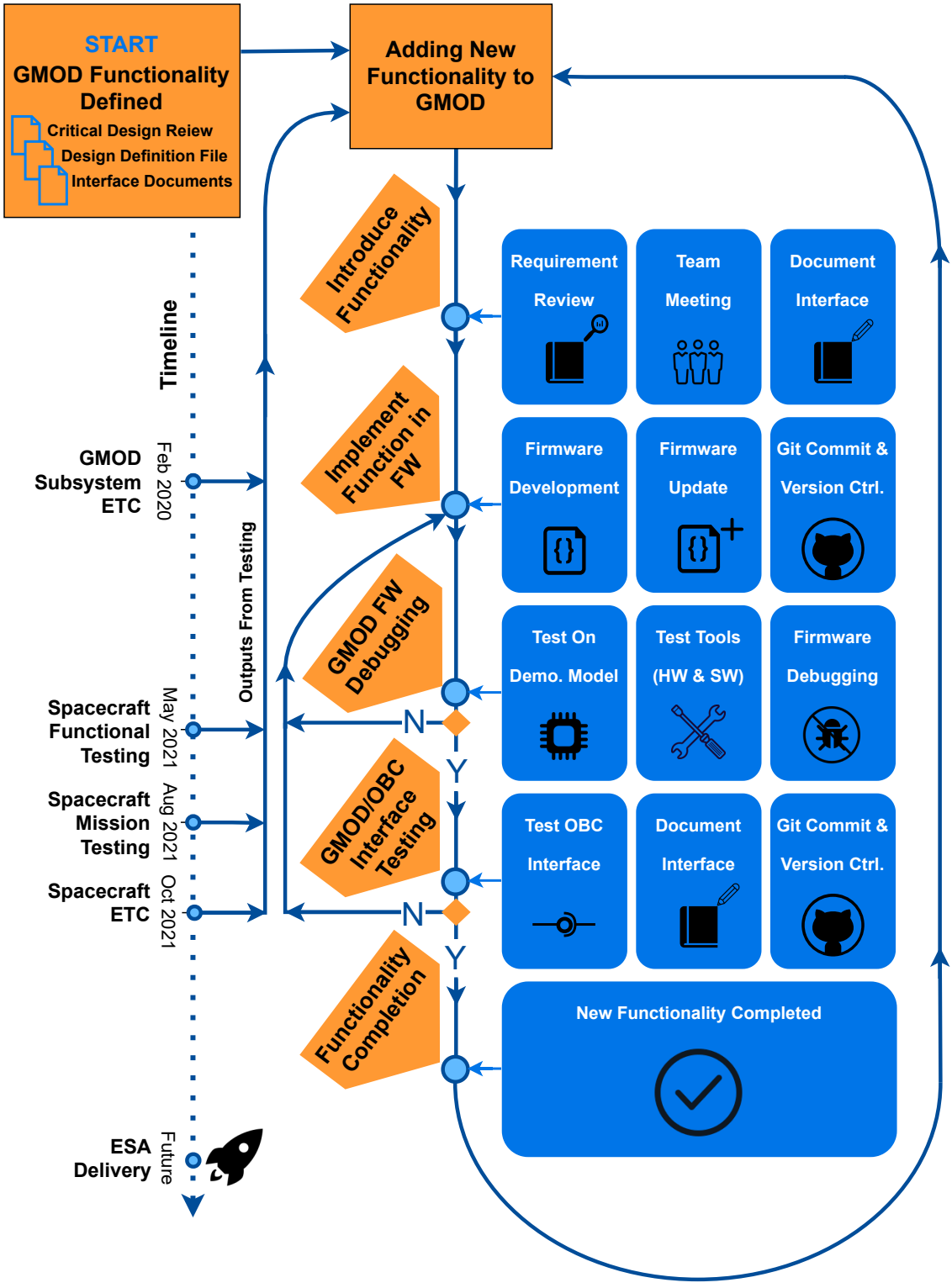

Figure 7.1: Process flow diagram describing the addition and development of new functionality. This figure shows the cycle of introduction of new functionality, derived from mission documentation and test campaigns as it is implemented and tested on a subsystem and system level. This is discussed in detail in Section 7.1.

et al. 2021f) and system level (Dunwoody et al. 2022c), which may also require pre-campaign functional and mission tests (Doyle et al. 2021; Doyle et al. 2022b). All of these tests can be used to inform additions or amendments to the existing functionality, providing feedback not found within the scope of the basic payload firmware requirements. Furthermore, these tests should be used as key milestones along the path of development. Certain functionality (and corresponding tests of this functionality) are required at these milestones (i.e. pre/post vibration functional tests), thus the build up to these tests can be used to assign priority and pacing to certain blocks of functionality. It is important to ensure that priority is maintained and the appropriate time is allocated where needed. As in Figure 7.1, requirements, documentation and testing all feed into development of new functionality, with some additions being introduced as outputs from test campaigns throughout the project life cycle.

Introducing Functionality:
Payload requirements are initially distilled into individual deliverables during a review of the documentation or through team meetings post testing. In some cases, these deliverables may be so low level that they do not appear in the design documents. Interface documents (between the OBC and payload) can then be produced which outline the operations and form of communications. For instance, an interface document may describe the command structure to activate certain functionality on the payload. In more intricate situations, an interface document may explicitly outline how this functionality is expected to behave if that operation impacts the interface. For example, on GMOD, a "Function List" exists with all commands, descriptions of their operation, the size of data expected to be received and transmitted and any fail scenarios listed. Similarly, in the case of complex operations like the serving of full channel TTE data from GMOD to the OBC, a more detailed overview of how the functionality should be implemented was produced. This is primarily used as an aid during firmware development, particularly regarding OBC/GMOD interface development. We have found in our experience that it is sufficient to produce these documents as required, without firm document control, but that a final iteration would be appropriately documented for OBC interfacing.

Implementing Functionality:
This functionality is then implemented in C/C++ using the CCS[1] IDE provided by TI. An important part of this development is version control. This is performed using the Git version control tool. Upon completion of the new functionality, committing and pushing to the Git remote, the firmware is then tested.

Firmware Debugging:
Before testing new functionality with the OBC, it is tested and debugged separately on a test setup (as shown in Figure 7.2) replicating the OBC interface to confirm all functional requirements are met. This is done using GSE, some having been developed and used during the EIRSAT-1 ETC. Additionally, it is possible to drill further into the firmware operation mid-execution using the CCS IDE debugging capabilities, which offer numerous breakpoint, timing

[1] https://www.ti.com/tool/CCSTUDIO

and variable reporting tools. If a bug is found or the functionality does not behave as expected the firmware is revised with edits to the firmware code, as seen in Figure 7.1. When testing is complete, a binary file is generated after compilation, which is renamed with the version ID and timestamp of creation. The version ID code records major, minor and patch updates in a two byte ID as in Table 7.1.

Table 7.1: The version ID convention adopted for the GMOD firmware development. The DM version of the firmware was developed before this flow and versioning convention was adopted. As such, the DM firmware version is simply considered V0.

Model Version	**Major 4 Bits (0-15)**	**Minor 8 Bits (0-255)**	**Patch 4 Bits (0-15)**
DM	V0	-	-
EQM	0x1	0x00 - 0xFF	0x0 - 0xF
FM	0x2	0x00 - 0xFF	0x0 - 0xF

The version ID is also hardcoded into the firmware and is accessible over I^2C. A major increment indicates the firmware model. A minor increment may be any change judged to be larger than a patch. A patch update could be something as small as a bug fix or comment correction (a rollover of the patch increment from 0xF to 0x0 implies a minor increment has occurred). For example, V1.2.3 is encoded as two bytes as 0x1023. When completed the firmware is tagged on Git using its version ID for later reference.

GMOD/OBC Interface Testing:

Once there is confidence in the newly developed firmware the interface between the OBC and GMOD is tested. The binary file is reformatted into serial bootloader commands used by the OBC to program GMOD. The OBC can then command and control GMOD using the Mission Control Software (MCS)[1], provided by Bright Ascension. Throughout these tests the general operation of the new functionality can be confirmed for both OBC and GMOD while any deviations or changes to the interface can be discussed in a post test context. Any deviations from the original interface can be agreed and amended by revision of functionality. Once satisfied, the new functionality is considered complete and the cycle begins anew, as in Figure 7.1. Development of GMOD's DM firmware was produced in a closed loop without input from the OBC software team, hence the unusual version code. This was acceptable for this iteration, as it was intended to simply demonstrate the instrument operation as a standalone system. However future iterations have strict interfacing between the OBC and GMOD and require close collaboration with the OBC software team. The EQM version was redeveloped from the ground up using this flow.

[1] Bright Ascension: Mission Control Software

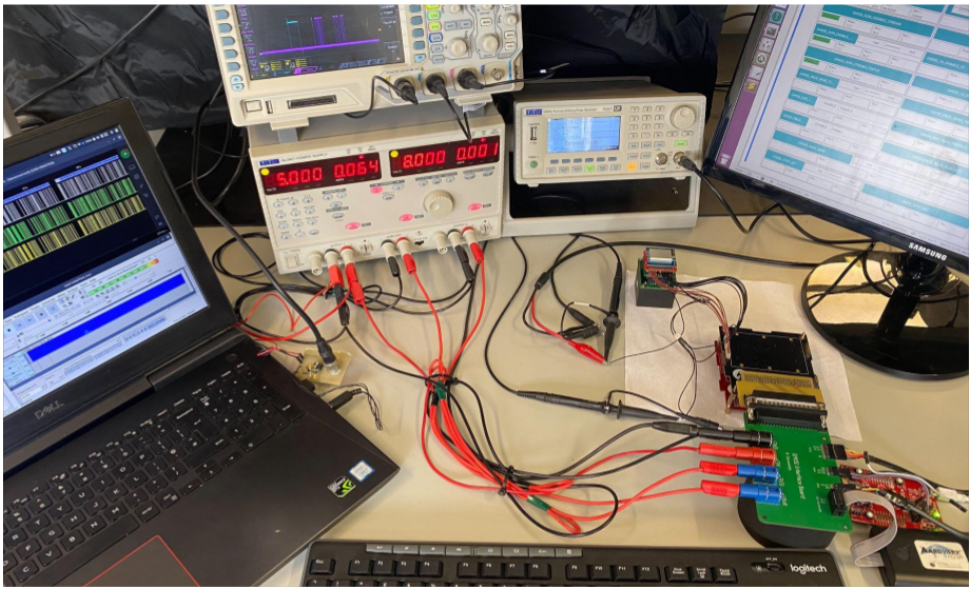

Figure 7.2: The hardware setup used to test GMOD firmware, as used during the testing described in Chapter 6, including the motherboard, interface board, Total Phase Aardvark, MSP-EXP430FR5994 LaunchPad and a Future Technology Devices International (FTDI) UART module.

7.2. Development Tools and Resources

It's not possible to describe a universal configuration for testing firmware applicable to all. However, many of the tools used with GMOD are generic, CoTS and for the most part relatively accessible. Similarly, while other payloads use different hardware and may be locked into a given device manufacturer's documentation, compilers and drivers, many reputable manufacturers share the same level of high quality in these areas. For this reason, we describe the development and test tools used, such that other teams might find similar services provided by their chosen device manufacturer.

MSP-EXP430FR5994 Launchpad:
Development kits are intended to provide a starting point for unfamiliar audiences. These kits allow the users to develop skills when working with embedded devices as well as in understanding the fundamentals of the device and its peripherals. For instance, TI produces the MSP-EXP430FR5994 LaunchPad, with similar kits for their range of products. These are invaluable tools to begin firmware development by exploring the limits and potential quirks of the chosen device while also allowing the user to evaluate its suitability, potential design ideas and capabilities before incorporating them into their application. By far its most useful application is its ability to act as a programmer for any MSP430 device with accessible SBW pins. The LaunchPad PCB consists of two blocks: the MSP430 target and the eZ-FET debug probe. The eZ-FET, which is connected to the target device via jumper pins, can be broken out from the LaunchPad and connected to any MSP430FR5994 device. This provides access to TIs debugging tools in CCS, TIs EnergyTrace capabilities (for live power management analysis) and a low-cost programmer, which as compared to a generic flashing device would normally be priced up to €200

per unit. The LaunchPad can be seen in Figure 7.2.

TI Code Composer Studio:
CCS is an Eclipse based IDE which supports TIs MSP430 devices. As such, CCS allows the creation of project profiles which can be integrated with Git, a source code editor, compilation and even register and memory browsing on active debugging code along with all the other general debugging operations. Furthermore, given that CCS is built upon the Eclipse open framework, there is no licence fee to access or develop using CCS, a quality which is especially advantageous for university teams.

TI MSP430 Driverlib:
Depending on the application, a choice can be made on how the firmware developer interacts with the device peripherals in C/C++. For the MSP430 there is the option for direct register level interaction (the developer directly sets/resets bits in the device/peripheral control registers) or indirect interaction where the developer may use a set of abstracted libraries developed by TI called Driverlib. This is very useful for several reasons as it allows almost immediate access to the device peripherals without in-depth knowledge of the MSP430, but also may be used as a reference when looking for an example implementation.

TI Documentation and Examples:
Developing for hardware of course requires reference to device documentation. This is a must for successful development of any application. TI have compiled a comprehensive user manual and data sheet for the MSP430FR5994 while also providing application reports describing best practice and the use of the device peripherals. TI provides a number of example scripts in the TI Resource Explorer, describing in detail how to operate the device and the internal peripherals for both register level and Driverlib applications.

TI Ground Support Equipment:
Testing of firmware requires simulation of the intended interface between the payload and the spacecraft. A GMOD interface board was built to break out the PC/104 header for the ETC. GMODs primary channels of communication are through I^2C (command and control) and 128k baud asynchronous serial (science data). To allow control of GMOD in the absence of the OBC, a Total Phase Aardvark I^2C/SPI Adapter is used to interface with GMOD using Python scripts. Readout of science data over serial can be achieved using any generic USB to serial interface, in the case of GMOD an FTDI LC234X UART module was selected. To emulate the role of the OBC and MCS during testing, a Python Jupyter Notebook was developed which provides access to the GMOD command set. Both the Total Phase Aardvark and FTDI LC234X modules can be seen in Figure 7.2.

7.3. Discussion and Lessons Learned

Structure is Essential:
Firmware development needs structure, primarily based around the requirements of the payload, but also in terms of the scheduling of deliverables and priority assigned to functional blocks.

Structure is informed by the existing documentation from mission planning, testing and design.

Know When Enough is Enough:
A reference is made to the time allocation regarding firmware development. Typically if firmware works as expected, satisfies the requirement criteria and has been tested - little can be gained by further modification. There are diminishing returns when fixating on the implementation of functionality, particularly when it comes to the impact on schedules.

Balancing Schedules:
As a student team consisting mostly of PhD and Masters students, working on a demanding project such as CubeSat development means maintaining a balance between academic work and work related to EIRSAT-1. This is not at all straightforward and the amount of time required to be dedicated to the project should not be underestimated.

Testing Firmware:
There is no "one size fits all" when it comes to firmware/hardware testing. However, from our experience, we have found it is important during testing to introduce a level of "randomness" as expected during actual operation, to better stress the firmware. For one example, as discussed in Chapter 6, externally triggering GMOD with periodic pulses does not test the robustness of the firmware in the same way as triggering randomly in time, which better simulates realistic detections and strains detector readout, access to flash and transmission of data to the OBC. Another aspect is unit testing firmware. Typically firmware developed for embedded systems is not usually unit tested. This is often due to the belief that it is impossible or impractical due to hardware specifics, or simply because it is acceptable on embedded systems for there to be no defined boundary between pure software and hardware/register manipulation. However, unit testing during development on embedded systems is possible. Test driven development (TDD) has a number of benefits, including reduced time spent debugging, confidence in the final product, continued confidence after modification of the firmware and well-structured code, which stands as objectively reliable. While unit test development was considered with the production of the GMOD firmware, it would have been most successful if it has been adopted from the start and given the level of the firmware as it is now, it has not yet been retroactively implemented.

7.4. Conclusion

This chapter presents the payload firmware development approach of the GMOD firmware. The importance of a structured development cycle, availing of manufacturer resources, balancing PhD and project related work as well as adequate stress testing of the firmware have all been highlighted. In conclusion, there is no single way to develop payload firmware, however it is hoped this discussion as published may offer some advice and a starting point to other teams to begin their own payload firmware development.

Chapter 8

Conclusions and Future Developments

GMOD Instrument Overview

This thesis presents a review of the literature regarding the current understanding of GRBs, spaceborne gamma-ray instrumentation and future prospects for the use of CubeSat experiment payloads for high-energy astronomy, as detailed in Chapter 1. A comprehensive breakdown of the GMOD experiment hardware is presented in Chapter 2. The construction and the components used have been described with an emphasis on the use of modern technology, such as the low voltage requirement and small form factor SiPMs and the high performance $CeBr_3$ scintillator. Much of this is contrasted against other instrument technology and configurations in Chapter 1 (e.g. more complex detectors like Compton and pair production telescopes). My contributions to GMOD development are detailed in this thesis and include the development of the GMOD hardware, the assembly and testing of the DM iterations of the motherboard as well as contributing to the testing of the detector assembly during the initial and later phases of integration of the EQM and FM model versions (Chapter 4, Chapter 5 and Chapter 6).

In Chapter 3 the GMOD firmware and operation is presented, the development of which I heavily contributed to. This includes the development of the C/C++ firmware used on the MSP430 and its continuous testing (e.g. Chapter 6). This was along side larger tests such as mission testing and the subsystem ETC (Chapter 5). Many of the lessons learned during this development have been distilled in Chapter 7. The discussion on the GMOD firmware in Chapter 3 begins with the fundamental philosophy established for the payload controller, dictating much of the structure of its implementation, including the communication convention, data products, firmware modes and the readout operation. The latter is discussed in detail given the complexity of the reception, storage and service processes for science data.

GMOD Concept to Design

The remaining chapters follow mostly in chronological order of occurrence. Chapter 4 describes the early design choices for the GMOD payload as well as the origin as the GRD instrument concept. The initial test on the SiPMs and $LaBr_3$:Ce based scintillator detector are described, which underpinned the design for the proposed and CDR designs of GMOD. This is followed by the balloon flight test campaign of the GMoDem detector, which was a major milestone in the development and testing of the instrument and represents my start on the project in which I participated in the early analysis of the flight data and the first draft of the publication. The SiPM radiation testing at the PSI within a 101.4 MeV proton beam line concludes this chapter, from which I contributed as a participating member in conducting the experiment.

Environmental Testing

The subsystem level ETC described in Chapter 5 begins by discussing the intentions of the ETC, the approach and documentation used. The EGSE is then described along with the demonstration iteration of the GMOD firmware. This is followed by a breakdown of simulations produced prior to the ETC, which are used to derive the test levels and set up and finally the operation and results for both the vibration and TVAC testing. To conclude Chapter 5, the post ETC measurements of instrument performance after environmental are discussed. This was a multi disciplinary campaign and was completed thanks to the full effort of the GMOD and EIRSAT-1 team. My contribution during this time includes the preparation of the demonstration firmware, production of test documentation, participation during testing and proceedings publication and presentation of the work at the International Conference for Space Optics (ICSO 2021). As mentioned however, this was a team effort and some aspects of the preparation such as the simulations, bakeout, development of the EGSE were conducted prior to the ETC or were managed by other members of the EIRSAT-1 team.

Firmware Development and Testing

Finally the HITL testing of the GMOD FM firmware is presented, which describes a simulation of the response of the firmware to GRB events by producing timed pulses (which were based on Fermi GBM data) using external triggers encoded into a WAV file output. The results of this test gave further confidence in the ability of the firmware to operate as intended during its mission operations. Both aspects of firmware testing were performed by myself, with an invaluable input and guidance from the GMOD team. The results of which were published in the proceedings and presented at the 8th IEEE International Conference on Space Mission Challenges for Information Technology (SMC-IT, July 26–30, 2021) and the SPIE Astronomical + Instrumentation Conference 2022 (17–22 July 2022).

Lessons Learned

Finally the lessons learned throughout the development of firmware for GMOD were described in Chapter 7, including details on the process flow of writing firmware for the payload, the versioning scheme, the development tools used and the resources. During development of the GMOD firmware, it was noticed that there was a distinct lack of literature on instrument firmware for large missions compared to hardware. In some respects justifiably, as the sharing of specifics on firmware can be prohibited or excessively hardware specific. This section was compiled for presentation at the 4^{th} Symposium on Space Educational Activities (SSEA) (April 2022) to encourage the sharing of ideas around the development of firmware, while the lessons learned are hoped to find an audience with other teams in the development of their firmware for future GRB detecting CubeSat payloads.

Closing Remarks and Future Outlook

The beginning of the multi-messenger era opened a new window into observing the universe. It is clear from the discussions in Chapter 1, that while the existing fleet of large GRB detecting spacecraft have excelled in their mission objectives, they continue to operate beyond their intended lifetime. Furthermore, with the upcoming O4 observing run for GW observatories, as well as the planned improvements in detection performance over the next decade, the ability to provide a full sky coverage for GRB detection is essential. As such the only feasible way to provide this coverage is through the use of GRB detecting CubeSats. These CubeSats will allow clusters of GRB detecting instruments to be flown, providing the optimal view of the sky and complete detection of transients which may be detected in coincidence with GW events. Furthermore, CubeSats provide a platform to test unflown or low TRL technology, feeding in to the accelerated introduction of silicon based photodetectors on larger missions.

The Gamma-Ray Module (GMOD) is one such instrument which will address these necessities, along with other GRB detecting CubeSats, like BurstCube, CAMELOT, HERMES (Fuschino et al. 2019), GIFTS and GRBAlpha (Pál et al. 2020). As it stands, the GMOD FM hardware and firmware are complete and are currently assembled with the EIRSAT-1 spacecraft in preparation for delivery and launch. It is expected that EIRSAT-1 and the GMOD payload will be launched in early 2023 and soon after will contribute to the efforts in GRB science, joining the many GRB detecting CubeSats which have been in development over the past decade. Moving forward from the work presented in this thesis in particular, a new 6U CubeSat called the Gamma-Ray Investigation of the Full Transient Sky (GIFTS) has been proposed. This mission will use six larger detectors based on GMOD and will be capable of independent localisation. The readout of multiple GMOD like instruments on a single spacecraft presents new challenges in terms of the processing and the power required for operation. A greater processing capability will be needed to manage the readout of this cluster which can be performed by a system-on-chip (SoC) FPGA solution with deployable solar panels making this task feasible with respect to the processing and power requirements expected. As such, GIFTS will build on the development and flight heritage for the GMOD mission. The results and performance of the GMOD payload will further the technology used in these spacecraft and will provide development, testing, operations and TRL experience for the next generation of CubeSat satellites and GRB detecting missions.

Appendices

Appendix A

Additional Simulated Detections

A collection of additional 1024 ms binned light curves for the simulated GRB detections discussed in Chapter 6, using the FM model firmware. The events have been binned from the TTE data products generated during the HITL testing and correspond to entries in Table 6.1 from Chapter 6. An example of this is shown in Figure 6.8, as 1024 ms binned light curves for the long GRB trigger, GRB190114873.

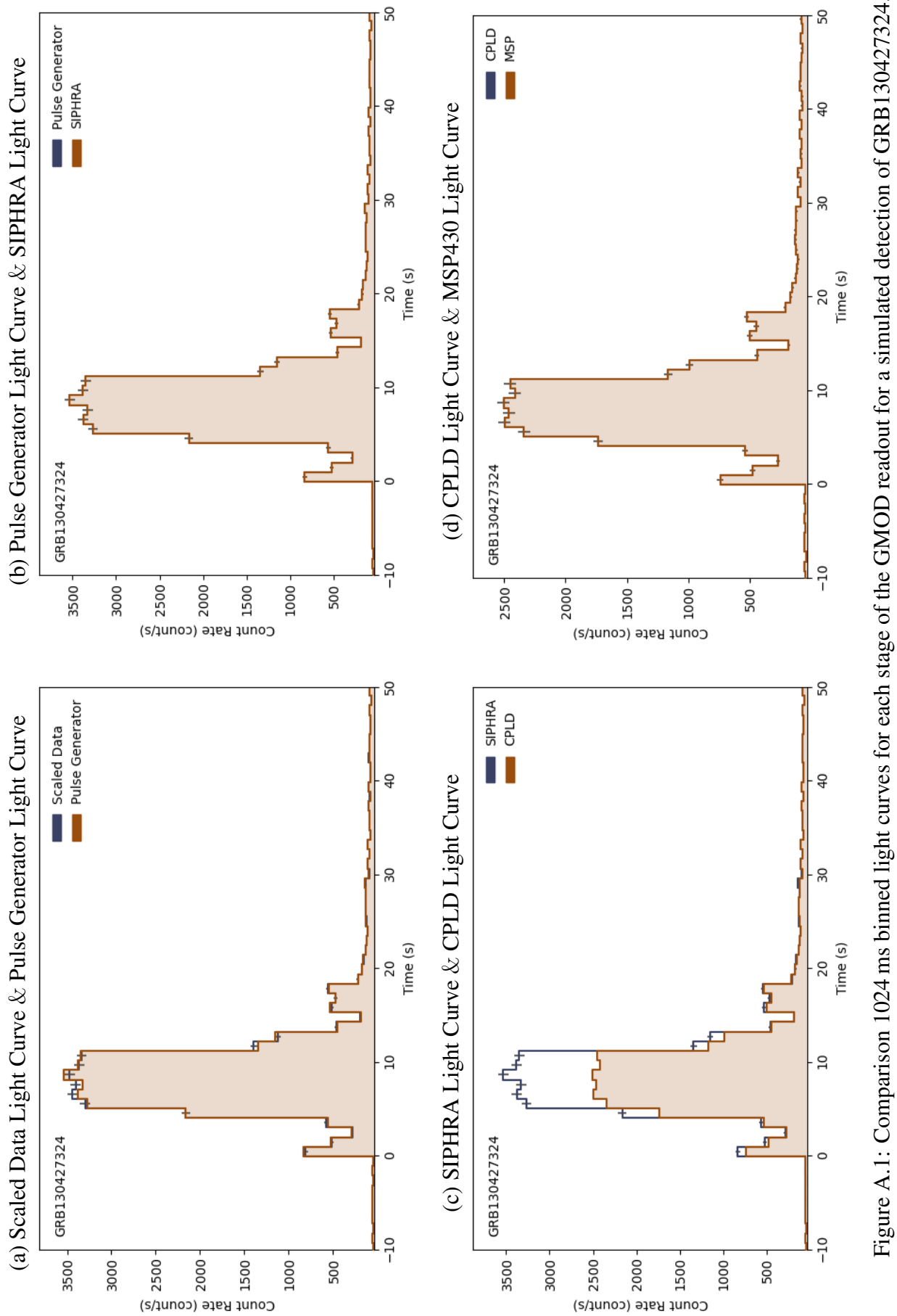

Figure A.1: Comparison 1024 ms binned light curves for each stage of the GMOD readout for a simulated detection of GRB130427324.

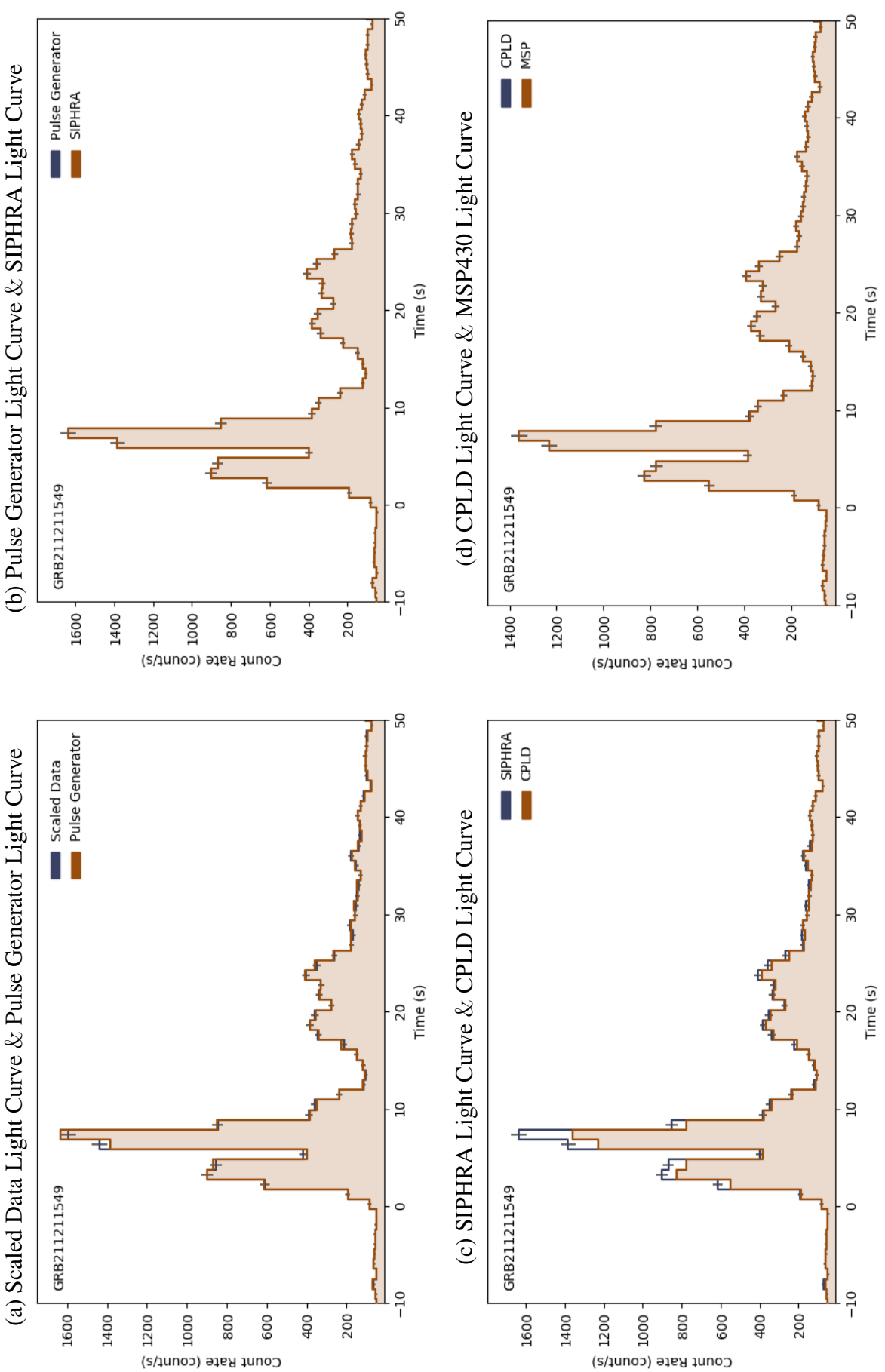

Figure A.2: Comparison 1024 ms binned light curves for each stage of the GMOD readout for a simulated detection of GRB211211549.

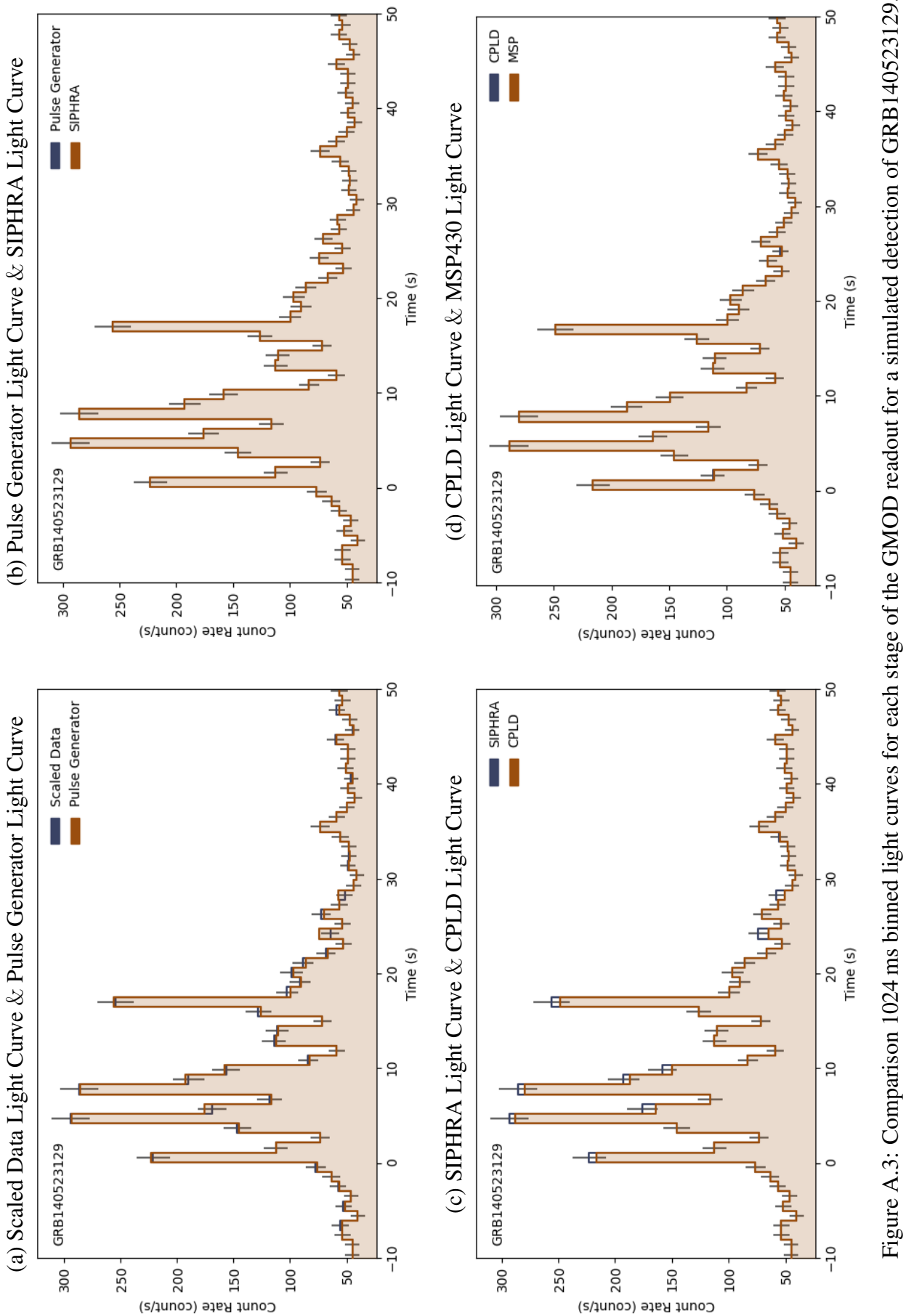

Figure A.3: Comparison 1024 ms binned light curves for each stage of the GMOD readout for a simulated detection of GRB140523129.

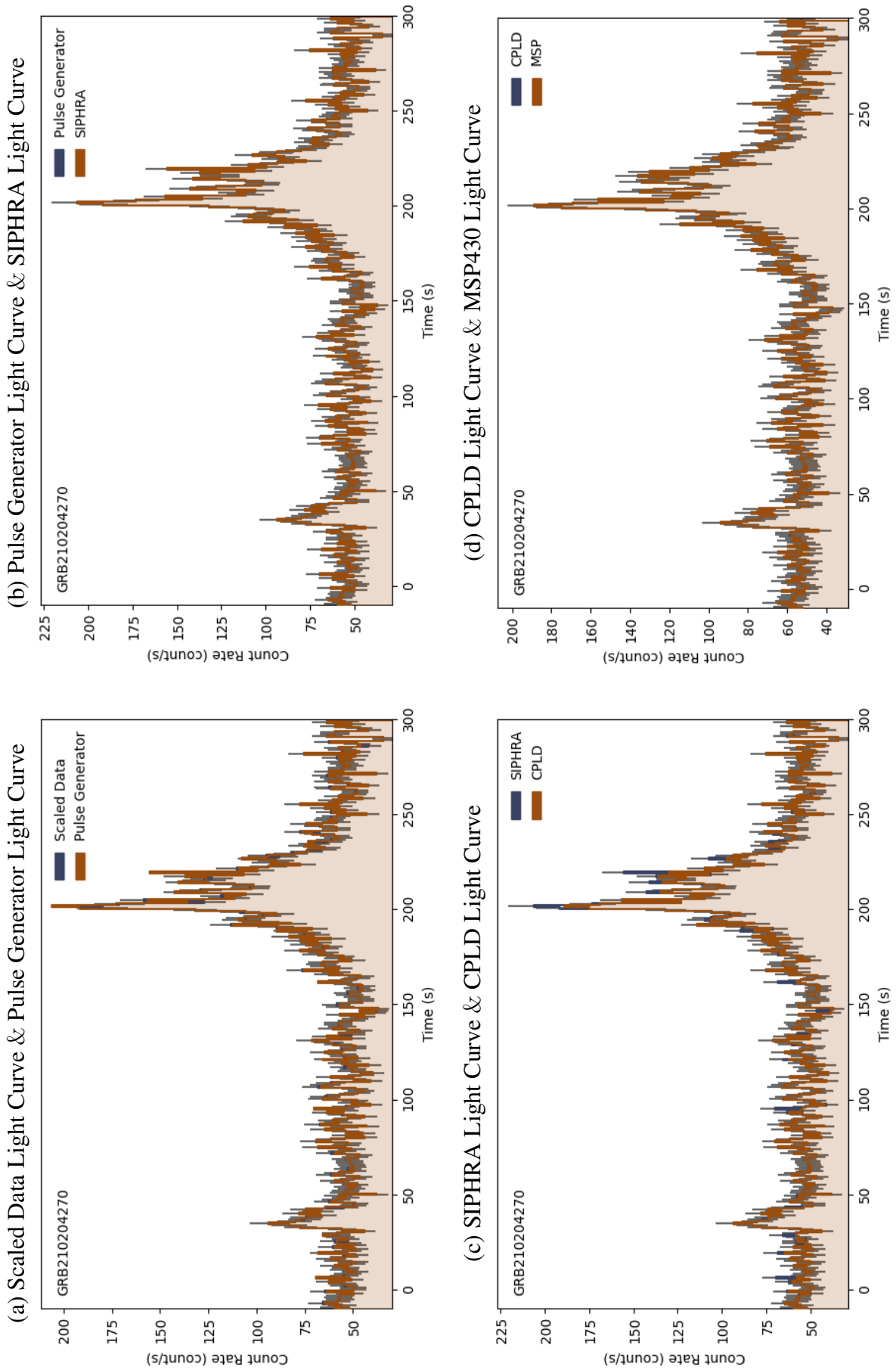

Figure A.4: Comparison 1024 ms binned light curves for each stage of the GMOD readout for a simulated detection of GRB210204270.

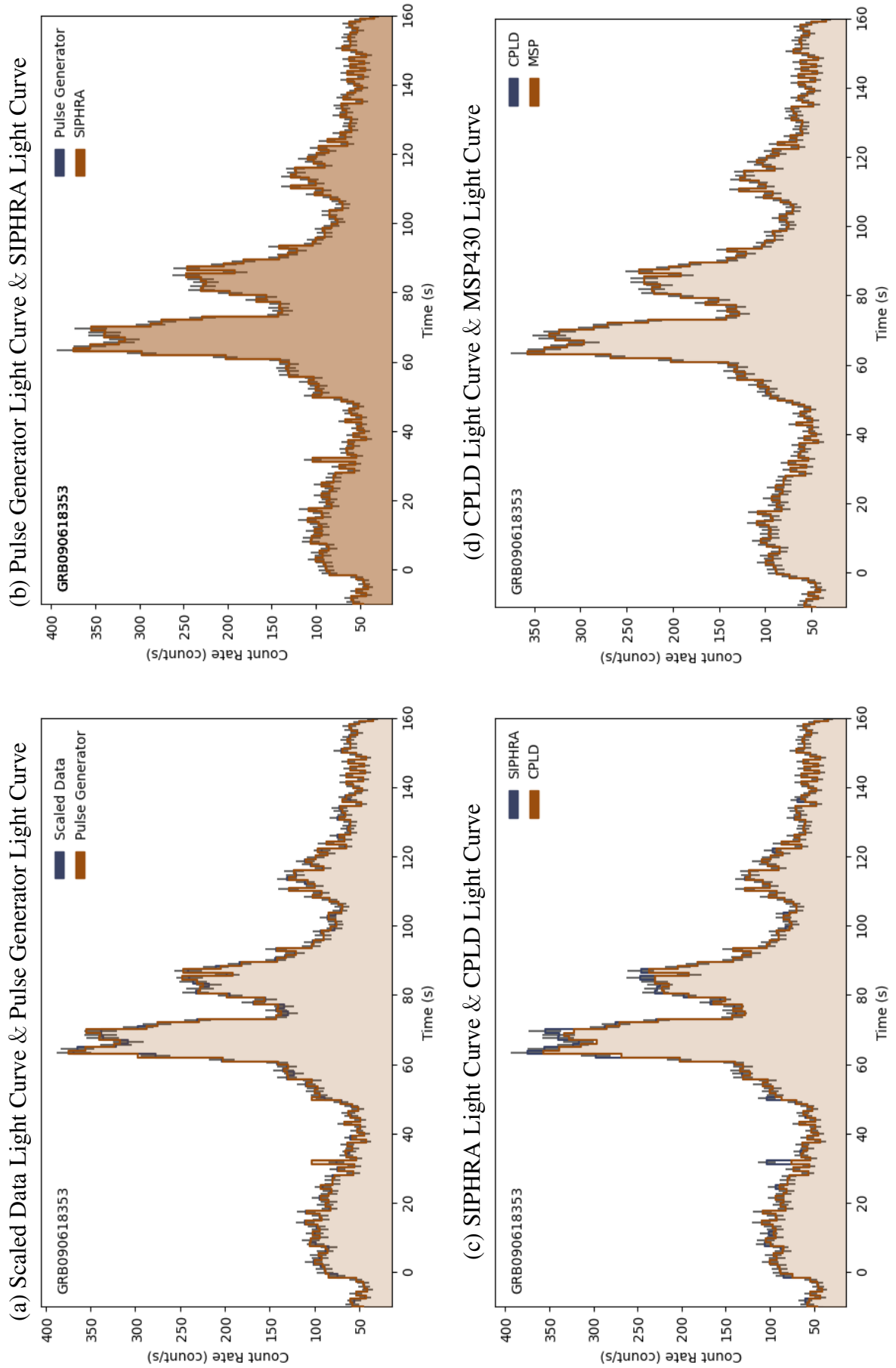

Figure A.5: Comparison 1024 ms binned light curves for each stage of the GMOD readout for a simulated detection of GRB090618353.

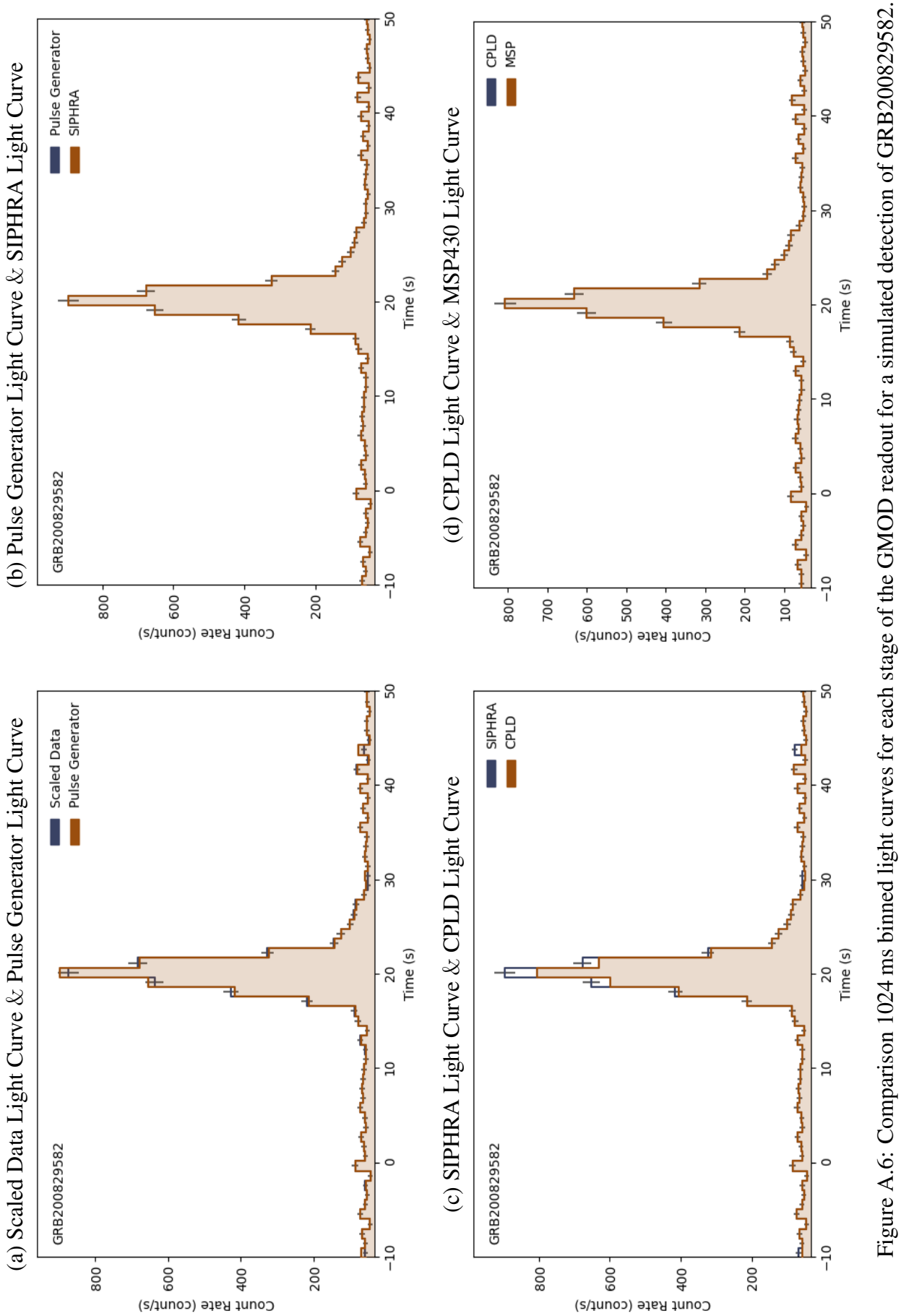

Figure A.6: Comparison 1024 ms binned light curves for each stage of the GMOD readout for a simulated detection of GRB200829582.

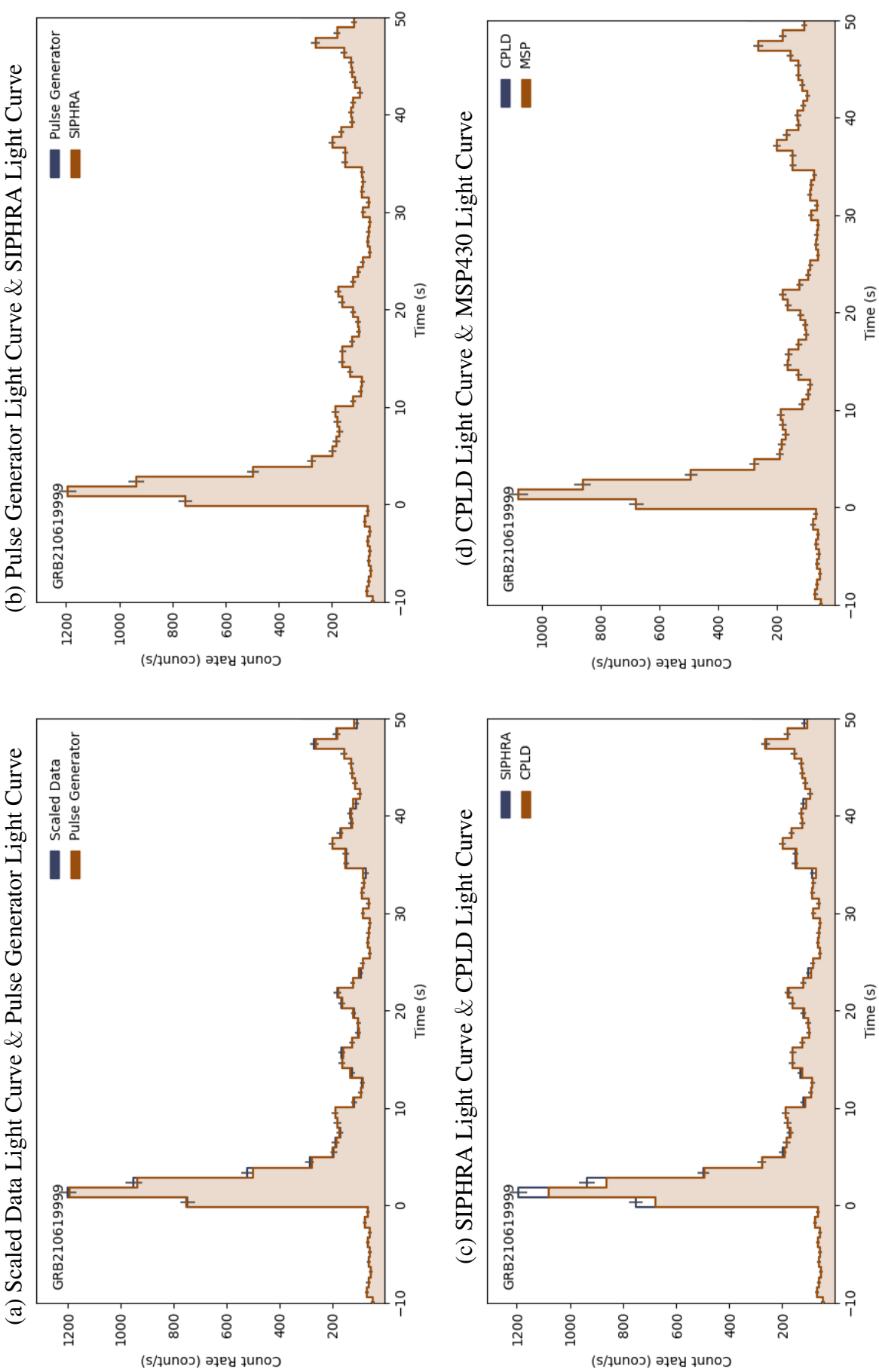

Figure A.7: Comparison 1024 ms binned light curves for each stage of the GMOD readout for a simulated detection of GRB210619999.

Appendix B

Publications and Presentations

First Author

1 Joseph Mangan et al. (Apr. 2021f). "The environmental test campaign of GMOD: a novel gamma-ray detector". In: *International Conference on Space Optics — ICSO 2020*. Ed. by Bruno Cugny et al. Vol. 11852. International Society for Optics and Photonics. SPIE, pp. 471–491. DOI: 10.1117/12.2599225. URL: https://doi.org/10.1117/12.2599225

2 Joseph Mangan et al. (July 2021e). "Embedded Firmware Development for a Novel CubeSat Gamma-Ray Detector". In: *2021 IEEE 8th International Conference on Space Mission Challenges for Information Technology (SMC-IT)*, pp. 14–22. DOI: 10.1109/SMC-IT51442.2021.00009

3 Joseph Mangan et al. (2022c). "Experiences in firmware development for a CubeSat instrument payload". In: *4th Symposium on Space Educational Activities (SSEA): Barcelona, 27-29 April, 2022*. Symposium on Space Educational Activities (SSEA). Universitat Politècnica de Catalunya. ISBN: 9788419184405. DOI: 10.5821/conference-9788419184405.024. URL: http://hdl.handle.net/2117/368782

4 Joseph Mangan et al. (2022d). "Performance analysis of embedded firmware for the detection of gamma-ray bursts on a 2U CubeSat". In: *Space Telescopes and Instrumentation 2022: Ultraviolet to Gamma Ray*. Ed. by Jan-Willem A. den Herder et al. Vol. 12181. International Society for Optics and Photonics. SPIE, 121815A. DOI: 10.1117/12.2627064. URL: https://doi.org/10.1117/12.2627064

Contributing Author

1 Alexei Ulyanov, David Murphy, Joseph Mangan, et al. (2020). "Radiation Damage Study of SensL J-series Silicon Photomultipliers Using 101.4 MeV Protons". In: *Nuclear Instruments and Methods in Physics Research Section A: Accelerators, Spectrometers, Detectors and Associated Equipment* 976. https://doi.org/10.1016/j.nima.2020.164203, p. 164203. ISSN: 0168-9002

2 David Murphy, Alexey Ulyanov, Sheila McBreen, Maeve Doyle, Rachel Dunwoody, Joseph Mangan, et al. (2021a). "A Compact Instrument for Gamma–Ray Burst Detection on a CubeSat Platform I:Design Drivers and Expected Performance". In: *Experimental Astronomy*. DOI: 10.1007/s10686-021-09779-9

3 David Murphy, Joseph Mangan, et al. (2021b). "Balloon flight test of a CeBr3 detector with silicon photomultiplier readout". In: *Experimental Astronomy* 52.1-2, pp. 1–34. DOI: 10.1007/s10686-021-09767-z

4 David Murphy, Alexey Ulyanov, Sheila McBreen, Maeve Doyle, Rachel Dunwoody, Joseph Mangan, et al. (2022). "A Compact Instrument for Gamma–Ray Burst Detection on a CubeSat Platform II:Detailed Design and Laboratory Measurements". In: *Experimental Astronomy*

5 Tomás Ahumada, Leo P. Singer, Shreya Anand, Michael W. Coughlin, Mansi M. Kasliwal, Geoffrey Ryan, Igor Andreoni, S. Bradley Cenko, Christoffer Fremling, Harsh Kumar, Peter T. H. Pang, Eric Burns, Virginia Cunningham, Simone Dichiara, Tim Dietrich, Dmitry S. Svinkin, Mouza Almualla, Alberto J. Castro-Tirado, Kishalay De, Rachel Dunwoody, Pradip Gatkine, Erica Hammerstein, Shabnam Iyyani, Joseph Mangan, et al. (July 2021). "Discovery and confirmation of the shortest gamma-ray burst from a collapsar". In: *Nature Astronomy* 5.9, pp. 917–927. DOI: 10.1038/s41550-021-01428-7. URL: https://doi.org/10.1038%2Fs41550-021-01428-7

6 Tomás Ahumada, Shreya Anand, Michael W. Coughlin, Igor Andreoni, Erik C. Kool, Harsh Kumar, Simeon Reusch, Ana Sagués-Carracedo, Robert Stein, S. Bradley Cenko, Mansi M. Kasliwal, Leo P. Singer, Rachel Dunwoody, Joseph Mangan, et al. (June 2022). "In Search of Short Gamma-Ray Burst Optical Counterparts with the Zwicky Transient Facility". In: *apj* 932.1, 40, p. 40. DOI: 10.3847/1538-4357/ac6c29. arXiv: 2203.11787 [astro-ph.HE]

Presentations (Poster and Oral)

1 *GMOD: The Gamma-Ray Module on EIRSAT-1*, The 4^{th} Symposium of the Committee on Space Research (COSPAR): Small Satellites for Sustainable Science and Development, November 4 - 8, 2019, Herzliya, Israel, (Oral Presentation).

2 *The Environmental Test Campaign of GMOD, a Novel Gamma-Ray Detector*, International Conference on Space Optics - ICSO 2020, 29 March - 2 April 2021, Virtual. Proceedings, (Oral Presentation).

3 *Embedded Firmware Development for a Novel CubeSat Gamma-ray Detector*, The 8^{th} IEEE International Conference on Space Mission Challenges for Information Technology (SMC-IT 2021), July 26 - 30, 2021, Virtual. Website, (Oral Presentation).

4 *Experiences in firmware development for a CubeSat instrument payload*, The 4^{th} Symposium on Space Educational Activities (SSEA), April 27 - 29, 2022, Barcelona, Spain. Website.

5 *Performance analysis of embedded firmware for the detection of gamma-ray bursts on a 2U CubeSat*, SPIE Astronomical Telescopes + Instrumentation 2022, July 17 - 22 2022, Montréal, Canada. Website, (Poster Discussion).

Appendix C

Conferences and Workshops

Conferences

1 *Towards a Network of GRB Detecting Nanosatellites* , September 13 - 14, 2018, Budapest, Hungary. Website.

2 *The 3rd Symposium on Space Educational Activities (SSEA)*, September 16 - 18, 2019, University of Leicester, United Kingdom. Website.

3 *The 4th Symposium of the Committee on Space Research (COSPAR): Small Satellites for Sustainable Science and Development*, November 4 - 8, 2019, Herzliya, Israel.

4 *International Conference on Space Optics — ICSO 2020* , 29 March - 2 April 2021, Virtual. Proceedings.

5 *The 8th IEEE International Conference on Space Mission Challenges for Information Technology (SMC-IT 2021)*, July 26 - 30, 2021, Virtual. Website.

6 *The 4th Symposium on Space Educational Activities (SSEA)*, April 27 - 29, 2022, Barcelona, Spain. Website.

7 *SPIE Astronomical Telescopes + Instrumentation 2022* , July 17 - 22 2022, Montréal, Canada. Website.

8 *Monitoring the High-Energy Sky with Small Satellites*, September 6 - 8, 2022, Brno, Czech Republic. Website.

Workshops

1 *ESA Academy Concurrent Engineering Workshop*, April 30 - May 3, 2019 ESA ESEC-Galaxia, Transinne, Belgium. Website.

2 *ESA Academy Concurrent Engineering Workshop*, April 30 - May 3, 2019 ESA ESEC-Galaxia, Transinne, Belgium. Website.

3 *Fly Your Satellite! Online Soldering Course*, February 16 - 18 February, 2021, Virtual.

Appendix D

Authored GCN Circulars

Authored

1 J. Mangan, S. Lesage, C. Meegan, et al. (May 2022b). "GRB 220528A: Fermi GBM Observation". In: *GRB Coordinates Network* 32155, p. 1

2 J. Mangan, R. Dunwoody, C. Meegan, et al. (May 2022a). "GRB 220527A: Fermi GBM Observation". In: *GRB Coordinates Network* 32133, p. 1

3 J. Mangan, R. Dunwoody, C. Meegan, et al. (Dec. 2021d). "GRB 211211A: Fermi GBM observation". In: *GRB Coordinates Network* 31210, p. 1

4 R. Dunwoody, J. Mangan, C. Meegan, et al. (Nov. 2021). "GRB 211120548: Fermi GBM observation". In: *GRB Coordinates Network* 31131, p. 1

5 J. Mangan, R. Dunwoody, C. Meegan, et al. (June 2021b). "GRB 210421B: Fermi GBM detection". In: *GRB Coordinates Network* 30225, p. 1

6 J. Mangan, R. Dunwoody, S. Lesage, et al. (Jan. 2021a). "GRB 210119A: Fermi GBM observation". In: *GRB Coordinates Network* 29328, p. 1

7 J. Mangan, C. Meegan, and Fermi GBM Team (Dec. 2020b). "GRB 201208A: Fermi GBM observation". In: *GRB Coordinates Network* 29017, p. 1

8 J. Mangan, R. Dunwoody, C. Meegan, et al. (Aug. 2020a). "GRB 200826A: Fermi GBM observation". In: *GRB Coordinates Network* 28287, p. 1

Contributing Author

1 R. Dunwoody, J. Mangan, C. Meegan, et al. (Mar. 2022a). "Correction to GCN 31689: Fermi GBM Report of GRB 220305A should be GRB 220305B". in: *GRB Coordinates Network* 31690, p. 1

2 R. Dunwoody, J. Mangan, C. Meegan, et al. (Mar. 2022b). "GRB 220305A: Fermi GBM observation". In: *GRB Coordinates Network* 31689, p. 1

3 J. Mangan, R. Dunwoody, C. Meegan, et al. (Nov. 2021c). “GRB 211118A: Fermi GBM detection”. In: *GRB Coordinates Network* 31125, p. 1

4 S. Lesage, R. Dunwoody, J. Mangan, et al. (Jan. 2021). “GRB 210120A: Fermi GBM detection”. In: *GRB Coordinates Network* 29361, p. 1

5 S. Lesage, P. Veres, C. Meegan, J. Mangan, R. Dunwoody, et al. (Dec. 2020). “GRB 201227A: Fermi GBM observation”. In: *GRB Coordinates Network* 29206, p. 1

6 R. Dunwoody, J. Mangan, C. Meegan, et al. (Sept. 2020b). “GRB 200914A: Fermi GBM observation”. In: *GRB Coordinates Network* 28424, p. 1

7 R. Dunwoody, C. Fletcher, J. Mangan, et al. (Aug. 2020a). “GRB 200809B: Fermi GBM detection”. In: *GRB Coordinates Network* 28244, p. 1

8 C. Fletcher, R. Dunwoody, J. Mangan, et al. (July 2020). “GRB 200714E: Fermi GBM observation”. In: *GRB Coordinates Network* 28108, p. 1

Bibliography

A.Einstein (1905). “On a Heuristic Point of view Concerning the Production and Transformation of Light”. In: *Annalen der Physik, 17*, pp. 132, 148.

Abbott, B. P. et al. (Oct. 2017a). “Gravitational Waves and Gamma-Rays from a Binary Neutron Star Merger: GW170817 and GRB 170817A”. In: *The Astrophysical Journal Letters* 848.2, p. L13. DOI: 10.3847/2041-8213/aa920c. URL: https://dx.doi.org/10.3847/2041-8213/aa920c.

Abbott, B. P. et al. (Oct. 2017b). “GW170817: Observation of Gravitational Waves from a Binary Neutron Star Inspiral”. In: *Phys. Rev. Lett.* 119 (16), p. 161101. DOI: 10.1103/PhysRevLett.119.161101. URL: https://link.aps.org/doi/10.1103/PhysRevLett.119.161101.

Ahmed, Syed Naeem (2017). *Physics and Engineering of Radiation Detection (Second Edition)*. Ed. by Syed Naeem Ahmed. First Edition. Elsevier. ISBN: 978-0-12-045581-2. DOI: https://doi.org/10.1016/B978-0-12-801363-2.00002-4. URL: %5Chref%7Bhttps://www.sciencedirect.com/science/article/pii/B9780128013632000024%7D.

Ahumada, Tomás et al. (July 2021). “Discovery and confirmation of the shortest gamma-ray burst from a collapsar”. In: *Nature Astronomy* 5.9, pp. 917–927. DOI: 10.1038/s41550-021-01428-7. URL: https://doi.org/10.1038%2Fs41550-021-01428-7.

Ahumada, Tomás et al. (June 2022). “In Search of Short Gamma-Ray Burst Optical Counterparts with the Zwicky Transient Facility”. In: *apj* 932.1, 40, p. 40. DOI: 10.3847/1538-4357/ac6c29. arXiv: 2203.11787 [astro-ph.HE].

Arneodo, Francesco et al. (2021). “A Review of Requirements for Gamma Radiation Detection in Space Using CubeSats”. In: *Applied Sciences* 11.6. ISSN: 2076-3417. DOI: 10.3390/app11062659. URL: https://www.mdpi.com/2076-3417/11/6/2659.

Aslan, A.R. et al. (Sept. 2014). “Development and in Orbit Testing of an X-Ray Detector Within a 2U CubeSat”. In: DOI: 10.13140/2.1.1720.7046.

Atteia, J.-L. et al. (Dec. 2021). “The SVOM mission”. In: *International Journal of Modern Physics D* 31.05. DOI: 10.1142/s0218271822300087. URL: https://doi.org/10.1142%2Fs0218271822300087.

Atwood, W. B. et al. (June 2009). “The Large Area Telescope on the Fermi Gamma-Ray Space Telescope Mission”. In: *The Astrophysical Journal* 697, pp. 1071–1102. DOI: 10.1088/0004-637X/697/2/1071. arXiv: 0902.1089 [astro-ph.IM].

Autodesk, Inc. (2018). “Autodesk Nastran User’s Manual”. In: 2018.

Bagagli, R. et al. (2008). “Environmental tests of the flight GLAST LAT tracker towers”. In: *Nuclear Instruments and Methods in Physics Research Section A: Accelerators, Spectrometers, Detectors and Associated Equipment* 584.2, pp. 358–373. ISSN: 0168-9002. DOI: https://doi.org/10.1016/j.nima.2007.10.035. URL: https://www.sciencedirect.com/science/article/pii/S0168900207022176.

Bailes, M. et al. (Apr. 2021). "Gravitational-wave physics and astronomy in the 2020s and 2030s". In: *Nature Reviews Physics* 3.5, pp. 344–366. DOI: 10.1038/s42254-021-00303-8.

Band, D. et al. (Aug. 1993a). "BATSE Observations of Gamma-Ray Burst Spectra. I. Spectral Diversity". In: *apj* 413, p. 281. DOI: 10.1086/172995.

— (Aug. 1993b). "BATSE Observations of Gamma-Ray Burst Spectra. I. Spectral Diversity". In: *apj* 413, p. 281. DOI: 10.1086/172995.

Barthelmy, S. D. et al. (May 1998). "The GRB coordinates network (GCN): A status report". In: *Gamma-Ray Bursts, 4th Hunstville Symposium*. Ed. by Charles A. Meegan et al. Vol. 428. American Institute of Physics Conference Series, pp. 99–103. DOI: 10.1063/1.55426.

Beechert, Jacqueline et al. (2022). "Calibrations of the Compton Spectrometer and Imager". In: *Nuclear Instruments and Methods in Physics Research Section A: Accelerators, Spectrometers, Detectors and Associated Equipment* 1031, p. 166510. ISSN: 0168-9002. DOI: https://doi.org/10.1016/j.nima.2022.166510. URL: https://www.sciencedirect.com/science/article/pii/S0168900222001243.

Bellm, Eric C. (2014). *The Zwicky Transient Facility*. DOI: 10.48550/ARXIV.1410.8185. URL: https://arxiv.org/abs/1410.8185.

Bhagyaveni, M. A et al. (2016). *Introduction to Analog and Digital Communication*. River Publishers.

Bhat, P. et al. (Apr. 2016). "The 3rd Fermi GBM Gamma-Ray Burst Catalog: The First Six Years". In: *The Astrophysical Journal Supplement Series* 223, p. 28. DOI: 10.3847/0067-0049/223/2/28.

Bhat, P. N. et al. (Sept. 2011). "An overview of the current understanding of Gamma Ray Bursts in the Fermi era". In: *Bulletin of the Astronomical Society of India* 39.3, pp. 471–515. arXiv: 1111.4909 [astro-ph.HE].

Bissaldi, E. et al. (May 2009). "Ground-based calibration and characterization of the Fermi gamma-ray burst monitor detectors". In: *Experimental Astronomy* 24.1-3, pp. 47–88. DOI: 10.1007/s10686-008-9135-4. arXiv: 0812.2908 [astro-ph].

Bloser, Peter F. et al. (2016). "The Advanced Scintillator Compton Telescope (ASCOT) balloon project". In: *Space Telescopes and Instrumentation 2016: Ultraviolet to Gamma Ray*. Ed. by Jan-Willem A. den Herder et al. Vol. 9905. International Society for Optics and Photonics. SPIE, 99056K. DOI: 10.1117/12.2233230. URL: https://doi.org/10.1117/12.2233230.

Boella, G. et al. (1997). "BeppoSAX, the wide band mission for X-ray astronomy". In: *Astron. Astrophys. Suppl. Ser.* 122.2, pp. 299–307. DOI: 10.1051/aas:1997136. URL: https://doi.org/10.1051/aas:1997136.

Burns, Eric (Nov. 2020). "Neutron star mergers and how to study them". In: *Living Reviews in Relativity* 23.1. ISSN: 1433-8351. DOI: 10.1007/s41114-020-00028-7. URL: http://dx.doi.org/10.1007/s41114-020-00028-7.

Camp, Anna et al. (2016). “Determination of LaBr3(Ce) internal background using a HPGe detector and Monte Carlo simulations”. In: *Applied Radiation and Isotopes* 109. Proceedings of the 20th International Conference on Radionuclide Metrology and its Applications 8–11 June 2015, Vienna, Austria, pp. 512–517. ISSN: 0969-8043. DOI: https://doi.org/10.1016/j.apradiso.2015.11.093. URL: https://www.sciencedirect.com/science/article/pii/S0969804315303328.

Cavallo, G. et al. (July 1978). “A qualitative study of cosmic fireballs and gamma-ray bursts”. In: *Monthly Notices of the Royal Astronomical Society* 183.3, pp. 359–365. ISSN: 0035-8711. DOI: 10.1093/mnras/183.3.359. eprint: https://academic.oup.com/mnras/article-pdf/183/3/359/2943441/mnras183-0359.pdf. URL: https://doi.org/10.1093/mnras/183.3.359.

Cieślak, Michał J. et al. (2016). “Coded-aperture imaging systems: Past, present and future development – A review”. In: *Radiation Measurements* 92, pp. 59–71. ISSN: 1350-4487. DOI: https://doi.org/10.1016/j.radmeas.2016.08.002. URL: https://www.sciencedirect.com/science/article/pii/S1350448716301524.

Compton, Arthur H. (May 1923). “A Quantum Theory of the Scattering of X-rays by Light Elements”. In: *Phys. Rev.* 21 (5), pp. 483–502. DOI: 10.1103/PhysRev.21.483. URL: https://link.aps.org/doi/10.1103/PhysRev.21.483.

Connaughton, V. et al. (Feb. 2015). “LOCALIZATION OF GAMMA-RAY BURSTS USING THE FERMI GAMMA-RAY BURST MONITOR”. In: *The Astrophysical Journal Supplement Series* 216.2, p. 32. DOI: 10.1088/0067-0049/216/2/32. URL: https://doi.org/10.1088%2F0067-0049%2F216%2F2%2F32.

Coulter, D. A. et al. (Dec. 2017). “Swope Supernova Survey 2017a (SSS17a), the optical counterpart to a gravitational wave source”. In: *Science* 358.6370, pp. 1556–1558. DOI: 10.1126/science.aap9811. URL: https://doi.org/10.1126%2Fscience.aap9811.

Dado, Shlomo et al. (2022). “Critical Tests of Leading Gamma Ray Burst Theories”. In: *Universe* 8.7. ISSN: 2218-1997. DOI: 10.3390/universe8070350. URL: https://www.mdpi.com/2218-1997/8/7/350.

De Angelis, Alessandro et al. (Oct. 2017). “The e-ASTROGAM mission”. In: *Experimental Astronomy* 44, pp. 1–58. DOI: 10.1007/s10686-017-9533-6.

Dicke, R H (Jan. 1968). “SCATTER-HOLE CAMERAS FOR X-RAYS AND GAMMA RAYS.” In: *Astrophys. J., 153: L101-6(Aug. 1968).* DOI: 10.1086/180230. URL: https://www.osti.gov/biblio/4487785.

Doherty, Kevin et al. (June 2016). “High-Temperature Solar Reflector Coating for the Solar Orbiter”. In: *Journal of Spacecraft and Rockets* 53, pp. 1–8. DOI: 10.2514/1.A33561.

Doyle, Maeve (2022). “Update on the status of the Educational Irish Research Satellite (EIRSAT-1)”. In: *Proceedings on the 4nd Symposium on Space Educational Activities*. URL: TBD.

Doyle, Maeve et al. (2022a). “Design, development, and testing of flight software for EIRSAT-1: a university-class CubeSat enabling astronomical research”. In: *Software and Cyberinfras-*

tructure for Astronomy VII. Ed. by Jorge Ibsen et al. Vol. 12189. International Society for Optics and Photonics. SPIE, p. 1218915. DOI: 10.1117/12.2627464. URL: https://doi.org/10.1117/12.2627464.

Doyle, Maeve et al. (2022b). "Mission Test Campaign for the EIRSAT-1 Engineering Qualification Model". In: *Aerospace* 9.2. ISSN: 2226-4310. DOI: 10.3390/aerospace9020100. URL: https://www.mdpi.com/2226-4310/9/2/100.

Doyle, Maeve. et al. (2021). "Mission Testing for Improved Reliability of CubeSats". In:

Drout, M. R. et al. (Dec. 2017). "Light curves of the neutron star merger GW170817/SSS17a: Implications for r-process nucleosynthesis". In: *Science* 358.6370, pp. 1570–1574. DOI: 10.1126/science.aaq0049. URL: https://doi.org/10.1126%2Fscience.aaq0049.

Drozdowski, Winicjusz et al. (July 2008). "CeBr Scintillator Development for Possible Use in Space Missions". In: *Nuclear Science, IEEE Transactions on* 55, pp. 1391–1396. DOI: 10.1109/TNS.2007.908579.

Dunwoody, R. et al. (Aug. 2020a). "GRB 200809B: Fermi GBM detection". In: *GRB Coordinates Network* 28244, p. 1.

Dunwoody, R. et al. (Sept. 2020b). "GRB 200914A: Fermi GBM observation". In: *GRB Coordinates Network* 28424, p. 1.

— (Nov. 2021). "GRB 211120548: Fermi GBM observation". In: *GRB Coordinates Network* 31131, p. 1.

— (Mar. 2022a). "Correction to GCN 31689: Fermi GBM Report of GRB 220305A should be GRB 220305B". In: *GRB Coordinates Network* 31690, p. 1.

— (Mar. 2022b). "GRB 220305A: Fermi GBM observation". In: *GRB Coordinates Network* 31689, p. 1.

Dunwoody, Rachel et al. (2022c). "Thermal Vacuum Test Campaign of the EIRSAT-1 Engineering Qualification Model". In: *Aerospace* 9.2. ISSN: 2226-4310. DOI: 10.3390/aerospace9020099. URL: https://www.mdpi.com/2226-4310/9/2/99.

EIRSAT-1 (2017). *Fly Your Satellite! 2017 CubeSat Proposal: EIRSAT-1*. Tech. rep. University College Dublin, Ireland.

Erkal, Jessica et al. (2017). "EIRSAT-1 Design Definition File - Rev 1.0". unpublished.

ESA Education Office (Apr. 2018). "Fly Your Satellite': Design Specification Version 2.5, (ESA) Education". In: Rev. 2.5. Rev. 2.5, ESA-DG-SET-2018-1553.

Fenimore, E. E. et al. (Feb. 1978). "Coded aperture imaging with uniformly redundant arrays". In: *Appl. Opt.* 17.3, pp. 337–347. DOI: 10.1364/AO.17.000337. URL: https://opg.optica.org/ao/abstract.cfm?URI=ao-17-3-337.

Fishman, G. J. et al. (Feb. 1992). "The BATSE experiment on the Compton Gamma Ray Observatory: status and some early results." In: *NASA Conference Publication*. Vol. 3137. NASA Conference Publication, pp. 26–34.

Fishman, Gerald J. et al. (May 1994). "The First BATSE Gamma-Ray Burst Catalog". In: *apjs* 92, p. 229. DOI: 10.1086/191968.

Fletcher, C. et al. (July 2020). “GRB 200714E: Fermi GBM observation”. In: *GRB Coordinates Network* 28108, p. 1.

Fuschino, F. et al. (Aug. 2019). “HERMES: An ultra-wide band X and gamma-ray transient monitor on board a nano-satellite constellation”. In: *Nuclear Instruments and Methods in Physics Research Section A: Accelerators, Spectrometers, Detectors and Associated Equipment* 936, pp. 199–203. DOI: 10.1016/j.nima.2018.11.072. URL: https://doi.org/10.1016%2Fj.nima.2018.11.072.

Galama, T. J. et al. (Oct. 1998). “An unusual supernova in the error box of the gamma-ray burst of 25 April 1998”. In: *nat* 395.6703, pp. 670–672. DOI: 10.1038/27150. arXiv: astro-ph/9806175 [astro-ph].

Garutti, E. et al. (2019). “Radiation damage of SiPMs”. In: *Nuclear Instruments and Methods in Physics Research Section A: Accelerators, Spectrometers, Detectors and Associated Equipment* 926. Silicon Photomultipliers: Technology, Characterisation and Applications, pp. 69–84. ISSN: 0168-9002. DOI: https://doi.org/10.1016/j.nima.2018.10.191. URL: https://www.sciencedirect.com/science/article/pii/S0168900218315055.

Gehrels, N. (Jan. 1997). “Use of νF_ν spectral energy distributions for multiwavelength astronomy.” In: *Nuovo Cimento B Serie* 112B.1, pp. 11–15.

Gehrels, N. et al. (Aug. 2004). “The Swift Gamma-Ray Burst Mission”. In: *The Astrophysical Journal* 611, pp. 1005–1020. DOI: 10.1086/422091.

Ghirlanda, G. et al. (June 2007). “Blackbody components in gamma-ray bursts spectra?” In: *Monthly Notices of the Royal Astronomical Society* 379.1, pp. 73–85. ISSN: 0035-8711. DOI: 10.1111/j.1365-2966.2007.11890.x. eprint: https://academic.oup.com/mnras/article-pdf/379/1/73/3921441/mnras0379-0073.pdf. URL: https://doi.org/10.1111/j.1365-2966.2007.11890.x.

Gilmore, Gordon et al. (1995). *Practical gamma-ray spectroscopy*. Wiley.

Gobain, Saint (2021). *Lanthanum Bromide Scintillators Performance Summary*. Products Technical Note. Saint Gobain.

Goldstein, A. et al. (Oct. 2017). “An Ordinary Short Gamma-Ray Burst with Extraordinary Implications: Fermi-GBM Detection of GRB 170817A”. In: *The Astrophysical Journal* 848.2, p. L14. DOI: 10.3847/2041-8213/aa8f41. URL: https://doi.org/10.3847%2F2041-8213%2Faa8f41.

Goldstein, Adam et al. (2022). *Fermi GBM Data Tools: v1.1.1*. URL: https://fermi.gsfc.nasa.gov/ssc/data/analysis/gbm.

Greiner, J. et al. (2012). “GRIPS - Gamma-Ray Imaging, Polarimetry and Spectroscopy”. In: *Exper. Astron.* 34, pp. 551–582. DOI: 10.1007/s10686-011-9255-0. arXiv: 1105.1265 [astro-ph.HE].

Guertin, S. M. et al. (2015). “Radiation Test Results for Common CubeSat Microcontrollers and Microprocessors”. In: *2015 IEEE Radiation Effects Data Workshop (REDW)*, pp. 1–9. DOI: 10.1109/REDW.2015.7336730.

Gundacker, Stefan et al. (Aug. 2020). “The silicon photomultiplier: fundamentals and applications of a modern solid-state photon detector”. In: *Physics in Medicine and Biology* 65.17, 17TR01. DOI: 10.1088/1361-6560/ab7b2d. URL: https://doi.org/10.1088/1361-6560/ab7b2d.

Hartman, R. C. et al. (July 1999). “The Third EGRET Catalog of High-Energy Gamma-Ray Sources”. In: *The Astrophysical Journal Supplement Series* 123.1, p. 79. DOI: 10.1086/313231. URL: https://dx.doi.org/10.1086/313231.

Hirata, K. et al. (Apr. 1987). “Observation of a neutrino burst from the supernova SN1987A”. In: *prl* 58.14, pp. 1490–1493. DOI: 10.1103/PhysRevLett.58.1490.

Hjorth, Jens et al. (2011). “The Gamma-Ray Burst - Supernova Connection”. In: DOI: 10.48550/ARXIV.1104.2274. URL: https://arxiv.org/abs/1104.2274.

Hurley, K. et al. (May 2006). “Mars Odyssey Joins the Third Interplanetary Network”. In: *The Astrophysical Journal Supplement Series* 164.1, pp. 124–129. DOI: 10.1086/501352. URL: https://doi.org/10.1086%2F501352.

Hurley, K. et al. (Aug. 2013). “THE INTERPLANETARY NETWORK SUPPLEMENT TO THE FERMI GBM CATALOG OF COSMIC GAMMA-RAY BURSTS”. In: *The Astrophysical Journal Supplement Series* 207.2, p. 39. DOI: 10.1088/0067-0049/207/2/39. URL: https://doi.org/10.1088/0067-0049/207/2/39.

Hurley, K. et al. (2021). “THE INTERPLANETARY NETWORK”. In: *Progenitors, Environments and Host Galaxies from the Nearby to the Early Universe*. Les Ulis: EDP Sciences, pp. 459–464. ISBN: 9782759810024. DOI: doi:10.1051/978-2-7598-1002-4.c076. URL: https://doi.org/10.1051/978-2-7598-1002-4.c076.

IceCube Collaboration et al. (July 2018). “Multimessenger observations of a flaring blazar coincident with high-energy neutrino IceCube-170922A”. In: *Science* 361.6398, eaat1378, eaat1378. DOI: 10.1126/science.aat1378. arXiv: 1807.08816 [astro-ph.HE].

Idaho National Engineering & Environmental Laboratory (1999 (Original 1974)). *Gamma-Ray Spectrum Catalogue: Ge(Li) and Si(Li) Detector Spectra*. Idaho National Engineering & Environmental Laboratory.

IDEAS (2022). *Galao – ROIC Development Kit*. Product Overview. IDEAS, Oslo Norway.

International Organization for Standardization (2004). *Arc Welding and Cutting - Tungsten Electrode - Classification (ISO 6848: 2004)*. ISO. URL: https://www.iso.org/standard/40551.html.

Johnstone, Alicia (2021). *CubeSat Design Specification:REV 14*. URL: %5Chref%7Bhttps://static1.squarespace.com/static/5418c831e4b0fa4ecac1bacd/t/5f24997b6deea10cc52bb016/1596234122437/CDS+REV14+2020-07-31+DRAFT.pdf%7D.

JAXA (Jan. 2015). *JEM Payload Accommodation Handbook - Vol. 8 - Small Satellite Deployment Interface Control Document*. Standard. Japan Aerospace Exploration Agency (JAXA).

Kanbach, G. et al. (2005). “Development and calibration of the tracking Compton/Pair telescope MEGA”. In: *Nuclear Instruments and Methods in Physics Research Section A: Ac-*

celerators, Spectrometers, Detectors and Associated Equipment 541.1. Development and Application of Semiconductor Tracking Detectors, pp. 310–322. ISSN: 0168-9002. DOI: https://doi.org/10.1016/j.nima.2005.01.071. URL: https://www.sciencedirect.com/science/article/pii/S0168900205001567.

Klesh, A. et al. (2013). "Proceedings of the Small Satellite Conference". In: *Small Satellite Constellations: Strength in Numbers*.

Knoll, Glenn F. (2012). *Radiation Detection and Measurement 4th Edition*. John Wiley and Sons.

Kochanek, Christopher S. et al. (Nov. 1993). "Gravitational Waves and gamma -Ray Bursts". In: *The Astrophysical Journal* 417, p. L17. DOI: 10.1086/187083. URL: https://doi.org/10.1086%2F187083.

Kouveliotou, Chryssa et al. (Aug. 1993). "Identification of Two Classes of Gamma-Ray Bursts". In: *apjl* 413, p. L101. DOI: 10.1086/186969.

Laviron, A. et al. (Dec. 2021). "COMCUBE: A constellation of CubeSats to measure the GRB prompt emission polarization". In: *SF2A-2021: Proceedings of the Annual meeting of the French Society of Astronomy and Astrophysics. Eds.: A. Siebert*. Ed. by A. Siebert et al., pp. 105–108.

Lazzati, Davide (Feb. 2005). "Precursor activity in bright, long BATSE gamma-ray bursts". In: *mnras* 357.2, pp. 722–731. DOI: 10.1111/j.1365-2966.2005.08687.x. arXiv: astro-ph/0411753 [astro-ph].

Lesage, S. et al. (Dec. 2020). "GRB 201227A: Fermi GBM observation". In: *GRB Coordinates Network* 29206, p. 1.

Lesage, S. et al. (Jan. 2021). "GRB 210120A: Fermi GBM detection". In: *GRB Coordinates Network* 29361, p. 1.

Li, Liang (2021). *Standard GRB Spectral Models "Misused"?* DOI: 10.48550/ARXIV.2103.11091. URL: https://arxiv.org/abs/2103.11091.

Lindström, Gunnar (2003). "Radiation damage in silicon detectors". In: *Nuclear Instruments and Methods in Physics Research Section A: Accelerators, Spectrometers, Detectors and Associated Equipment* 512.1. Proceedings of the 9th European Symposium on Semiconductor Detectors: New Developments on Radiation Detectors, pp. 30–43. ISSN: 0168-9002. DOI: https://doi.org/10.1016/S0168-9002(03)01874-6. URL: https://www.sciencedirect.com/science/article/pii/S0168900203018746.

Longair, Malcolm S. (2011). *High Energy Astrophysics*. 3rd ed. Cambridge University Press. DOI: 10.1017/CBO9780511778346.

Lucchetta, Giulio (2021). *MeVCube: a CubeSat for MeV astronomy*. DOI: 10.48550/ARXIV.2108.03307. URL: https://arxiv.org/abs/2108.03307.

Maggiore, Michele et al. (Mar. 2020). "Science case for the Einstein telescope". In: *Journal of Cosmology and Astroparticle Physics* 2020.03, pp. 050–050. DOI: 10.1088/1475-7516/2020/03/050. URL: https://doi.org/10.1088%2F1475-7516%2F2020%2F03%2F050.

Mangan, J. et al. (Aug. 2020a). "GRB 200826A: Fermi GBM observation". In: *GRB Coordinates Network* 28287, p. 1.

Mangan, J. et al. (Dec. 2020b). "GRB 201208A: Fermi GBM observation". In: *GRB Coordinates Network* 29017, p. 1.

Mangan, J. et al. (Jan. 2021a). "GRB 210119A: Fermi GBM observation". In: *GRB Coordinates Network* 29328, p. 1.

Mangan, J. et al. (June 2021b). "GRB 210421B: Fermi GBM detection". In: *GRB Coordinates Network* 30225, p. 1.

— (Nov. 2021c). "GRB 211118A: Fermi GBM detection". In: *GRB Coordinates Network* 31125, p. 1.

— (Dec. 2021d). "GRB 211211A: Fermi GBM observation". In: *GRB Coordinates Network* 31210, p. 1.

— (May 2022a). "GRB 220527A: Fermi GBM Observation". In: *GRB Coordinates Network* 32133, p. 1.

Mangan, J. et al. (May 2022b). "GRB 220528A: Fermi GBM Observation". In: *GRB Coordinates Network* 32155, p. 1.

Mangan, Joseph et al. (July 2021e). "Embedded Firmware Development for a Novel CubeSat Gamma-Ray Detector". In: *2021 IEEE 8th International Conference on Space Mission Challenges for Information Technology (SMC-IT)*, pp. 14–22. DOI: 10.1109/SMC-IT51442.2021.00009.

Mangan, Joseph et al. (Apr. 2021f). "The environmental test campaign of GMOD: a novel gamma-ray detector". In: *International Conference on Space Optics — ICSO 2020*. Ed. by Bruno Cugny et al. Vol. 11852. International Society for Optics and Photonics. SPIE, pp. 471–491. DOI: 10.1117/12.2599225. URL: https://doi.org/10.1117/12.2599225.

Mangan, Joseph et al. (2022c). "Experiences in firmware development for a CubeSat instrument payload". In: *4th Symposium on Space Educational Activities (SSEA): Barcelona, 27-29 April, 2022*. Symposium on Space Educational Activities (SSEA). Universitat Politècnica de Catalunya. ISBN: 9788419184405. DOI: 10.5821/conference-9788419184405.024. URL: http://hdl.handle.net/2117/368782.

— (2022d). "Performance analysis of embedded firmware for the detection of gamma-ray bursts on a 2U CubeSat". In: *Space Telescopes and Instrumentation 2022: Ultraviolet to Gamma Ray*. Ed. by Jan-Willem A. den Herder et al. Vol. 12181. International Society for Optics and Photonics. SPIE, 121815A. DOI: 10.1117/12.2627064. URL: https://doi.org/10.1117/12.2627064.

Mazets, E. P. et al. (Mar. 1981). "Recent Results from the Gamma-Ray Burst Studies in the KONUS Experiment". In: *apss* 75.1, pp. 47–81. DOI: 10.1007/BF00651384.

McEnery, J. et al. (Jan. 2020). "All Sky Medium Energy Gamma-ray Observatory (AMEGO): Exploring the Extreme Multimessenger Universe". In: *American Astronomical Society Meeting Abstracts #235*. Vol. 235. American Astronomical Society Meeting Abstracts, p. 372.15.

Meegan, C. et al. (Sept. 2009). "The Fermi Gamma-ray Burst Monitor". In: *The Astrophysical Journal* 702, 791, pp. 791–804. DOI: 10.1088/0004-637X/702/1/791. arXiv: 0908.0450 [astro-ph.IM].

Mehta, Sanjeev et al. (Aug. 2020). "3UCubed: The IMAP Student Collaboration CubeSat Project". In: *36th Annual Small Satellite Conference*. URL: https://digitalcommons.usu.edu/smallsat/2022/all2022/337/.

Meier, Dirk et al. (June 2016). "SIPHRA 16-Channel Silicon Photomultiplier Readout ASIC". In: DOI: 10.13140/RG.2.1.1460.8882.

Microsoft/IBM (1991). *Multimedia Programming Interface and Data Specifications 1.0.* , (Accessed: 28 June 2022).

Mitchell, L. J. et al. (2017). *The MERger-event Gamma-Ray (MERGR) Telescope*. DOI: 10.48550/ARXIV.1711.03631. URL: https://arxiv.org/abs/1711.03631.

Mitchell, Lee et al. (2022). "Radiation damage assessment of SiPMs for scintillation detectors". In: *Nuclear Instruments and Methods in Physics Research Section A: Accelerators, Spectrometers, Detectors and Associated Equipment* 1040, p. 167163. ISSN: 0168-9002. DOI: https://doi.org/10.1016/j.nima.2022.167163. URL: https://www.sciencedirect.com/science/article/pii/S0168900222005320.

Mitchell, Lee J. et al. (2019). *Strontium Iodide Radiation Instrument (SIRI) – Early On-Orbit Results*. DOI: 10.48550/ARXIV.1907.11364. URL: https://arxiv.org/abs/1907.11364.

Mitchell, Lee J. et al. (2021). "Radiation damage assessment of SensL SiPMs". In: *Nucl. Instrum. Meth. A* 988, p. 164798. DOI: 10.1016/j.nima.2020.164798. arXiv: 2003.08213 [physics.ins-det].

Mitrofanov, I.G. et al. (2010). "The Mercury Gamma and Neutron Spectrometer (MGNS) on board the Planetary Orbiter of the BepiColombo mission". In: *Planetary and Space Science* 58.1. Comprehensive Science Investigations of Mercury: The scientific goals of the joint ESA/JAXA mission BepiColombo, pp. 116–124. ISSN: 0032-0633. DOI: https://doi.org/10.1016/j.pss.2009.01.005. URL: https://www.sciencedirect.com/science/article/pii/S003206330900021X.

Mizushima, Tsubasa et al. (2020). "Study on possible proton-induced background of LaBr3(Ce) scintillator in a low-Earth orbit". In: *X-Ray, Optical, and Infrared Detectors for Astronomy IX*. Ed. by Andrew D. Holland et al. Vol. 11454. International Society for Optics and Photonics. SPIE, 114542S. DOI: 10.1117/12.2560810. URL: https://doi.org/10.1117/12.2560810.

Moiseev, Alexander (Aug. 2017). "All-Sky Medium Energy Gamma-ray Observatory (AMEGO)". In: p. 798. DOI: 10.22323/1.301.0798.

Moiseev, Alexander A et al. (2015). "Compton-Pair Production Space Telescope (ComPair) for MeV Gamma-ray Astronomy". In: *arXiv: Instrumentation and Methods for Astrophysics*.

Monteiro, João P. et al. (2019). “Integration and Verification Approach of ISTSat-1 CubeSat”. In: *Aerospace* 6.12. ISSN: 2226-4310. URL: https://www.mdpi.com/2226-4310/6/12/131.

Mortimer, R K et al. (Mar. 1954). “THE GAMMA-RAY PINHOLE CAMERA WITH IMAGE AMPLIFIER”. In: DOI: 10.2172/4396790. URL: https://www.osti.gov/biblio/4396790.

Müller, D. et al. (Sept. 2020). “The Solar Orbiter mission”. In: *Astronomy and Astrophysics* 642, A1. DOI: 10.1051/0004-6361/202038467. URL: https://doi.org/10.1051%2F0004-6361%2F202038467.

Murphy, David et al. (Apr. 2018). “EIRSAT-1: The Educational Irish Research Satellite”. In: *Proceedings on the 2nd Symposium on Space Educational Activities* 0. URL: $http://www.hit.bme.hu/~bacsardi/SSEA/SSEA2018_proceedings.pdf$.

Murphy, David et al. (2021a). “A Compact Instrument for Gamma–Ray Burst Detection on a CubeSat Platform I:Design Drivers and Expected Performance”. In: *Experimental Astronomy*. DOI: 10.1007/s10686-021-09779-9.

Murphy, David et al. (2021b). “Balloon flight test of a CeBr3 detector with silicon photomultiplier readout”. In: *Experimental Astronomy* 52.1-2, pp. 1–34. DOI: 10.1007/s10686-021-09767-z.

Murphy, David et al. (2022). “A Compact Instrument for Gamma–Ray Burst Detection on a CubeSat Platform II:Detailed Design and Laboratory Measurements”. In: *Experimental Astronomy*.

Nobashi, Daiki et al. (2021). “Performance evaluation of GAGG(Ce)/LFS scintillator and MPPC array readout with ASIC”. In: *Nuclear Instruments and Methods in Physics Research Section A: Accelerators, Spectrometers, Detectors and Associated Equipment* 986, p. 164811. ISSN: 0168-9002. DOI: https://doi.org/10.1016/j.nima.2020.164811. URL: %5Chref%7Bhttps://www.sciencedirect.com/science/article/pii/S0168900220312080%7D.

NanoRacks (Dec. 2013). *NanoRacks CubeSat Deployer (NRCSD) Interface Control Document*. Standard. 18100 Upper Bay Road, Suite 150, Houston, TX 77058, (815) 425-8553: NanoRacks.

Oates, S R et al. (Aug. 2021). “Swift UVOT follow-up of gravitational wave alerts in the O3 era”. In: *Monthly Notices of the Royal Astronomical Society* 507.1, pp. 1296–1317. DOI: 10.1093/mnras/stab2189. URL: https://doi.org/10.1093%2Fmnras%2Fstab2189.

OnSemiconductor, 2017 (2018). *J-Series SiPM Sensors: Silicon Photomultipliers (SiPM), High PDE and Timing Resolution Sensors in a TSV Package, Rev6*. URL: https://www.onsemi.com/pub/Collateral/MICROJ-SERIES-D.PDF (visited on 01/10/2020).

Otte, Adam Nepomuk et al. (Feb. 2017). “Characterization of Three High Efficiency and Blue Sensitive Silicon Photomultipliers”. In: *Nuclear Instruments and Methods in Physics Research Section A: Accelerators, Spectrometers, Detectors and Associated Equipment* 846,

pp. 106–125. ISSN: 0168-9002. DOI: 10.1016/j.nima.2016.09.053. URL: http://dx.doi.org/10.1016/j.nima.2016.09.053.

Pál, András et al. (2020). *GRBAlpha: A 1U CubeSat mission for validating timing-based gamma-ray burst localization*. DOI: 10.48550/ARXIV.2012.01298. URL: https://arxiv.org/abs/2012.01298.

Parajuli, Raj Kumar et al. (2022). "Development and Applications of Compton Camera - A Review". In: *Sensors* 22.19. ISSN: 1424-8220. DOI: 10.3390/s22197374. URL: https://www.mdpi.com/1424-8220/22/19/7374.

PC/104 Consortium (2015). URL: https://pc104.org/wp-content/uploads/2015/03/PCI104_Express_v3_0.pdf.

Perkins, Jeremy S. et al. (2017). "BurstCube: A CubeSat for Gravitational Wave Counterparts". In: *PoS* ICRC2017, p. 760. DOI: 10.22323/1.301.0760.

Poolakkil, S. et al. (May 2021). "The Fermi-GBM Gamma-Ray Burst Spectral Catalog: 10 yr of Data". In: *The Astrophysical Journal* 913.1, p. 60. DOI: 10.3847/1538-4357/abf24d. URL: https://doi.org/10.3847/1538-4357/abf24d.

Preece, Robert et al. (Apr. 2016). "Which E_{peak}? The Characteristic Energy of Gamma-ray Burst Spectra". In: *apj* 821.1, 12, p. 12. DOI: 10.3847/0004-637X/821/1/12. arXiv: 1603.02962 [astro-ph.HE].

Quarati, F.G.A. et al. (2012). "Study of 138La radioactive decays using LaBr3 scintillators". In: *Nuclear Instruments and Methods in Physics Research Section A: Accelerators, Spectrometers, Detectors and Associated Equipment* 683, pp. 46–52. ISSN: 0168-9002. DOI: https://doi.org/10.1016/j.nima.2012.04.066. URL: https://www.sciencedirect.com/science/article/pii/S0168900212004457.

Quarati, F.G.A. et al. (2013). "Scintillation and detection characteristics of high-sensitivity CeBr3 gamma-ray spectrometers". In: *Nuclear Instruments and Methods in Physics Research Section A: Accelerators, Spectrometers, Detectors and Associated Equipment* 729, pp. 596–604. ISSN: 0168-9002. DOI: https://doi.org/10.1016/j.nima.2013.08.005. URL: https://www.sciencedirect.com/science/article/pii/S0168900213011297.

Rando, R et al. (Feb. 2019). "e-ASTROGAM: a space mission for MeV-GeV gamma-ray astrophysics". In: *Journal of Physics: Conference Series* 1181, p. 012044. DOI: 10.1088/1742-6596/1181/1/012044. URL: https://doi.org/10.1088/1742-6596/1181/1/012044.

Rau, A. et al. (2005). "The 1st INTEGRAL SPI-ACS gamma-ray burst catalogue". In: *A&A* 438.3, pp. 1175–1183. DOI: 10.1051/0004-6361:20053159. URL: https://doi.org/10.1051/0004-6361:20053159.

Renker, D et al. (Apr. 2009). "Advances in solid state photon detectors". In: *Journal of Instrumentation* 4.04, P04004–P04004. DOI: 10.1088/1748-0221/4/04/p04004. URL: https://doi.org/10.1088/1748-0221/4/04/p04004.

Řípa, Jakub et al. (2020). "A comparison of trapped particle models in low Earth orbit". In: *Space Telescopes and Instrumentation 2020: Ultraviolet to Gamma Ray*. Ed. by Jan-Willem A. den Herder et al. Vol. 11444. International Society for Optics and Photonics. SPIE, 114443P. DOI: 10.1117/12.2561011. URL: https://doi.org/10.1117/12.2561011.

Savchenko, V. et al. (Oct. 2017). "INTEGRAL Detection of the First Prompt Gamma-Ray Signal Coincident with the Gravitational-wave Event GW170817". In: *apjl* 848.2, L15, p. L15. DOI: 10.3847/2041-8213/aa8f94. arXiv: 1710.05449 [astro-ph.HE].

Schönfelder, Volker (2001). *The Universe in Gamma Rays*. Heidelberg, Germany: Springer-Verlag Berlin Heidelberg.

Schönfelder, Volker et al. (2013). "Imaging through Compton scattering and pair creation". In: *Observing Photons in Space: A Guide to Experimental Space Astronomy*. Ed. by Martin C. E. Huber et al. New York, NY: Springer New York, pp. 225–242. ISBN: 978-1-4614-7804-1. DOI: 10.1007/978-1-4614-7804-1_11. URL: https://doi.org/10.1007/978-1-4614-7804-1_11.

Schoolcraft, Josh et al. (Mar. 2017). "MarCO: Interplanetary Mission Development on a CubeSat Scale". In: Springer, pp. 221–231. ISBN: 978-3-319-51940-1. DOI: 10.1007/978-3-319-51941-8_10.

Sherwin, Daire et al. (Apr. 2018). "Wave-based attitude control of EIRSAT-1, 2U cubesat". In:

Smartt, S. J. et al. (Nov. 2017). "A kilonova as the electromagnetic counterpart to a gravitational-wave source". In: *nat* 551.7678, pp. 75–79. DOI: 10.1038/nature24303. arXiv: 1710.05841 [astro-ph.HE].

Stein, Timo A. et al. (2019). "Radiation Testing of the IDE3380 SiPM Readout ASIC". In: *2019 19th European Conference on Radiation and Its Effects on Components and Systems (RADECS)*, pp. 1–7. DOI: 10.1109/RADECS47380.2019.9745675.

Tavani, Marco (May 1996). "Shock Emission Model for Gamma-Ray Bursts". In: *Phys. Rev. Lett.* 76 (19), pp. 3478–3481. DOI: 10.1103/PhysRevLett.76.3478. URL: https://link.aps.org/doi/10.1103/PhysRevLett.76.3478.

Tavani, Marco et al. (Mar. 2003). "The AGILE instrument". In: *X-Ray and Gamma-Ray Telescopes and Instruments for Astronomy*. Ed. by Joachim E. Truemper et al. Vol. 4851. Society of Photo-Optical Instrumentation Engineers (SPIE) Conference Series, pp. 1151–1162. DOI: 10.1117/12.461312.

The European Space Agency for the members of ECSS (2002). *ECSS-E-ST-10-03A. Space engineering: Testing*. The European Space Agency (ESA).

— (2008a). *ECSS-E-ST-10-03A. Space engineering: Thermal control general requirements*. The European Space Agency (ESA).

— (2008b). *ECSS-Q-ST-70-02C. Thermal vacuum outgassing test for the screening of space materials*. The European Space Agency (ESA).

— (2009a). *ECSS-E-ST-32-10C. Structural factors of safety for spaceflight hardware*. The European Space Agency (ESA).

The European Space Agency for the members of ECSS (2009b). *ECSS-M-ST-10C. Space project management: Project planning and implementation*. The European Space Agency (ESA). URL: https://ecss.nl/standard/ecss-m-st-10c-rev-1-project-planning-and-implementation/.

— (2010). *ECSS-E-HB-10-02A. Verification guidelines*. The European Space Agency (ESA). URL: https://ecss.nl/hbstms/ecss-e-10-02a-verification-guidelines/.

— (2012). *ECSS-E-ST-10-03C. Space engineering: Testing*. The European Space Agency (ESA). URL: https://ecss.nl/standard/ecss-e-st-10-03c-testing/.

— (2018). *ECSS-Q-ST-10-09C. Space product assurance: Nonconformance control system*. The European Space Agency (ESA). URL: https://ecss.nl/standard/24183/.

Topinka, Martin et al. (Jan. 2014). "Gamma-ray burst afterglows with the Watcher robotic telescope". In: *Revista Mexicana de Astronomia y Astrofisica: Serie de Conferencias* 45, pp. 65–68.

Ubbels, W. J. et al. (2005). "Delfi-C3: a Student Nanosatellite as a Test-Bed for Thin Film Solar Cells and Wireless Onboard Communication". In: *Proceedings of 2nd International Conference on Recent Advances in Space Technologies*, pp. 167–172. DOI: 10.1109/RAST.2005.1512556.

UK Ministry of Defense and Defense Safety Authority (2020). *Management of radiation protection in defence: part 2 guidance (JSP 392): Chapter 29: items and components containing thorium (December 2020)*. URL: %5Curl%7Bhttps://assets.publishing.service.gov.uk/government/uploads/system/uploads/attachment_data/file/946164/JSP_392_Chapter_29_-_THORIUM__Alt_Text_.pdf%7D.

Ulyanov, A. (2013). "Study of silicon photomultipliers for the readout of scintillator crystals in the proposed GRIPS γ–ray astronomy mission". In: *PoS* INTEGRAL 2012, p. 148. DOI: 10.22323/1.176.0148. arXiv: 1302.5786 [astro-ph.IM].

Ulyanov, A. et al. (2017a). "Using the SIPHRA ASIC with an SiPM array and scintillators for gamma spectroscopy". In: *2017 IEEE Nuclear Science Symposium and Medical Imaging Conference (NSS/MIC)*, pp. 1–3.

Ulyanov, Alexei et al. (Feb. 2016). "Performance of a Monolithic $LaBr_3$:Ce Crystal Coupled to an Array of Silicon Photomultipliers". In: *Nuclear Instruments and Methods in Physics Research A* 810, pp. 107–119. DOI: 10.1016/j.nima.2015.11.148.

Ulyanov, Alexei et al. (Feb. 2017b). "Localisation of Gamma-Ray Interaction Points in Thick Monolithic $CeBr_3$ and $LaBr_3$:Ce Scintillators". In: *Nuclear Instruments and Methods in Physics Research A* 844, pp. 81–89. DOI: 10.1016/j.nima.2016.11.025. arXiv: 1701.05548 [astro-ph.IM].

Ulyanov, Alexei et al. (2020). "Radiation Damage Study of SensL J-series Silicon Photomultipliers Using 101.4 MeV Protons". In: *Nuclear Instruments and Methods in Physics Research*

Section A: Accelerators, Spectrometers, Detectors and Associated Equipment 976. https://doi.org/10.1016/j.nima.2020.164203, p. 164203. ISSN: 0168-9002.

Vedrenne, Gilbert et al. (2009). *Gamma-Ray Bursts: The Brightest Explosions in the Universe*. Springer.

von Kienlin, A. et al. (Apr. 2020). "The Fourth Fermi-GBM Gamma-Ray Burst Catalog: A Decade of Data". In: *The Astrophysical Journal* 893.1, p. 46. DOI: 10.3847/1538-4357/ab7a18. URL: https://doi.org/10.3847/1538-4357/ab7a18.

Wall, Ronan et al. (2017). "Fly Your Satellite! 2017 CubeSat Proposal EIRSAT-1". unpublished.

Walsh, Sarah et al. (Apr. 2020). "Assembly Integration and Verification Activities for a 2U CubeSat EIRSAT-1". In: *Proceedings of the 3rd Symposium on Space Educational Activities*. DOI: 10.29311/2020.33. URL: http://dx.doi.org/10.29311/2020.33.

Walsh, Sarah et al. (2021). "Development of the EIRSAT-1 CubeSat through Functional Verification of the Engineering Qualification Model". In: *Aerospace* 8.9. ISSN: 2226-4310. DOI: 10.3390/aerospace8090254. URL: https://www.mdpi.com/2226-4310/8/9/254.

Werner, Norbert et al. (2018). *CAMELOT: Cubesats Applied for MEasuring and LOcalising Transients - Mission Overview*. DOI: 10.48550/ARXIV.1806.03681. URL: https://arxiv.org/abs/1806.03681.

Winkler, C. et al. (Nov. 2003). "The INTEGRAL mission". In: *Astronomy and Astrophysics* 411, pp. L1–L6. DOI: 10.1051/0004-6361:20031288.

Woolf, Richard S. et al. (2022). "Characterization of Glowbug: a gamma-ray telescope for bursts and other transients". In: *Space Telescopes and Instrumentation 2022: Ultraviolet to Gamma Ray*. Ed. by Jan-Willem A. den Herder et al. Vol. 12181. International Society for Optics and Photonics. SPIE, 121811O. DOI: 10.1117/12.2630543. URL: https://doi.org/10.1117/12.2630543.

Yu, Yun-Wei et al. (2022). *Gamma-Ray Bursts*. DOI: 10.48550/ARXIV.2204.04417. URL: https://arxiv.org/abs/2204.04417.

Zhan, S. et al. (2010). "Dendritic Growth on the Die Under Hermetic High Temperature Operation". In: *2010 Prognostics and System Health Management Conference*, pp. 1–6. DOI: 10.1109/PHM.2010.5413500.

Zhang, Dali et al. (Mar. 2019). "Energy response of GECAM gamma-ray detector based on LaBr3:Ce and SiPM array". In: *Nuclear Instruments and Methods in Physics Research Section A: Accelerators, Spectrometers, Detectors and Associated Equipment* 921, pp. 8–13. DOI: 10.1016/j.nima.2018.12.032. URL: https://doi.org/10.1016%2Fj.nima.2018.12.032.

Zoglauer, A. and Andritschke, R. and Schopper, F. (Oct. 2006). "MEGAlib - The Medium Energy Gamma-ray Astronomy Library". In: 50.7-8, pp. 629–632. DOI: 10.1016/j.newar.2006.06.049. URL: https://ui.adsabs.harvard.edu/abs/2006NewAR..50..629Z.